University of Southampton

Faculty of Engineering and Physical Sciences

Bioengineering Science

Continuous-flow reactors for large-scale production of nanoparticles

by

Domenico Andrea Cristaldi

ORCID ID https://orcid.org/0000-0002-8279-1496

Thesis for the degree of Doctor of Philosophy

May 2020

Al Trio

Abstract

Nowadays, nanoparticles are involved in an enormous amount of applications, including energy-saving and material science, anti-cancer and antimicrobial therapies, drug delivery and the treatment of infectious and parasitic diseases. However, they are often expensive to purchase or challenging to produce. Specifically, achieving fine control over their size and/or shape, by managing the correct stoichiometry of the reaction, is a crucial task to accomplish. This challenge becomes even more demanding for researchers working towards large-scale production processes.

Continuous-flow reactors have been previously used to address those issues. However, their manufacturing, particularly for devices containing nano- and micro-sized channels, requires not only expensive materials but also laborious protocols, which must be performed within exclusive facilities under controlled environmental conditions (such as cleanrooms).

Identifying an economically favourable and simple-to-perform translation from batch-synthesis to large-scale flow-production of size- and shape-controlled nanomaterials, was the main aim of the present PhD project.

Particularly, cost-effective flow-reactors were conceived and manufactured using 3D printing, either directly or via the soft-lithographic approach. The latter method was the most adopted, and allowed the realisation of the here called 3D printed replica mould casted (3DP-RMC) flow-reactors. The high-resolution Objet Connex 350 and the fused deposition modeling (FDM) Ultimaker 2+ 3D printers were tested, and their moulds were characterised and compared. The research led to the development of novel methods and protocols such as the pump-free 3D printed reactor-in-a-centrifuge (RIAC), light-activated flow-reactors, the thermally-controlled flow-synthesis and the bonding procedure via pressure-sensitive adhesive tape.

The effectiveness and reliability of the conceived reactors were proven through the synthesis of representative inorganic and organic nanoparticles. From the inorganic nanomaterials' perspective, silver nanoparticles (AgNPs) were selected as largely applied in numerous fields, ranging from drug delivery to antibacterial and sensing, due to the combined effects of the material itself and their shape- and size-dependent optical properties.

Although silver nanospheres (AgNSs) were produced, due to a parallel collaboration with the Defence Science and Technology Laboratory (Dstl), particular attention was focused on the batch- to flow-synthesis translation of near infrared (NIR) absorbing silver nanoprism (AgNPrs). The low reproducibility of the batch method was demonstrated as well as the improvements made on the customised flow-reactors. For the latter, the UV-vis and TEM characterisations demonstrated the production of AgNPrs with a consistent wavelength absorbance maxima (WA_{max}) of ~ 870 nm and a ~ 30% improved SD. Moreover, regarding the large-scale goal, AgNPrs were obtained at the operating flor-rate of tens of mL/min, which is notably higher when compared to the previously published flow-studies, which operated at more than 5 mL/hour.

Manufacturing improvements were made and reactors were generally designed and tested, based on the application, to achieve the desired control over the mixing regimes, chemical ratios and stoichiometry, as well as to minimise production costs.

In order to validate their feasibility for the production of organic nanomaterials, and to demonstrate their robustness and reliability, nanovesicles such as liposomes and niosomes were also produced.

RIAC and 3DP-RMC bonded on pressure-sensitive adhesive tape were able to produce silver nanospheres with a WA_{max} of 404 and 398 nm respectively, and liposomes having a diameter < 250 nm. The possibility of drastically simplifying the manufacturing protocols and reducing the production cost of continuous-flow devices was highlighted by the pressure-sensitive adhesive tape solution, that allows manufacturing flow-reactors at <£5 per device and a fabrication time <24 hours.

Differently, the optical fibre embedded devices were used for the first photo-assisted flow-bioproduction of silver nanospheres (AgNSs) by bacteria. Finally, by using high-resolution 3D printed moulds, reactors bonded on glass were demonstrated to be sealed even when operating submerged into a thermal bath at 50 °C.

Table of Contents

Table of Tables

Table of Schemes

Table of Figures

Table of Figures

Table of Figures

Table of Figures

Table of Appendix figures

Table of Appendix figures

Research Thesis: Declaration of Authorship

Print name:	Domenico Andrea Cristaldi

Title of thesis:	Continuous-flow reactors for large-scale production of nanoparticles

I declare that this thesis and the work presented in it are my own and has been generated by me as the result of my own original research.

I confirm that:

1. This work was done wholly or mainly while in candidature for a research degree at this University;
2. Where any part of this thesis has previously been submitted for a degree or any other qualification at this University or any other institution, this has been clearly stated;
3. Where I have consulted the published work of others, this is always clearly attributed;
4. Where I have quoted from the work of others, the source is always given. With the exception of such quotations, this thesis is entirely my own work;
5. I have acknowledged all main sources of help;
6. Where the thesis is based on work done by myself jointly with others, I have made clear exactly what was done by others and what I have contributed myself;
7. Delete as appropriate None of this work has been published before submission or Parts of this work have been published as:

[Add references here] otherwise delete

Signature:		Date:	03/04/2020

Acknowledgements

I would like to thank my supervisors
Dr Xunli Zhang, Dr Eugen Stulz and Dr Dario Carugo,
who provided me an opportunity to join their team,
supporting me on my studies and related works.

Furthermore, a special thanks goes to my colleagues and lab mates,
for helping me in both research and life.

Thanks to all the amazing friends that shared this
intense period with me through good and bad times.

Thanks to my flatmates, my life was flowing because of you.

Thanks to S. for supporting me from far away
regardless the direction of our paths.

Last, but not least,

I am extremely thankful to my family, for being close to me against the distance.

Definitions and Abbreviations

A	Absorbance
*****	refers to the oxygen plasma treatment
/	refers to the adhesive tape bonding
3DP-RMC	3D printed replica mould casted
Å	Angstrom
ABS	Acrylonitrile dutadiene styrene
$AgNO_3$	Silver nitrate
AgNPrs	Silver nanoprisms
AgNPs	Silver nanoparticles
AgNSs	Silver nanospheres
A_{max}	Absorbance maxima (intensity)
AuNPs	Gold nanoparticles
CA	Capping agent
CAD	Computer-aided design
CR-1	Chemicals ratio test 1
CR-2	Chemicals ratio test 2
CR-3	Chemicals ratio test 3
De	Dean number
D_h	Hydraulic diameter
DLP	Digital light processing
DLS	Dynamic light scattering
DMA	Dimethylamine
ε	Extinction coefficient
EM	Electromagnetic spectrum
FDM	Fused deposition modelling
H_2O_2	Hydrogen peroxide
HBL	hydrophilic-lipophilic value
HCl	Chloridric acid

HFF	Hydrodynamic flow focusing
HR	High resolution
I	Intensity of the transmitted light
I_o	Intensity of the incident light
IR	Infra-red
K	Diffusion coefficient
l	Optical path length
LOC	Lab-on-Chip
LSPR	Localised surface plasmon resonance
LSPR	Localised surface plasmon resonance
μ	dynamic viscosity of the fluid
MHA	16-mecaptohexadecanoic acid
mL/h	Millilitre/hour
mL/min	Millilitre/minute
$NaBH_4$	Sodium Borohydrate
NIR	Near infra-red
nm	Nanometers
NPs	nanoparticles
OC350	Objet Connex 350
OD	Optical density
OD_{max}	Maximum optical density
OF	Optical fibre
PDI	Poly dispersity index
Pe	Péclet number
PLA	Polylattic acid
PVP	Polyvinylpyrrolidone
P_{wet}	Wetted perimeter
Qdot	Quantum dots
r	Radius
rcf	Relative centrifugal force
Re	Reynolds number

rpm	Revolution per minute
RT-1	Reproducibility test 1
RT-2	Reproducibility test 2
SD	Standard deviation
SEM	scanning electron microscopy
SERS	Surface-enhanced raman scattering
SiO_2@AgNPr	Silica coated silver nanoprisms
ST	stereolithgraphy
T	Transmittance
TA	Tannic Acid
TEM	Transition electron microscopy
TEOS	Tetraorthosilicate
TSCD	Tri-sodium citrate dihydrate
Tt	gel-to-liquid transition temperature
u	Kinematic viscosity of the fluid
U2+	Ultimaker 2+
UV-Vis	Ultraviolet-visible spectroscopy
v	fluid velocity
VR	Volume ratio
WA_{max}	Wavelength of Absorbance maxima
w_f	Estimated focused stream width
WHO	World Health Organization
XPS	X-ray photoelectron spectroscopy
XRD	x-ray diffraction
λ	Wavelength
µMi-REM	micromilling-replica moulding
ρ	fluid density
τ_{mix}	Mixing time

Chapter 1 Introduction and Overview

Starting from a general perspective, and leading toward a more detailed description, this Chapter presents an overview of the research project - placed in the wider scientific context - including the fundamental concepts and state-of-the-art. It starts with a general introduction to nanoparticles, their categories and applications. Furthermore, the main aim is introduced and its rationale discussed. Nanoparticles' properties and characterisation techniques are reported, as well as an overview on microfluidics, in order to understand the principles of this technique and its advantages for the production of nanomaterials.

This is followed by a detailed explanation of the objectives of the study and the description of the thesis' structure. A high-level literature review is included in this Chapter, summarising state-of-the-art and research gaps.

1.1 Nanoparticles: an overview

Simply defined as any material having dimensions within the nanometer scale in width, length and thickness, nanoparticles (NPs) have been widely adopted since ancient times. They are in fact, the cause of specific colours in pigments or properties of materials. The iridescence of a famous decorative Roman cup exposed at the British Museum – known as "the Lycurgus cup" and made in AD 400 - is a perfect example. Romans obtained an iridescent surface that maintains a green colour under reflected light, but reveals a brilliant red when the light shines through. Only in 1990, with the advent of the atomic force microscopy (AFM) technique, it was discovered that this characteristic behaviour is due to an alloy of gold, silver and copper when a specific ratio occurs.[1] Mediaeval Romans also added metal particles into glass to create stained windows for decorations. Interestingly, in this case, the different shades of the reflected colour are due to different sizes of the same nanomaterial (silver nanoparticles). These examples prove that, despite they didn't have knowledge of the underlying chemical-physical processes, artisans of the past learned from what it can be nowadays considered a purely empirical approach, by following precise preparation procedures.

The composition of nanomaterials can be of any kind, including organic, metallic, inorganic or even hybrid. The Maya Blue pigment is an example of a hybrid organic/inorganic nanostructured material, composed of palygorskite, clay and indigo.[2]

Nanomaterials started to be employed long time ago, but the intuition that led researchers to a deeper scientific understanding of their chemical and physical properties is relatively recent. An interesting report by A. Nordman *et al.*[3] describes the historical path that seems to crown Herbert Gleiter as the father of nanotechnology. Apparently, Gleiter's intuition was sparked after J. Ziman *et al.* defined the "Principles of the Theory of Solids" in 1964. Ziman *et al.* stated that the change in properties of most crystalline solids is due to any geometrical anomaly such as vacancy, impurities, defects or imperfections that disturb the regularity of arrangement of atoms. This mainly occurs near the boundaries, when the chemical structure of the materials has to rearrange, in order to reach its lower and most stable energy level. In 1981 Gleiter *et al.* noted a dramatic change of the material properties when diminishing the material size, due to the proportional increase of the rearrangement effect of the boundary layer.

Since then, nanomaterials have been distinguished based on their length in the XYZ directions and categorised into two groups, namely one and zero-dimensional, such as thin-films or quantum wells, nanowires, and quantum dots respectively.[4] Nowadays the definition of nanoparticles has in fact become more specific, including any material having dimensions within 100 nm in height, width, and depth.[5] Since the Ziman and Gleiter period, nanoparticles made of any material or

combination of materials, have been therefore studied, characterised, and produced in order to push the scientific knowledge forward, and to be able to embrace the largest and most challenging amount of applications.

Researchers are currently able to regulate nanoparticles' properties by choosing their composition and structure, managing size and shape, and also modifying their surface to convey additional or complementary functions (Figure 1.1).[6]

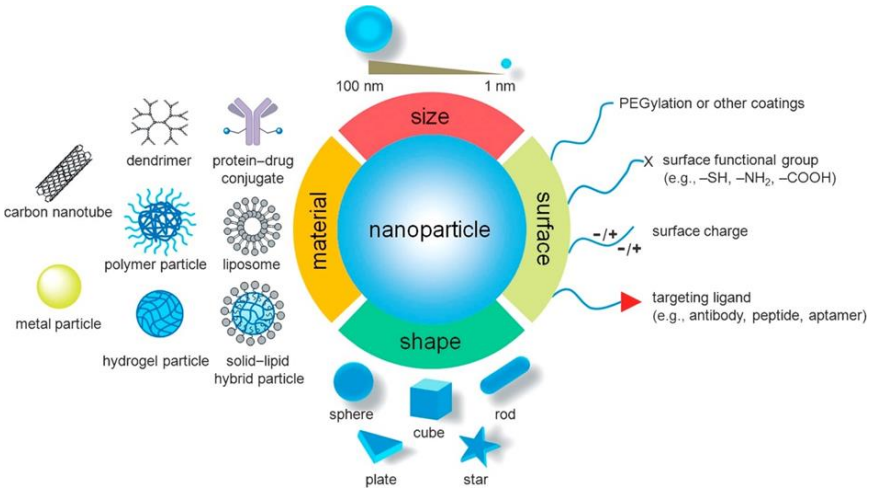

Figure 1.1 Graphical representation of various nanoparticles, and their size range, shape and surface coating.[6]

Many examples can be mentioned to describe nanoparticles' functions. For instance, carbon nanotubes (or nanosheets) are entirely made of carbon atoms covalently connected to each other's following a trigonal planar geometry. This specific geometry allows the carbon's spare valence electron to give the characteristic directional electrical conductivity to the nanomaterial.[7] These have been developed from a more prominent carbon structure known as the spherical molecule of fullerene.[8] However, considering their well-known low solubility, carbon nanomaterials could not have been as revolutionary as they are now without the parallel investigation of their chemical functionalization processes,[9] which allow them to be adopted for an enormous spectrum of applications.[10,11]

Organic nanoparticles typically include any material, or combination of materials, having organic nature. Some examples include polymers,[12] molecules (i.e. dendrimers), or a combination of those in the form of covalently connected units or as supramolecular aggregates.[13] Regarding the applications of nanomaterials, polymers and lipids are widely adopted as organic nanomaterials for health-related purposes such as therapeutics, or for improvements in diagnostic[14], primarily due to their biocompatibility.

In contrast, gold (Au), silver (Ag), platinum (Pt) or any nanostructured noble metal, lie into the inorganic nanomaterial category, and more specifically into the group of metal nanoparticles (MNPs).[15] As previously mentioned, gold nanoparticles (AuNPs) have been adopted for a long time and a review of their history, size-related properties and applications, is provided by Didier and Astruc.[16] Silver nanoparticles also present enhanced antibacterial properties, which make them appropriate for applications in food industry or biomedicine (i.e. packaging, biosensors etc.).[17]

In general, inorganic nanomaterials can be made of an incredibly vast combination of inorganic elements. Oxides such as titanium dioxide (TiO_2), zinc oxide (ZnO), silicon dioxide (silica, SiO_2), for instance, are applied in fields like cosmetics, coatings and photocatalytic applications. It is also worth to mention that multi-layered quantum dots (Qdot) are leading the semiconductor and optoelectronic research fields.[4]

Finally, the combination of organic/inorganic nanoparticles has paved the way to the field of hybrid nanomaterials, which clearly unlocks a colossal potential in any field, from electrochemistry to drug delivery.[18,19]

The hypothetically infinite combination of nanoparticles that might be created, and related chemical and physical properties, reflects the likewise great number of applications nanoparticles can be adopted for. A visual overview of the variety of fields involved is presented in Figure 1.2.

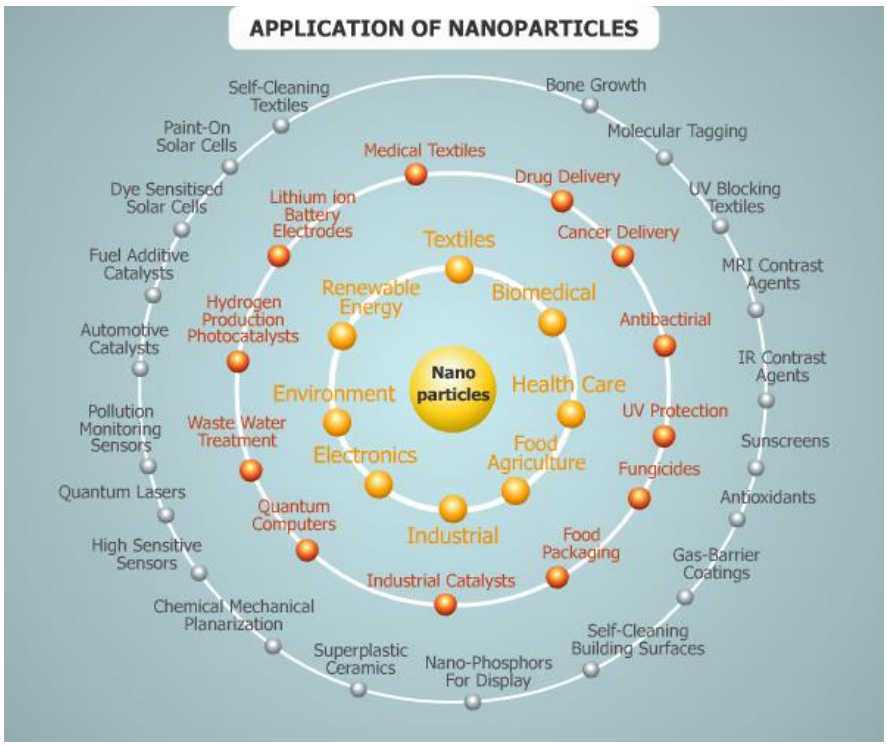

Figure 1.2 Schematic representation of the fields of application of nanoparticles (source: prochimia.com).

Notably, nanoparticles are largely employed in medicine-related applications, and their synthesis might involve difficult procedures, or be expensive to accomplish. Consequently, the improvement

of their synthesis, already critical at a laboratory scale, becomes extremely significant when aiming at large-scale production.

It is legitimate to state that covering the entire state-of-the-art for all nanomaterials and possible applications would be an entire research topic on its own. This is made even more ambitious when considering the possibilities that researchers have nowadays to functionalise nanoparticles with other molecules and tune them for specific goals. Nevertheless, some of the latest progress on nanoparticle's technology, divided into composition, properties and applications, are presented in Table 1.1.

Table 1.1: Latest developments in nanomaterial's composition and applications

Nature	Properties	Applications	References
Organic	Photoacoustic; Energy conversion; Carrier, encapsulation; SERS (surface enhanced Raman scattering) pH sensitivity Long-term fluorescence;	Photoacoustic; Photothermal conversion; Theranostic; Bioimaging; Probe and sensors; High-contrast and selective staining; Imaging;	Jiang and Pu 2017[20] Wu *et al.* 2019[21] Madamsetty *et al.* 2019[22] Guan *et al.* 2019[23] Chang *et al.* 2019[24] Boucard *et al.* 2018[25] Ahmed *et al.* 2019[26]
inorganic	Fluorescence; UV-Vis absorption and LSPR NIR absorption Biodegradability; Magnetic; Photoactivation;	Optical sensing; Photocaltalisis towards green chemistry; Thermal nanofluids Cancer theranostic; Environmental and biomedical Antibacterial;	Ng *et al.* 2016[27] Peiris *et al.* 2016[28] Kimpton *et al.* 2020[29] Zhou *et al.* 2020[30] Mohammed *et al.* 2017[31] Miller *et al.* 2015[32]
Hybrid	Engineering; High surface/bulk ratio; Functionalisation; Photothermal	Antibacterial; Catalysis; DNA sensors; Multimodal imaging;	Miller *et al.* 2015[32] Park *et al.* 2015[33] Kaur *et al.* 2018 [34] Shi *et al.* 2018[35]

1.2 Thesis rationale and selection of nanomaterials

For a better understanding of the rationale behind the present research project, some concepts have to be introduced. Firstly, although it is described in detail at the end of this Chapter (Aim and objectives, section 1.5), an anticipation of the main purpose of the research is appropriate.

The present research aims at finding the most simple and cost-effective manufacturing solution for continuous-flow reactors that are suitable for the meso- to large-scale production of size- and shape-controlled nanoparticles.

In this context, meso-scale refers to production flow rates between 1 and 10 mL/min, whereas large-scale refers to production flow rates in the order of tens of mL/min. Nanoparticle's size and shape are highly dependent on reagents' stoichiometry. Therefore, flow-reactors have been chosen for their greater capacity of controlling mixing between chemical species compared to batch synthesis. On the other hand, as discussed later in the thesis, flow-reactors can be expensive to produce, or may not be simple to operate by non-expert users. Consequently, this research aimed at improving the state-of-the-art in continuous flow reactors to achieve simplified manufacturing methods, with a view towards large-scale production of nanoparticles. In order to demonstrate the efficiency of the devices developed in this research, two types of model nanoparticles (organic and inorganic) were selected. In particular, attention was devoted to nanomaterials which present challenges in relation to the control of their physical properties during production.

Specifically, silver nanoparticles, having spherical and prismatic shape, were selected as a model for metal/inorganic nanomaterials, whereas vesicles (liposomes and niosomes) as an organic/supramolecular model nanomaterial.

As already anticipated, and further discussed in Chapters 2 and 4, silver nanoprisims (AgNPs) largely satisfy the requirement for applicability across numerous fields. Particularly, they exhibit extremely diverse shape-related optical properties. They are therefore a suitable candidate for demonstrating both mixing efficiency of flow-reactors as well as control over reagents' stoichiometry during their synthesis. Silver nanospheres (AgNSs) can be chemically mutated to AgNPrs, which drastically changes their optical property, giving an intense absorption band in the near-infrared (NIR) region of the electromagnetic spectrum. This chemical-physical property leads to a second reason for selecting AgNPs in this research, which relates to an ongoing collaboration with the Defence Science and Technology Laboratories (Dstl).

In order to demonstrate the versatility of the manufactured flow-reactors, vesicles were chosen as an organic representative. They can be formed using several formulations and protocols, and are one of the most employed carriers for drug delivery. Attention was devoted especially on liposomes

and niosomes, which have a broad range of biomedical applications and are ideal candidates for achieving simultaneous synthesis and drug encapsulation within flow-reactors. The production of vesicular systems can be translated from batch to flow-synthesis in order to achieve size-control of the supramolecular aggregates.

In order to better understand why and how inorganic nanoparticles are related to specific properties, it is appropriate to familiarise with several concepts such as the electromagnetic spectrum and Black Body theory, absorption of the electromagnetic radiation (ER), and localised surface plasmon resonance (LSPR). Moreover, the microfluidic approach is described as well as the adopted nanoparticle's characterisation methods such as ultraviolet-visible spectrophotometry (UV-Vis), transmission electron microscopy (TEM) and dynamic light scattering (DLS).

1.2.1 Electromagnetic radiations

The waves that propagate through space radiantly, transporting the electric and magnetic components, are defined as the electromagnetic (EM) radiation.[36]

The EM spectrum includes all the known wavelengths that range from the radio waves to the gamma-rays, in which the visible spectrum is represented by all colours we are able to see by eye and covers a very small portion of wavelengths (Figure 1.3).

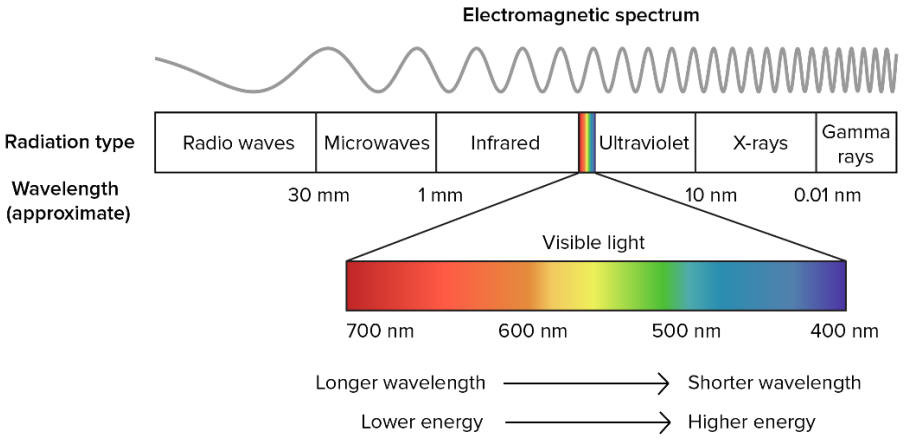

Figure 1.3 Representation of the electromagnetic spectrum showing a magnified view of the visible portion between ultraviolet and infrared (image from catalyticcolor.com).

Even though this is widely acknowledged nowadays, the relation between electromagnetic radiation and energy was understood from the most brilliant minds during 1900-1916, and it was finally explained by the Planck-Einstein relation.[37] Equation [1] shows the correlation between wavelength (λ), defined as the distance between two exact points of the electromagnetic wave (i.e. two peaks or two lows), the frequency (ν) which refers to the number of waves per time unit, and the speed of light ($c = 299\ 792\ 458\ m/s$):

$$\nu = \frac{c}{\lambda} \; ; \qquad [1]$$

Equation [2] shows the correlation between the frequency and the Planck's constant (h = $6.62607004 \times 10^{-34}\ m^2kg/s$), with respect to the energy (E):

$$E = h\nu; \qquad [2]$$

It can be stated that the smaller the wavelength the higher is the frequency, which is directly related to the energy. Generally, the visible light range (Figure 1.3) is considered as the energy separation gap between ionizing and non-ionizing radiations. Particularly, ionizing radiations possess enough energy to be able to remove an electron from the external shell of specific atoms, or break molecular bonds, thus creating ions. In contrast, non-ionizing radiations can only stimulate vibrations on materials' bonds without structural modifications.

X-rays are a common form of high energy radiation adopted for medical purposes. Ranging from 10^{-9} to 10^{-12} m (λ), X-rays possess enough energy to easily pass through soft organic tissues while being limited when reaching the more dense bone structures. This is the basic concept behind radiological films for recognising bone fractures or misalignments. At the same time, the so-called "dose of radiation" is a parameter that must be taken into consideration to minimise potentially dangerous pathologies - as side effects of prolonged exposure - such as DNA mutations. For these reasons, they are classified by the World Health Organization (WHO) as carcinogenic, although the benefits of X-ray technology far outweigh the potential negative consequences of using them. In analytical and material chemistry-related fields, X-rays are suitable for usage in techniques such as X-ray photoelectron spectroscopy (XPS),[38] and X-ray diffraction (XRD), as well as in imaging techniques such as transmission electron microscopy (TEM) and scanning electron microscopy (SEM).

On the other hand, Infrared Radiations (IR), are less energetic and predominantly involved in heat transfer phenomena. Particularly, the near infra-red (NIR), which ranges from 0.7 to 3 μm in wavelength, covers almost 50 % of the solar energy spectrum ($0.3 < \lambda < 3$ μm), followed by the heat radiation (i.e. thermal infrared), which can reach up to 50 μm in λ.[39] Moreover, being non-ionizing radiations, the IR range results in a less invasive effect on organic tissue and therefore it's more suitable for biological applications.[40]

1.2.2 Radiation absorption and black body

When encountering a material, the incident electromagnetic wave can be transmitted, reflected, diffracted and/or absorbed. The latter phenomenon, and the most interesting for this project,

occurs for materials in which an electron transition - from a ground to an excited state - is allowed. Measuring absorption is therefore extremely useful to determine and characterise materials, molecules and their interactions. The absorbance capability of any material is compared to the ideal black body introduced by Kirchhoff, which constitutes an attempt to summarize the state of knowledge in radiative heat transfer in 1860.[41] The black body is considered capable of absorbing all incident electromagnetic radiation, independent from its angle of incidence or frequency. Moreover, in a thermal equilibrium condition, it emits the highest amount of energy at every frequency, with complete independence from the direction of the emissions.[41]

1.2.3 Localised Surface Plasmon Resonance (LSPR)

The capacity of metal nanoparticles to interact with the electromagnetic radiation, giving useful optical outputs, is due to a phenomenon called localized surface plasmon resonance (LSPR).

This can be considered as the most important reason why NPs are directly involved in many applications. Nevertheless, the electromagnetic-field enhancement indirectly caused by the LSPR is the fundamental principle behind techniques such as surface-enhanced Raman scattering (SERS).[42] Willets states that plasmonic materials such as gold, silver and copper, are capable of supporting LSPR as they possess a negative real and small positive imaginary dielectric constant. Moreover, the resonance condition occurs, for nanoparticles only, when their size is smaller than the wavelength of the incident EM (Figure 1.4).

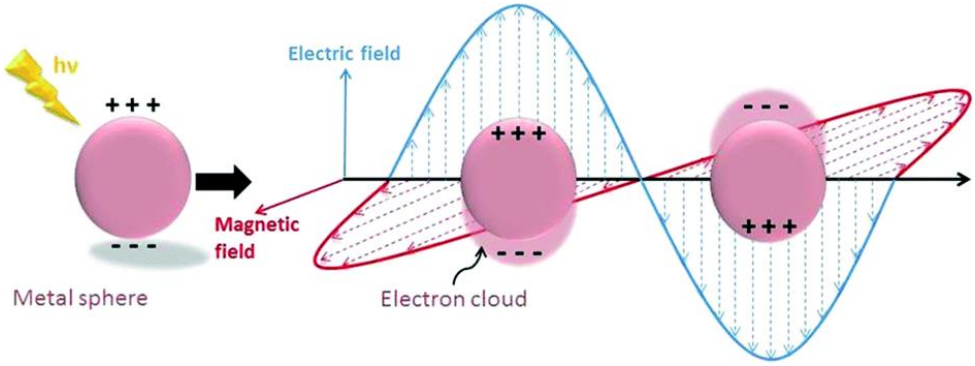

Figure 1.4 Representation of the surface plasmon resonance on the electrons of silver nanospheres.[28]

Under the action of an electromagnetic field, nanoparticles' electrons start to oscillate, transforming energy from the incident electromagnetic wave into, for example, thermal energy in an absorption process.[43] LSPR is detected as absorption, and the range, intensity and shape of the absorbance band are attributable to factors such as the interaction with the solvent, coating material, aggregation, size, and most importantly the shape of the nanoparticles. The latter gives the precious advantage of regulating the wavelength of the absorption peak by tuning the size

and/or the shape of a specific nanomaterial.[43] The great benefit of gold and silver nanoparticles is related to the fact that the LSPR effect lies within the visible range of the electromagnetic spectrum, making these materials highly suitable for sensing applications.

1.3 Characterisation techniques

The characterisation techniques mainly adopted for the research project are: ultraviolet-visible spectroscopy (UV-Vis); transmission electron microscopy (TEM); dynamic light scattering (DLS). Although these methods are widely established, a general overview of their basic principles and applications is herein presented.

1.3.1 Ultraviolet-visible spectroscopy (UV-Vis)

Ultraviolet-visible (UV-Vis) spectrophotometry is a widely adopted characterisation technique that allows detecting the interaction between incident electromagnetic radiations, within the ultraviolet-visible wavelength range, and the fluid sample. The principle is based on the capacity of certain molecules or colloidal nanoparticles to absorb the incoming radiation energy resulting in the excitation of the sample's electrons from a ground to an excited energy state. Intuitively, this is the most commonly used technique for the previously mentioned LSPR analysis.

Briefly, a monochromator positioned on the other side of the sample opposite to the light source allows scanning the sample to obtain the transmittance value (*T*) for each wavelength, expressed as the percentage ratio between the intensity of the transmitted and the incident light (Figure 1.5).

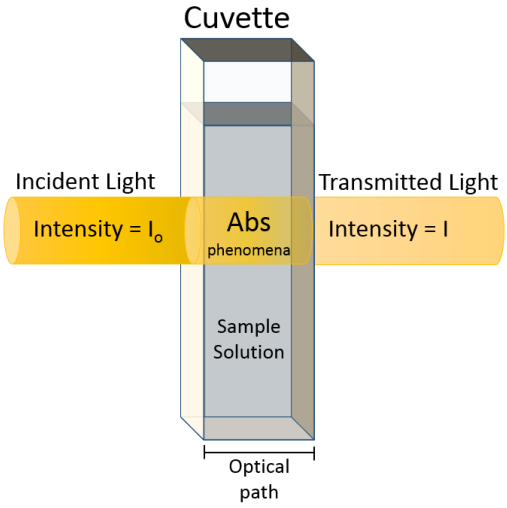

Figure 1.5 Schematic representation of the UV-vis spectrophotometric principle. The collimated incident light travels through the sample positioned into a quartz cuvette (sample holder), which then transmits a less intense radiation.

Molecules having delocalised electrons, such as aromatic rings, have a propensity for absorbing energy, due to the $\pi - \pi^*$ electron transition, which is suitable for supramolecular UV-Vis titrations.[44] Non-bonging electrons are also commonly shifted to anti-bonding orbitals by the energy absorbed through the light. Therefore, the absorbance bands are characteristic for each electron transition, and sensitive to the surrounding environment of the sample. UV-Vis spectroscopy is in fact adopted for detailed evaluation of the behaviour of particles or molecules,

giving important information on concentration,[45] aggregation, supramolecular interactions,[44] interaction with the surrounding environment or solvent, and so on.

The concentration of the sample can be calculated based on Lambert-Beer law (Equation 3). In particular, the absorbance (*A*) can be derived from the measured *T* value, and correlated with the length of the optical path length (*l*) and the extinction coefficient (ε), which is a characteristic value of the sample under specific conditions (such as solvent variations).

$$A = log\frac{1}{T} = -logT = \varepsilon lC \qquad [3]$$

Generally operating in the 190 - 900 nm range, UV-Vis is widely adopted due to its simplicity of usage while permitting accurate measurements. Moreover, excluding photodegrading samples, this is a non-destructive technique.

1.3.2 Transmission electron microscopy (TEM)

Transmission electron microscopy (TEM) is generally regarded as one the most powerful characterisation methods for imaging nanostructures due to its nanometer- to atomic-scale resolution. Figure 1.6 shows a visual summary of the most employed microscopy techniques, compared to the human eye limit, in the 1 Å to 1 mm range.

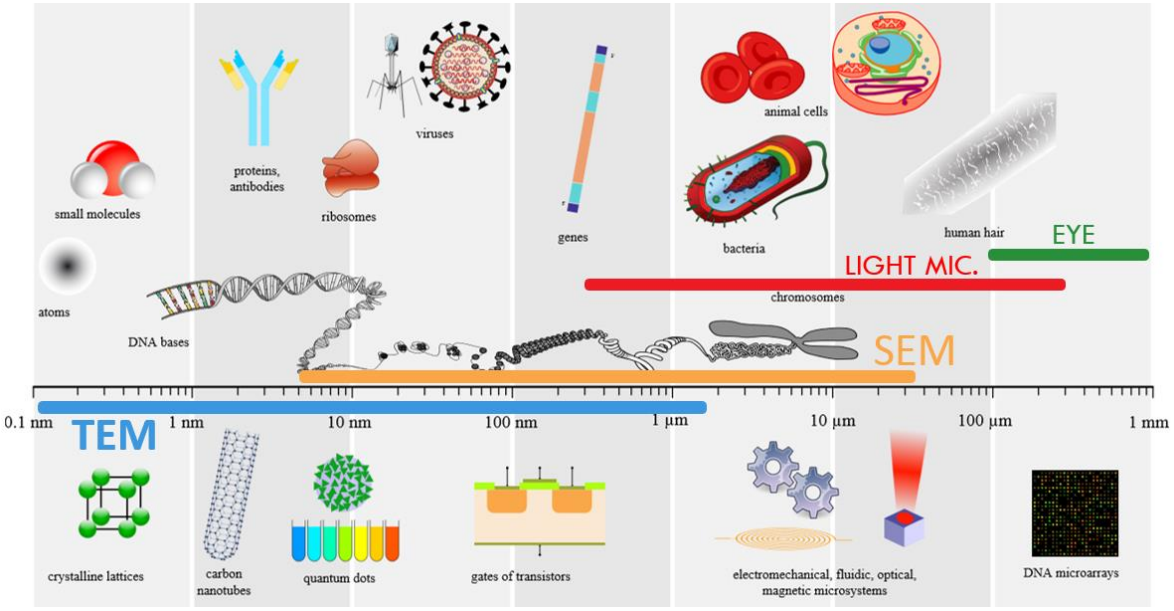

Figure 1.6 Graphical representation of organic and inorganic nanomaterials in the sub-millimetre scale, associated with the coloured bands representing the detectable range for eye (green), light microscopy (red), scanning electron microscopy (green), and transmission electron microscopy (blue). Image modified by commons.wikimedia.org.

The figure also highlights examples of organic and inorganic systems (above and below the scale bar respectively), for a general correlation between imaging methods and dimensions. With respect to the organic samples, this ranges from human hair to molecules, passing through cells and proteins, whereas microarrays, microsystems and quantum dots are examples of inorganic materials. Moreover, coloured bars in the figure differentiate between the most common microscopy-based imaging techniques.

The photoelectric effect is the underlying phenomena that allows TEM to be such a powerful tool. Briefly, in a transmission electron microscope, electrons are produced from an electron gun and driven to the space holder passing through a sequence of magnetic lenses. Once the incident electrons reach the specimen, a portion of those is transmitted or diffracted whereas others interact with the analysed matter producing events such as secondary, back-scattered, Auger electrons as well as X-ray or visible light (Figure 1.7).

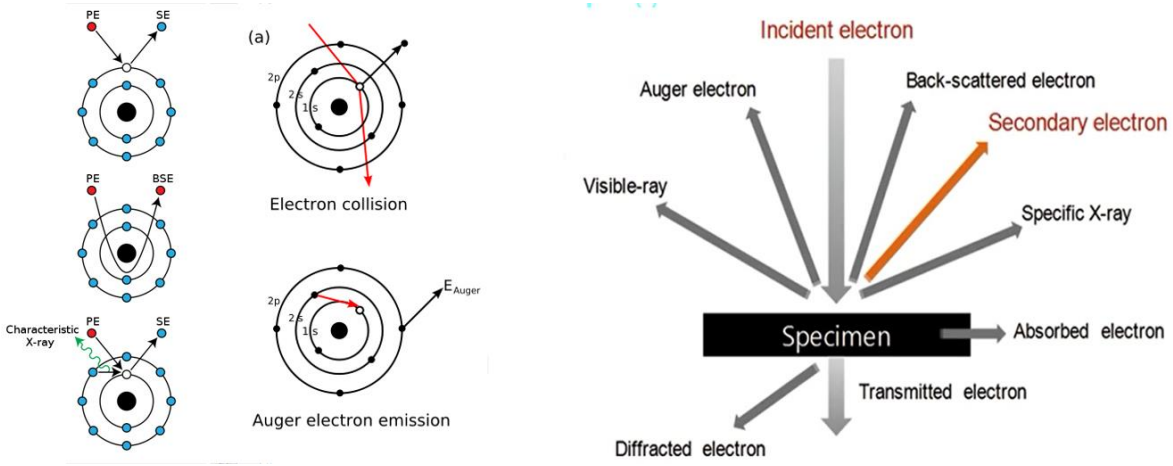

Figure 1.7 Schematic representation of the effect of incident radiation on an atom (left). Representation of all the secondary radiations obtained after the incident radiation impacts the specimen. Transmitted and diffracted electrons can pass through the sample (combined figures from wikipedia.org)

In inorganic constituents, TEM is capable of giving information about crystal structures and atomic plans, particularly when equipped with diffractometers.[46] When aiming at morphological analysis of these materials the sample preparation only requires a support grid (often carbon and farvar coated, to be transparent to the incident electron), in which an aliquot of inorganic sample is drop-casted and positioned inside the vacuumed chamber of the TEM.

Differently, materials having an organic nature present several issues: i) they cannot be positioned in a vacuum as they have a high water content, ii) due to their organic nature, they cannot create enough contrast for the TEM to resolve the structure, and iii) they have to be solidified and sliced for allowing electrons to be transmitted, thus avoiding image overlapping due to the sample thickness. Laborious protocols need to be performed to overcome these limitations. These start with chemical fixation, to preserve the organic sample with minimal alteration of volume and

morphology from the native state (commonly with glutaraldehyde (GA), paraformaldehyde, osmium tetroxide, uranyl acetate (UA) and tannic acid), and continue with post-fixation using osmium tetroxide. The osmication enhances contrast, which is important during the analysis with TEM. In order to introduce contrast inside the samples, post-staining procedures can also be performed using heavy metal salts, such as uranyl formate (or acetate), ammonium molybdate, methylamine tungstate.[47]

After fixation with buffered fixatives, the sample is dehydrated at increasing concentrations of a solvent (a combination of either alcohol or acetone with propylene oxide) to enable infiltration with a liquid resin. Epoxy resin is most commonly used in conventional TEM (supersaturated and surrounded by resin); the cured resin block containing the organic material is thinly sectioned (40–150 nm). However, in the last decade, cryo-electron microscopy has been highly improved and, in combination with dedicated software analysis, it has moved the detection limit towards single proteins and molecules. An interesting overview about the state of the art of cryo-electron microscopy was recently published by D. Lyumkis.[48]

1.3.3 Dynamic light scattering (DLS)

Important information on the sample's size can be obtained by a dynamic light scattering (DLS) technique, which allows to calculate the hydrodynamic radius of macromolecules in solution, when illuminated unilaterally.[49] Also known as photon correlation spectroscopy (PCS), this technique permits the study of several properties such as dimensions and behaviour of macromolecules in solution, based on the chosen coupling of the light source and the detector of the setup. The main example is known as the Tyndall effect, and relates to studies on disperse or colloidal systems, and the capacity of such systems to scatter light in all directions.[50]

For diluted solutions of very small and non-conducting particles, subject to constant volume concentration, the relative intensity of the light scattered at right angles to the axis of illumination is given by the following Equation [4]:

$$I = \frac{kv}{\lambda 4}\left(\frac{n_i^2 - n^2}{n_i^2 + 2n^2}\right)^2 \qquad [4]$$

where k is a constant of proportionality; v, the mean volume of the particles; λ the wavelength of the light used; and n_i and n are the indices of refraction of disperse phase and medium respectively. Within a given system, for which n_i and n are constant, the magnitude of the Tyndall effect is directly proportional to the mean volume of the particles. The condition and changes of dispersion of a system are therefore directly related to the Tyndall effect.

Although DLS is an effective tool for dimensional analysis, it suffers from some limitations. Primarily, the technique is very sensitive to temperature and solvent viscosity, which must be precisely controlled and quantified in order to obtain reliable results. Moreover, as it is not able to resolve particles that are too close to each other, it is considered a low-resolution technique.[49]

As a commonly-used technique, DLS was employed in this project for gathering information on the size dispersity of organic vesicles (liposomes) and combined with TEM for reliable morphological and size distribution analysis.

1.4 Microfluidics

The term "*Microfluidics*" generally refers to the widely accepted definition given by G. M. Whitesides (Nature 2006):[51]

"Microfluidics is the science and technology of systems that process or manipulate small (10^{-9} to 10^{-8} litres) amounts of fluids, using channels with dimensions of tens to hundreds of micrometres."

In its definition, Whitesides highlights the importance of the channel size and identifies a specific dimensional range. Notably, microfluidics is not only the miniaturization of a macroscale experiment, but the physical scaling-down brings with it additional characteristics. At these dimensional scales, the fluid flow is typically laminar, since viscous forces dominate over inertial forces, and transport of chemical species is often governed by diffusion. Moreover, some important physical properties, such as surface area-to-volume ratio and surface tension, do not simply scale linearly with reducing the size of a physical domain.[52]

Laminar flow is characterized by a steady fluid motion with fluid streamlines parallel to each other having high momentum of diffusion and low momentum of convection, whereas turbulent flow is typically characterized by the presence of vortices and flow metrics fluctuate in space and time. The flow regime depends on the fluid velocity, fluid physical properties (density and viscosity), and geometrical properties of the fluidic domain.

Whitesides[51] describes that, at the early stages of microfluidics development, four main research fields were mostly involved: (i) analysis, (ii) biodefence, (iii) molecular biology, and (iv) microelectronics; all of which contributed strongly to the growth of this technology. Analytics was overall widely used, especially in microanalytical methods such as gas-phase chromatography (GPC), high-pressure liquid chromatography (HPLC) and capillary electrophoresis (CE).

Biodefence applications have had a significant rise after the 1990s due to DARPA's (Defence Advanced Research Projects Agency) significant investments. At that time, microfluidic systems

were designed and used as chemical and biological detectors, in order to prevent biological attacks after the end of the cold war.

In those years, research fields such as genomics and molecular biology were rising, and required further technological developments, particularly in the fabrication of microarrays with higher sensitivity and resolution. Microfluidics became a useful technology platform to address those requirements.

The growth of microelectronics was particularly accelerated with the introduction of photolithography, which represented a significant step towards scaled-up production of microfluidic devices. Many microelectromechanical systems (MEMS) were thus fabricated involving the use of glass or highly transparent polymers such as polydimethylsiloxane (PDMS).

Microfluidics allows the realization of multi-step experiments in small devices, referred to as lab-on-chip (LOC) (Figure 1.8), with the main advantages being fine kinetic control, *in situ* process characterization, and minimal waste in chemicals or resources. Nowadays, microfluidics is covering an extremely wide range of applications ranging from electronics handle processing and conduction of electrical signals in rigid circuits,[53] to the synthesis of different nanoparticles for biomedical purposes.[54] Furthermore, the growth of microfluidics is manifest in increased commercial translation of devices by major manufacturing industries and enterprises, for various applications (human diseases, genomics, diagnostics, molecular testing, genotyping, microarray analysis, cell analysis etc.).[55]

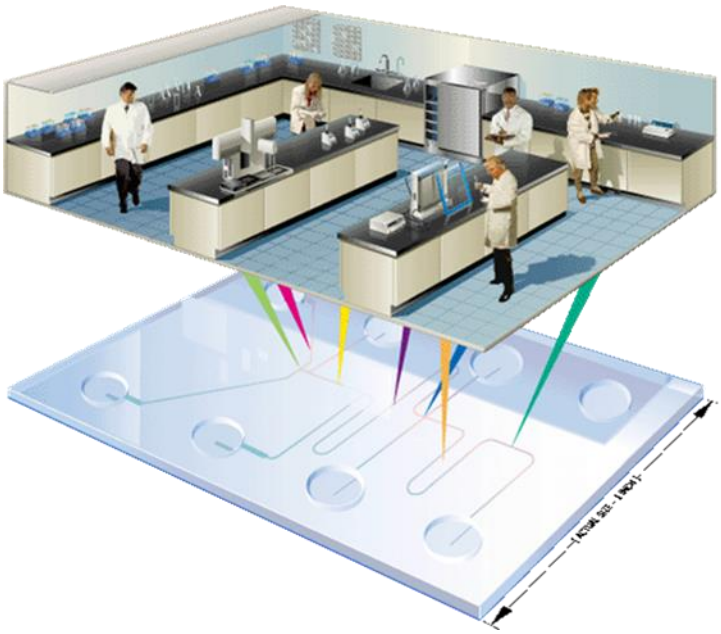

Figure 1.8 Graphic representation of the lab-on-a-chip concept: the translation of laboratory protocols to a single miniaturised device. (Image from http://lab-on-chip.gene-quantification.info/)

Generally, kinetic control over the synthesis of nanoparticles is an important pre-requisite in order to regulate the size and shape of the end product. The diffusion-dominated mixing provided by microfluidic systems has in fact been exploited for controlled synthesis of inorganic particles, such as core-shell nanoparticles,[56] or to modulate the self-assembly of drug delivery vehicles such as liposomes.[57]

However, limitations of the technique must be considered, especially if aiming at large-scale and industrially viable production. Firstly, the high manufacturing costs are related to the materials and facilities involved in the production of these devices. Fabrication methods can also be extremely complicated and time-consuming as further described (1.4.2). Moreover, the size of the channels limits the maximum flow rate achievable (due to the high backpressure) and could also often lead to channel's clogging during production of nanomaterials at industrially relevant concentrations, especially for colloids.

1.4.1 Fundamentals and mixing

The flow regime in microfluidic architectures is crucial. It could be laminar, transitional, or turbulent (though uncommonly seen), based on the design and dimension of the channels, fluid's velocity and physical properties. The Reynolds number (*Re*) (Equation 5), is a dimensionless value adopted to identify the flow regime under the assumptions of: (i) constant viscosity (Newtonian fluid) and density (incompressible fluid), (ii) straight channel, and (iii) negligible body forces and pressure across the fluid film.[52]

$$Re = \frac{\rho\, v\, D_h}{\mu} = \frac{v\, D_h}{u} \qquad [5]$$

where ρ (Kg/m^3) and v (m/s) are fluid density and mean velocity, respectively; D_h (m) is the hydraulic diameter of the channel; μ (Kg/m·s) is the fluid dynamic viscosity, and u (m^2/s) is the fluid kinematic viscosity.

The hydraulic diameter (D_h) can be determined (Equation 6) by the wetted perimeter P_{wet} (m), and the channel cross-sectional area A (m^2):[52]

$$D_h = \frac{4A}{P_{wet}} \qquad [6]$$

Reynolds numbers (*Re*) up to 1500 generally correspond to laminar flow. For *Re* greater than 2500 the flow is typically turbulent. The range between 1500 and 2500, however, is considered as a transitional regime. Normally, *Re* in microfluidic devices is significantly lower than 100, and the flow is thus in a laminar regime.[52]

The dimensionless Péclet (*Pe*) number[58] is used to define the mixing regime in a physical domain. It represents the ratio between advective and diffusive mass transport (Equation 7), and is calculated as follows:

$$Pe = \frac{l\,v}{K} \qquad [7]$$

where *l* (m) is the length of the channel, *v* (m/s) is the fluid velocity, and *K* (m^2/s) is the diffusive coefficient. At *Pe* < 1 diffusion dominates over advection, whereas at *Pe* > 1 advection dominates. The mixing is typically considered convection-dominated at *Pe* greater than 2.

From the definition of Reynolds and Péclet numbers, it is evident that the channel geometry significantly affects the flow and mixing regimes. The achievable total flow-rate also influenced by the *Re* and *Pe*, but is mostly limited by the increasing backpressure. For a given fluid and channel architecture, greater volumetric flow rate leads to greater backpressure. Specifically, the relationship between flow rate and pressure drop is given by the Hagen–Poiseuille's law (Equation 8).[59] For a Newtonian liquid flowing through a circular channel with circular cross-section of radius (*r*), and in laminar flow conditions, the pressure drop along the channel (ΔP) can be calculated from:

$$\Delta P = \frac{8\mu l Q}{\pi r^4} = \frac{8\mu l}{r^2} v \qquad [8]$$

From which it is possible to derive that the volumetric flow rate Q is equal to:

$$Q = \frac{\pi \Delta P r^4}{8\mu l} \qquad [9]$$

Where, *l* (m) is the length of the channel, *Q* (cm^3/s) is the volumetric flow rate, *v* (m/s) is the average velocity of the fluid and μ (Kg/m·s) is the fluid viscosity. Equations [8] and [9] clearly highlight the effect of the channel's cross-sectional area on fluid's pressure and/or volumetric flow rates, as any small variation to the channel's hydraulic diameter strongly influences these flow metrics.

However, not only is the cross-sectional area important, but also the channel shape in the length direction. For instance, the above dimensionless numbers are not able to capture effects resulting

from alterations in the geometry along the channel (i.e., due to the presence of a curvature in the channel centreline). In fact, a curved channel (i.e. spiral-like) would have a greater mixing compared to a straight channel of the same length, when operated at specific conditions that induced secondary flows (Figure 1.9).[60] Secondary flow (described more in details Chapter 3, in section 3.2) in curved channels occurs in the form of vortices – in a plane perpendicular to the main flow direction - caused by the rising of inertial forces. These inertial effects can be increased by operating the device at increasing volumetric flow rates (or Reynolds numbers).

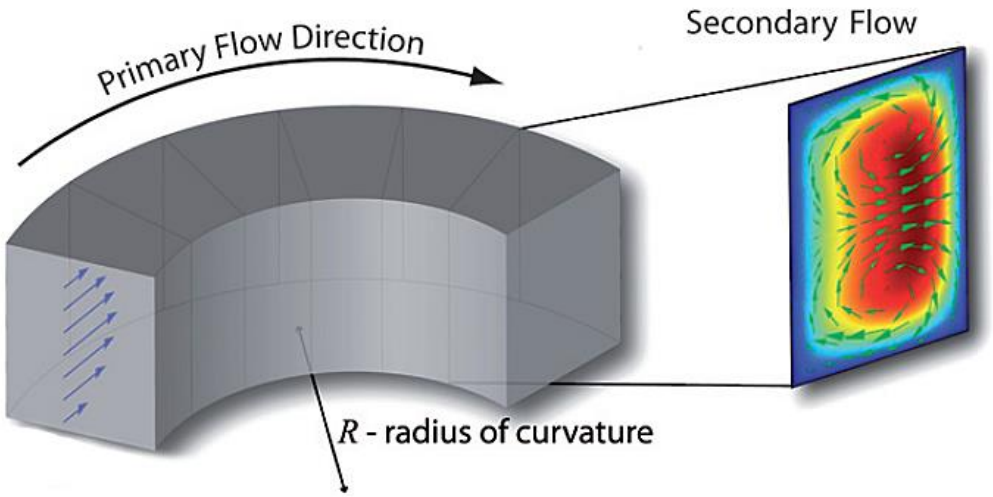

Figure 1.9 Graphical representation of a section of a curved channel and its respective radius. The primary flow follows the channel architecture, whereas internal vortexes representing the secondary flow are visible in the cross sectional plane (right).

Notably inertial forces can play a crucial role on flow and mixing processes in microfluidic systems[61], where Dean number (*De*) (Equation 10) is employed to quantify the effect of channel curvature on the flow field, and specifically on the onset of secondary flows. It is calculated as follows:

$$De = Re\sqrt{\delta} \qquad [10]$$

where: $$\delta = \frac{D_h}{2\,R} \qquad [11]$$

The Dean number relates the Reynolds number with the channel geometry, and specifically the channel radius of curvature (*R*). Therefore, specifically designed flow-channels and boundary conditions in a device can be developed to improve reaction's control.

In order to achieve successful scaling-up of nanoparticle's production, it is crucial to gain a pervasive understanding of the mixing regime in these devices. Fluid transport and the mixing of chemical species do not simply scale linearly with the size of the channels or the flow rates of the reaction. Notably, for a diffusion-dominated mixing process, increasing the channel width would result in a significant increase in the diffusion (and mixing) time required to achieve complete mixing.

To overcome this limitation, the concept of flow-focusing has been introduced in the late 1990s, in which the mixing time and length can be significantly reduced by hydrodynamic focusing of a flow stream. In its typical configuration, shown as example in Figure 1.10, a flow-focusing device has three inlets converging into a junction, where the liquid introduced from the central inlet (Solvent A) is focused by the two lateral streams (Solvent B).

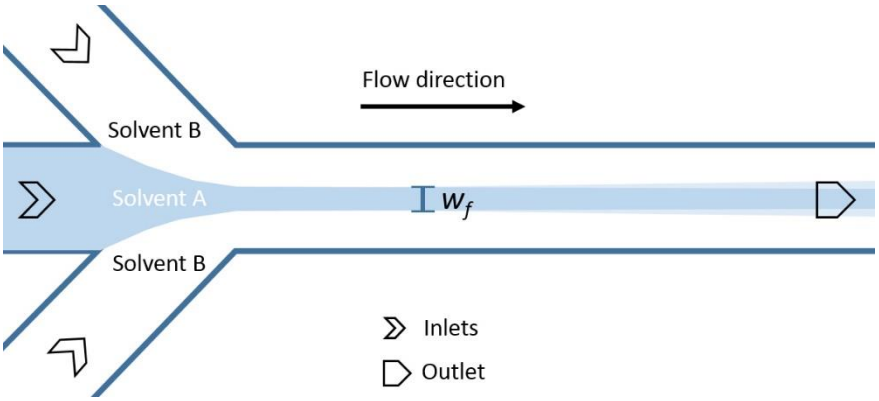

Figure 1.10 Graphical representation of an HFF junction with three inlets converging into a junction were the central stream is focused. Operating parameters can be varied in order to regulate the focused stream width (w_f).

The mixing time (τ_{mix}) needed to achieve complete mixing in this device configuration can be obtained by relating the theoretically or experimentally estimated focused stream width (w_f), with the diffusion coefficient (K) of the solvents:[62]

$$\tau_{mix} = \frac{w_f^2}{4\,K} \qquad [12]$$

The mixing time thus scales with the central stream width squared. This means that, if one would like to scale up the w_f of a 10 cm long microfluidic channel from 100 μm to 1 mm, the equivalent channel length for achieving complete mixing would be 10 m, which poses limitations in terms of manufacturing and priming volumes.

Hydrodynamic flow focusing (HFF) and curved channels can be convenient design features to be considered when translating microfluidic reactors to the millifluidic scale, allowing enhanced

control over diffusion and/or advection-based mixing regimes. In fact, depending on the reactor dimensions, and consequently on the volume capacity, these devices can be classed as either nano- (1–100 nm), micro- (100 nm to 1 mm) or milli-fluidics (1–10 mm).[63] In this definition, IllG refers to the inner dimensions of the reactor's features (i.e. therefore micro-structured reactor would be a more accurate definition), and implies the association with tiny reactors, in terms of outer dimensions, with corresponding low production rates. For clarity, in this context a most general definition is thus applied for micro- and milli-fluidics, which refers to the volume capacity of the device being in the order of microliters (μL) and millilitres (mL) respectively.

Microfluidics is - without doubts - a high-performance technique that however requires complex or expensive manufacturing procedures (see Chapter 3). Differently, the millifluidic approach presents several advantages, including the cost-effectiveness, rapidity and versatility of manufacturing. Moreover, although for millifluidics the surface-area-to-volume ratio remains high, and the relatively large cross-sectional area causes a slower diffusion process, challenges such as high pressure drop and low lifetime are minimised. The latter is a very important advantage for the applications presented in this research.[64]

In order to achieve complete mixing using millifluidics, specifically designed architectures and boundary conditions need to be identified. However, the potential higher throughput and greater device's lifetime for millifluidic systems, makes them a suitable design choice to achieve the main aim of this research. Millifluidic devices also have great potential for parallelisation, which would enhance throughput even further, for possible uses in industrial-scale production. For instance, in the case of microfluidic droplet generators (MFDGs), the throughput of a single device is usually not more than 10 g/h, or less than 100 kg per year, and parallelisation is necessary to increase the product throughput.[65]

Therefore, in this study, meso-scale flow rates (1 to 10 mL/min) per single device were aimed for the production of organic vesicles. This was comparable with what in the literature is defined as high throughput production.[66] Differently, tens of mL/min (large-scale) were aimed for the flow production of inorganic nanomaterials. This would strongly improve previously reported rates of microfluidic-production of AgNPrs, which are in the order of a few mL/h.[67] In order to achieve these production rates, attention in this project was devoted to advection-dominated forms of mixing within scaled-up mixers.

1.5 Aim and objectives of the PhD project

The main **aim of the research project** is to develop and build cost-effective continuous-flow reactors, to facilitate the synthesis of size-controlled organic and inorganic nanoparticles towards their meso- to large-scale production.

Based on the rationale outlined in Section 1.2, silver nanoparticles (spheres and prisms) were selected as representative inorganic nanomaterials, whereas liposomes (and niosomes in one case) were chosen as a model organic material.

In order to reach this high-level aim, several objectives needed to be accomplished:

The **first objective** was to reproduce, develop and optimise a batch protocol for the synthesis of silver nanoparticles. With respect to AgNPrs, this had to favour the production of particles with a red-shifted A_{max}. Most importantly, the protocol needed to be translatable into flow-systems. The **second objective** was to develop cost-effective, fast, easy-to-make, as well as reproducible and reliable methods to manufacture flow-reactors for the production of the selected organic and inorganic nanoparticles. The **third objective** related to the characterisation and testing of such developed reactors, to verify that they meet the following criteria. The size of the channels should be uniform and with a good degree of fidelity when compared to the CAD drawings. Moreover, the structure must prevent leakages at relatively high total flow rates. If needed, flow-focusing conditions must be easy to achieve. The possibility to operate devices at the desired mixing regime and tune mixing efficiency is also critical. The lifetime of the device was also evaluated, as well as the possibility to re-use it. The **fourth objective** was to demonstrate the efficacy and repeatability of the manufactured reactors by synthesising inorganic nanoparticles. This objective was particularly focused on the production of AgNPrs, as well as the ability to improve control over particle's size and reproducibility with respect to batch protocols. Similarly, the **fifth objective** was to validate such reactors for the synthesis of liposomes with clinically acceptable diameter. This also included the demonstration of the effectiveness of a specifically conceived device for the production of size-controlled niosomes under thermally controlled conditions.

Objectives were refined throughout the research based on the findings obtained at any specific stage of the study. Moreover, specific focus was also devoted to parallel objectives in some cases, which contributed to developing specific aspects or functionalities of flow-reactors. One of such objectives related to the evaluation of a batch procedure for the synthesis of silica-coated AgNPrs that could be translatable into flow-devices.

1.6 Organisation of the Thesis

The first chapter presented an overview of the research background. In particular, nanoparticles were introduced, together with their range of applications; techniques that allow their characterisation were also described, as well as principles and advantages of microfluidics. Finally, the aim and objectives of the research were stated.

The thesis is organised into a sequence of Chapters, each corresponding to a specific stage or application area of the developed technologies. In each Chapter, the literature review addressing a specific aspect of the research is analysed in greater detail. This is followed by the description of the employed methods, the results and their discussion, and conclusions.

Specifically, **Chapter 2** is focused on the batch synthesis of AgNPs. The evaluation of a suitable formulation for silver nanoparticles (nanoprisms in particular) is presented, in order to identify the most effective formulation in the perspective of a flow-synthesis translation. Chemicals concentrations and stoichiometry, and solvent volume ratios are examined and discussed. Reactors designs, and the diverse manufacturing processes, are presented In **Chapter 3**. This Chapter covers all the employed or conceived manufacturing methods for the cost-effective production of flow reactors based on the selected application. The production of every conceived design is detailed in this Chapter independently from the purpose of its realisation. The subsequent Chapters are separated by the nature of the produced nanoparticles. The production of inorganic and organic nanoparticles is covered in **Chapters 4** & **5**, respectively. This includes UV-Vis, TEM and DLS characterization of nanomaterials to demonstrate reactors' efficiency. Finally, **Chapter 6** presents a coating protocol for AgNPs with a layer of silica, whereas **Chapter 6** highlights conclusions and future work, including details about the parallel improvement of the silica coating procedure of AgNPrs. Finally, additional research projects carried out during the PhD programme, as well as supporting information, are presented in the **Appendix section**.

Chapter 2 Batch Synthesis of Silver Nanoparticles: understanding silver nanoparticles towards translation to flow-production

2.1 Introduction and state-of-the-art: silver nanoparticles

Silver nanoparticles have been largely employed since ancient times and – more recently – they have gained significant interest because of their antibacterial,[68,69] optical,[70] and conductive[71] properties. The applications of AgNPrs range from infrared absorption[72] and thermofluids,[73] through photocatalysis[74] and optoelectronics,[75] to many bio-related applications.[76]

The value of AgNPs in these applications is largely attributed to the previously mentioned shape- and size-related LSPR, which gives AgNPs a wider range of optics-associated capabilities. Intensive research has demonstrated that various geometries can be obtained including Ag nanospheres,[77] nanocubes,[78] nanorods,[79] nanowires,[80] and nanoprisms.[81]

Nevertheless, a further key property is related to their very high surface-area-to-volume ratio, which is significantly higher when compared to bulk materials, improving nanoparticle's properties when compared to the macroscopic scale.[82]

Concerning their synthesis, nanomaterials can be generally produced through either bottom-up or top-down approaches.[83] The bottom-up approach relies on the self-assembly process which, after seed generation, leads to the formation of nanostructures. Quantum dots and formation of nanoparticles from colloidal dispersions are common examples.[15] In contrast, the top-down approach starts from macroscopic structures, which can then be reduced to nanoscale systems.[15]

In this research, AgNPs were produced *via* a bottom-up batch synthesis approach, with the goal of finalising the most suitable batch protocol for further translation to flow-synthesis. Although the production of spherical nanoparticles was mainly carried out, a focus of the research was also on finding the simplest yet most appropriate protocol for obtaining particles of prismatic shape and consistency in size.

2.1.1 Synthesis of silver nanospheres

For the batch synthesis of AgNSs, several chemical, physical and biological processes have been explored.[84] In the most applied chemical procedures, an ionic Ag precursor is reduced by a specific agent, or method, to its metallic state. This starts the nucleation with formation of seeds, followed by controlled growth of nanoparticles. Various reaction parameters can be regulated for achieving the desired product including reaction temperature, pH, concentration, type of precursor, reducing and stabilizing agents, and of course the molar ratio between those.[85]

The important aim of minimising particles' aggregation is related to the choice of the capping or stabilising agent. An exhaustive overview of synthetic methods for AgNSs was presented in 2014 by Iravani et al.[5] Furthermore, a recent and more updated overview was presented by Lee et al. in 2019.[86] for AgNSs and their production towards application in nanomedicine.

Although chemical methods are the most applied, among the physical procedures, the evaporation-condensation[5] and laser ablation[87] techniques are worth mentioning. The latter, in particular, is an example of a top-down approach in which a bulk metal solid within a liquid is irradiated with a laser.

Both methodologies are able to generate larger quantities of AgNPrs with respect to batch synthesis, and at high purity without the use of harmful chemicals or generation of toxic waste. However, capping agents are not usedin these methods, thus agglomeration is a great challenge to be overcome. Moreover, both approaches consume greater power, and require a relatively longer

synthesis and complex equipment, all of which make them not straightforward and increase their operating cost.[86]

Among the biological approaches, many alternatives have been explored. One of the most recent papers states that an aim in this area is to develop "*a green, eco-friendly, low priced biotechnology that gives advancement over both chemical and physical methods*".[88] The biosynthetic approach aims at improving the scalability of the process and particle's stability, while minimising the use of hazardous chemicals.[89] Recently, in a collaboration with T. Mabey, a review was published on the use of biological processes present within bacteria to mitigate metallic contaminants in their environment, as a potential solution to these challenges.[90] On the other hand, little control over the particle's morphology has been achieved in biological systems.

Table 2.1 Synthesis of AgNSs: an overview (adapted from Iravani et al.)[5]

Method	Silver precursor	Reducing agent	Stabilizing agent	Size (nm)
Chemical reduction	$AgNO_3$	DMF	-	<25
Chemical reduction	$AgNO_3$	$NaBH_4$	Surfactin(a lipopeptide biosurfactant)	3-28
Chemical reduction	$AgNO_3$	Trisodium citrate (initial)+SFS (secondary)	Trisodium citrate	<50
Chemical reduction	$AgNO_3$	Trisodium citrate	Trisodium citrate	30-60
Chemical reduction	$AgNO_3$	Ascorbic acid	-	200-650
Chemical reduction	$AgNO_3$	$NaBH_4$	DDA	~7
Chemical reduction	$AgNO_3$	Paraffin	Oleylamine	10-14
Chemical reduction (Thermal)	$AgNO_3$	Dextrose	PVP	22±4.7
Chemical reduction (thermal)	$AgNO_3$	Hydrazine	-	2-10
Chemical reduction (oxidation of glucose)	$AgNO_3$	Glucose	Gluconic acid	40-80
Chemical reduction (polyol process)	$AgNO_3$	Ethylene glycol	PVP	5-25
Chemical reduction (polyol process)	$AgNO_3$	Ethylene glycol	PVP	50-115
Electrochemical (polyol process)	$AgNO_3$	Electrolysis cathode: titanium, anod: Pt	PVP	~11
Chemical reduction (Tollen)	$AgNO_3$	m-Hydroxy benzaldehyde	SDS	15-260
Physical synthesis	Ag wires	Electrical are discharge, water	-	~10
Physical synthesis	$AgNO_3$	Electrical are discharge	Sodium citrate	14-27
Chemical reduction (microemulsion)	$AgNO_3$	Hydrazine hydrate	AOT	<1.6; 2-5
Photochemical reduction (pulse radiolysis)	$AgClO_4$	Ethylene glycol	-	17-70
Photochemical reduction (microwave radiation)	$AgNO_3$	Ethylene glycol	PVP	5-10
Photochemical reduction	$AgNO_3$	UV light	-	4-10
Photochemical reduction (X-ray radiolysis)	Ag_2SO_4	X-Ray	-	~28
Photochemical reduction (X-ray radiolysis)	$AgNO_3$	CMCTS, UV	CMCTS	2-8

DMF (N,N'-Dimethylformamide); $NaBH_4$ (Sodium borohydrate); SFS (Sodium formaldehyde sulphoxylate); DDA (Dodecanoic acid); PVP (Polyvinyl pyrrolidone); SDS (Sodium docecyl sulphate); AOT (Bis (2-ethylhexyl)surfosuccinate); CMCTS (Carboxymethylated chitosan).

Further studies are needed to understand biological mechanisms, the proteomics involved and, in particular, the right equilibrium with toxicity. Nevertheless, bacteria- and flow-production have been combined, with the help of a physical trigger. Preliminary results on the first photo-assisted bio-flow-synthesis of AgNSs are herein presented (Chapter 4, section 4.3.1.3).

Other than biological approaches, green chemistry methods have also been adopted to minimise the use of harmful chemicals. Many alternatives have been explored, from plant extracts [91] to compounds such as alkaloids, phenolic compounds, terpenoids, enzymes, co-enzymes, proteins, and sugars to reduce ionic Ag to its metallic oxidation state.[92] Thus, flow-translation of a green synthesis method was also evaluated in this study by re-adapting exhisting batch protocols (preliminary results are presented in Appendix A). Among the many alternatives available, the most recent tannic acid (TA) procedure was chosen, as TA plays both roles of reducing agent and capping/stabilising agent.[93,94] In this case, in order to obtain a monodisperse sample of AgNSs, the thermodynamic control is crucial and the reaction should be performed under reflux conditions followed by purification. The synthesis process was then readapted into a novel conceived reactor (Section 4.3.1.2).

The reducing agent method is considered as the most commonly adopted approach, which involves reagents such as sodium borohydride ($NaBH_4$), elemental hydrogen, polyol process, Tollens reagent, N, N-dimethylformamide (DMF), and poly (ethylene glycol)-block copolymers in aqueous or non-aqueous solutions.[5] Following this method, the first indication of AgNPs having a spherical shape is due to the characteristic colour observed just after adding the reducing agent.[77] The absence of oxidizing agent allows the $NaBH_4$ to act without competitors in the kinetics of the reaction. This happens in the presence of capping agents such as tri-sodiun-citrate-dehydrate (TSCD) and polyvinyl-pirrolidone (PVP), which permits to achieve size control while limiting aggregation. This widely established method, slightly adjusted based on previous studies from our research group,[95] was adopted in the present project for the production of AgNSs.

2.1.2 UV-Vis characterisation of Silver nanoparticles

Under UV-Vis characterisation, spherical AgNPs show a single quasi-symmetric absorption band, with an absorbance maximum that lies in a 390 - 450 nm wavelength range, and results in a stable yellow/orange coloured colloidal solution.[96] In the context of the present thesis, the intensity of the band peak is indicated as A_{max}, whereas the corresponding wavelength (where the A_{max} lies), is defined as WA_{max}.

Being a sphere the most symmetric geometric configuration, in the case of isotropic nanospheres, electrons have one dipole oscillation which leads to a stable absorption band centred at about 400 nm for 10 nm particles in water.[97] As a typical example, Figure 2.1, represents the characteristic absorption band as calculated by Paramelle *et al*.[98] Measuring the WA_{max} shifts is, therefore, a powerful method for gathering information about nanoparticle's size (sphere's diameter), aggregation phenomena and the effect of the surrounding medium (solvent, molecules and so on). Paramele presented a rigorous study on the relation between the absorption band and the extinction coefficient for citrate capped AgNSs, to enable estimation of particle concentration.[98]

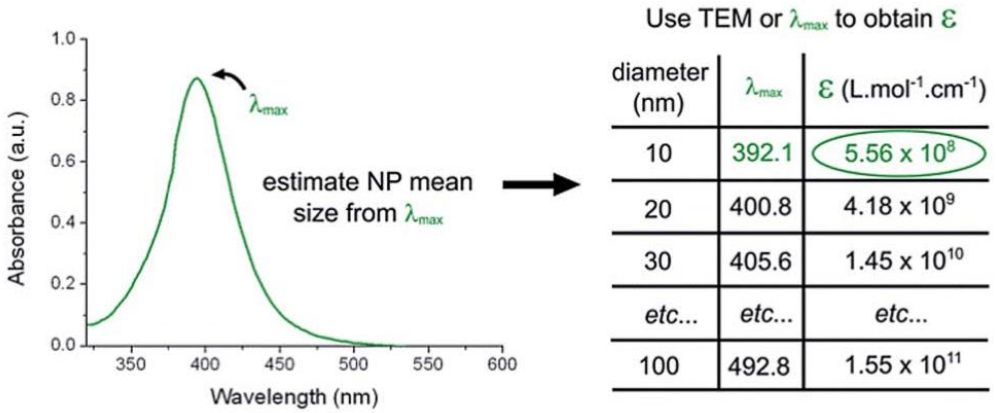

Figure 2.1 The UV-Vis spectrum of a representative sample of AgNSs having WA_{max} = 409 nm*; (Inset) AgNSs colloidal solution as reference colour.*[98]

2.1.3 Synthesis of silver nanoprisms

To synthesize AgNPs in prismatic shape, a more precise control of the stoichiometry during the reaction is required. This makes it a suitable reaction system for the present study in several aspects: i) a flow reactor may provide control over the reaction; and ii) the intense and broad LSPR absorption in the 750-900 nm range is appropriate for NIR applications.[99]

Considering the prismatic shape of the particles, the edge length, the height, the thickness and the aspect ratio, are the most important parameters to be considered for desired products (Figure 2.2,

left panel).[81] Millstone *et al.* also described how absorption, and therefore perceived colour solution, are strongly dependent upon particle shape (Figure 2.2, right panel).

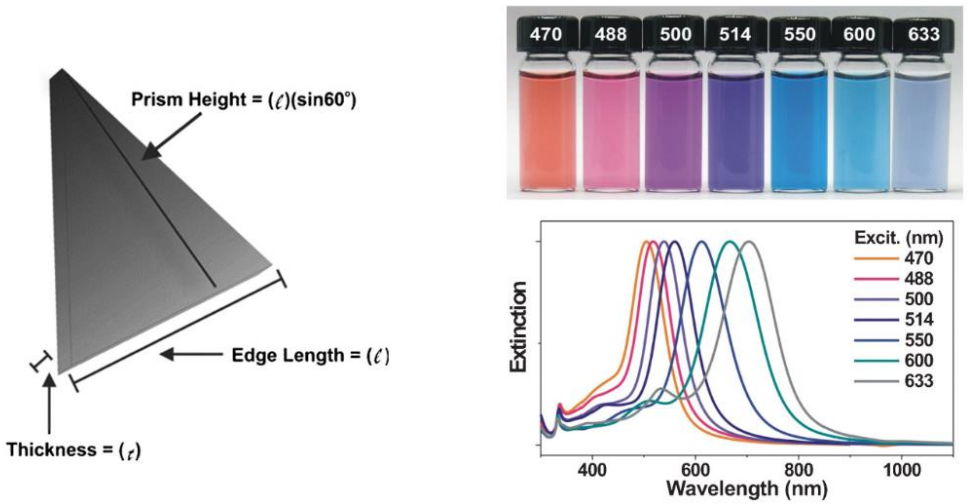

Figure 2.2.Left) Prismatic shape representation. Right) Colour of the solutions and respective absorption spectra of silver nanoprsism at different sizes (from Millstone et al.)[81]

The most important parameter related to the main shift in the absorption spectrum is the prism edge length, with a most enhanced bathochromic shift for bigger particles.[100] However, tip truncation also occurs. Particles with rounded tips generate a plate-like geometry, which is different from sharp tip breaking, therefore are considered as hexagonal nanoprisms.[81] This is crucial information to be taken into consideration for a flow-reactor design for red-shifted absorption. Furthermore, the anisotropy of the particles exhibits three separate and characteristic LSPR bands. A general AgNPRs sample reveals a sharp peak at around 330 nm and, moving towards higher wavelength based on the size, a shoulder followed by the main absorption band. These absorbance bands are attributed to the out-of-plane quadrupoles, in-plane quadrupoles and in-plane dipoles, respectively.[97]

It is interesting to see how the theoretical results from the calculated LSPR absorption spectra (Figure 2.3A relate to the experimental results in terms of WA_{max} for each of the three electron transition. Moreover, the work of Pastoriza-Santos and Liz-Marzan also allows the visualization of the in-plane electron distribution (Figure 2.3B) within the prismatic geometry.[100].

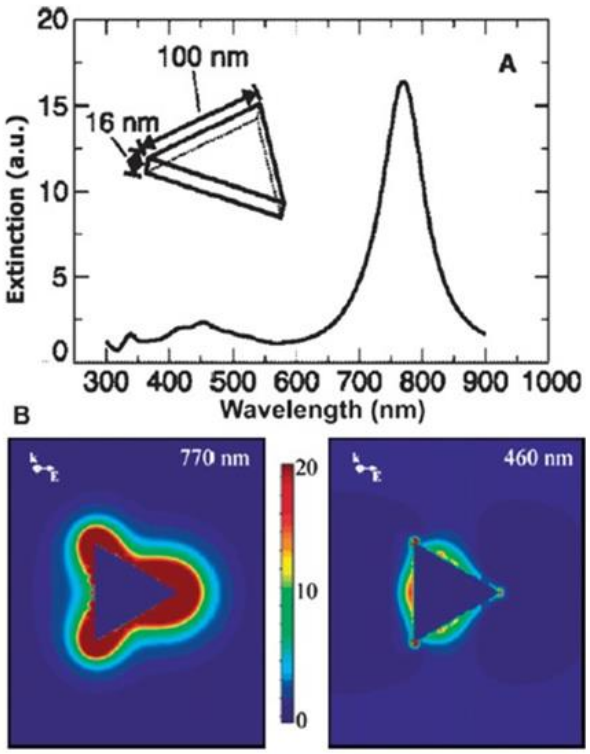

Figure 2.3 Calculations of the absorption spectra for 100 x 16 nm (length x thickness) AgNPrs (A), and the in-plane electron distribution (B) for the dipoles (left, 770 nm) and the quadrupoles (right, 460 nm).[100]

2.2 Synthesis of silver nanoprisms with a re-adapted protocol

Many synthetic routes were examined for the production of AgNPrs. All of them aimed at achieving control over the particle's shape, which can be improved by tuning parameters such as metal ion precursor and its concentration, reducing agent ratios, surfactant concentration, pH, as well as irradiation wavelength in the case of physical methods.[81] For instance, the photo induced conversion of AgNSs to nanoprisms was firstly reported by R. Jin *et al.,* [101] and further simplified by Saade and De Araújo in 2014,[102] using light emitting diodes (LEDs).

On the other hand, work on batch protocols has mainly focused on the type of reducing agent. The use of ascorbic acid at room temperature with poly(sodium styrenesulphonate) (PSSS) as a stabiliser by Aherne et al. represented a starting point, inspiring the present study and the need to better understand the involved growth mechanism.[103] More recently, pH-controlled reactions were also proposed, by varying the dosage of a sodium hydroxide pentanol solution in a more complex ternary system containing water, polyvinylpyrrolidone and n-pentanol.[104] Nevertheless, sodium borohydride ($NaBH_4$), widely used for making spheres, has also been employed as reducing agent for obtaining the prismatic shape.[105.106] This is a well-known method that was also investigated as a

function of the type of capping agent. Trisodium citrate dehydrate (TSCD, or citrate) was tested alone or in combination with polyvynilpirrolidone (PVP) as a further stabilising agent by Zhang *et al.*, who also carried out several experiments on alternative carboxyl compounds. Most importantly, they analysed the role of hydrogen peroxide (H_2O_2) as a key reagent for counterbalancing the reduction process by $NaBH_4$.

Panzarasa *et al.*[97] proposed a similar synthetic route but without using PVP as a secondary capping agent, thus involving fewer chemicals. In this work, the prismatic shape of nanoparticles was characterised by UV-vis spectroscopy, which is the primary technique adopted for such synthesis. Due to its simplicity, in this chapter the Panzarasa method was reproduced to verify its reproducibility. The aim was also to set the basis for the understanding of the synthesis, and at the same time, obtain data for the future batch- to flow-synthesis translation and comparisons. This is discussed in Chapter 4, both with considerations on the manufactured cost-effective flow-reactors designed for the translation to the flow-synthesis.

Recently, a more controlled synthesis of citrated-capped AgNPrs was presented by Haber *et al*.[107] The high level of size-control achieved in this work is related to the UV-vis characterisation, which demonstrated. Although it is not common to present size-related TEM data measuring particles one-by-one, Haber estimated nanoprism sizes and related them to the absorbance spectra of colloidal suspensions in his supporting information. Although not precisely indicated, the particle edge length referring to solutions with WA_{max} of 515, 550, 580, 600, 620 and 730 nm was reported, showing variations between a minimum of~30 nm (for WA_{max} of 515 nm) to a maximum of ~90 nm (for WA_{max} of 730 nm). From the graph is notable that the error bar also increases for bigger particles, however, it is not clear if it is related to SD or max-min values. A similar, but better described, TEM counting method was used in this project for comparing batch to flow synthesis results. On the other hand, Haber's procedure started from already produced seeds, and required overnight reaction and further steps. This is not particularly suitable for transition into a flow-reactor that aims at continuous production at the meso- to large-scale, which is the main goal of this research related to AgNPrs, as further improvement of the previous work of our research group.[67] Based on the idea of adopting said synthetic route, some necessary modifications were made in this study in terms of reagents, channel geometries, and mixing regimes (Chapter 4).

Based on the literature review, the research gap that the initial part of this project aimed to address was the development of a meso- to large-scale flow-production solution for the synthesis of AgNPrs. Particularly, the goal is to evaluate if the Panzarasa method can be translated to flow-synthesis using cost effective reactors to finding a simple flow-based approach for improving the lack of control over particle's size and shape when operating a batch synthesis. Specifically, it is

important to avoid adopting complex or long procedures, which might also involve expensive instrumentation. Therefore, finding the most simple but effective batch synthesis protocol, able to create AgNPrs with shifted absorption towards the NIR, was the initial step of the research.

2.3 Adopted synthetic method for silver nanoprisms

The simplest solution proposed by Panzarasa was therefore adopted in this the project for several reasons: i) it is a well-known procedure; ii) it minimises undesirable side reactions; iii) it allows easier purification processes as less side products are obtained; and iv) it helps in diminishing material or equipment costs, which is beneficial to achieve meso- or large-scale production.

The synthesis utilises silver nitrate ($AgNO_3$) as Ag precursor and $NaBH_4$ as a reducing agent, while it employs citrate as a capping agent[106] instead of PVP. Hydrogen peroxide (H_2O_2) is also involved in the reaction. Being a gentle oxidising agent, H_2O_2 has the delicate yet crucial role to compete with $NaBH_4$ thus slowing down the reduction process.[105]

The following two reactions are involved in the overall process, making the prisms formation quite sensitive to any small stoichiometric change:

$$NaBH_4 + 8\ AgNO_3 + 4\ H_2O \rightarrow Na[B(OH)_4] + 8\ Ag^{(0)} + 8\ HNO_3 \quad [13]$$

$$2\ Ag^{(0)} + H_2O_2 + 2\ H^+ \rightarrow 2\ Ag^+ + 2\ H_2O \quad [14]$$

Importantly, the role of the citrate is critical. In nature, silver nanostructures tend to grow following a hexagonal close packing structure; this means that they have two preferential Miller indexes: the (100) and the (111) planes.[108] This particular structure unlocks the citrate potential, which has the tendency to bind preferentially to the (111) planes of the forming crystals rather than the (100) planes.[103] As illustrated in Figure 2.4, the formation of a prism (right) starts from a seed (left), passes through an intermediate hexagonal geometry (or hexagonal prisms), where the citrate has the main capping role on the (111) planes, blocking the growing mechanism in that direction while allowing the prism to form towards the 100 directions.

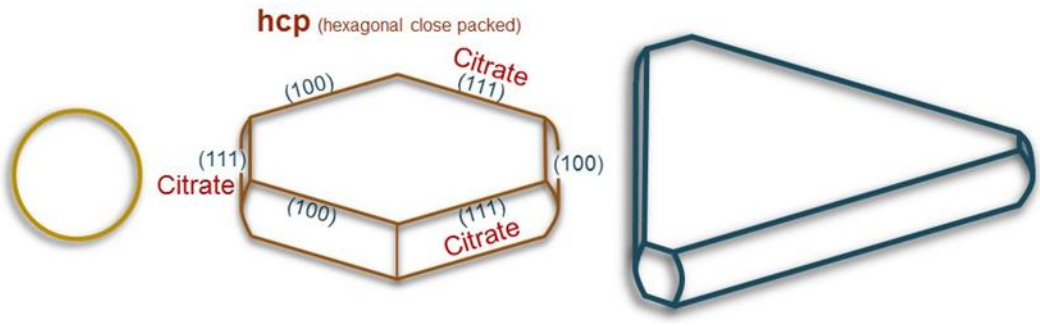

Figure 2.4 Graphical representation of the mechanism of AgNPrs formation.

Clearly, the activity of the capping agent withstands its own kinetics, which must match with the reducing/oxidising agents' competition; this appears to be key principle underlying AgNPrs size regulation.[105]

Moreover, trisodium citrate dihydrate (TSCD) can have a secondary, but not less important role, in addition to their function as capping agent. It acts as a buffer to neutralise the excess amount of nitric acid developed during the reduction step:

$$Na_3C_3H_5(COO)_3 + HNO_3 \rightarrow Na_2HC_3H_5(COO)_3 + NaNO_3 \quad [15]$$

The ratio of reducing agent to oxidizing agent has therefore a relevant role in the mechanism. For this reason, three different reactant ratios were investigated in this study.

Regarding the solvents, the previous batch synthesis was carried out in water. The preparation included two main stages: a stirring solution containing the precursor, capping agent and oxidising agent ($AgNO_3$, TSCS and H_2O_2 respectively), and a fast injection of reducing agent, in a small but highly concentrated volume (less than 1 mL, based on the total volume of the synthesis).

A batch synthesis reproducibility test has been carried out to demonstrate how important the fast injection of $NaBH_4$ in influencing the production of prisms. However, this is a crucial aspect and also limitation that has to be overcome for the translation to flow-synthesis. The flow approach requires samples to be injected into the flow reactor through syringes. This means that samples have to be previously prepared, and be stable over time into the syringe. This is particularly relevant for a highly reactive reducing agent which, if kept in water, would rapidly diminish its concentration, leading to stoichiometrically unbalanced reactions. For this reason, $NaBH_4$ was introduced into an alcoholic solution made of isopropyl alcohol (IPA). Preliminary studies on the batch synthesis volume ratios were carried out to evaluate the limit of the solvent in achieving production of prismatic particles.

2.4 Materials and methods

2.4.1 Chemicals

AgNPs produced in the present research, both in a spherical or prismatic shape, were synthesized using silver nitrate 99.9999% ($AgNO_3$) as precursor. Tri sodium citrate dehydrate ≥ 99.0% (TSCD), polyvinylpyrrolidone (PVP), sodium borohydride 99% ($NaBH_4$) and a 30 % solution of hydrogen peroxide (H_2O_2). All reagents were purchased from Sigma Aldrich UK (Gillingham, UK).

Regarding the solvents, water-based syntheses throughout the entire project were carried out employing Milli-Q water collected from the Milli-Q Gradient A10 system (Merck Millipore, USA), equipped with the QGard purification filter. For alcoholic-based reactions, propan-2-ol (or isopropyl alcohol, IPA) of laboratory reagent grade was purchased from Fisher Chemical (UK), and used for batch- and flow-procedures.

Details of the preliminary batch green synthesis approach are shown in Appendix A.1.

2.4.2 Batch synthesis of silver nanospheres

AgNPs having a spherical geometry were produced following an established protocol previously adopted in our research group.[95]

Briefly, 1.16 mM solution (30.5 mL) of $AgNO_3$ was prepared in a 100 mL rounded flask, using milli-Q water and left under stirring at 400 rpm. Meanwhile, 1.8 mL of a 0.25 M solution of TSCD and 1.8 mL of a 0.20 M solution of PVP (30 kDa), were prepared and added to the silver solution. The stirring was increased at 600 rpm and left for 10 minutes. During this time, a 0.1 M solution of $NaBH_4$ was freshly prepared and 300 µL of the reducing agent was quickly added after the 10 minutes stirring. Reagents concentrations in the final volume were: $AgNO_3$ (1.0 mM); TSCD (12.8 mM), PVP (10 mM) and $NaBH_4$ (0.85 mM)

2.4.3 Batch synthesis of silver nanoprisms: reagents' reliability

Although several synthetic conditions were tested, starting from the chosen protocol taken from literature,[97] the final adjusted protocol is as follows. A rounded bottom flask was fed with 50 mL of milli-Q water containing $AgNO_3$ 0.1 mM and trisodium citrate dehydrate (TSCD) and left under magnetic stirring at 400 rpm for couple of minutes. Then, 250 µL of a fresh solution of H_2O_2 (30%) was added into the flask, and the stirring rate increased to 600 rpm for exactly 7 minutes. In the meantime, a freshly prepared solution of $NaBH_4$ 0.1 M was generated and 0.5 mL was quickly

injected into the stirring reaction at the end of the 7 minutes. The final concentration of the reducing agent in the total volume was 1.0 mM.

2.4.4 Reproducibility test

Although all resulted in slightly red-shifted UV-Vis spectra with the characteristic features of the prismatic shaped AgNPs, reactions tended to perform differently, in particular in relation to the WA_{max}. Batch reproducibility tests were therefore performed for a better understanding of the behaviour of the reaction.

Adopting the final protocol, experiments RT-A (reproducibility test A) and RT-B (reproducibility test B) were designed as follow:

RT-A) A mother solution for each chemical was prepared to have enough volume for the preparation of three 50 mL batch syntheses. Identical conditions in chemicals preparation, chemical concentration, protocol and reaction conditions (600 rpm stirring at room temperature and light) were maintained.

RT-B) A second mother solution was prepared separately, having the same theoretical concentration for comparison with the previous RT-A, but separately prepared (this would take into consideration the error of the operator during the weighting processes). From the same mother solution, a proportionate amount of reagents was calculated for a 250 mL batch synthesis to evaluate the effect of the volume (i.e stirring efficiency)

Observation on these aspects of the process are discussed in the Reproducibility section (2.4.4).

2.4.5 Effect of the solvent: volume ratio.

Aiming at translation to flow reactors, and due to the high reactivity that $NaBH_4$ has with water, isopropyl alcohol (IPA) was adopted as an alternative solvent. Initially, a water-IPA 50-50% (v/v) was performed to simulate a flow rate ratio (FRR) of 1. To prepare for that, a milli-Q water portion (25 mL), containing $AgNO_3$, TSCD and H_2O_2, was left under stirring (600 rpm) for 7 minutes before adding the same volume of the IPA solution containing $NaBH_4$. Concentrations of reagents were maintained proportionate to the chosen batch protocol.

Experiments were then prepared following the same procedure, for five samples having the water/IPA volume ratios of 5, 6, 7, 8, and 9. Moreover, reaction time was monitored until the solution turned blue indicating the formation of prisms, to gather information on the kinetics of the reaction and inform the subsequent design of flow-reactors. Solutions were prepared for a total

volume of 25 mL. The silver precursor, capping agent and oxidising agent were contained into the water phase. Differently, the needed amount of $NaBH_4$ was dissolved in a 10% water / 90% IPA solution for volume ratios reported in Table 2.2.

Table 2.2 Water/IPA calculation for samples' preparation.

Volume Ratio	5	6	7	8	9
Volume water (mL)	20.750	21.430	21.876	22.327	22.500
Volume (mL) IPA90%/Water10%	4.250	3.570	3.124	2.783	2.500

2.4.6 Nanoparticles characterization

The UV–Vis characterization of AgNSs was carried out using a Varian Cary300Bio UV–Vis spectrophotometer. All measurements were performed in the 200–850 nm range, with an increment step of 0.5 nm. Unless specified otherwise, samples were prepared by diluting 1 mL solution from the reaction up to 3 mL with milli-Q water, and collected in a quartz cuvette. After each test, the cuvette was cleaned by washing with aqua ragia (5 mL HNO_3 conc. + 15 mL HCl conc.). The baseline was subtracted from each experimental condition (i.e., considering the specific Milli-Q/IPA volume ratio). For some experiments, a custom made cuvette holder was 3D printed and connected with a portable optical fibre spectrometer in order to extend the scanning spectral window up to 1400 nm (Appendix A.2).

Transmission electron microscopy (TEM) characterization of AgNSs was also performed. Images were acquired using the TEM Hitachi HT7700. AgNPs were prepared by drop-casting of the colloidal synthesis solution (5 µL), on carbon and Formvar coated Cu/Pd 200 mesh grids suspended with a tweezer (Figure 2.5), and left to dry under atmospheric conditions at room temperature and low light exposure.

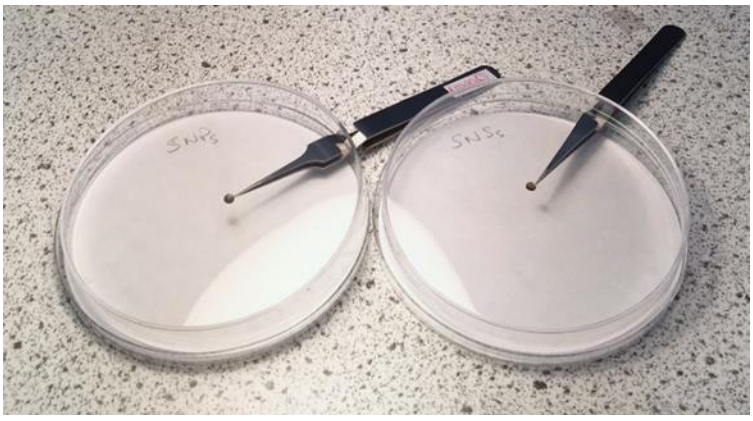

Figure 2.5 Drop-casted sample preparation example (light was turned on only for taking the picture)

For AgNPrs distribution analysis, a wider window TEM imaging (4 to 6 μm width) was taken in order to contain the larger amount of particles and be as much representative as possible of the overall sample. The software Image-J was then employed for measuring the length of the edge for each particle. Results were then imported in Origin for plotting of size distribution graphs.

2.5 Results and discussion

2.5.1 UV-Vis and TEM characterisation of silver nanospheres

The produced AgNSs showed a yellow colloidal solution as expected, and as confirmed by the characteristic UV-Vis band shape, which is typical of the LSPR related to the spherical shape of such nanomaterials (Figure 2.6, left panel). Moreover, TEM imaging was performed confirming the average particle size relative to the detected WA_{max} of 398 nm (Figure 2.6 right panel). The established protocol was readapted for future flow-synthesis.

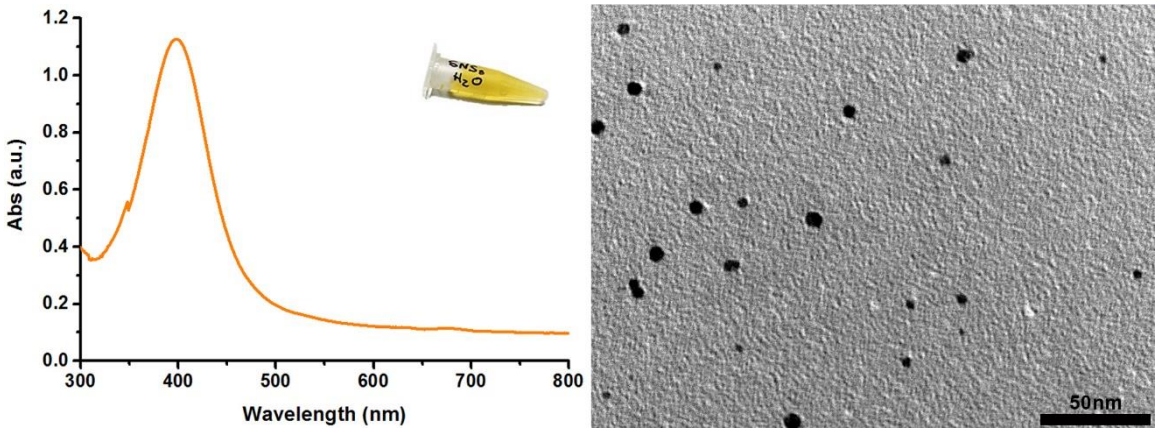

Figure 2.6 Left) UV-Vis spectrum of AgNSs showing the characteristic WAmax at 398 nm. Right) Respective TEM imaging (scale bar 50 nm).

2.5.2 UV-Vis and TEM characterisation of AgNPrs: preliminary synthesis

Although it closely followed the protocol reported in earlier publications,(Panzarasa 2015) the initial synthesis did not perform as expected, often resulting in a dark-brown coloured solution.

Therefore, variations of the protocol were attempted. Specifically, the reaction was carried out with a total volume of 100 mL, varying the H_2O_2/$NaBH_4$ ratio while maintaining the $AgNO_3$ and TSCD concentrations at 0.1 mM and 1.5 mM, respectively. Three alternatives were selected with the H_2O_2 and $NaBH_4$ concentrations of:

a) H_2O_2 (70 mM); $NaBH_4$ (1 mM);

b) H_2O_2 (0.16 M); $NaBH_4$ (2 mM);

c) H_2O_2 (0.16 M); $NaBH_4$ (4 mM);

Figure 2.7 reveals remarkable absorbance shifts and changes in shape, also clearly visible by the samples' colour. Analysing these features, and comparing them with the black dotted line (which represents results taken from the literature), all samples displayed a sharp peak at around 330 nm. As previously stated, this indicates the out-of-plane quadrupoles typical of the plated-like structures, which is part of the prisms mechanism formation. For the purple solution (purple line, sample **a**), this peak appears slightly shifted, which can be the result of aggregation or staking phenomena between plates. For the same sample, the WA_{max} occurred at 570 nm (blue-shifted) indicating smaller particles dimensions, truncation or rounded shape. Moreover, the shoulder band, typically generated by the in-plane quadrupoles, is not enhanced and looks englobed into the main in-plane dipoles band.

By increasing the $H_2O_2/NaBH_4$ ratio, the light blue sample (Figure 2.7B) displays a broad red-shifted main band with a broadening band, but the intensity appears to be lower. Further augmenting the reducing agent concentration, a darker blue sample was produced (Figure 2.7C). The bathochromic shift, in this case, is more than 100 nm compared to the reference spectrum, bringing the maximum to 850 nm, thus implying absorption closer to the NIR. However, the broad band suggested a wide particle's size distribution.

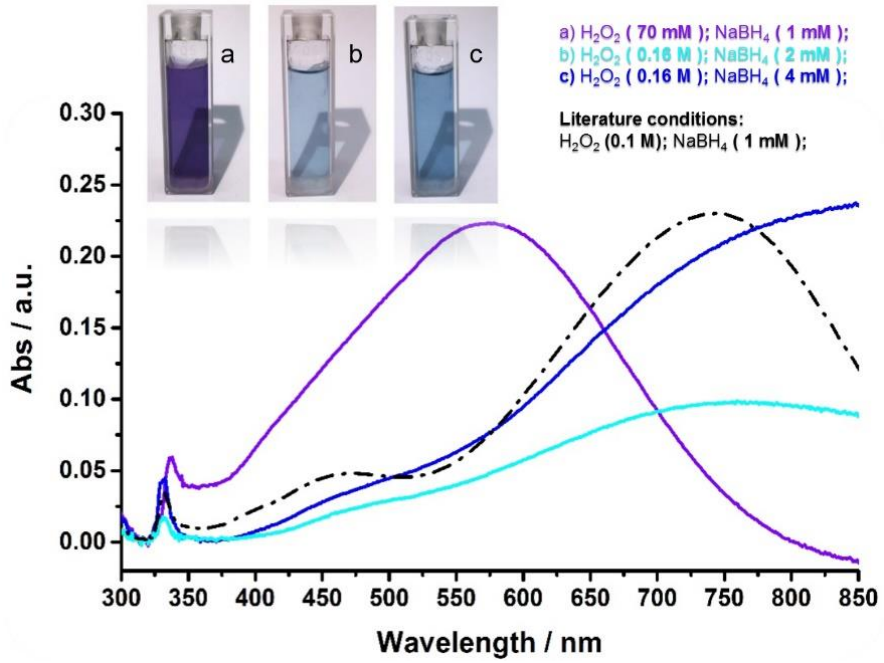

Figure 2.7 UV-Vis spectra of AgNPrs synthetized by varying the $H_2O_2/NaBH_4$ ratio while maintaining $AgNO_3$ and TSCD constant at 0.1 mM and 1.5 mM, respectively.

In previous studies[100] it was observed that there was a direct correlation between absorption red-shift and the size of the prisms. In general, bigger prisms (in terms of longer edge length) resulted in a more enhanced bathochromic shift. Therefore, although these samples did not represent high-

quality products, imaging characterisation was performed in order to get further understanding of the particle's production process and for comparison with results from the literature.

Transmission electron microscopy characterisation of samples A and C confirmed the results obtained from the UV-Vis spectra. AgNPrs from the purple solution (sample A) appeared smaller in edge length as well as clustered by plane to plane stacking aggregation, which explained both the red-shift of the 330 nm peak and the blue-shift of the main band (Figure 2.8). Moreover, these clustered samples allowed measuring the thickness of the particles as they lies sideways due to the face-to-face stacking. This resulted in the average thickness of 13 nm, for prims smaller than 50 nm in length, that also allowed estimating the aspect ratio.

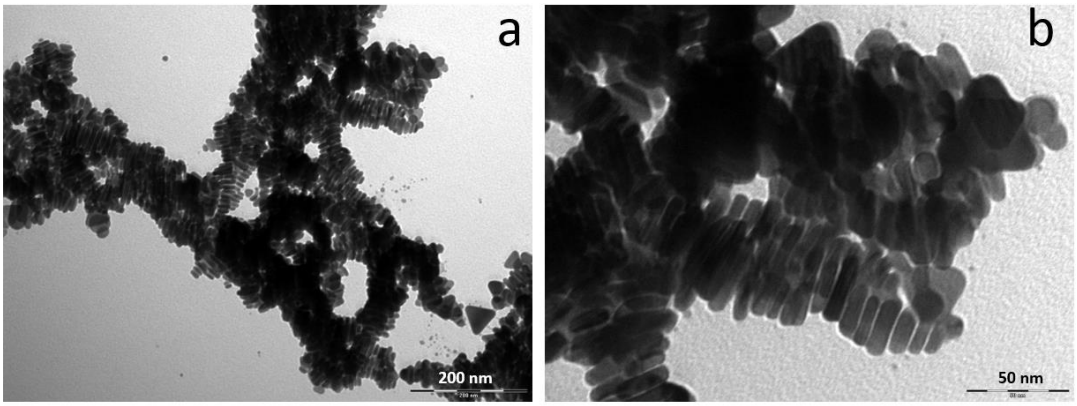

Figure 2.8 TEM images of AgNPrs aggregates: a) scale bar 200 nm; b) 50 nm.

On the other hand, optical bathochromic shift for the darker-blue sample **c**, is due to the larger average size of the AgNPrs produced. The smallest prisms in sample **c** is presented in Figure 2.9A having an almost perfect prismatic shape and the edge length of around 80 nm. Although minor distortions were observed, the shape is maintained for bigger size prisms (with an edge length of 120 nm, Figure 2.9B). Interestingly, although remarkably more fragile, a 300 nm slightly etched prism is shown (Figure 2.9C). This also generated interest in the ability to generate larger particles.

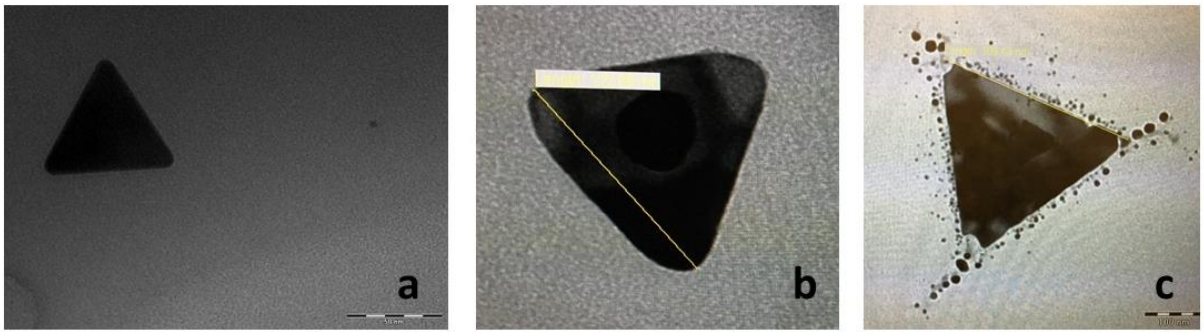

Figure 2.9 TEM images of particles of different size taken from the dark blue sample (sample c). Measured edge length using Image-J software: 80 nm (a), 120 nm (b), and 300 nm (c).

With the unresolved UV-vis spectrum of the sample **c** (cyan line in Figure 2.7), a TEM imaging was performed. Figure 2.10 shows the etched and rounded prisms-like particles. A broad size distribution, as well as a poor shape accuracy, is notable as suggested by the UV-vis characterisation, confirming the low quality of the sample in terms of uniformity of particle's geometry.

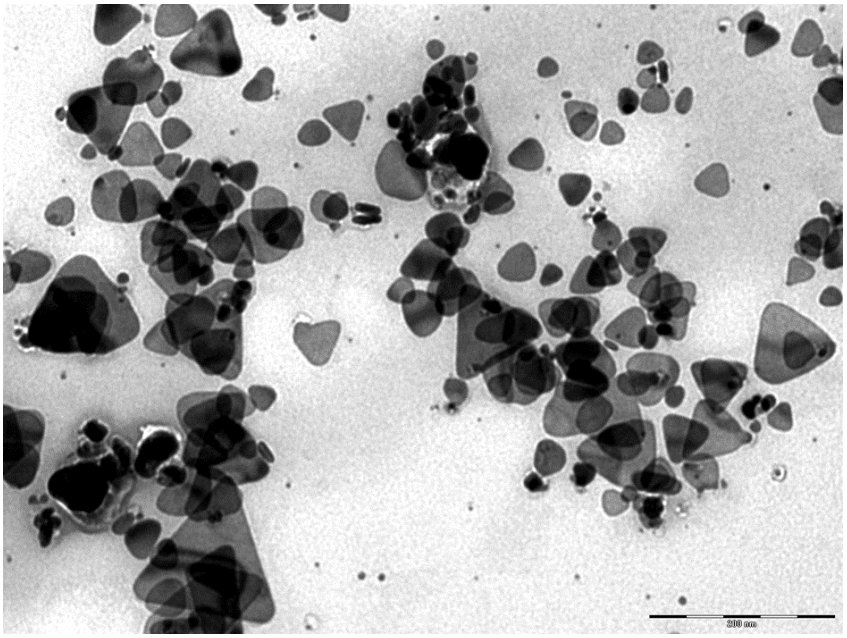

Figure 2.10 TEM image showing variation in particle's size in the light blue sample (sample b). Scale bar 200 nm.

These samples demonstrated how small variations in the stoichiometry of the reaction can strongly affect the production outcome. Moreover, these initial tests highlighted how important is reagents' quality and fresh preparation in terms of reliability of the synthesis process.

2.5.3 Batch synthesis of silver nanoprisms: reducing agent method

Chemicals such as $NaBH_4$ and H_2O_2 tend to undergo a fast degradation, which depends on their age and storage conditions and is due to their interaction with air or humidity. In practice, fresh chemicals were adopted and the Pansaraza procedure followed;[97] the reaction was recorded with a camera for a better evaluation of the colour changing over time (Figure 2.11). The observed changes in colour during the reaction, starting from yellow to dark blue, indicated the transition process of particle's shape from spheres to prisms as observed in previous work,[103] and agreed with the literature.[97]

Figure 2.11 Change in colour over time for a 100 mL batch synthesis of AgNPrs.

As shown in Figure 2.11, the solution turned instantly from colourless to a pale yellow after adding $NaBH_4$, reaching a dark orange in the first 30 seconds. As explained from the literature, it indicated the initial formation of nanoparticles of spherical shape. The accompanying production of gas bubbles was due to the formation of a mixture of H_2 and O_2.[109] In the subsequent minutes, the solution became darker having burgundy and purple variations, until reaching a deep blue colouration after 2 minutes.

The UV-Vis spectrum evidently exhibits three separate LSPR bands. The sharp peak at 331 nm, a well defined shoulder band at around 460 nm, and the most intense and broad band at 745 nm attributable to the out-of-plane quadrupoles, in-plane quadrupoles and in-plane dipoles transition, respectively.[97]

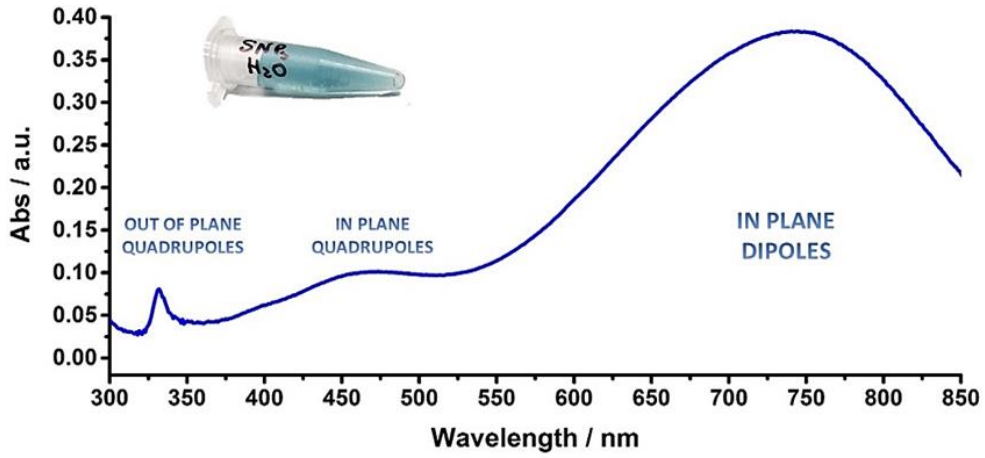

Figure 2.12 UV-Vis spectra of AgNPrs following the batch synthesis procedure reported in the literature[97]

The TEM imaging confirmed a better defined prismatic shape of the produced particles, having sharp edges and just slightly rounded tips. Figure 2.13 shows a representation of their size distribution, indicating AgNPrs ranging from less than 50 to more than 100 nm in edge length.

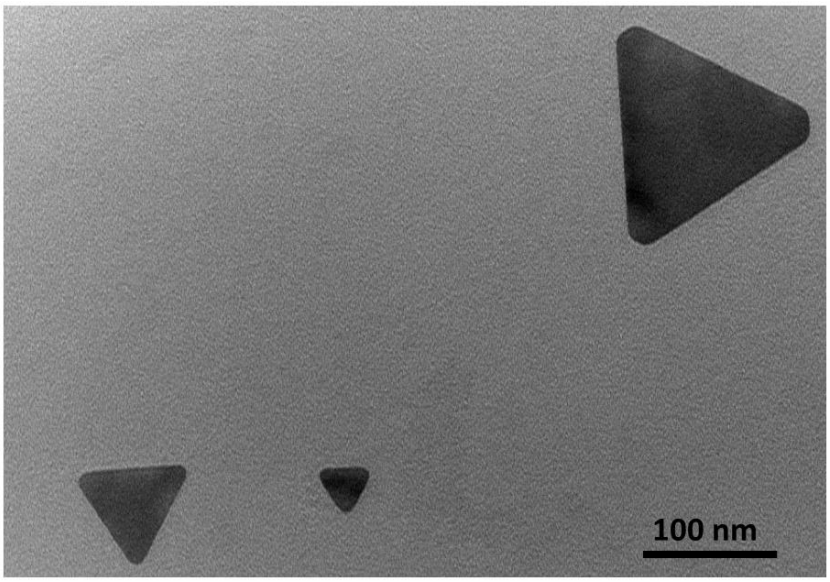

Figure 2.13 TEM imaging of a magnified area. AgNPrs are present having an edge-length from less than 50 nm to more than 100 nm.

2.5.4 Purification by centrifugation: the effect of the capping agent on the AgNPrs absorption

A purification test was performed in order to evaluate the effect of removing the capping agent on the LSPR. The reaction was adjusted until obtaining an enhanced red-shit of the main absorption

band for NIR related applications. This occurred when slightly increasing the concentration of the capping agent and the oxidising agent, while maintaining the silver source and the reducing agent concentrations as in the literature, and waiting less time during the vigorous stirring process before the addition of the reducing agent (7 minutes). A thermal camera imaging was also performed in order to evaluate the heat absorption of the particles (results summarised in Appendix A.3).

The purification procedure was carried out by centrifugation (15 minutes, 10'000 rpm), followed by removing the supernatant and washing twice with water. Figure 2.14 shows the comparison between the AgNPrs solution directly from the reaction (black line), the sample once purified and re-diluted in water (blue line), and the removed supernatant (cyan dotted line). It is very interesting to note that the peak of the purified sample (blue line) is shifted by roughly 100 nm towards lower wavelengths compared with the reaction solution (black line). This is probably due to the extraction of the citrate during the washing process, which alters the surface interaction of the prisms, and therefore their LSPR absorption.

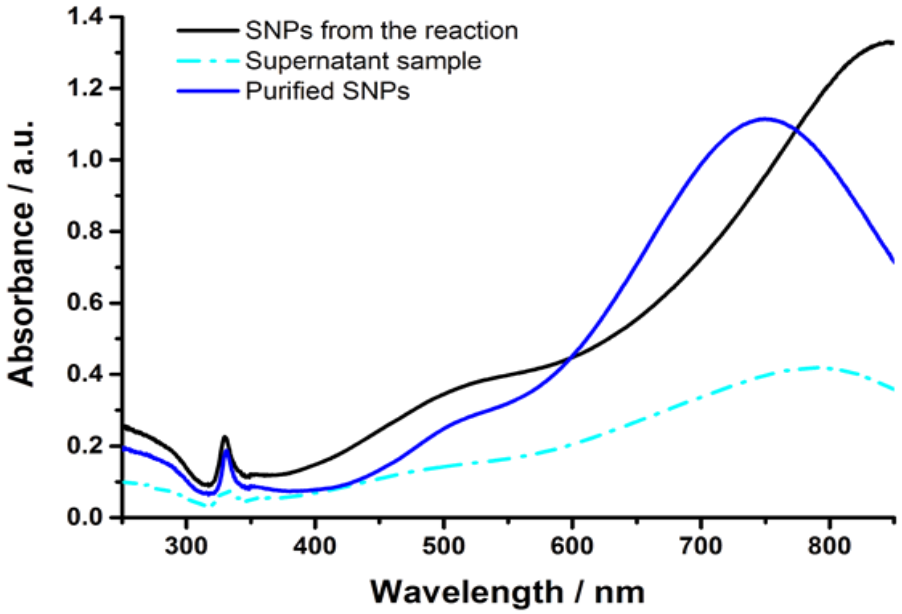

Figure 2.14 UV-vis absorption of the SNPs solution from the reaction without any treatment (black line), the purified sample (blue line) and the supernatant (cyan dotted line).

However, although every repetition of the synthesis gave the same blue coloured solution with the typical UV-vis spectrum shape that suggested the formation of prisms, WA_{max} values were not constant. This demonstrated the disadvantage of the batch approach, and led to the design of a more specific reproducibility test, as detailed below.

2.5.5 Reproducibility test (RT): silver nanoprisms batch test and UV-Vis comparisons.

In order to minimise any operator dependant error, and at the same time to compare different preparation procedures, parallel batch syntheses were conducted and compared to evaluate the reproducibility of the process.

Figure 2.15 shows five rounded bottom flasks, labelled with coloured rectangles indicating the reproducibility test (RT) followed by the number of the sample (three for RT-A and two for RT-B). Notably, the kinetics of the reaction is strongly affected by any variation in chemicals concentration, which can easily occur when weighting a small amount of solid materials. Although the procedure is described in the Materials and Methods section (2.4.4), further clarification on the experimental rationale is given below.

Samples were prepared with the *same chemical preparation,* in which mother solutions were individually prepared by weighting the specific amount of reagent and diluting it in water for each chemical. With this procedure, the operator's error during the weighting process is translated to each batch repetition, keeping the batches theoretically identical. On the other hand, samples with the *same chemical concentration* refer to samples for which reagents do not come from the same mother solution, although they are prepared with the same concentration.

Samples in RT-A had the *same chemical preparation* to each other, as well as samples RT-B. Differently, all the samples in RT-A hade the *same chemical concentration* to the samples in RT-B. Particularly, the concentrations were calculated in proportion to the volume for the 250 mL flask in (RT-B1). The colour code assignment was also used to assist the subsequent UV-Vis comparison.

As can be seen from Figure 2.15 it is possible to note that all the flasks contain a blue coloured solution, indicating the prismatic shape of the particles, except for RT-A1. This helped in verifying the extreme importance of the protocol in terms of its kinetics. It was observed that, not only was the sequence of the chemicals' addition important, but also the time interval between additions and particularly the velocity of the injection of the reducing agent.

The dark/yellow colour in of RT-A1 is due to the slower addition of $NaBH_4$, resulting from an incorrect addition process. In RT-A1 (black), when adding the $NaBH_4$ with the Eppendorf pipette, the solution touched the edges of the flask, slowing dropping into the solution.

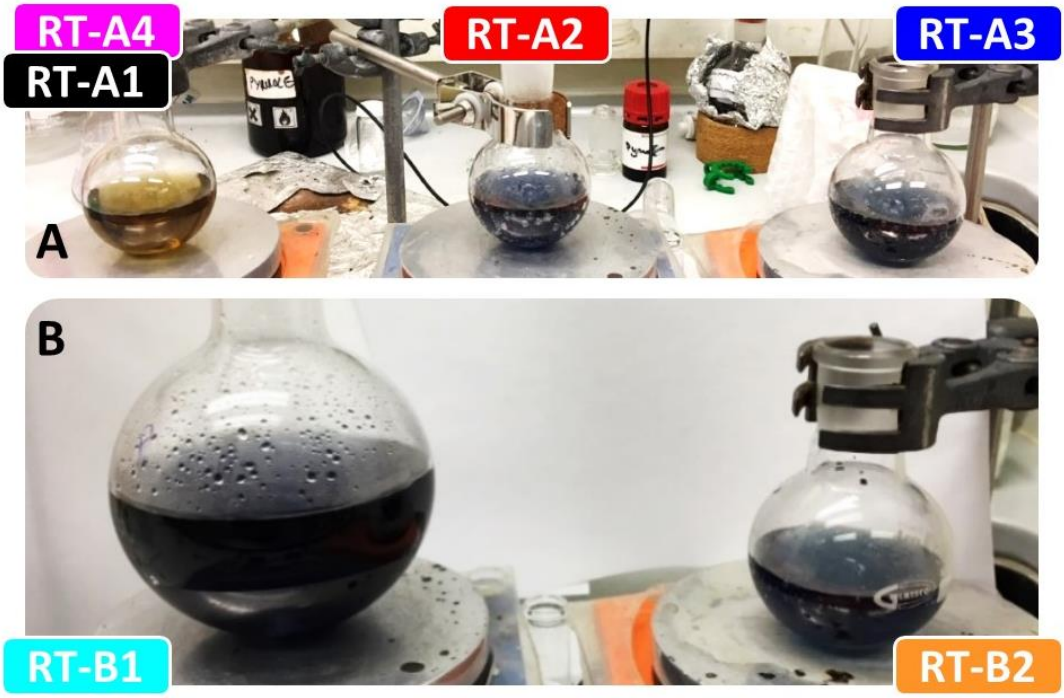

Figure 2.15 Rounded bottom flasks for the reproducibility test. A) Three 50 mL syntheses having the same chemical concentration and preparation to each other. B) Volume test between a 250 mL and a 50 mL having the same chemical concentration and preparation to each other's, and same chemical concentration compared to the volume.

This strongly affected the labile balance of the mechanisms previously explained, ending up with the production of AgNSs as notable from Figure 2.16 (black line). Therefore, the injection speed of the $NaBH_4$ into the solution had a major effect on the kinetics and, as a consequence, on the proceeding of the reaction.

Differently, AgNPrs were obtained from samples RT-A2 and RT-A3 (red and blue lines, respectively). However, although produced under the identical operating conditions, they showed a different shape of the absorption band, particularly related to the main in-plane-dipole band. The first reaction was then re-prepared after 50 minutes from the chemical preparation (RT-A4, Magenta). This variation allowed to verify a further alteration of the parameters, related in this case to the freshness of the reagents. The RT-A4 sample resulted in a broader and less resolved UV-vis shape, this is particularly notable when relating the in-plane-dipole band with the shoulder associated with the in-plane-quadrupoles.

Regarding samples RT-B 1 and 2 (cyan and orange respectively), although the absorption bands reveal the typical shape of the AgNPrs, the shift in WA_{max} highlights a notable variation in particle's size.

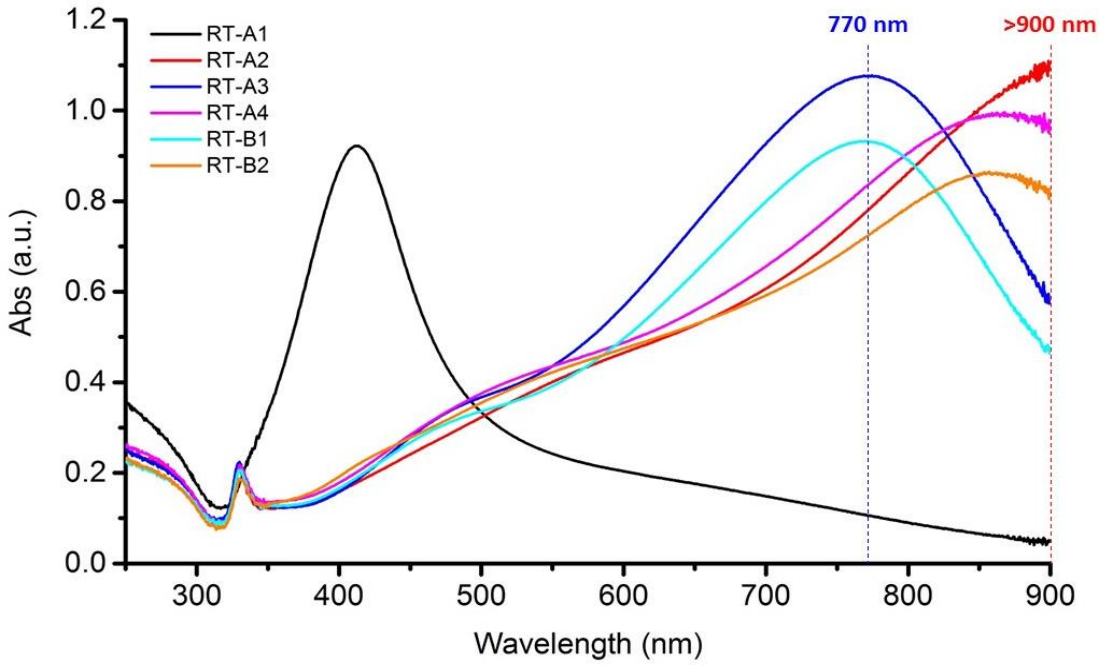

Figure 2.16 UV-vis batch reproducibility comparisons.

The resemblance between RT-A4 and RT-B2 is interesting to discuss further. This shows the effect of leaving the $NaBH_4$ in water before the synthesis in 50 mL, which might be similar to that of carrying out a larger 250 mL volume reaction. This may be attributable to differences in the mixing kinetics and regime occurring in a larger volume, which would affect the quality of the seeds growth for RT-B2. Similarly, $NaBH_4$ in RT-A4 would have a weaker effect due to its activity deteriorating due to it being dissolved in water for a prolonged time.

The experiments demonstrated the lack of reproducibility for AgNPrs when synthesized *via* a simple batch synthesis protocol. However, it also demonstrated the suitability of a batch protocol (adapted from the literature) to produce particles having a red-shifted A_{max}.

2.5.6 Size distribution of AgNPrs *via* TEM characterisation

Transmission electron microscopy studies were carried out to perform a more direct evaluation of the size and shape of the nanoprisms. In particular, to gain a better understanding of the relationship between the WA_{max} and the nanoparticle's average size, the two most representative batch products from the reproducibility test (Figure 2.15) were selected based on the quality of their absorption spectra as well as their difference in absorbance maxima: RT-A3 (WA_{max} 770 nm) and RT-A2 (WA_{max} > 900 nm).

An extended field of view was captured during the TEM analysis, with the purpose of observing a representative area, to be able to examine a statistically large number of particles and perform a

size distribution analysis. The length of the particle's edge was measured with the software Image-J, using the scale bar as a reference length. The TEM of the sample RT-A3 (WA_{max} 770 nm), displayed in Figure 2.17 (scale bar 200 nm), exhibits an extremely high production quality in terms of the triangular shape, with almost absent spherical particles as suggested by the UV-Vis characterisation. Differently, Figure 2.18 displays the TEM for the RT-A2 sample (WA_{max} 900 nm). Also in this case, the prismatic shape of the particles is observed, demonstrating the effectiveness of the formation mechanism through the chosen simplified procedure. For the RT-A2 sample, particles appeared to be more dispersed; however, this is balanced by the increased size of the prisms as justified by the UV-Vis characterisation (scale bar 500 nm). The prismatic shape is clearly predominant for both samples, with some visible variations. In terms of particle size in the two figures, prisms in Figure 2.18 appear visibly bigger on average.

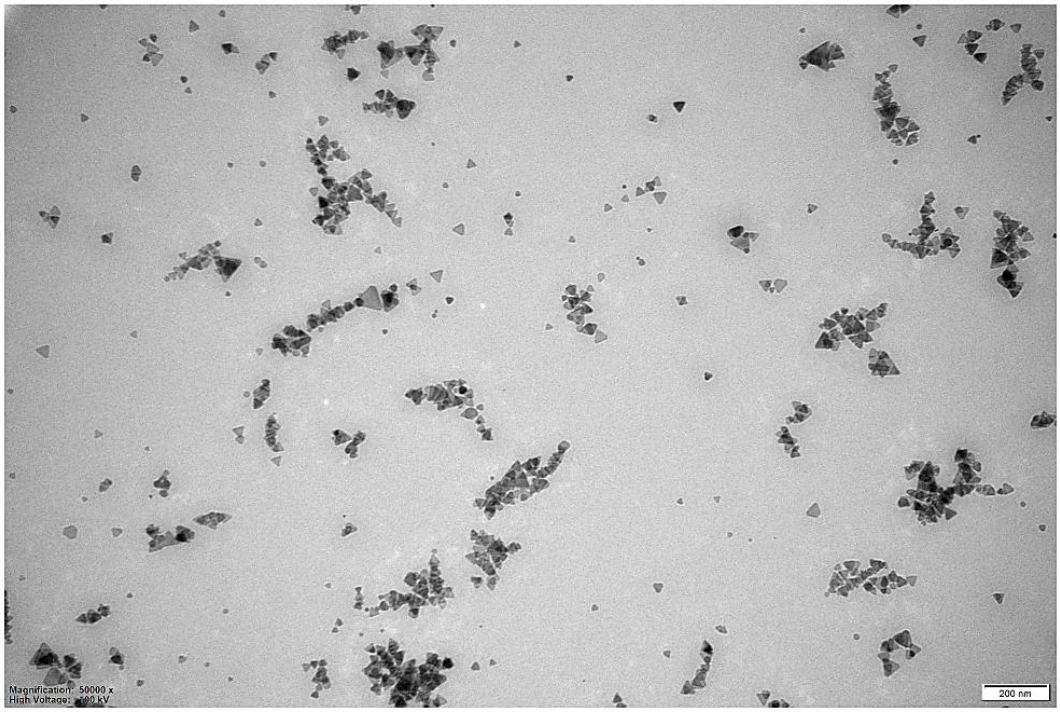

Figure 2.17 TEM image of the RT-A3 sample (scale bar 200 nm).

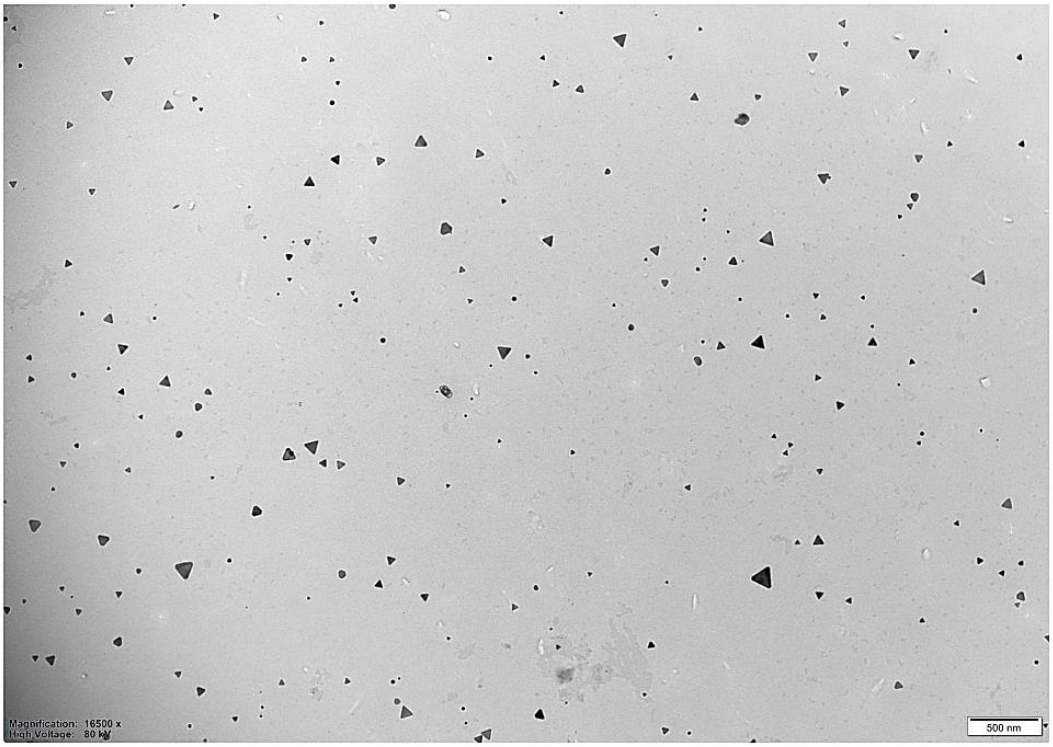

Figure 2.18 TEM image of the RT-A3 sample (scale bar 500 nm).

The size distribution was analysed by measuring the length of the particle's edge in each image. The results are illustrated in Figure 2.19 for the two samples, where the average size was determined on 378 and 149 counts for the RT-A3 and RT-A2 samples, respectively.

The particle's size is shown in histograms against counts, which are separated by 5 nm intervals. In terms of population, the histograms show the greatest proportion of particles for RT-A2 was slightly larger (45 nm) compared to the 35 nm of the RT-A3. However, for the sample with the WA_{max} > 900 nm a broader size distribution is notable, including the presence of several prisms over 100 nm. Unfortunately, differently from the high symmetric AgNSs, AgNPrs do not have an attributable extinction coefficient, due to the unpredictable number of Ag atoms per particle with respect to the prism dimensions. This would affect LSPR and therefore it is not possible to define the effect of bigger prisms, or size population, on the absorbance wavelength shift or intensity. Consequently, the average size of the AgNPrs was extrapolated through a normal distribution function (Figure 2.19).

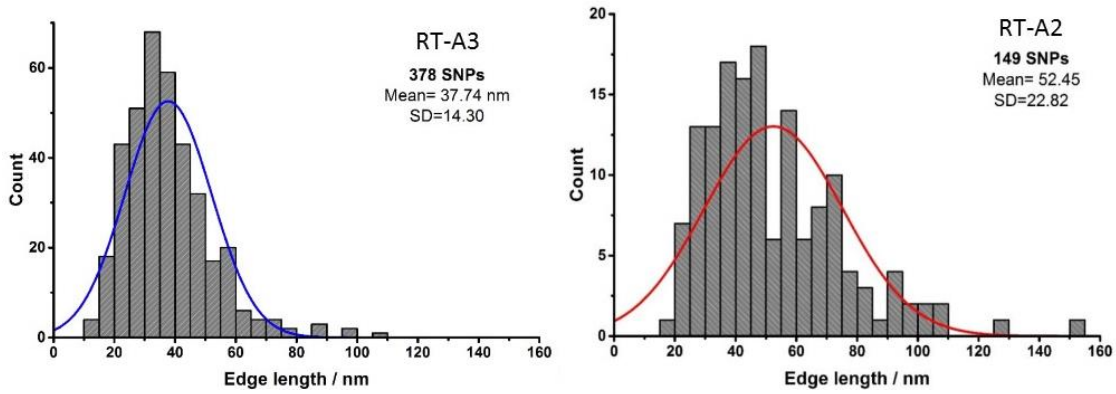

Figure 2.19 Size distribution analysis. Particle's length was measured by using the software Image-J, from the TEM images for the samples RT-A3 and RT-A2 (left and right panels respectively).

The calculated blue and red Gaussian functions in Figure 2.19 (left and right), indicate an average particle's size of 37.74 nm (Standard deviation, SD=14.30) for the RT-A3 sample with a 770 nm WA_{max}; whilst the RT-A2 sample revealed a particle's mean size of 52.45 nm (SD=22.82) having WA_{max} > 900 nm.

The increased size of the sample RT-A2 has therefore proven the strong bathochromic shift (> 100 nm) of the main AgNPrs absorption band. Moreover, these combined UV-Vis/TEM/size-distribution characterisation clarified the output of AgNPrs and represented a solid foundation and also a starting point for further flow synthesis approaches.

2.5.7 The role of the solvent

In view of the translation to flow-synthesis, reagents needed to be prepared to be injected into the flow-reactor after preparation. This may not be suitable for the reducing agent employed, due to its tendency to degrade over time. Therefore, referring to the protocol reported in Session 2.4.5, the water:IPA volume ratio was optimised. Initially, to simulate what could be a suitable flow rate ratio, a preliminary batch test was performed maintaining the same concentration of chemicals and adopting a water:IPA volume ratio (VR) of 1:1 (Figure 2.20). The reaction evolved in a completely different manner when compared to that performed in water only.

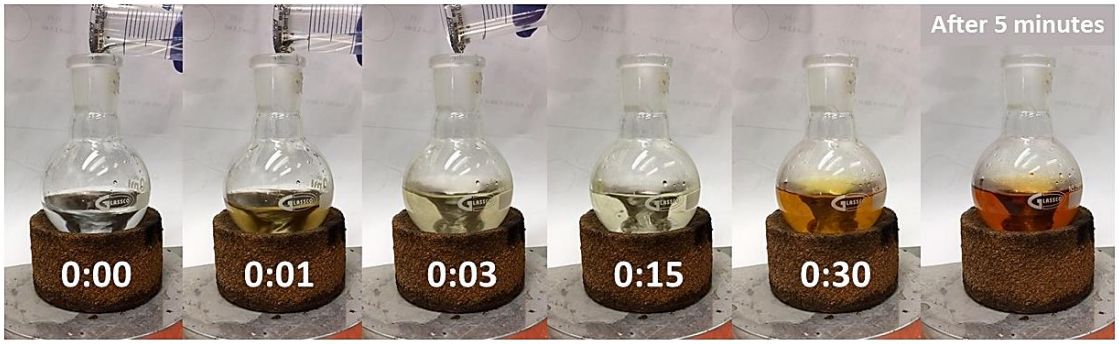

Figure 2.20 Batch reaction filmed to observe the relative colour variations. Time frame were captured as indicated in the figure. Volume ratio water:IPA was of 1:1.

In this approach, the water phase (25 mL), containing $AgNO_3$, TSCD and H_2O_2 was left under stirring for 7 minutes before adding the same volume (25 mL) of the IPA solution containing $NaBH_4$ (time 0:00). When pouring the IPA solution inside the flask, an instantaneous colour change was observed from transparent to brown/yellow (T = 0.01 s). However, by the end of the pouring (T = 0:03 s), the solution lost its intensity in colour, displaying a very pale yellow. This shade remained until 30 seconds, after which the yellow/orange shade typical of nanospheres appeared. No further variation was observed for almost 5 minutes. The solution just darkened without showing the expected blue colour. More detailed studies were carried out for different water/IPA VR volume ratios of 5, 6, 7, 8, and 9. UV-Vis results are shown in Figure 2.21 (left panel), and the reaction time periods needed for turning to blue colour (characteristic colour of the prismatic shape) for associated samples are shown in Figure 2.21 (right panel).

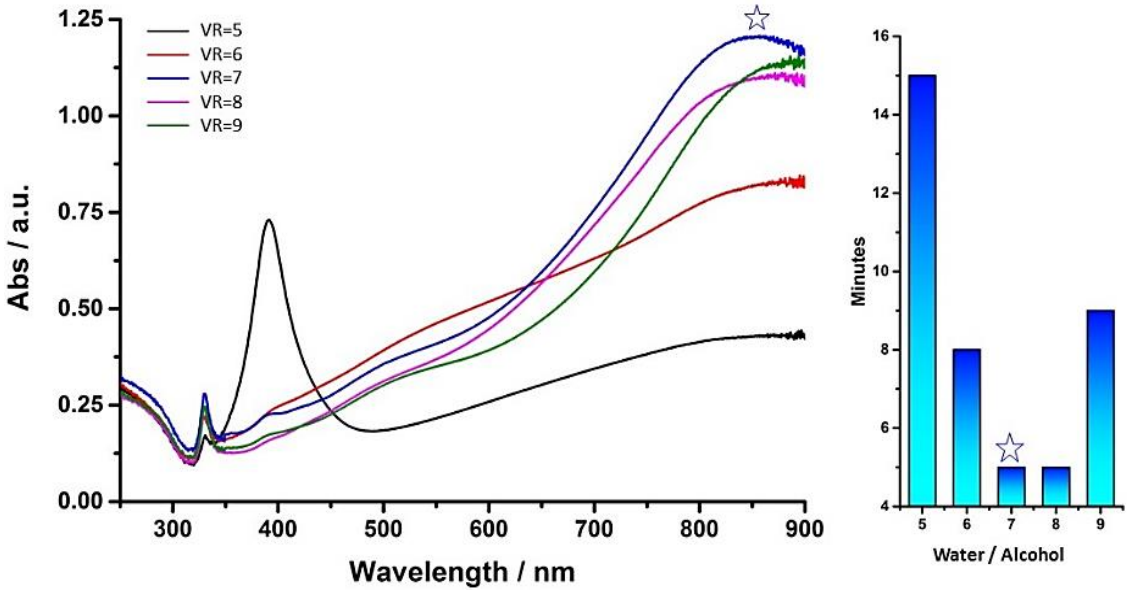

Figure 2.21 Left) Batch volume ratio test. UV-Vis spectra when varying the H_2O/IPA ratio. Right) Time related to the colour transition indicating the formation of AgNPrs. The VR of 7 represented the best combination between faster kinetic, A_{max} and red-shifted WA_{max} (indicated with a star).

As seen from the UV-Vis spectra in Figure 2.21 (left panel), an interesting trend is clearly notable. Sample VR = 5, for instance, displays an intense band at just below 400 nm which is indicative of the presence of spherical particles, and a very broad and yet not defined band increasing from 500 to 900 nm. This, in combination with a small and sharp peak at 330 nm, indicates the formation of plates particles, probably mainly circular or slightly prismatic considering the non-enhanced shoulder due to the in-plane-quadrupole.

Moreover, the solution just turned dark grey after 15 minutes, as in Figure 2.21 (right panel). The VR = 6 sample shows a different and more desirable behaviour; the absorbance rises in the region of higher wavelengths, but also in this case the shape is not well defined. On the positive side, the time for the blue-ish colour appearance decreased to 8 minutes. Differently, the shape of the spectrum of VR = 7 is well defined and the most intense of all. Moreover, the kinetics seems to be the fastest (< 5 minutes). VR = 8 behaves similar to the sample at VR = 7 overall, but from a closer look it appears having a less defined shape and a lower in absorption intensity. On the other hand, the VR = 9 sample presented a well-defined shape, which also appeared slightly shifted towards the NIR. However, the kinetics appeared slower (9 minutes). The VR = 7 was therefore selected as the suitable starting volume ratio for translation to flow-synthesis.

2.6 Conclusions

The synthetic methods and formation mechanism of AgNPs having spherical and prismatic shape were presented. Reaction conditions taken from the literature were adopted for both particles, with particular attention to nanoprisms. This is a different protocol if compared to the previous studies presented by other research groups,[95] and it was chosen in order to obtain the simplest yet reliable synthesis adopting fewer chemicals for the specific flow-translation. For this reason, several aspects of the protocol were evaluated. The importance of reliable reagents was proven and discussed while attempting AgNPrs production.

Although time-consuming, this was crucial for understanding UV-Vis characterisation, which was key to the interpretation of results from subsequent reactions. The chosen batch protocol was then reproduced and slightly changed to increase the probability of a bathochromic shifted absorption band of the produced sample. Studies on the reproducibility were also performed with a detailed size distribution analysis. Finally, the reaction was repeated for testing different volume ratios between water and IPA, to identify an optimal value for flow synthesis.

This first approach allowed a deep understanding of the behaviour of the reaction, and was a crucial step for further experiments needed to achieve flow synthesis.

Chapter 3 Continuous-flow Reactors: Design and Manufacturing

3.1 Introduction

Continuous-flow reactors exhibit unique characteristics over their batch counterparts, as they provide enhanced stoichiometric control and increased production yield, while reducing waste of expensive or hazardous chemicals.[110] Over the last two decades, numerous chemical syntheses have been performed within nano-, micro- and milli-fluidic reactors.[111] Particularly, various flow-reactor configurations have been developed for the production of organic vesicles[112,113,66] and inorganic nanomaterials.[114] This Chapter presents several cost-effective and easy-to-make manufacturing methods for the construction of flow-reactors. Some of these are reproductions or developments of existing designs, whereas some others were newly conceived. In this Introduction section, the state-of-the-art for the design and fabrication of microfluidic chips and flow-reactors is presented with research gaps highlighted, followed by a detailed characterisation of the proposed methods.

3.1.1 Devices' fabrication techniques

Many different fabrication approaches are available for producing microfluidic chips (or lab-on-chip; LOC), often adopting the same manufacturing technologies employed for microelectronics. Among these, the most commonly used are high-resolution methods, such as mask-based photo-lithography, dry and wet etching, laser cutting and thin film deposition.[115] Despite its high cost, photo-lithography in particular (Figure 3.1)[116] has been widely used to manufacture continuous-flow reactors at high spatial resolution, in terms of both size and shape of the channels.[117] It is based on the light exposure of light-sensitive polymers, which are reactive to ultraviolet (UV) light with wavelengths in the range of 193–436 nm. In this method, a bi-dimensional opaque mask is appositely produced having the shape of the channel as negative space. The mask is subsequently positioned over a photo reactive resin and light exposure is applied. The mask can be arranged at various distances from the polymer's surface, achieving different results based on contact, proximity or projection printing. Light exposure causes the photoresist to be chemically modified, so that the exposed areas either become soluble (positive tone photoresist) or insoluble (negative tone resist) to a solvent in the subsequent developing step.[115]

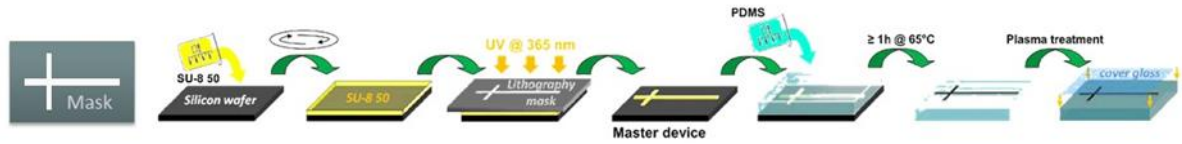

Figure 3.1 Representation of multiple and expensive steps typically carried out during manufacturing of LOC devices by photo-lithography.[116]

Alternatively, etching techniques are based on the chemical removal of layers from the surface of a wafer during manufacturing. For instance, thin film materials (SiO_2, Si_3N_4, and metals) can be etched by chemical solutions such as buffered hydrofluoric acid, hot phosphoric acid, and other strong acid mixtures.[115] The etching process is characterized by two main parameters: the selectivity (S), which is the etching rate of different materials, and the anisotropy (A), which is the relation between the lateral and the vertical etch rate of the material. When A = 0, the etch process is fully isotropic (i.e. etch rates are equal in all directions). On the other hand, if A = 1 it is anisotropic (i.e. etch rate is direction-dependent) (Figure 3.2).[115]

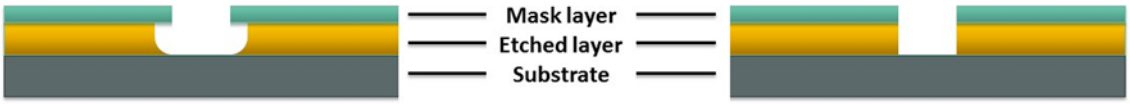

Figure 3.2 The effect of isotropic etching (left) and anisotropic etching (right) highlights the effect of these processes on the channel geometry. (image redesigned from literature)[115]

Moreover, anisotropic wet chemical etching, in particular, is crystal plane dependent, and the process outcome is related to the etch rates within specific etch solutions. The different etch rates of the crystal planes can be effectively used for building three-dimensional mechanical and fluidic microdevices (i.e. silicon etched with 40% Potassium hydroxide (KOH) solution at 80°C).[115]

Manufacturing miniaturised continuous-flow reactors using one of the methods described above, however, often requires the use of expensive materials and laborious protocols, and frequently requires environmentally controlled conditions and highly specialised facilities (i.e. cleanrooms).[118] Additionally, the whole process (i.e., from the design of the device architecture to the end product) is highly time consuming. The combination of these factors has hindered the widespread adoption of these reactor technologies by industries and researchers, particularly in the non-specialised or less-resourced laboratories.

Over the last decade, efforts have been made to develop more cost-effective and user-friendly non-photolithographic manufacturing approaches,[119] including paper-based chips [120] and flexible microfluidic devices using a desktop digital craft.[121] Additionally, coaxial glass reactors were conceived and applied for nanoparticles' production purposes.[122]

A family of techniques for manufacturing reactors using elastomeric stamps or moulds, called soft-lithography, has been drastically improved over the last 20 years,[123] with growing focus on the scalability of manufacturing processes.[124] With soft-lithography, silicone elastomers such as polydimethylsiloxane (PDMS) are commonly used as the constitutive material of the channel replica.[118] Recently, efforts have been made to develop more cost-effective and user-friendly manufacturing approaches.[119] Techniques such as micromilled replica moulding (µMi-REM)[125] have shown great advantages relating to the reduction of costs and simplification of procedures, while maintaining comparable performance to reactors generated via photolithography, in terms of ability to resist a broad range of temperatures and fluid pressures.

With these techniques, it is possible to entirely avoid all of the photolithographic steps needed to create master moulds, including the expensive process of mask's fabrication. For instance, the µMi-REM technique recently developed by Carugo *et al.*[125] has described the fabrication of positive epoxy masters obtained from negative micromilled moulds (made of polymethyl methacrylate,

PMMA). This procedure did not require the fabrication of photomasks *via* photo-lithography, thus avoiding the need for cleanroom facilities. The method, however, requires the use of micromilling machines, which can be expensive. In this case, as in the majority of LOCs, the final device can be entirely made of polydimethylsiloxane (PDMS), or the PDMS replica can be bonded onto a glass substrate. PDMS belongs to a group of polymeric organosilicon compounds that are commonly referred to as silicones.[126] This material is not only relatively cheap and easy to use, but it is also inert, nontoxic, biocompatible, non-flammable, optically transparent (down to λ=300 nm), and it has thermal stability up to 186 °C (in air).[115] Most importantly, it can be bonded to itself, and a series of other materials like glass or quartz, *via* exposure to oxygen plasma.[127] More specifically, PDMS comprises of repeated polydimethylsiloxane units (—O−Si$(CH_3)_2$−) which, under oxygen plasma exposure, substitute the methyl groups (−CH3) with hydroxyl groups (−OH), creating silanol groups. This treatment, other than making the exposed surface highly hydrophilic, allows the condensation of silanol groups between two surfaces in contact. Stable covalent Si-O-Si bonds are created after losing a water molecule, ensuring a direct bonding between two PDMS layers or PDMS and glass.[128] However, a disadvantage of PDMS is that it can swell when exposed to some nonpolar organic solvents such as toluene and hexane.[115] Moreover, PDMS is permeable to air, which can be convenient depending on the application.[129]

3.1.2 3D printing in soft-lithography: state-of-the-art and limitations.

Recently, three-dimensional (3D) printing has emerged as a cost-effective and robust technology to either fabricate flow reactors in a single step,[130,131] or to generate master moulds for soft-lithography.[132] The manufacturing process is similar to the µMi-REM method, with a difference in the mould construction process. Moulds are 3D printed, which may pose some limitations depending on the complexity or size of the channel architecture and the 3D printer used. The notably shorter manufacturing process, compared to photo-lithography, can be seen in Figure 3.3.

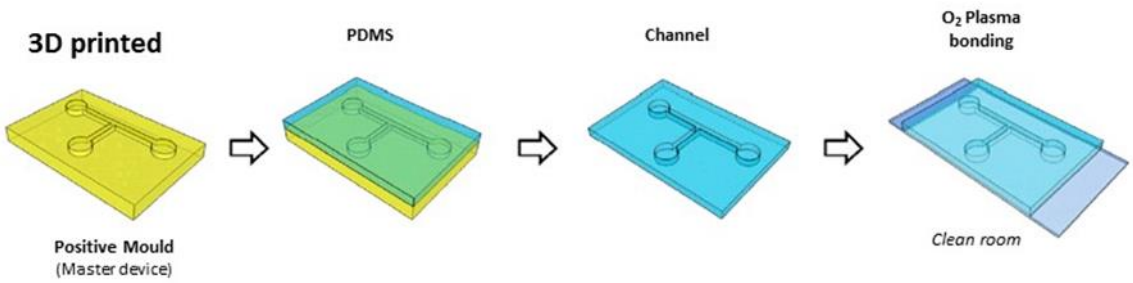

Figure 3.3 Fabrication steps of the 3D printed replica mould process (adapted from Carugo et al.) [125]

Comina *et al.*[133] demonstrated the fabrication of 3D printed positive moulds in a single step, using high-resolution 3D printing (with a channel width down to 50 μm). Similarly, 3D PDMS microfluidic reactors can be fabricated *via* UV-activated 3D printing, as described by Chan *et al*.[130] Although 3D printing of master moulds may be more straightforward to perform when compared to μMi-REM, the procedure might require specific post-printing treatments of the master mould (as discussed in section 3.3.1.1).[132,133] In addition to the manufacturing process, oxygen plasma treatment has been used for the bonding step in the case of both devices, the 3D printed and the micromilled replica mould architectures.

Alternatively, microfluidic devices could be entirely 3D printed instead of being used as a mould for the PDMS replica, as demonstrated by Kitson *et al.*[64] This method is cost-effective and easy-to-perform; however, devices are not optically transparent, thus limiting the potential for optical monitoring of flow and mixing processes. Moreover, the material's porosity, roughness, or chemical composition might create some disadvantages, depending on the application. Optical transparency of 3D printed channels was recently improved by Gaal *et al.*[134], using a custom-built 3D printer to create PLA/PDMS architectures. However, careful adjustments of a custom 3D printer were needed during the printing process, for which an experienced operator is needed. An interesting mini-review, presented by Chen *et al*. highlights recent trends in 3D printing of flow devices.[135] With recent studies on novel resin formulations for stereolithgraphy (SL) 3D printing with Digital Light Processing (DLP),[136] developments have also been made in terms of the microchannel dimensions obtainable using 3D printing. With this technique, the generation of remarkably small microchannels was demonstrated (i.e., 18 × 20 μm).[137]

Furthermore, bonding alternatives to oxygen plasma treatment have also been improved. For example, Serra *et al.*[138] recently demonstrated the use of commercially available sealing tape (Thermalseal RTS™) for the bonding of various substrates; however, the PDMS channel architectures were fabricated from micromilled brass masters, rather than more cost-effective approaches.

3.1.3 Technological challenge and research questions

With the aim of reducing costs and simplifying the manufacturing protocol of continuous-flow reactors towards meso- to large-scale production of nanoparticles, 3D printing replica mould casting (3DP-RMC) was selected as a suitable manufacturing method to be implemented in this project. Flow-through reactors produced with this method were tested for evaluating several performance indicators. Moreover, a novel entirely 3D printed and pump-free reactor concept was developed.

The key research questions that needed to be addressed were:

- How important is the precision of the channel's architecture, thus the high accuracy of the manufacturing method, on the repeatability of the nanoparticle production process?
- What is the impact of channel's geometry on the ability to control the mixing regime and effectiveness of the reaction?
- Where does the boundary lie between simplicity of the manufacturing and reliability of the reactor?

3.1.4 Research gaps and the proposed solutions

The master mould production *via* 3D printing has definitely simplified the manufactuing process for realising continuous-flow reactors, if compared to photolithography, but brings with it some limitations. Particularly, in order to accurately manufacture moulds containing micrometre-sized features, expensive or customizable 3D printers are generally required.[137] Moreover, the PDMS channel replica fabricated *via* soft-lithography require sealing to a substrate (typically glass or PDMS), which is often achieved by treatment with oxygen plasma.[125,133] The need for sophisticated instrumentation has thus far limited the scalability of microfluidic-based flow reactor technologies, hindering their industrial translation or adoption by less-resourced research laboratories.

In the present research, a novel cost-effective and facile manufacturing process was developed. 3D printed mould casted architectures, bonded on pressure-sensitive adhesive tape (3DPM-C/Tape), could be manufactured at a cost of <£5 per device and a fabrication time <24 hours. This involved 3D printed master moulds made using desk 3D printers to manufacture PDMS channel replica, which were then manually sealed to a pressure-sensitive adhesive tape without the need for oxygen plasma treatment.[139]

In addition to the manufacturing process, the scalability of flow reactors is also affected by the type of fluid dispensing system used to deliver reagents. The large majority of microfluidic devices are operated using expensive and bulky syringe pumps, which profoundly limits the simultaneous operation of multiple reactors.[65] To avoid the use of syringe pumps, alternative technologies have been developed, including the so-called lab-on-a-CD (or lab-on-a-disk; LoaD) concept, in which microfluidic channels are incorporated within a Compact Disc (CD) sized disk.[140] The spinning motion of the disk generates three main forces (centrifugal, Euler, and Coriolis), which can be tuned to deliver reagents through the channels at controlled rates.[141] Although LoaDs containing branched channel architectures are suitable for complex applications such as microarrays,[142] only small fluid

volumes can be processed with this method, and the associated manufacturing techniques are significantly more complex compared to rapid prototyping.

The use of centrifugal forces to enhance automation of DNA extraction from whole blood samples and purification of His-tagged proteins has also been demonstrated by Kloke *et al.*, using the so-called LabTube devices.[143] These devices have also been employed for the detection of foodborne microorganisms.[144] Due to their complex architecture, LabTube cartridges require multiple manufacturing procedures, including injection moulding, LED scanning, stereolithography, and thermal sealing. Nonetheless, due to its simplicity of usage, the latter method inspired the present research. Actuated by an ordinary centrifuge, the reactor developed in this study only relies on the use of a 3D printed flow-through architecture (referred to as reactor-in-a-centrifuge, or RIAC).[145] Depending on the centrifuge used, several rigs can be employed simultaneously without additional instrumentation, allowing for parallel testing and optimisation. This approach remains simple, but can potentially be expanded to include temperature-controlled centrifuges (for hot or cold applications) and continuous flow centrifuges, both of which are commercially available or could be custom-built. The versatility of reactors made using both techniques was demonstrated *via* the production of AgNPs and liposomes, further discussed in Chapters 4 and 5, respectively.

3.2 Design criteria and reactors overview

The manufacturing processes presented in this Chapter are applicable for any geometry or design as long as it overcomes 3D printing limitations. Nevertheless, the achievement of size- and shape-control, in particular for AgNPrs, but also for the chosen organic models (liposomes and niosomes), is highly dependent on the mixing regime. The architecture and flow-conditions play a crucial role in the transport of chemical species within a reactor; therefore, throughout this research, several approaches were tested.

Particularly, the prototyping of the reactors was continuously refined throughout the entire research period, by applying continuous improvements to the architectures until the research goals were reached. Although the research was dedicated to the developing of cost-effective, simplified and reliable manufacturing procedures for continuous-flow devices, defining the most adequate design architecture for each synthesis was very important. Aiming at meso- to large-production of inorganic and organic NPs, designs that allowed controlled and enhanced mixing regimes at relatively high TFRs (up to 50 mL/min), were prioritised. Particularly, two types of geometries were

investigated based on their reported efficacy for microfluidic-based production of nanoparticles: hydrodynamic flow-focusing (HFF) and serpentine-like channels.

HFF (already introduced in 1.4.1) was employed for the synthesis of niosomes as it allows high control of the stoichiometry of the reagents by varying the FRR, as shown in Figure 3.4.

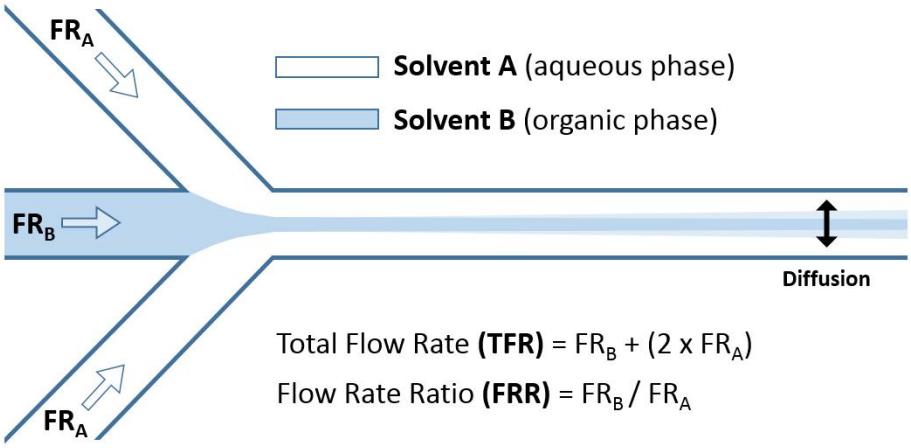

Figure 3.4 Representation of the hydrodynamic flow focusing configuration (readapted from Garcia-Manrique et al.). [146] *Solvent A is introduced from the two side inlets ad the same flow rate (FR); Solvent B in introduced through the central inlet as a different FR. The flow rate ratio can be regulated to allow a stable HFF at the junction. Moreover, a high control over the reaction can be achieved by modifying the flow rate ratio (FRR) and the total flow rate (TFR).*

Moreover, compared to a common two inlets mixing-channel, this configuration increases the contact area between the central and the lateral streams, enhancing the diffusive mixing, which can be further regulated by changing the value of TFR (Figure 3.4).

Similarly, the first designed reactor for AgNPrs was inspired by previous research in this area [67,147] where the HFF junction was connected to alternating straight and curved channels (see section 3.3.2.1). However, the manufacturing approach, as well as materials, reagents, concentrations, TFRs and FRRs employed in these studies, differed from earlier investigations. Changes were made with the specific goal of simplifying the synthesis while maintaining control over the reaction. Although Zmijan presented AgNPrs production through a continuous-flow approach, reactors were manufactured *via* a photolithographic technique, and could be operated at TFR of around 6 mL/h. Differently, this research aims at demonstrating the possibility of producing such particles through cost-effective reactors at TFRs of tens of mL/min.

For the synthesis of AgNPrs (4.2.2), the HFF geometry was subsequently modified into a two-inlet device with a curved-serpentine mixing channel. In fact, curves in the channel can induce secondary flow enhancing mixing (section 1.4.1). This depends on several factors such as the channel cross-section, TFR, channel's radius of curvature and aspect ratio, as described in details by Nivedita *et al.*[148]

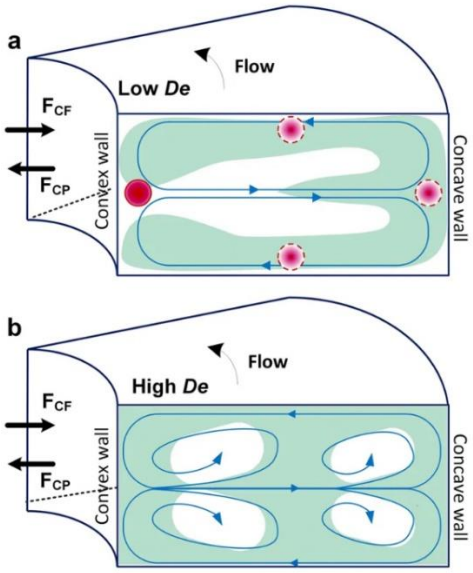

Figure 3.5 Secondary flow induced by the increased inertial forces within a curved channel. Representation of the counter-rotating vortices created at low and high Dean number (De). Image is taken from Nivedita et al. [148]

Figure 3.5 shows the two counter-rotating vortices can be induced at high *De* number (b), with respect to a low *De* (a), which is the principle that allows a more efficient yet controllable mixing. Although generally used for more complex applications such as blood cells separation,[149] in this context inertial microfluidics[150] was employed in order to achieve a faster mixing to overcome the kinetically slow synthesis of AgNPrs, while still providing large-scale outputs.

Moreover, manufacturing improvements and novel flow-methods were established as further discussed throughout the thesis. Among those, a simple two-inlets straight mixing channel was employed for developing a novel cost-effective manufacturing method that substituted the oxygen plasma bonding procedure with a commercially available pressure-sensitive adhesive tape.[139] Moreover, a novel synthesis procedure was entirely conceived by using 3D printed reactors-in-a-centrifuge (RIAC).

Finally, more complex architectures were designed for the photo-assisted flow-biosynthesis of AgNSs with the use of an optical fibre (OF) light source. This component of the research project was based on a collaboration with the Defence Science and Technology Laboratory (Dstl) in collaboration with another PhD student, Thomas Mabey.

3.2.1 Reactors overview

The fabrication methods described are herein defined as 3D printed replica mould casted (3DP-RMC) bonded on tape, glass or PDMS. The bonding can occur by oxygen plasma treatment or

pressure-sensitive tape, which is indicated as "*" and "/", respectively. For instance, a 3D printed replica mould casted bonded on PDMS *via* oxygen plasma, is referred to as 3DP-RMC*PDMS, whereas, if bonded on adhesive tape, it would be indicated as 3DP-RMC/Tape.

The here presented Table 3.1 anticipates the final developed flow-reactors discussed throughout the research, based on the design architectures and their applications, as well as the expected advantages and manufacturing methods.

Table 3.1 Flow-reactors made for a specific application, describing the general advantages and corresponding manufacturing process.

Design architecture	Application	Expected Advantages	Manufacturing
Hydrodynamic flow-focusing (straight)	Temperature controlled flow-production of niosomes	-Stoichiometry control -Increased diffusive mixing -Strong bonding on glass -Thermal bath resistant	HR OC350*Glass
Hydrodynamic flow-focusing (curved)	Flow-synthesis of AgNPRs	-Stoichiometry control -Increased diffusive mixing combined with increased Dean flow at high TFRs	-HR OC350 3DP-RMC*Glass -U2+ 3DP-RMC*Glass
Two inlets curved serpentine	Flow-synthesis of AgNPRs	-Maximised mixing combining diffusion and secondary flow (higher De). -Novelty	-HR OC350 3DP-RMC*glass -U2+ 3DP-RMC*Glass
Two inlets straight channel	Flow-synthesis of AgNSs Flow-synthesis of liposomes	-Cost-effectiveness -Easy-to-perform -No oxygen plasma treatment -Large-scale production -Novelty	-U2+ 3DP-RMC/Tape -µMi-REM*Glass
Reactor-in-a-centrifuge (straight and spiral)	Synthesis of AgNSs Synthesis of liposomes	-Pump-free method -Cost-effectiveness -Novelty	3D printed with U2+
Photo-assisted (three designs)	Light-activated flow-biosynthesis of AgNs	-Cost-effectiveness -Novelty	HR OC350 3DP-RMC*glass (Bonded with corona plasma)

Moreover, a visual representation of the developed reactors is presented in Scheme 3.1, where devices are categorised by common features or applications. Other reactors that were manufactured but did not perform as desired are shown in Appendix B.

Scheme 3.1 Overview of the final employed architectures categorised by common features or application.

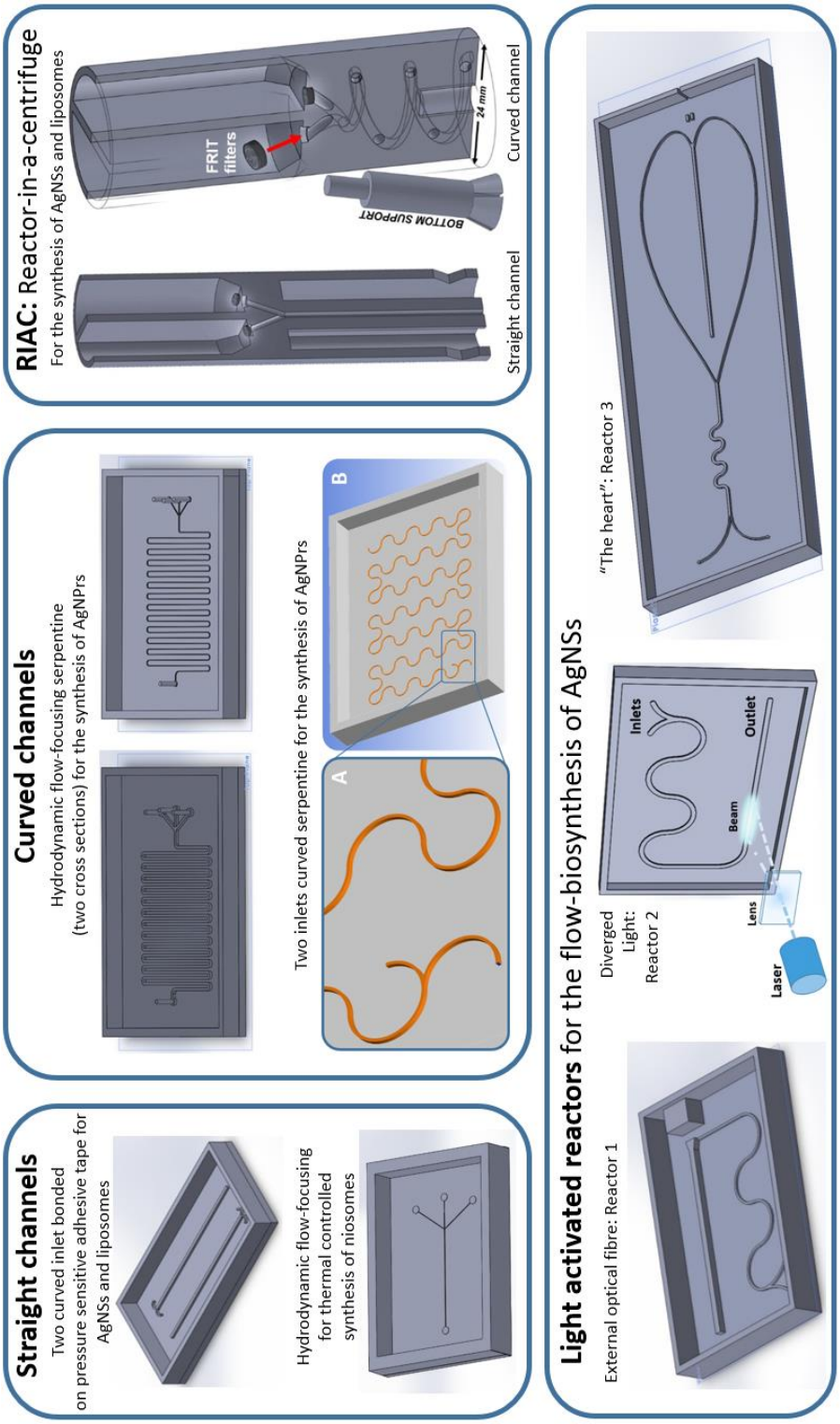

Finally, Scheme 3.2 illustrates development timeline for each prototype, which resulted from the process of progressive readjustment of device's architecture, material, manufacturing protocol, and reaction protocol.

Scheme 3.2 Reactor prototypes with respect to the research timeline and respective applications.

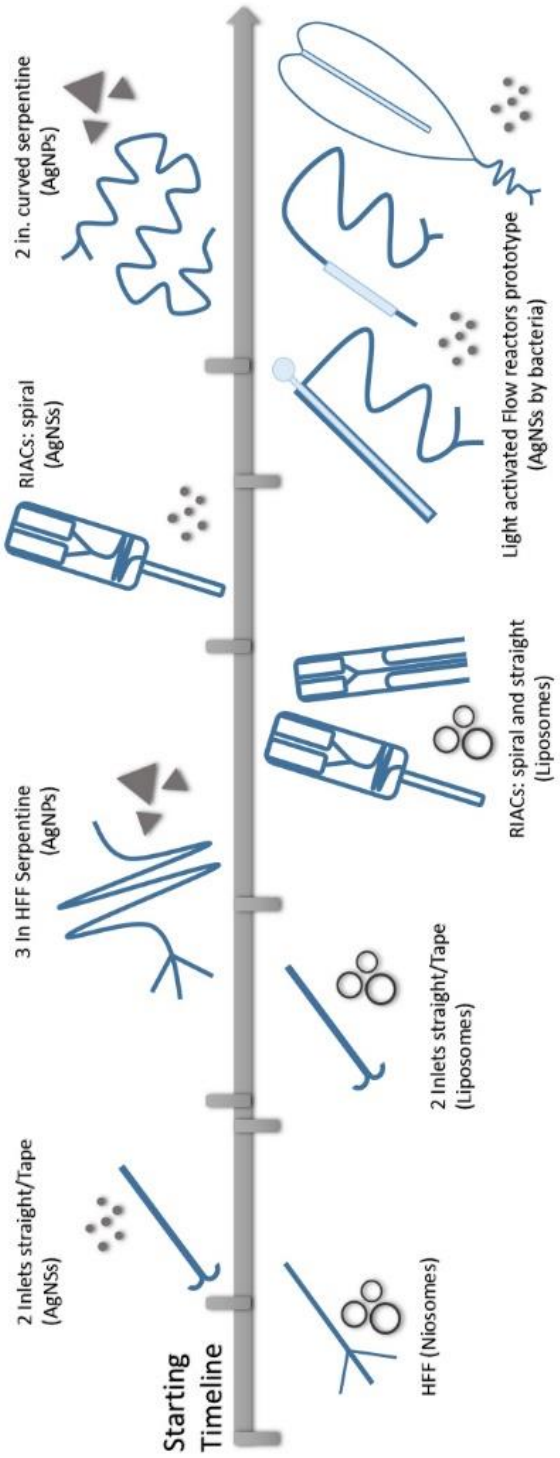

Regarding channel-sizes, reactors were generally built having millimetre-scaled architectures, and the cross-sectional dimension of 1.0 x 1.0 (w x h) was often selected as a representative scaled-up

dimension when compared to conventional microfluidic devices. However, when needed, variations were applied depending on the specific purpose. This seemed to be the perfect combination for achieving manufacturing simplicity, and at the same time, to achieve meso- to large-scale production flow rates (up to tens of mL/min). In fact, if these pressure-driven flow rates were to be employed through micron-sized devices (classic microfluidics with a squared cross-section of around 100 μm), both the average fluid velocity and pressure drop along the channel would be significantly greater, which is not ideal for the selected nanomaterials. As an example, a straight channel having cross-section of 1.0 x 1.0 mm (w x h) and 1 m in length, when operated at 10 mL/min with water (at 20 °C), it would register a pressure drop of 52 mbar. Differently, 52000 mbar would be calculated for a 100 x 100 μm (w x h), with the same length and operated at the same conditions. Furthermore, the pressure further increases for curved channels due to the effect of the secondary flow, which it is not quantifiable theoretically for alternate serpentine channels. However, it is important to underline that, in the present research, the attention was focused on the possibility of testing different designs and manufacturing methods for diverse applications, starting from a reference geometry or slightly modified variations of this geometry. This was preferred over a more detailed study on channel dimensions, which can always be improved in the future works, in order to demonstrate the feasibility of such flow reactors for the selected purpose.

3.2.2 Comparison between 3D printer

Comparison between expensive and economic 3D printers was the first step in this phase of the research, in order to evaluate the feasibility of using less expensive manufacturing approaches for the production of flow reactors (Figure 3.6). In order to compare significantly different technologies, and based on the available resources, a light-cured resin multi-jet 3D printer (worth approximately £150k) was compared with a common fused deposition modelling (FDM) “desk” 3D printer (value of £1.7 K), as shown in Figure 3.6.

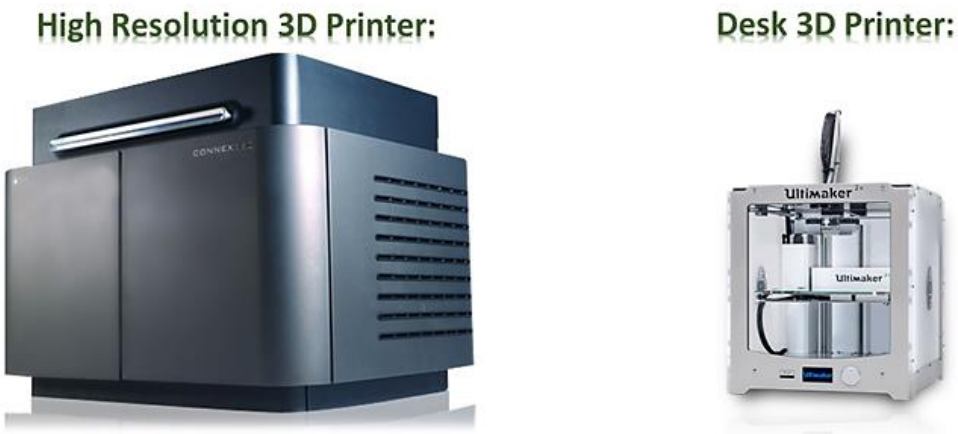

Figure 3.6 3D printers: Objet connex 350 (left); Ultimaker 2+ (right)

The high resolution (HR) Objet Connex™ 350 (OC350) adopts a technology that the company manufacturer calls PolyJet™, which allows creating smooth surfaces with high precision. With this technology, similar to inkjet document printing, the OC350 jets microscopic layers of a liquid photopolymer onto a build tray, and instantly cures them with UV light. The biggest advantage of this machine relates to the possibility of jetting different materials at the same time. The supporting material, for instance, is a soft rubber-like layer that is removable by high-pressure washing, leaving the clean prototyped piece underneath. For all printed pieces, a semi-transparent resin called VeroClear™ was used.

In contrast, the Ultimaker 2+ (U2+, Figure 3.6, right) is an FDM 3D printer. This technology is based on the thermal layer-by-layer extrusion of the printing material. Non-transparent polylactic acid (PLA) or acrylonitrile-butadiene-styrene (ABS) filaments are generally used as economic and reliable materials.

These studies and an in-depth characterisation of 3D printed moulds, using a desk and a high-resolution 3D printer, are presented in order to clarify the advantages and disadvantages of the manufacturing. This was also related to the accuracy of the designed architectures within the final 3D printed product.

3.3 Materials and Methods

A range of manufacturing methods were tested and different types of flow reactors were prototyped and produced during the project. Presented here are the developments in manufacturing methods for the most effective and finally adopted device configurations.

Alternative architectures or manufacturing methods attempted are shown in Appendix B (B.1, B.2 and B.3).

3.3.1 Device manufacturing procedures: 3D printed replica moulds

For all devices conceived for the 3D printed replica mould casting methodology, the positive moulds were designed using the CAD software Solidworks®. The channel architectures were extruded from a flat base, and side walls were designed in order to contain the poured PDMS. Other than the channel design, the main variables considered in the process were: the 3D printing technology, the material of the master mould, the treatment of the elastomer, and the bonding process (both material and technique). Scheme 3.3 shows the general steps (further discussed in detail) of the 3D printed mould casting procedure.

Scheme 3.3 Graphical representation of the manufacturing process of 3D printed replica mould reactors bonded on tape, PDMS or glass.

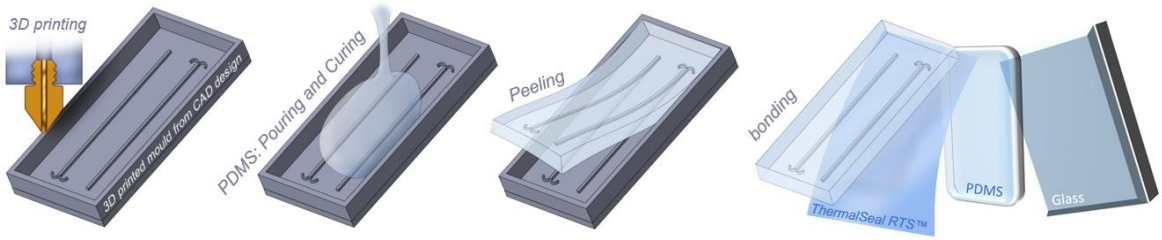

3.3.1.1 Step 1: 3D printing and mould treatments

As previously mentioned, the OC350 printer (Stratasys Ltd., USA) was adopted for high-resolution 3D printing. The material chosen for this machine was a semi-transparent resin called VeroClear™ and, when needed, a rubber-like removable supporting material (TangoBlackPlus™) was automatically created by the software based on the desired features. These moulds were printed by activating a final glossy treatment in order to make their surface as smooth as possible and minimise roughness. Differently, PLA was adopted for the U2+ printer (Ultimaker B.V., The Netherlands), equipped with a 0.4 mm nozzle. For all the U2+ printing, the following printing settings were adopted: bottom/top thickness=0.5 mm, fill density=100%, print speed=50 mm/s.

A 3D printing test was performed by designing an extruded geometry on a flat supporting base with channels of 2 cm in length, 1:1 aspect ratio and side dimensions of 1.0, 0.8, 0.6, 0.4, 0.2, 0.1 and 0.05 mm. These test samples were then printed by both OC350 and U2+ (Section 3.4.1).

Before moving to the next manufacturing steps, no further treatments were needed for PLA moulds made with U2+. On the other hand, VeroClear™ moulds needed to be flushed with IPA, then deionized water, followed by acetone, to remove impurities soluble in different solvents. Finally, moulds were placed into an oven at 60-70 °C overnight.

Furthermore, two post-treatment alternatives were needed before the PDMS pouring step due to the inhibitory effect of the resin on the curing agent:[130]

- **Temperature:** The mould was maintained at 60-70 °C until just before the pouring of the PDMS.
- **Aquapel®:** The mould was treated for making its surface more hydrophobic, using Aquapel®. In particular, Aquapel® was applied to the surface, followed by rapid drying using N_2 gas.

3.3.1.2 Step 2: PDMS preparation, pouring and curing

As suggested by the manufacturer, the PDMS mixture was prepared with 10% (by weight) of curing agent for all reactors presented, with the exception of the bonding procedure on pressure-sensitive adhesive tape, for which the amount of catalyser used was 8% by weight. The PDMS and curing-agent were then vigorously mixed inside a 50 mL centrifuge tube with a hooked spatula until a uniform and complete mixing was achieved. A degassing step was then needed and carried out by centrifuging at 3000 rpm for 10 minutes using the Eppendorf Centrifuge 5804 and Corning Centristar™ tubes (50 mL). The clear and transparent solution was then poured into the mould.

The degassing and curing step can be performed in two alternative ways:

- **Vacuum chamber:** If a vacuum chamber was available, the mould with the PDMS could be kept under vacuum until no bubbles were visible. The time depended on the volume and the thickness of the PDMS layer, as well as the complexity of the geometry. Generally, 50 mL PDMS reactors did not take over 1.5 h. The curing process occured inside an oven at 45 °C for roughly 2 hours.
- **Room temperature and pressure:** Alternatively, the reactor could be left at room temperature for 3-5 hours. During this period, the forming bubbles in contact with the channel were gently removed every 30-45 minutes with a thin tool (such as a needle). Once clear, the PDMS-mould was maintained at 35-40 °C overnight for curing.

3.3.1.3 Step 3: peeling, punching and bonding

The cured PDMS layer was easily peeled-off from the 3D printed moulds, obtaining the negative replica of the channels' architecture. A 1.5 mm manual biopsy punch with plunger (Miltex®, Fisher Scientific, UK) was used to pierce the upper PDMS layer at the inlets and the outlet, in order to allow the connection with external tubing. This was the final - and often the most delicate step with regards to the bonding method. While always keeping in mind the cost-effectiveness of the manufacturing approach, PDMS replica reactors were bonded to three different materials (tape,

PDMS and glass) using two different procedures (oxygen plasma treatment and adhesion to a pressure-sensitive material).

As PDMS and glass can withstand the same protocols, two different bonding methods were employed:

- **Oxygen plasma bonding:** this commonly adopted method was further tested in two variations: oxygen plasma chamber (clean-room) and oxygen plasma corona gun.

  The ***oxygen plasma chamber*** procedure was performed inside a clean room, at room temperature, using the PVA-TePla 300 plasma system. Samples were kept under the plasma environment for 30 seconds under vacuum. Cleaned and dry PDMS or glass slides, both with the PDMS replica moulds, were positioned inside the plasma system maintaining the surface to be bonded upwards. The vacuum chamber was activated, followed by inflow of oxygen. Plasma exposure occurred for 30 seconds. The following sequence of steps was executed as fast, but as accurately, as possible in order to avoid long interactions between the treated surface and air. The plasma action was stopped, the vacuum deactivated to allow the chamber door to open, and samples quickly removed, put in contact with each other and pressed by hand with the help of a rigid flat surface for better pressure distribution.

  Alternatively, the ***oxygen plasma gun*** treatment was performed under a fume hood, in the laboratory at room temperature. The corona plasma gun (purchased from Electrotechnicproducts, US) creates plasma sparks using the O_2 present in the air. The PDMS replica mould was positioned over a bench with the surface to be treated oriented upwards, together with another layer of either PDMS or glass. The gun was activated and manually passed above the surfaces (at a distance of about 1 cm from the surface) for 45 seconds. The two parts were then quickly connected, and positioned underneath a 5 kg weight for at least 2 hours (better if overnight).

- **Pressure-sensitive adhesive tape:** PDMS replica moulds were simply bonded on a commercially available pressure-sensitive adhesive tape (ThermalSeal RT™), which was purchased from Excel Scientific (USA).[139] The peeled-off reactors were positioned over the tape and left under pressure (underneath a 5 kg weight) overnight (further details are discussed in Section 3.4.2).

3.3.2 Designed reactors and tested bonding methods.

3.3.2.1 Three-inlet flow-focusing serpentine (3DP-RMC*Glass and 3DP-RMC*PDMS)

The first two reactors were designed following a concept previously developed by this research group, i.e., consisting of a serpentine mixing channel connected to three inlets and one outlet (Figure 3.7).[67] When aiming at large-scale production, incrementally larger cross-sectional areas of the mixing channel were considered. Two master moulds were designed, with the same layout and features, but with a different cross-sectional area.

The designs, shown in Figure 3.7, consist of three inlet channels joined at a 45-degree angle to form a hydrodynamic flow-focusing junction, and then a 1 m long mixing channel. Each device had two 90 degree turns (r = 1 mm), and 25 U-turns (r = 2 mm). The cross-section aspect ratio of 1:1 was kept for both designs, and dimensions were 1 mm × 1 mm and 250 μm × 250 μm (w × h) for Design *A* and Design *B,* respectively (Figure 3.7). Pillars with a diameter of 1.20 mm were initially designed at the inlets and outlet positions, to be extruded for 1 cm, in order to allow the connection with the microfluidics tubing and syringes. However, in subsequent printings, pillars were removed from the design, to avoid PDMS fractures during the peeling-off that could cause leaking, and the above-mentioned punching method was adopted.

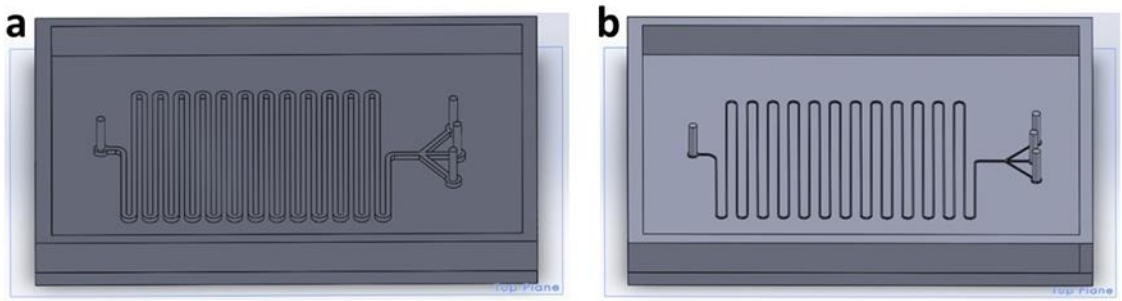

Figure 3.7 Flow-reactors master moulds' design of the 1.0 mm × 1.0 mm (a), and the 250 μm × 250 μm (b) channels. (Solidworks CAD).

The 1.0 x 1.0 mm design was printed using both 3D printers (OC350 and U2+), whereas the 250 × 250 μm was manufactured with the high-resolution machine only, due to limitations in the resolution of the U2+ printer. After post-treatment with Aquapel® for the VeroClear™ material, the PDMS replica moulds were created and peeled off the mould. The oxygen plasma treatment, adopting the PVA-TePla 300 plasma cleaner, was carried out inside the clean-room, and the reactors were sealed onto a microscope glass slide (50 x 70 mm, 1 mm in thickness; Corning® microscope slides, Sigma-Aldrich, Gillingham, UK) or a second and thin layer of PDMS cured inside a plastic Petri dish.

3.3.2.2 Two inlets curved serpentine for enhanced mixing (3DP-RMC*Glass and 3DP-RMC*PDMS)

While maintaining the same manufacturing protocol of the previous reactor (3DP-RMC*PDMS), the design concept was adapted in order to improve mixing efficiency, particularly when aiming at the synthesis of AgNPrs (further disused in Chapter 4). Regarding the device's architecture, the main differences with the previous design were the absence of the central inlet, leading to the absence of flow-focusing, and the elimination of straight paths between the curved units of the geometry. In this new design (Figure 3.8), the serpentine was continuously curved, changing orientation in order to enhance mixing, based on the increasing inertial forces[148] as for Dean's equation (Section 1.4.1).

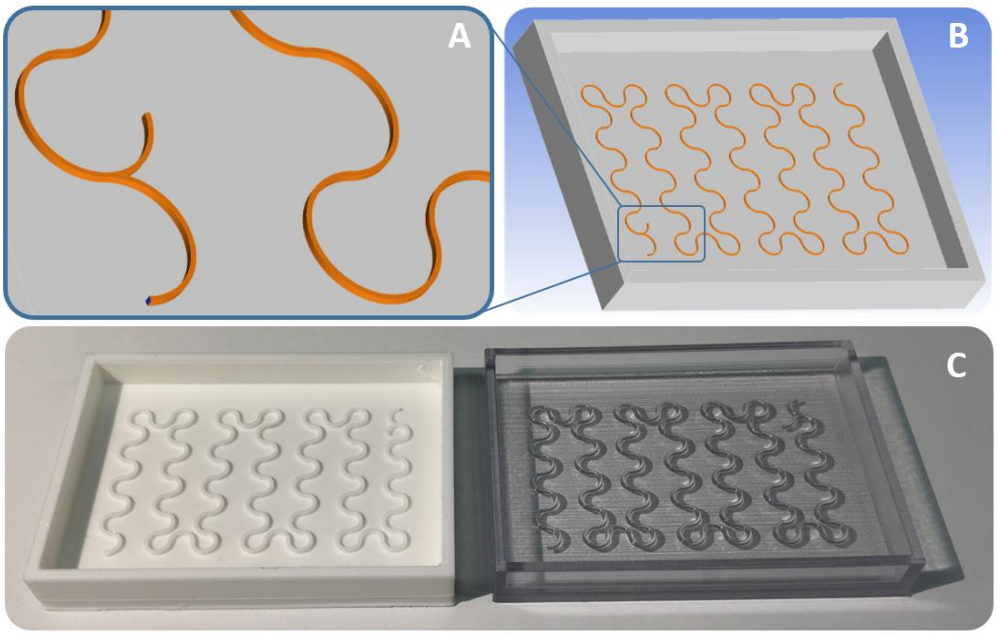

Figure 3.8 Two inlets curved serpentine reactor. CAD design (B) and magnification of the two inlets and junction between the inlet channels (A). C) 3D printed moulds in PLA using the U2+ printer (Left), and in VeroClear™ using the OC350 (Right).

The mixing channel's dimensions were designed to be 0.60 x 0.80 x 100.00 mm (w × h × l); the inlet channels had the same dimensions and each curve had a radius of 2 mm. The curved serpentine reactor was printed with both 3D printers (OC350 and U2+), and bonded on PDMS by oxygen plasma and corona plasma treatments.

These design variations were decided after the initial synthesis test of AgNPrs performed with the HFF flow-reactor, in combination with computational fluid dynamics (CFD) simulations (Chapter 4).

3.3.3 Two curved inlets to straight channel device's design and fabrication: 3D Printed Mould Casting bonded on adhesive tape (3DPM-C/Tape)

The CAD design of the curved to straight channel reactor consisted of two semi-circular inlet channels of 0.50 × 1.00 mm (w × h) having a radius of 1.50 mm. The junction converged into a straight channel of 1.00 × 1.00 × 60.00 mm (w × h × l). To facilitate prototyping and testing, two channels were designed for each mould (Figure 3.9). The master mould was made out of PLA using the U2+ 3D printer equipped with a 0.40 mm nozzle diameter. The 3D printing parameters were set as follow: bottom/top thickness = 0.5 mm, fill density = 100%, print speed = 50 mm/s.

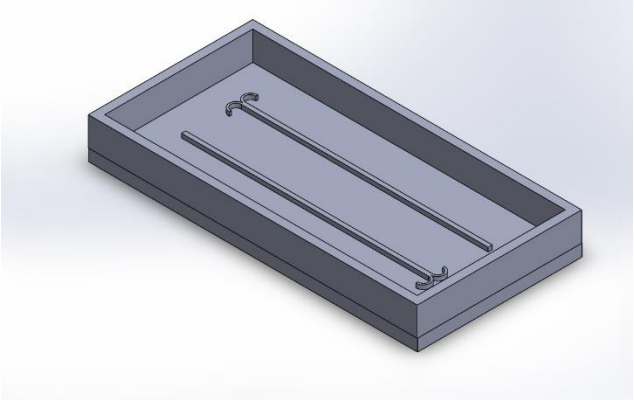

Figure 3.9 Two-channels architecture at the base of the master mould (CAD design with Solidworks).

For this device, PDMS replica were prepared using a 10.2/0.8 (w/w) ratio between the PDMS precursor and the curing agent (Sylgard® 184, Dow Corning Corporation, Michigan, USA). Degassing occurred by centrifugation (3000 rpm for 15 min), using an Eppendorf Centrifuge 5804 and Corning Centristar™ tubes (50 mL), and the pouring and curing procedure was performed at room temperature as previously stated (Step 2: PDMS preparation, pouring and curing). After peeling the PDMS replica off the master mould, a 1.5 mm diameter biopsy punch with plunger (Miltex®, Fischer Scientific, UK) was used to create inlet/outlet holes to connect the tubing. The ThermalSeal RT™ tape, purchased from Excel Scientific (USA), was adopted to perform the sealing of the PDMS replica mould.

3.3.3.1 Mould characterisation: morphology and profile

The morphology of the master mould of the 3DPM-C/Tape was characterised using a non-contact technique, using the optical Alicona Infinite Focus 3D profilometer (5× magnification lens, vertical resolution: 410 nm, lateral resolution: 6.59 µm). Moreover, in order to evaluate the printing repeatability, the same design was 3D printed three times, and two-dimensional (2D) images (at 2.5× magnification) were acquired to measure the channel's width at five equidistant locations along the mixing channel (separation distance between measurements = 2 mm). Measurements

were performed using Image-J software (NIH, USA). For comparison, a micro-milled replica mould reactor bonded on glass by oxygen plasma treatment (µMi-REM*Glass), having the identical design, and bonded on glass by oxygen plasma treatment (PVA-TePla 300 plasma system). The plasma was produced following the previously reported protocol.[125]

Same settings of the Alicona were used for the characterisation of test moulds made with PLA, whereas the profile of the semi-transparent VeroClear™ was characterised using the mechanical Taylor-Hobson profilometer.

3.3.4 Flow-focusing to straight channel for temperature-controlled synthesis

A second hydrodynamic flow focusing design was developed. The reactor comprised two lateral channels, symmetrically angled and merging into the mixing channel (Figure 3.10). The mould was produced in VeroClear™ to test the smallest printable dimensions declared by the manufacturer of the high-resolution Objet350 Connex™ (0.1 x 0.1 mm, w × h), for a mixing channel with a length of 23 mm. Three individual moulds were printed for size comparison through a mechanical profilometer (Talysurf-120 L, Taylor-Hobson, United Kingdom).

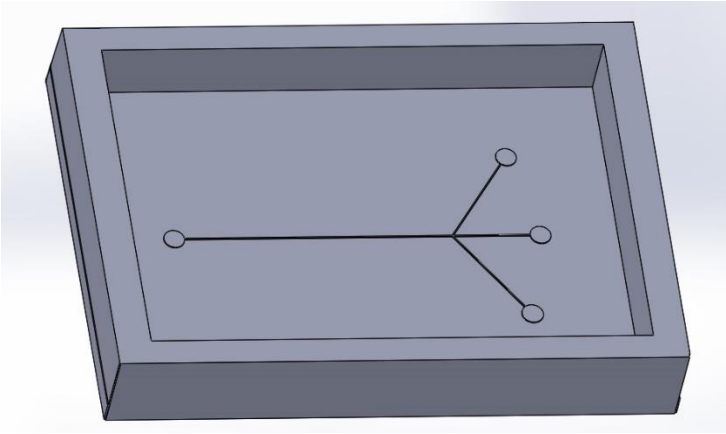

Figure 3.10 Thee inlets flow-focusing reactor design

Aquapel® pre-treatment, followed by the pouring, curing and punching procedures described before, were carried out. After the peeling-off step, PDMS architectures were sealed onto a microscope glass slide (50 x 70 mm; Corning® microscope slides, Sigma-Aldrich, Gillingham, UK); oxygen plasma bonding was carried out inside the clean-room using the PVA-TePla 300 plasma.

3.3.5 Reactor in a Centrifuge (RIAC): a novel pump-free concept of 3D printed mixers

The RIACs were designed using CAD software (Solidworks®), and 3D printed in polylactic acid (PLA) *via* a FDM 3D printer (U2+). The device architecture comprised two equally sized reservoirs

connected to a mixing channel through a Y-junction. Channels were embedded within a cylindrical body, which was designed to be hosted in a standard 50 mL centrifuge tube. After testing various prototypes (section 3.4.4), two different geometries of the mixing channel were evaluated and compared: straight (channel inner radius: 0.75 mm, channel length: 51 mm) and spiral (channel inner radius = 1.00 mm, radius of curvature = 6.5 mm, channel length = 102 mm, number of revolutions = 2), as shown in Figure 3.11A and B, respectively.

In both cases, RIACs were conceived to minimise the printing of supporting material inside both channels and reservoirs. A single-body and a two-component configuration (comprising the body and bottom support) were adopted for the straight and spiral RIACs, respectively (Figure 3.11A and B). The two-component configuration for the spiral geometry was created to avoid the presence of supporting material at the bottom surface of the reservoirs, or within the channel as described in the following section (3.4.4). The supporting material was present at the collecting area at the bottom of the straight RIAC and was removed after the 3D printing process (Figure 3.11C and D, before and after removal).

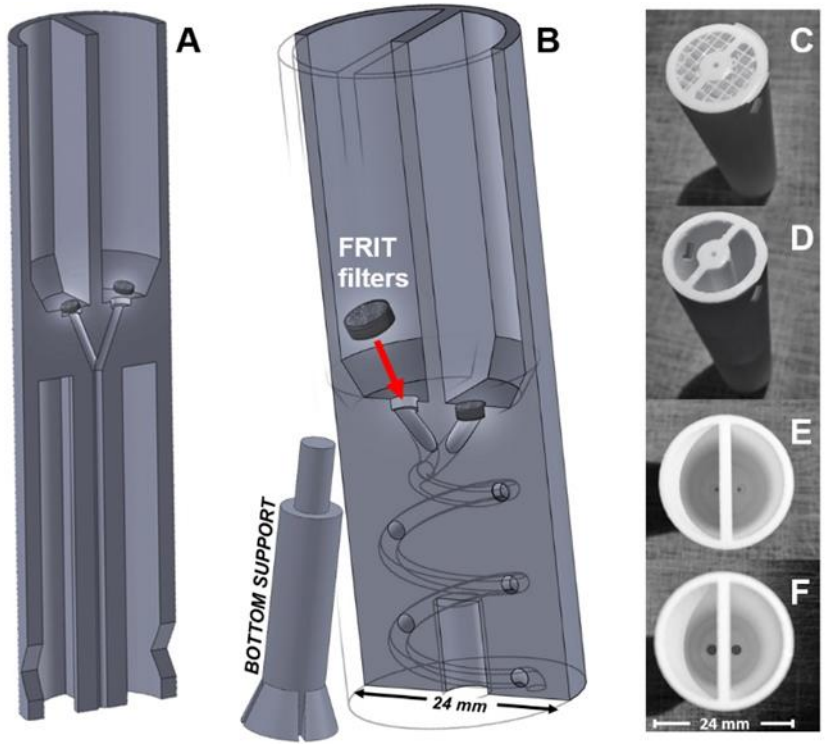

Figure 3.11 Cross-sectional CAD drawings of RIACs, for both straight (A) and spiral (B) mixing channels. Frit filters (3.175 mm in diameter) are inserted into a recess at the bottom of the reservoirs, as indicated by the red arrow.

An additional challenge was to prevent reagents from flowing through the device before actuation (i.e. leakage). Initially, a layer of filter paper or sponge was placed at the bottom surface of the reservoirs, but their performance was not satisfactory. A new design was subsequently developed which could host high performance liquid chromatography (HPLC) *frit* filters into a recess (Figure

3.11B and F). Devices could be operated at relative centrifugal forces (rcf) in the 28 - 1789 rcf range, with no detectable leakage through the frit seats or the body of the device. The lowest rcf corresponded to the minimum force required to drive fluids through the frit filters (with 2 mL of fluid in each reservoir). A structural integrity test was also performed, demonstrating successful operation without mechanical damage until a maximum of 13528 rcf.

For producing liposomes, the solvent exchange mechanism, commonly used in traditional microfluidic-based methods,[151] was adapted to identify suitable synthesis conditions. This method relies on the mixing between an organic solvent in which lipids are solubilised (in this case ethanol) and a non-solvent (water), leading to the self-assembly of lipids to form vesicular systems. The mean diameter and size dispersity (polydispersity index, PDI) of liposomes were determined by dynamic light scattering (DLS) from four independent repeats. Transmission electron microscopy (TEM) was performed on liposomes produced under the optimal operating conditions.

Additionally, as further described, AgNPs were produced by modifying a reducing agent method previously adopted for flow-synthesis,[139] in order to demonstrate the versatility of RIACs.

3.3.6 Reactor concepts for a photo-assisted flow-biosynthesis of silver nanoparticles in a bacteria culture

A novel concept of photo-assisted flow-bio-synthesis of AgNPs was conceived in collaboration with T. Mabey and the assistance of Dr P. He, who defined the formulation adopted for the nanoparticle's synthesis. The device consisted of a two-reagents mixing synthesis, adopting $AgNO_3$ and cell-free extract (CFE). Although various reactors were manufactured, those that led to the best synthesis conditions are herein presented. Moreover, results obtained using these reactors are presented in Chapter 4 (Photo-assisted flow-synthesis of silver nanoparticles in a bacteria culture: a possible solution 4.3.1.3)

3.3.6.1 External optical fibre: Reactor 1

The first flow reactor comprised of a two inlet curved serpentine (1 x 1 mm, w × h), connected to a straight channel (3 x 3 mm, w × h). As shown in Figure 3.12 (left), the connection between the two channels with different sizes was placed close to an extruded squared feature. This feature was designed such that the PDMS replica mould could host the connector of the optical fibre (OF), at 0.5 cm from the channel. In the final chip this would be the PDMS thickness that the light had to pass through, before reaching the inner part of the straight channel. Figure 3.12 (right) shows the ideal light path, which would be coaxial to the straight channel in order to interact with the flowing

through solution and catalyse the reaction. A 1.06 mm glass fibre optic was connected to the laser source (60 mW at 405 nm) and manually aligned.

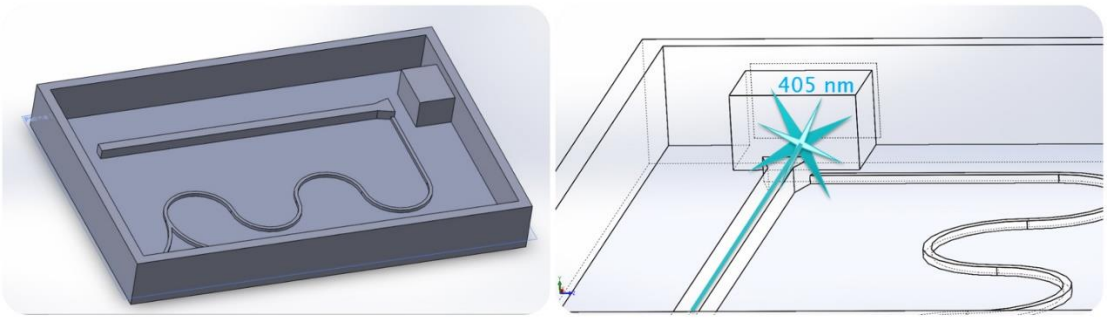

Figure 3.12 Reactor 1 CAD design (left); graphical representation of the optical path (right). PDMS wall thickness between the OF and the main photoreaction channel 5 mm.

The bonding of the peeled-off PDMS architecture was performed by corona plasma over a second layer of PDMS previously cured on a plastic box. This helped maintaining a solid overall structure of the reactor as the laser alignment could easily be lost due to bending of PDMS (Figure 3.13).

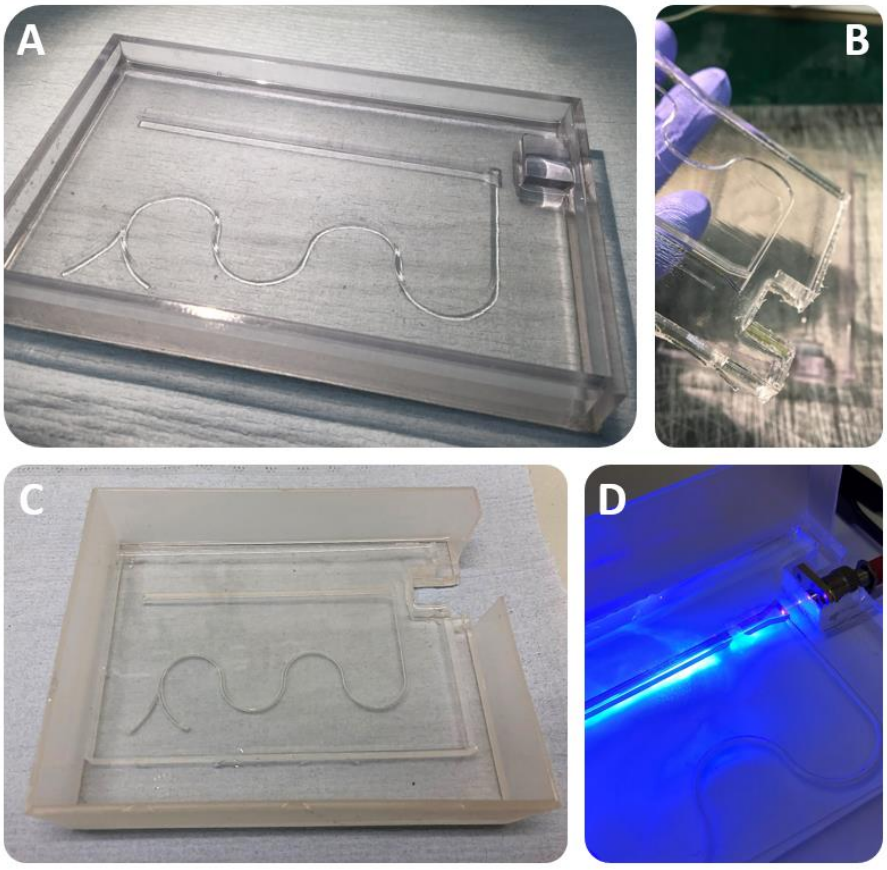

Figure 3.13 Manufacturing steps of the reactor 1 prototype. A) After PSMS pouring onto the VeroClear™ mould. B) Peeled-off architecture; C) after corona plasma bonding on the PDMS layer supported by the plastic box (connection site for the OF was manually cut off); OF aligned shining through the main straight channel filled with water.

3.3.6.2 Diverged light: Reactor 2

Although the first reactor demonstrated promising results, a second alternative was tested mainly due to bubbles formation in the first reactor (as further discussed in Chapter 4). Reactor 2 had a similar shape except for two features: angular architectures were avoided and the size, i.e. the cross-section of the channel, was maintained throughout the whole length (0.5 mm x 3.0 mm; h x w). This was decided in an attempt to minimise manual error during alignment, bubble formation and non-uniform flow velocity. In this case, the laser was shone orthogonally (from above) compared to the top plane of the reactor as shown in Figure 3.14. For doing so, a diverging lens was used to spread the beam along the flow channel.

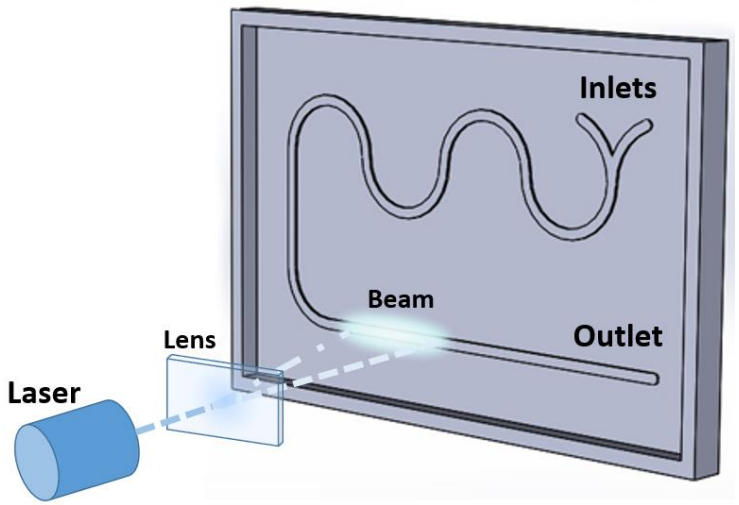

Figure 3.14 CAD design with highlighted ideal glow due to the diverged laser beam (lens) generated from the OF (laser).

3.3.6.3 The "heart": Reactor 3

After testing Reactors 1 and 2, their advantages and disadvantages were evaluated to create a third device for minimising bubbles formation and avoiding angled channels (details in Chapter 4). Particularly, an embedded OF system was realised, with guided features in the 3D printed mould in order to minimise the alignment error and improve reproducibility (Figure 3.15).

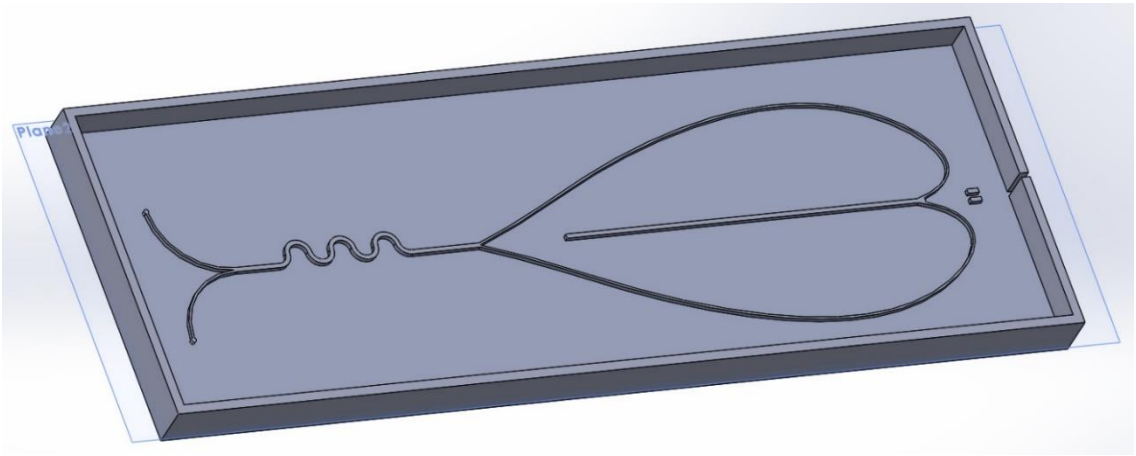

Figure 3.15 CAD design of Reactor 3 (the heart).

The OF (1.4 mm in external diameter) was positioned onto the 3D printed mould through a side aperture on the lateral wall and gently wedged between the two rectangular pillars extruded from the flat geometry. The architecture comprised two curved inlet channels (0.5 × 1.0 mm, w × h), connected through a junction, where the cross-section increased to 1 mm (aspect ratio = 1) channel. After the small curved section (r = 1.5 mm) the flow again divided in two channels (0.5 × 1.0 mm, w × h) and further reconnected in the proximity of the OF. This second junction was designed in such a manner that it resembled a hydrodynamic focusing reactor, with the difference of having the OF instead of the central inlet channel. This also allowed the OF to be positioned in front of a flat surface to minimise light refraction. After the second junction, the straight reaction channel was designed (aspect ratio 1).

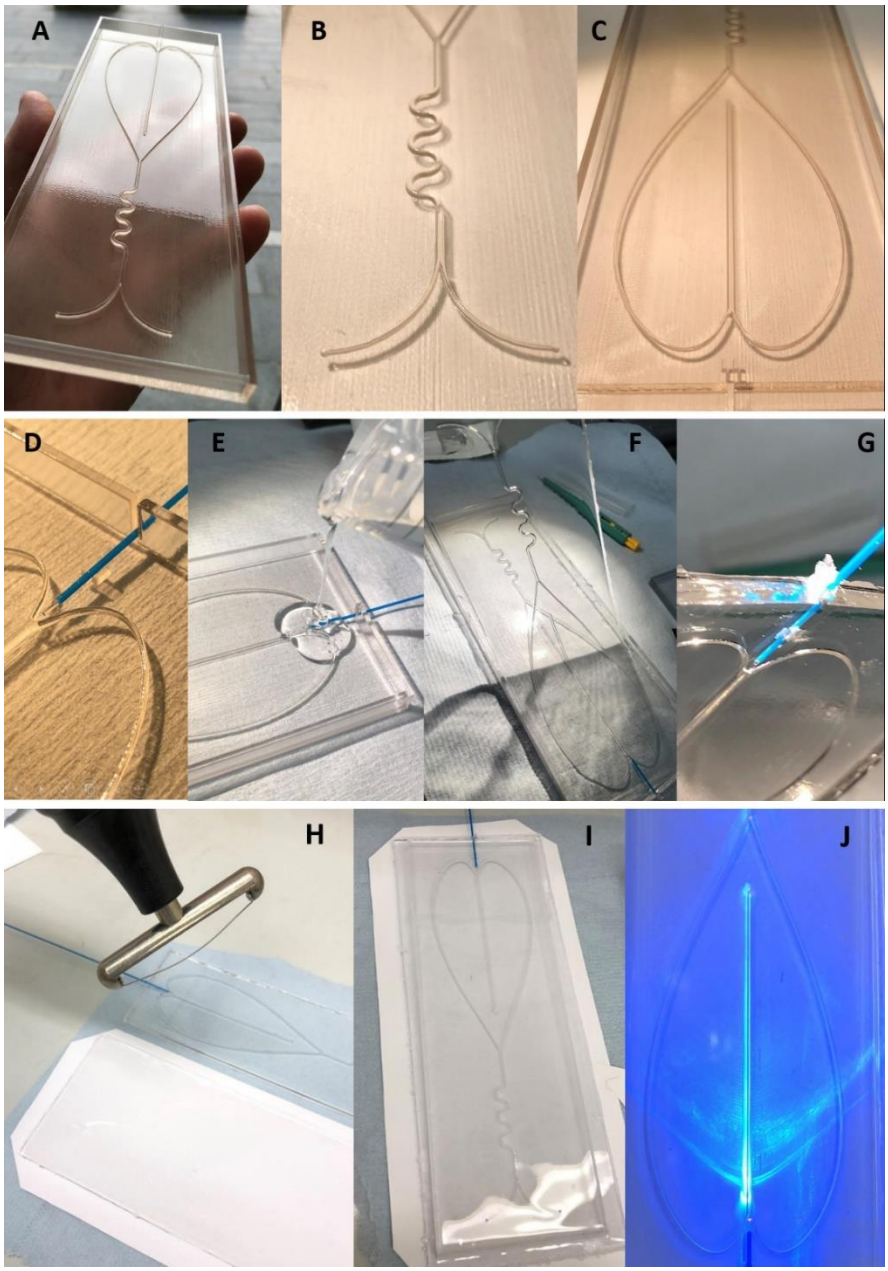

Figure 3.16 Manufacturing stages of Reactor 3 (A-H). The final product (I) and the first optical test (J), ad described in the main test.

The manufacturing steps presented in Figure 3.16 show the reactor production from the 3D printed mould (OC350, VeroClear™; A, B C), to the alignment of the OF (D), the PDMS pouring (E) and the delicate peeling-off process (F). The detail of the embedded OF is also shown (G). Finally, the corona plasma treatment (H) to obtain the final reactor (I) is shown. Once connected to the laser source, the channel appeared as shown in picture J. Results obtained using the photo-assisted flow-bioproduction of AgNSs are presented in Chapter 4.

3.4 Results and discussion

3.4.1 Moulds characterisation: Ultimaker 2+ vs Objet350 Connex™

When prototyping flow-reactors, the reproducibility of the designed geometry is a crucial parameter. Particularly, if the 3D printed architecture is very different from the designed one, theoretical flow predictions can be strongly affected, leading to considerable reductions in product yields or even failure. Therefore, although the 3D printer manufacturers indicated the printing limitations of their products, moulds were characterised to examine the faithful reproduction of the designed geometries. A test mould was designed for the high-resolution resin 3D printer (OC350) and the desk 3D printer (U2+), having channels with dimensions of 1.0, 0.8, 0.6, 0.4, 0.2, 0.1 and 0.05 mm and an aspect ratio of 1:1 (Figure 3.17).

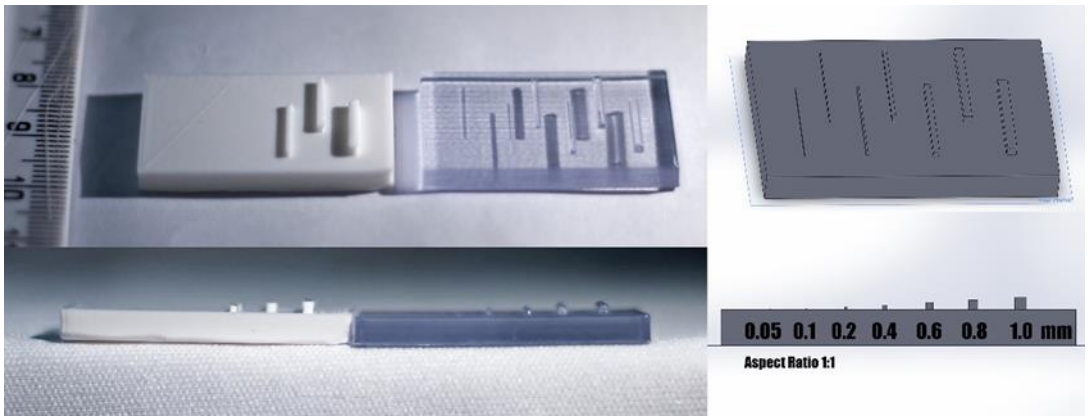

Figure 3.17 Designed size test mould (right) and printed moulds (left). U2+ 3D printer (white PLA material) and the High Resolution 3D printer OC350 (VeroClear™® resin material).

Considering that some slicing 3D printing software will ignore features below a critical size, the printing test was performed on the minimum size of 0.05 mm, which is bigger than the declared limit size for both 3D printers. This is estimated to be 0.03 mm for the HR OC350, and 0.02 mm (referring to the vertical layer deposition), for the U2+. The FDM mechanisms is in fact based on the extrusion of the 3D printing material, which is pushed through a heated portion close to the nozzle that operates at the melting temperature of the material. The nozzle is moved by automated arms based on the .STL file of the CAD geometry. Once extruded from the nozzle, the PLA solidifies after a short amount of time. Due to the nozzle pressure and movement, the extrusion is usually slightly wider than the nozzle diameter and shorter (depending on slicing software settings employed). This effect can be seen in Figure 3.17 where, as expected due to the 0.4 mm nozzle used for FDM, channels having smaller dimensions were not printed. Furthermore, despite having the same size of the nozzle, the 0.4 mm channel was also not printed. Nevertheless, the nominal size of 0.5 mm could be generated as further described (section 3.4.2).

Differently, the high-resolution OC350 uses a material jetting process that creates droplets of resin, which are later cured via UV light treatment. In this case, the size of the drop is one of the most important factors that impose the size limit of the machine, whereas parameters such as the curing time affect the design reproducibility, generally producing more rounded edges as further discussed. Based on the specifications, utilising VeroClear™ resin, the OC350 should have a minimum resolution of 0.03 mm. The OC350 was able to resolve the 0.1 mm designed feature - which was then adopted and characterised for the three-inlet straight channel device for the production of niosomes (section 3.4.3) - whereas the 0.05 mm architecture was not detectable. After this initial test, a profilometric characterisation was carried out starting from the PLA moulds.

3.4.1.1 3D Printed mould using Ultimaker 2+ printer: morphology and roughness

In the case of the non-transparent PLA material, optical profilometry (Alicona) was performed to obtain information about the accuracy of the design's reproduction and the roughness of the surface (Figure 3.18). This is generally important to know as, based on the flow conditions, surface roughness could affect the pressure gradient and frictional forces during experiments,[152] or create optical aberrations.

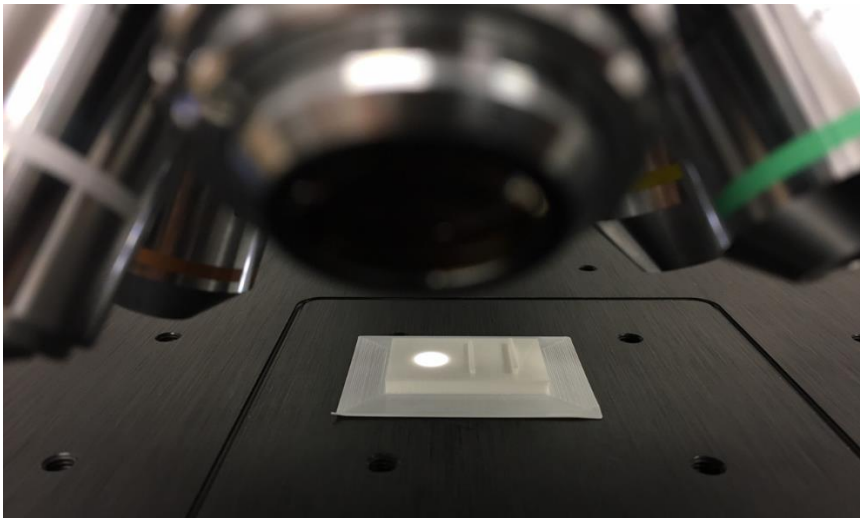

Figure 3.18 Test mould under the optical profilometer Alicona.

Two additional test channels were printed with different sizes but the same aspect ratio of 1.33. The 3D data extrapolated from the experimental values using the optical profilometer are shown in Figure 3.19.

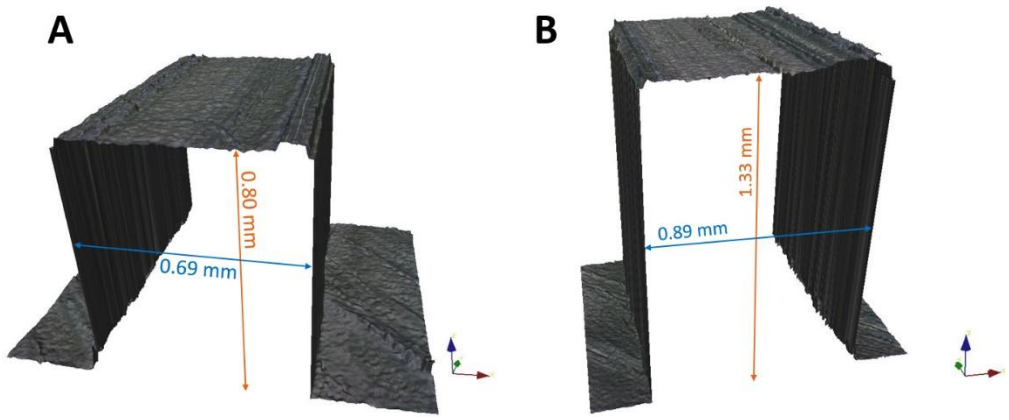

Figure 3.19 U2+ mould test using the Alicona microscope. 3D morphological reproduction of the designed 0.6 x 0.80 mm and 0.80 × 1.33 mm (width × height) channels (A and B respectively).

Specifically, channels were designed with a cross-section of 0.60 x 0.80 mm and 0.80 x 1.33 mm (w × h), for Channel A and B respectively. When compared with the nominal dimensions of both channels, it can be noted that the channel height was accurately reproduced whereas the width was affected by a constant 0.09 mm difference for both test channels. This was largely due to the orientation angle (90°) of the side-walls of the channels with respect to the light source of the profilometer. This effect is clearly visible in Figure 3.19, in which the side-walls of the channels are represented as the projection of the edge of the channel roof towards the base. Therefore, the width of the channel roof is 0.09 mm wider than the designed CAD and, although the side walls are not clearly detectable, it is possible to state that wider features are absent.

Nevertheless, the geometrical reproduction, in terms of the rectangular cross-section of the extruded geometry, appeared to be representative enough for such a cost-effective approach. Limitations might arise from the morphology and roughness of the flat base of the 3D printed master. This is crucial for achieving a uniform and durable sealing during manufacturing. From the morphological examinations, diagonal grooves can be observed in Figure 3.20 due to the oblique motion of the nozzle in the *x-y* plane during printing. The average roughness (Ra) value of the master mould was 6.56 μm, and the maximum peak-to-valley (Rz) value of 85.13 μm was detected in proximity to the diagonal features over the base surface.

Figure 3.20 Morphological characterisation of the 3D printed base including average roughness (Ra) and maximum peak-to-peak value (Rz).

3.4.1.2 3D Printed mould using Objet Connex 350 printer: morphology and cross-section

Moulds created in VeroClear™ using the HR 3D printer appeared to have a smoother surface at first sight (Figure 3.21). However, significant limitations were present. Firstly, moulds needed to be treated before PDMS pouring. In fact, the VeroClear™ resin tended to inhibit the curing process of the PDMS by reacting with the catalyser.[130] This did not allow the PDMS to solidify in proximity to the moulds' surface, making the peeling process difficult to achieve. Moreover, experimental examination and profilometric studies demonstrated poor channel cross-section reproducibility of the design geometry.

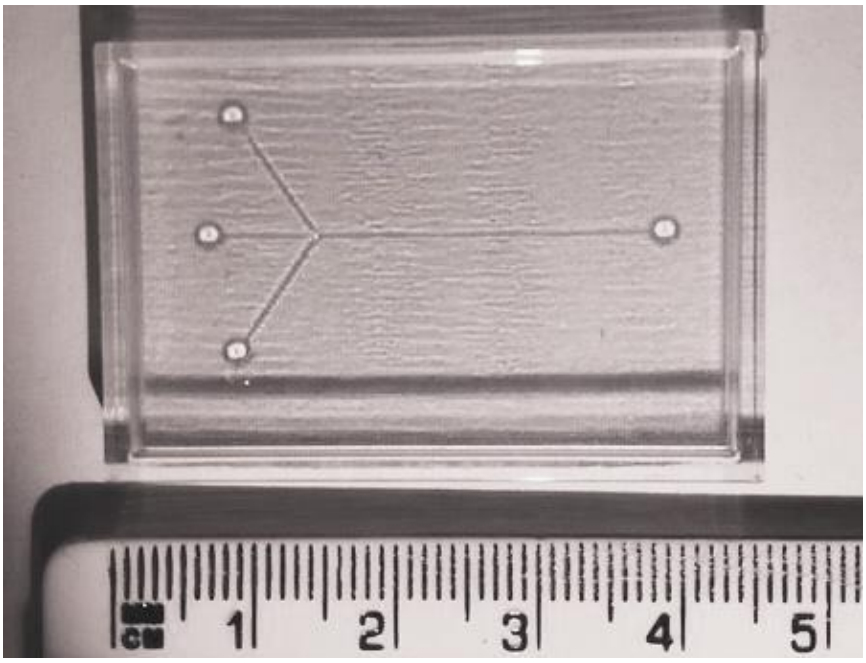

Figure 3.21 One of the three VeroClear™ 3D printed moulds 0.1 x 0.1 x 23 mm (w × h × l). The length is considered from the flow-focusing junction.

Although designed with a cross-section of 100 x 100 μm (w × h), the width of the channel was found to be notably bigger than the designed CAD, reaching more than 400 μm on average. This is clearly shown for the straight hydrodynamic flow focusing reactor inFigure 3.22. As shown in the same figure, this however did not affect the ability to achieve hydrodynamic flow focusing.

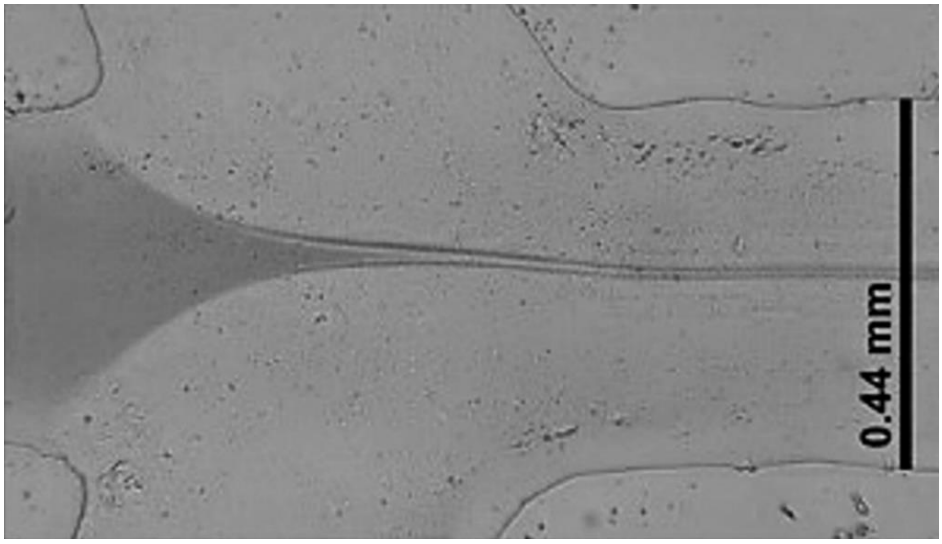

Figure 3.22 Channel width of the hydrodynamic flow-focusing straight reactor made by 3D printing replica mould casted bonded on glass via oxygen plasma. The 3D printed mould was made out of VeroClear™ resin.

However, multiple master moulds were printed and characterised for evaluating the design repeatability. Three equidistant measurements were taken for the characterisation of each mould

at 2 mm across the channel, perpendicular to it, using a mechanical Tylor-Hobson profilometer. Table 3.2 shows the collected data (width, height and cross-sectional area), both with average and standard deviation values over 3 measurements. A notable difference with the nominal value can be observed. The design reproduction for the OC350 is therefore far from accurate for small features.

Table 3.2 Results of the morphological characterisation measurements made on the three manufactured moulds, and comparisons with the CAD design dimensions.

Mould	Width um	Height µm	Cross-sectional Area µm
CAD	100	100	10000
3D-PM1	535 ± 40	47 ± 2	13090 ± 485
3D-PM2	423 ± 14	51 ± 1	11605 ± 262
3D-PM3	507 ± 28	68 ± 3	18007 ± 1092

However, this did not affect the reliability of the manufactured reactor which, maintaining a straight channel, allowed controlled hydrodynamic flow focusing. Moreover, the need of a durable bonding – which is crucial to allow submersion into a thermal bath for temperature control – was satisfactorily achieved. The results of reactor's characterisation, as well as its employment for the synthesis of niosomes (further discussed in Chapter 5, section 5.3.3) were published in collaboration with P. Manrique (University of Oviedo, Spain).[146]

3.4.1.3 Three-inlet flow-focusing serpentine: fabrication and flow tests

The three-inlet hydrodynamic flow focusing serpentine, designed as described in section 3.3.2.1 was 3D printed using VeroClear™ with the HR OC350 printer, and PLA with the U2+ printer. The long serpentine channel (1 meter in length), was chosen to maximise the mixing time, due to the much slower kinetics of the AgNPrs when compared with the AgNSs, as discussed in Chapter 2. Moreover, it was the longest channel possible to fit to a 5 x 7 cm glass slide. The serpentine shape was also chosen in order to increase the effects of the inertial force and enhance mixing.

Therefore, as depicted in Figure 3.23, positive moulds of the channels with a cross-section of 1.0 mm × 1.0 mm were successfully printed by both OC350 and U2+. Moreover, a 250 x 250 µm (w × h) channel was also printed with the same architecture to test the effect of a smaller channel on mixing.

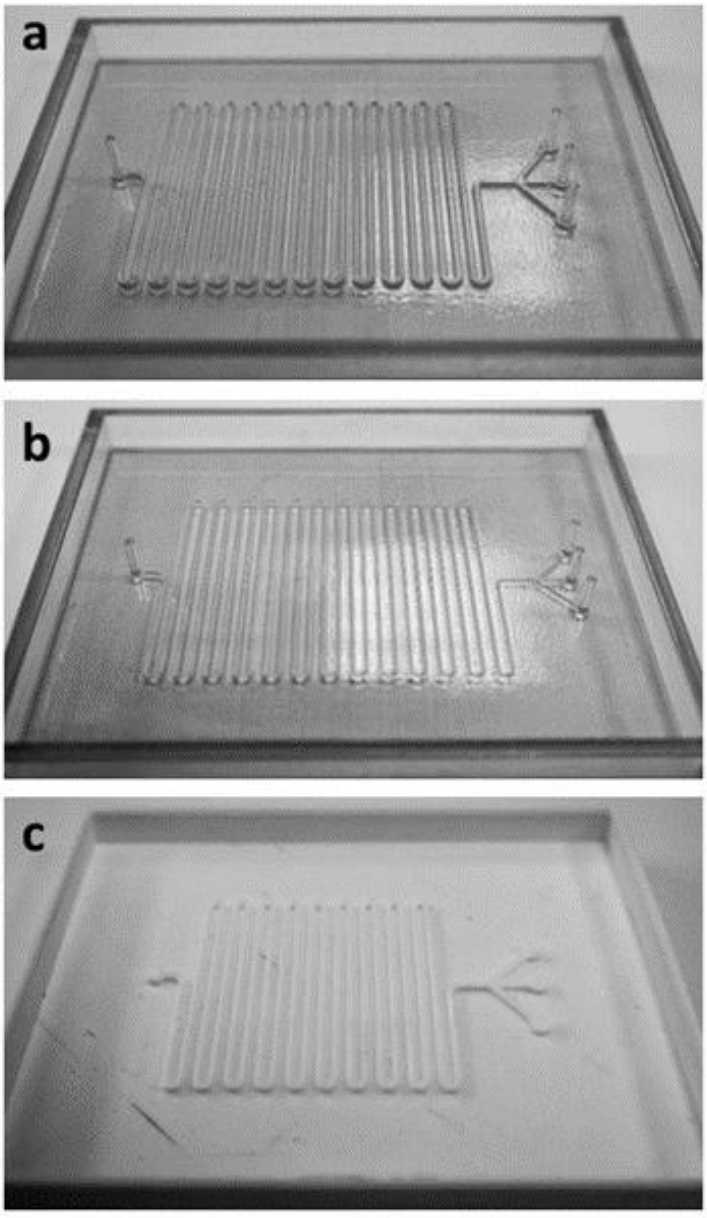

Figure 3.23 3D printed moulds: A) HR 3D printer OC350 mould (1.0 mm × 1.0 mm); B) OC350 mould (250 μm × 250 μm); C) desktop 3D printer U2+ (1.0 mm × 1.0 mm).

Once the PDMS 3D printed replica moulds were obtained, oxygen plasma bonding was carried out using the plasma chamber. This was carried out mainly to evaluate the quality of the bonding for the final chip manufactured using the U2+ mould. As expected, although the PVA-TePla 300 plasma system was used, the roughness of the PDMS layer did not allow adhesion onto the glass surface. Particularly, this left undesirable gaps, as notable from the diagonal lines in Figure 3.24B. From a more accurate observation, the diagonal lines correspond to the previously characterised grooves (3.4.1.1) formed by the motion of the nozzle during PLA extrusion. Leakages occurred during the first test.

Alternatively, a second PDMS replica was prepared from the U2+ mould and bonded onto another layer of PDMS by oxygen plasma. In this case, the PDMS/PDMS sealing resulted in complete bonding. This was likely due to the deformable nature of the material compared to glass, thus a greater contact surface under pressure was obtained (Figure 3.24D).

Differently, when using PDMS replicas created from the moulds printed with the OC350, the bonding was accomplished as expected and devices had greater optical quality (Figure 3.24a and c).

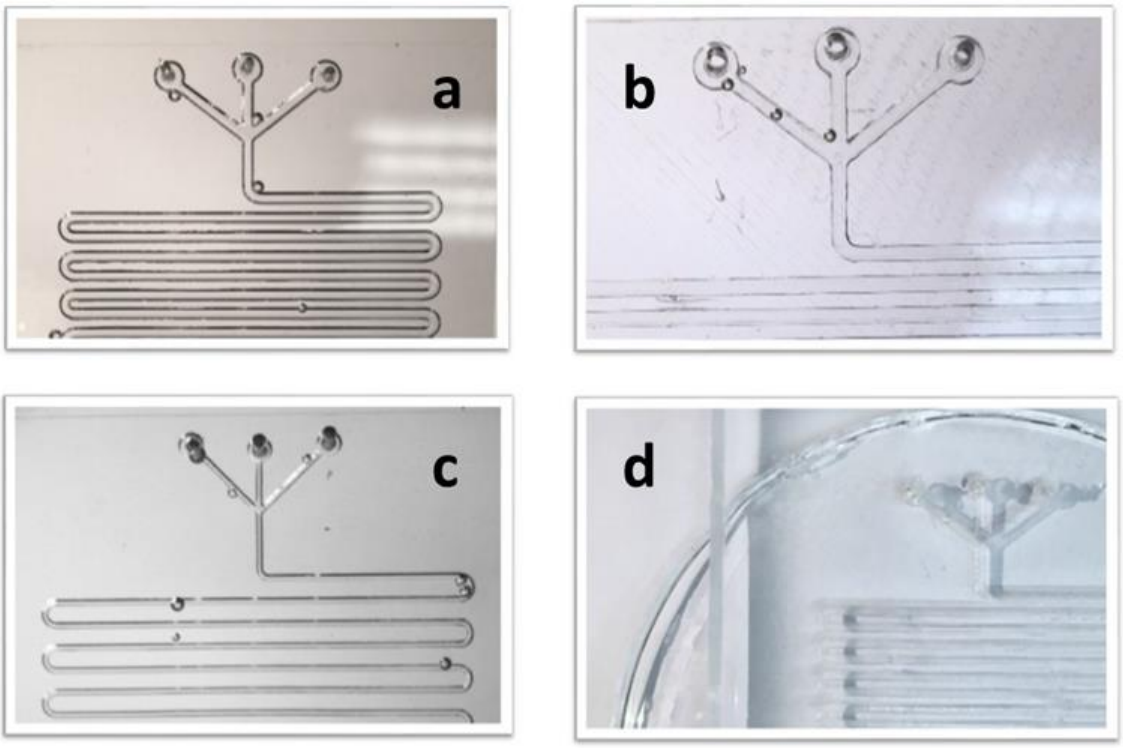

Figure 3.24 Images of the final devices after oxygen plasma treatment (view from above): a) PDMS (1 mm) cast from OC350 mould bonded to glass; b) PDMS (1 mm) cast from U2+ mould bonded to glass; c) PDMS (250 μm) cast from OC350 mould bonded to glass; d) PDMS (1 mm) cast from U2+ mould bonded to PDMS.

Visible bubbles in Figure 3.24 (a, b, and c) had no interference with the channels. Their formation occurred from the nucleation and further growth of microbubbles during the curing step of the protocol. Some of them were then trapped into the PDMS and remained above the channel. Following fabrication, the microfluidic device with a channel dimension of 1.0 mm × 1.0 mm (Figure 3.24a) was tested. Firstly, the absence of fluid leakage was confirmed *via* the manual injection of a food dye solution, indicating strong bonding between the PDMS and glass slide. Following that, a stable hydrodynamic flow focusing configuration was achieved using several water solution colourants (Figure 3.25). For further validation, the order of water and colourant was altered, testing all the inlets and obtaining controllable flow focusing, which is crucial for mixing control.

The device allowed the modulation of the width of the central stream by regulating inlet flow rates (Figure 3.25c and d). This is an extremely important regulation that allows stoichiometric control during the flow-synthesis.

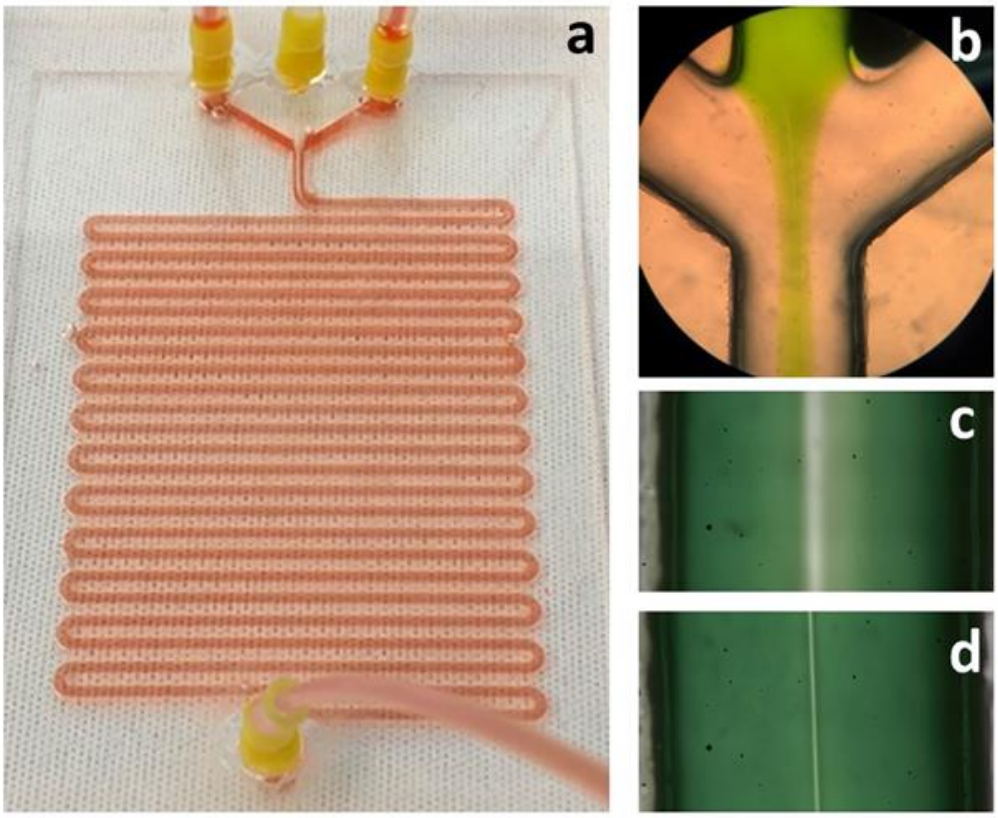

Figure 3.25 Flow focusing tests with colourants: a) Red colourant on the sides and water in the centre; b) Green colourant in the centre and water on the sides; c and d) diffusion control on the central stream. Channel width 1 mm in all figures.

These preliminary results demonstrated high control with a notably cost-effective manufacturing method. However, depending on the application, the manufacturing technique has to be reliable. Therefore, considering the lower manufacturing accuracy for small features, and in order to gather precise information for the fluidic calculations, further profilometric characterisations were performed on the 1.0 x 1.0 (w × h) CAD design.

The first limitation was encountered at the initial stage of the process due to the translucent nature of the VeroClear™ material. This characteristic did not allow for obtaining morphological data using the optical profilometer. The cross-sectional analysis was then carried out *via* the previously adopted Taylor-Hobson mechanical profilometer. However, a second limitation was noted; the large size of the extruded geometry of the channel – which had a 1 mm height – was not suitable for the conic shape and size of the profilometer tip. As illustrated in Figure 3.26, the resulting output from the first experiments showed a non-realistic estimate of the channel cross-section. This was due to the contact of the upper portion of the conically-shaped tip to the channel upper edge. The

red dotted line represents the initial result obtained in comparison with the realistic shape (Figure 3.26).

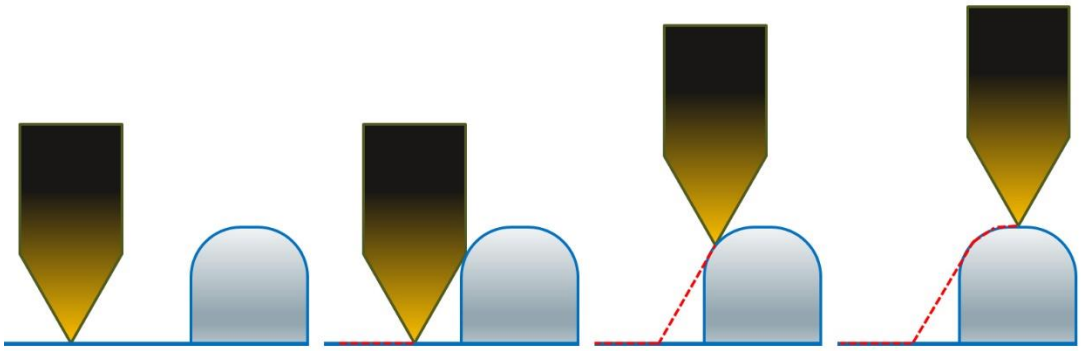

Figure 3.26 stages of the profilometer tip scanning the cross-section of the 3D printed extruded channel (from left to right). The red dotted line represents the non realistic result obtained by the profilometer.

To overcome this limitation, two techniques were combined for the reconstruction of the real channel cross section. Firstly, the samples were positioned at 45 degrees from the horizontal plane by using an angled plane (Figure 3.27a). The two lateral cross sections were then obtained for the left and right sides of the channel, just after the junction, as reported in Figure 3.27b and c. Although results were accurate at this angle, a key information was missing from this approach. In fact, it is not possible to obtain a precise estimate of the channel width, which would vary the calculated cross sectional area of the channel, significantly affecting the flow dynamic calculations.

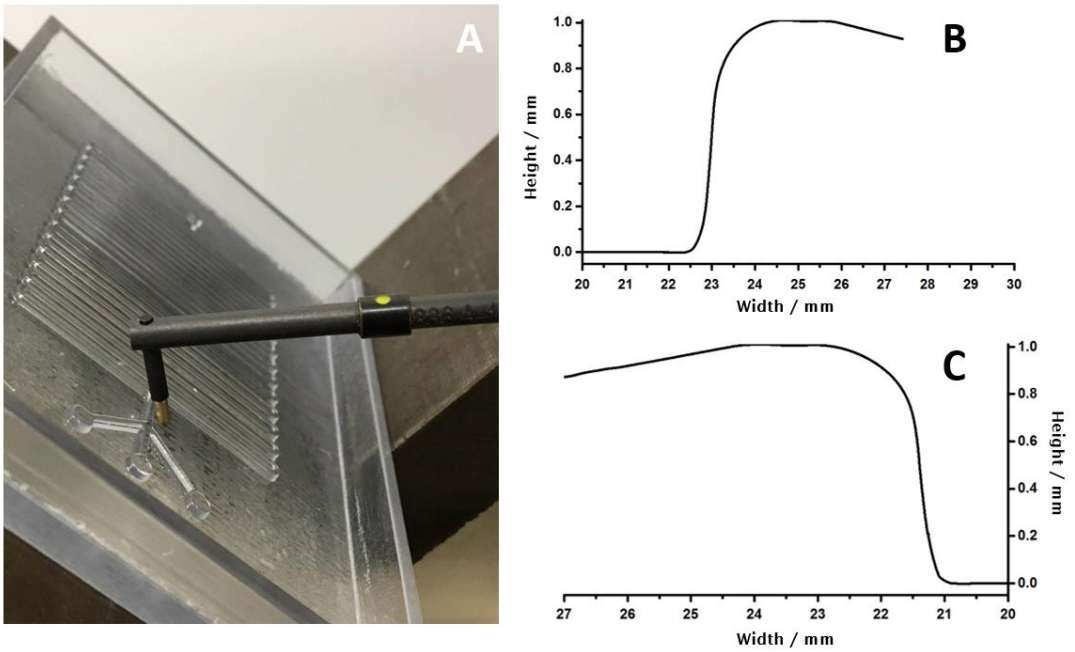

Figure 3.27 . A) OC350 mould test under the Taylor-Hobson profilometer (A). Profiles graph of the designed channel (solid black line) compared with the designed 1.00 mm × 1.00 mm (w × h) channel (dotted line). The design reproduction error for the HR 3D printer is enhanced for smaller channel sizes.

Therefore, a second measurement was performed. In this case, a custom-made laser profilometer, created at the Micro and Nanocharacterisation Laboratory of the University of Southampton, was tested directly on the peeled PDMS layer. Figure 3.28 shows the results and limitations of this technique when scanning the junction of the PDMS channel.

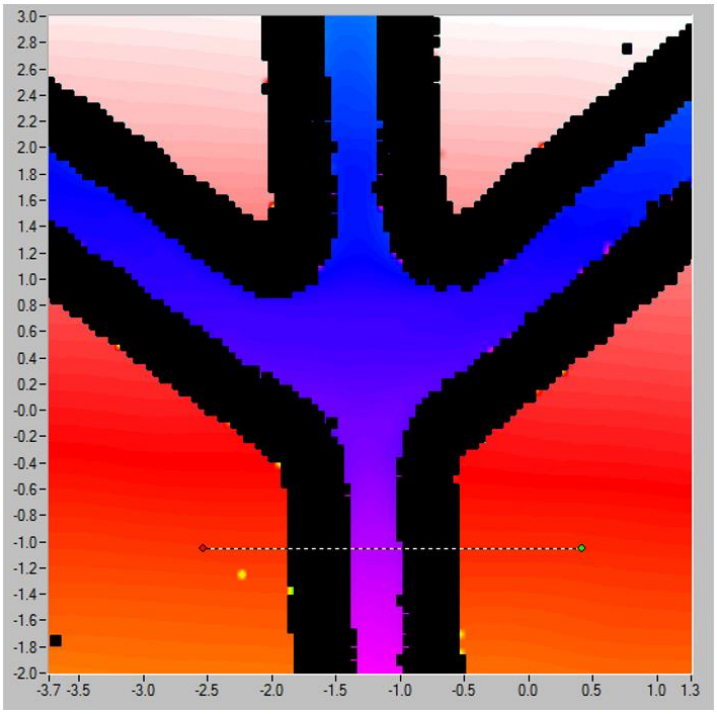

Figure 3.28 Junction region of the PDMS replica of the VeroClear™ 3D printed reactor scanned with the custom made laser profilometer.

Considering that the mould was inverted for the characterisation, the red grading in Figure 3.28 corresponds to the backscattered light from the bottom part of the PDMS that would be bonded onto the glass. Differently, the blue/purple grading gives information of the channel roof. The limitation of the technique is related to the black area in the image. In fact, the detection angle of the custom laser profilometer has a 17 degrees backscattered limit (compared to the axis normal to the surface). The characterisation of the same HFF junction, made with the U2+, is presented in the Appendix section (B.4). No light is therefore detected in the black zone, which confirmed that the channel curvature did not allow data collection. At this stage, the two characterisation techniques were combined. The latter (obtained with the laser profilometer) was able to give the exact distance of the channels wall at the bottom of the geometry by the cross sectional graph obtained (Figure 3.29), which corresponds to the dotted line in Figure 3.28.

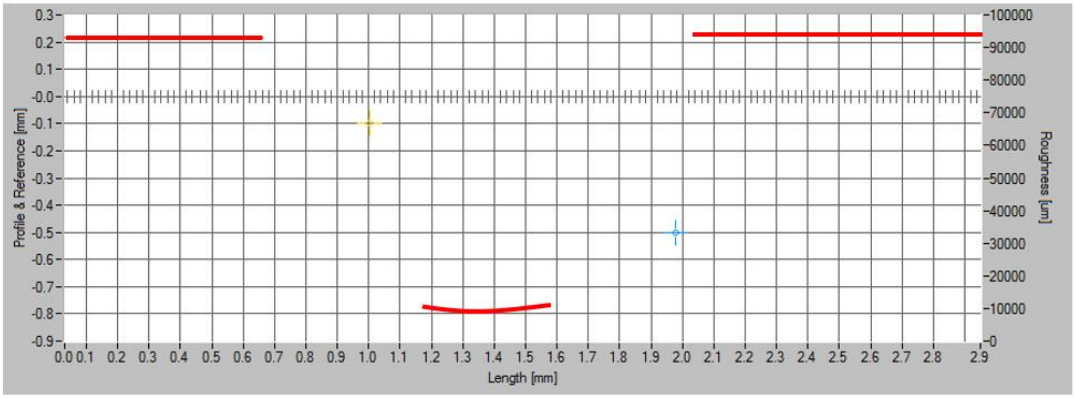

Figure 3.29 Partially detected cross section of the PDMS replica channel created from the HR VeroClear™ 3D printed mould after the junction (related to the dotted line in Figure 3.28)

On the other hand, the graph of the profile is obtained with the mechanical profilometer for both sides of the channel. When combining this information, an exact cross-section of the real 3D printed architecture is obtained. Moreover, data such as the cross-sectional area and the wetted perimeter, can be determined from image analysis with the software Image-J (NIH, USA) after creating a threshold image from the cross-sectional analysis (Figure 3.30).

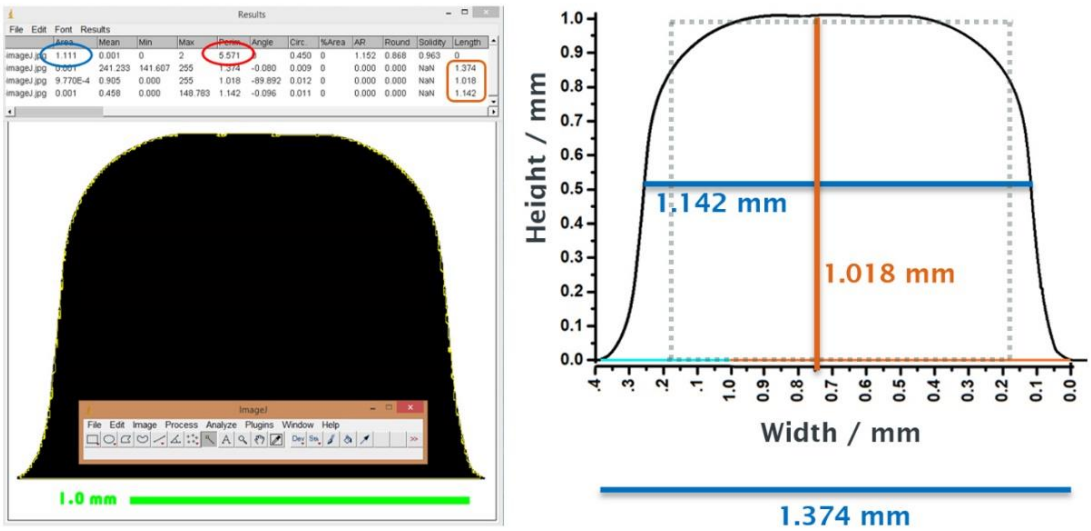

Figure 3.30 Left) Right) Profile graph of the designed channel (solid black line) compared with the designed 1.00 mm × 1.00 mm (width × height) channel (dotted line). The design reproduction error for the HR 3D printer is enhanced for smaller channel sizes.

The VeroClear™ and PLA moulds were further characterised. Figure 3.30 (right) shows how much the measured profile of the actual device deviates from the squared designed shape (dotted line). Differently, the cross-sectional analysis of the PLA extruded channel presented in Figure 3.31 C shows a sharp profile, more representative of the designed geometry. Moreover, the average width

of the FDM channel resulted in a more accurate with (1.01 mm) compared to the OC350 taken at half the high (1.142 mm).

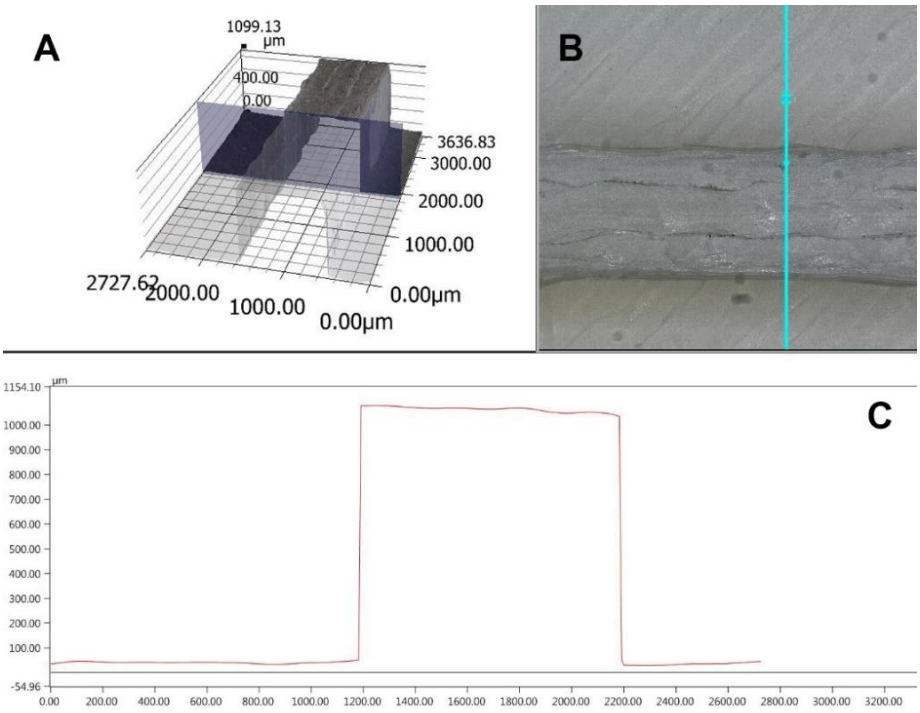

Figure 3.31 Cross section characterisation of the PLA mould. a) 3D representation b) Optical image c) Cross sectional plot.

The adopted technique also allowed the optical characterisation of the transparent PDMS replica moulds. Figure 3.32 highlights the surface of the peeled PDMS replica created from the PLA and VeroClear™ moulds (A and B respectively). The previously described diagonal grooves, related to the nozzle motion of the U2+ 3D printer, were already notable with a 20 X optical magnification (scale bar 1 mm). In contrast, the resin material created a very smooth surface, which is extremely suitable for bonding. Only smaller surface features were noted by tilting the sample up to 13 degrees.

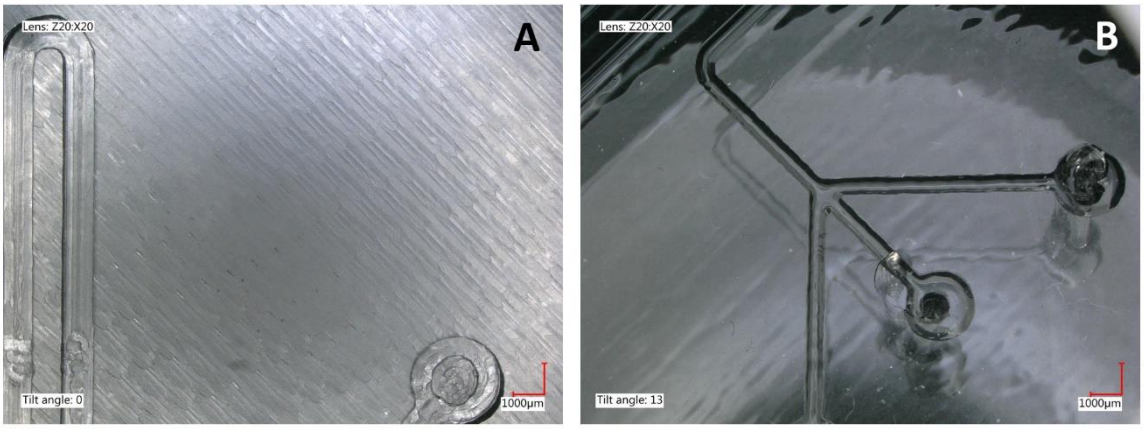

Figure 3.32 PDMS replica moulds from PLA (A) and VeroClear™ (B). Scale bar 1 mm, magnification 20 X, tilt angle 0 and 13 degrees for A and B respectively.

When increasing the magnification up to 200 X on the three-inlet flow-focusing serpentine (250 x 250 mm channel), only small spots can be noted (Figure 3.33A). These are likely created by the residual microbubbles; however, they did not create any limitation to the bonding efficiency, as the surface remained smooth enough (Figure 3.33B). On the other end, the difference between the designed geometry and the real channel was significant. The width of the created channel was approximately 564 µm instead of the designed 250 µm (Figure 3.33C).

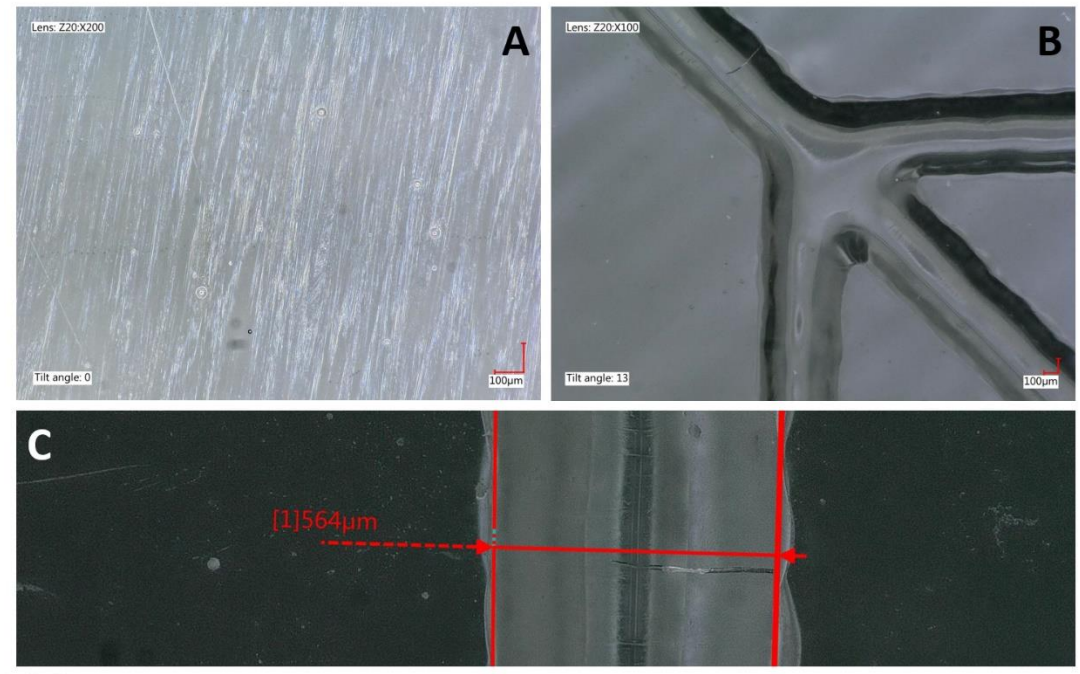

Figure 3.33 A) Flat PDMS area of the replica mould from the VeroClear™ printing; B) tiled view at 100 X magnification of the three-inlet flow-focusing serpentine (250 mm width design) and measurements of the real width of the device (C).

In addition to allowing effective oxygen plasma bonding on glass slides or PDMS flat surfaces, the smoothness of the PDMS replica created from VeroClear™ moulds also ensured effective bonding

on pressure-sensitive adhesive tape. Figure 3.34 shows the final device obtained for the three-inlet serpentine architecture (1 mm channel), bonded on tape.

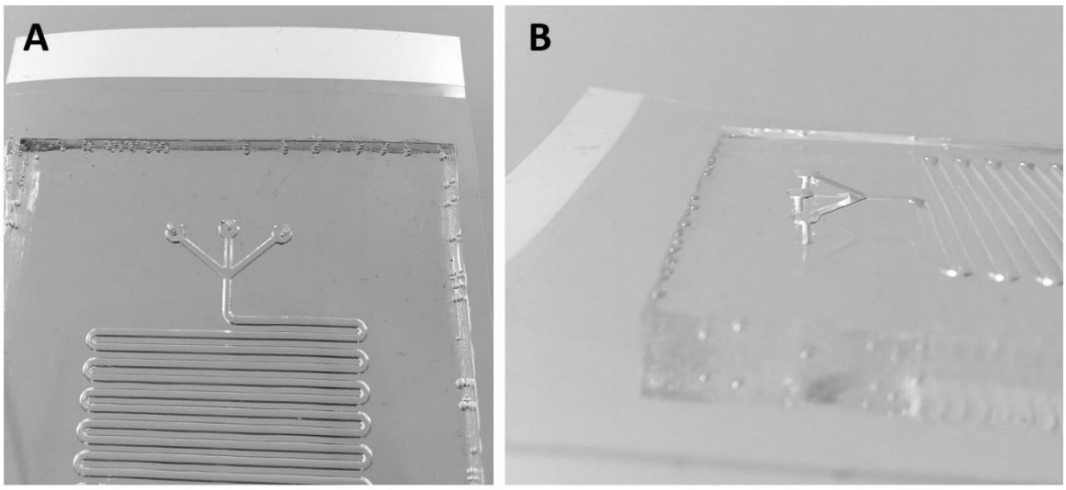

Figure 3.34 The 3DP-RMC reactor (three-inlet flow-focusing, 1 mm in width, aspect ratio 1) created from the HR mould and bonded on pressure-sensitive adhesive tape. A) bottom view; B) side view.

3.4.2 Straight channel bonded on pressure-sensitive tape

A specific characterization was carried out for the two curved inlets straight channel moulds produced in PLA using the U2+. Firstly, the accuracy of the reproduction of the designed channel size and shape was evaluated through morphological characterisation, using the Alicona optical profilometer. For doing so, three replicas of the design were 3D printed and the lens of the optical profilometer was focused on the upper part of the architecture (channel roof, Figure 3.35). In this manner, the width of the mixing channel was measured at five separate and equidistant locations along the channel. Similarly, the radius of curvature of the inlet channels was measured by using a reference circular geometry. Results are plotted in Figure 3.35A and B showing both the images and data. The U2+, printer equipped with a 0.4 mm nozzle, was able to print the 0.5 mm wide feature, which was not initially created in the first mould test (see section 3.4.1).

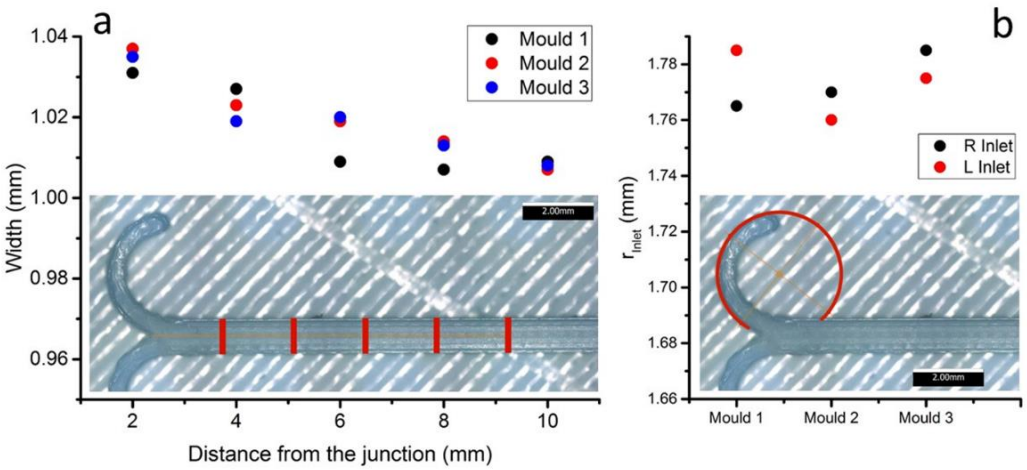

Figure 3.35 A) Width of the mixing channel at 2, 4, 6, 8, and 10 mm from the junction between inlets, for three different 3D printed moulds. An image of a representative channel (at 2.5×magnification) showing the measurement lines (red lines) is reported in the inset. B) Radius of curvature of both right (R) and left (L) inlet channels, for three different 3D printed moulds. A graphical representation of the measurement method is reported in the inset, for the right inlet channel.

The width of the mixing channel was comparable between the three moulds, with the maximum difference detected between mould n.1 and n.3 at 6 mm from the junction, and only equal to 0.0011 mm (Figure 3.35A). All moulds presented a slightly larger width just after the junction, which gradually decreased along the channel, reaching a plateau at around 8-10 mm from the junction (Figure 3.35A). The curvature radius of the inlet channels was also comparable for the three moulds (mean value = 1.770 ± 0.012 mm), and only slightly differed from the nominal value of 1.75 mm (Figure 3.35B).

Once good reproducibility of the architecture was confirmed, a first bonding test was carried out using a green-dyed water solution. As expected, the diagonal grooves in the PDMS layer promoted fluid leakage at the total flow rate of 5 mL/min. In Figure 3.36, leakage is clearly visible (white ellipse), as well as its diagonal orientation parallel to the grooves. Although smaller, a second leak was noted in the proximity of the inlets. Nevertheless, this was not as copious as expected, which gave confidence in further improvements.

Figure 3.36 Leakage after 5 mL/min, Channel width 1 mm.

Therefore, in order to overcome this limitation, variations in the PDMS mixture (monomer/curing agent ratio) were tested. Instead of using the suggested 10% value of curing agent:monomer ratio (by mass), 8% curing agent was used to reduce the PDMS stiffness. Softer PDMS allows easier deformation when compressed during the sealing procedure. Initially, manual pressure was applied using a plastic spatula (at an estimated pressure of 1 bar), followed by compression at ~0.5 bar for at least 1 hr. With this small variation in the protocol, no leaks were observed up to 20 mL/min, confirming the robustness of the sealing procedure. A video of the flow tests and AgNPrs synthesis, further discussed in Chapter 4, is available at *https://youtu.be/EpmnLZDXtBo*.

PDMS 3D printed replica mould reactors, created from desk FDM 3D printers, and bonded on pressure-sensitive adhesive tape, demonstrated a novel, cost-effective and easy to perform manufacturing method for the production of flow reactors, which were validated through the reproducible synthesis of AgNSs and liposomes (See Chapter 4 and 5 respectively).

3.4.3 Three-inlet hydrodynamic flow-focusing

In collaboration with P. Manrique (University of Oviedo), flow-focusing tests were carried out for characterising the mixing capacity of the reactor designed for the flow production of niosomes. As described in the literature[153], mixing efficiency was measured through the change in colour, from yellow to blue, of a pH indicator dye (bromoxylenol blue).

Briefly, bromoxylenol blue is yellowish at pH below 6.0 and blue at pH above 7.6. A saturated solution of dye in absolute ethanol acidified with acetic acid, was introduced in the central stream,

while phosphate buffered saline (PBS) solution, adjusted to pH 10.0 with 2M NaOH was added from the two lateral inlets. Therefore, the colour changing gives a clear indication of the mixing efficiency. For evaluating this, an inverted microscope equipped with a digital camera was used and images of the channel were extrapolated while operating the device. Specifically, the junction and the end of the channel were monitored and results are shown in Figure 3.37 for flow rate ratio (FRR) values of 5, 15, 25, 35, and 50. The FRR of 5 clearly shows the three coloured streams (central yellow stream and the two lateral blue streams). This is also noticeable for FRR of 15 and 25. Moreover, the faster the total flow rate, the shorter the residence time, leading to a less effective diffusion process. As confirmed by the absence of the yellow colour, the FRR of 35 and 50 improved the diffusion, this was also demonstrated when operating at TFRs of 50 and 100 µL/min. Moreover, only the FRR of 50 is able to give an efficient mixing if increasing the TFR up to 200 µL/min.[146] The visual representation in Figure 3.37 (right column) is shown with the intent of underlining the variation of the overall colour of the solution towards a bluish gradient, as well as the initial separation between the yellow and blue stream at lower FRR. Moreover, it is evident how higher FRRs reduces the central stream width (*Wt*), diminishing the volumetric cross-section of the central stream.

These characterisation results were crucial for a better understanding of the hydrodynamic focusing effect based on the channel architecture, and helped the selection of the TFR and FRR employed for the synthesis of organic vesicles, further described in Chapter 5.

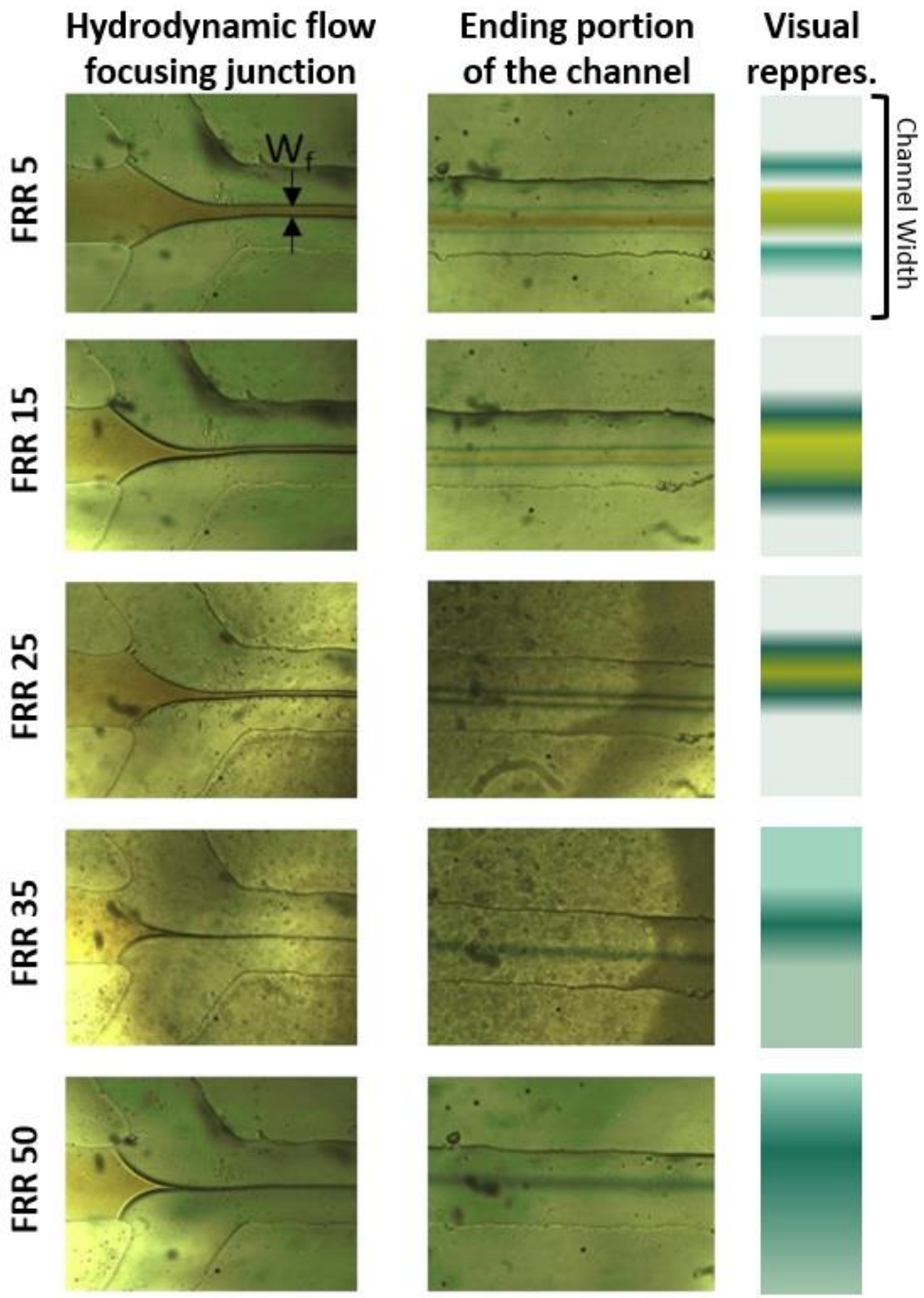

Figure 3.37 The first column (left) shows the diminishing of the width of the Wf when increasing the FRRs. The diffusive mixing at the end portion of the channel is shown in the central column as well as a graphical reproduction for a better visual understanding (right column).

3.4.4 RIAC: 3D printing limitation and tests

Compared to the above mentioned soft lithographic methods, a different process was required from the idealisation of the reactor in a centrifuge (RIAC) concept to the actual manufacturing, due to its more complex architecture and limited prior publications using similar approaches (as reported in 3.1.4). The first prototype was made of VeroClear™ resin using the high resolution OC350. The two channels were directly connected underneath each reservoir forming a Y junction, which further developed into a spiral mixing channel. Figure 3.38a shows the cross-section of the first RIAC device at -2 mm and +2 mm in Y (left and right) with respect to the cut X-Z plane (0 mm, centre). It also includes a visual representation of the RIAC hosted in a 50 mL centrifuge tube. The cut plane (0, centre) revealed the two channels connecting at the junction underneath the reservoirs, whereas the +2 mm cross-section (right) highlighted the outlet at the bottom of the main cylindrical body. A more detailed CAD visualization of the mixing channel architecture is shown in Figure 3.38b.

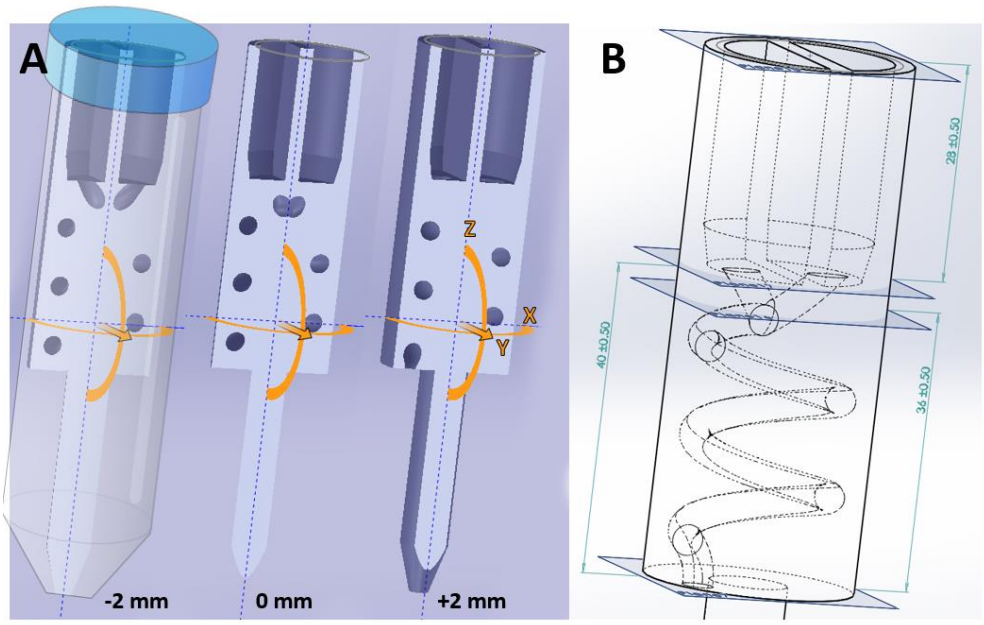

Figure 3.38 First design concept of the RIAC. A) Cross-sections of the device in the X-Z plane and visual representation when hosted into a centrifuge tube. B) Inner geometry of the mixing channel.

When creating the design of the geometry, a post-manufacturing step to clean the mould from the supporting material was considered. This was needed when the design comprised of a roof that would collapse if not adequately supported; or when design features, such as inclined surfaces, exceeded the printable angle limit. Consequently, when manufacturing the RIAC, particular attention was given to the architecture and the spatial orientation of the reactor. This included the evaluation of the angle of the spiral, the cross-section of the channel and the orientation of the geometry. In fact, although being considered a high-performance 3D printer, the OC350 operates by a resin drop method followed by UV light curing, therefore the supporting material was

necessary for geometries that exceeded the print angle limit (for example an architecture that comprises a roof). The challenge, in this case, was to create a single printable design for which the need of supporting material was minimised. Particularly, the machine used a rubber-like supporting material, which was generally removed after printing *via* a pressurised water jet treatment by handling the piece in a dedicated glove-box. Moreover, based on the manufacturer's information, the black supporting material can also be removed in basic water conditions by exposure to a solution of KOH.

Based on these evaluations, the first prototype was 3D printed (Figure 3.39). Although it appeared to provide an accurate representation of the architecture, it was not possible to effectively remove the supporting material from the spiral channel, even with a high-pressure water jet. Further treatment was attempted by submerging the entire reactor into an over-saturated water solution of KOH overnight, but this process was also not sufficient for removing the black rubber-like supporting material (as clearly visible in Figure 3.39).

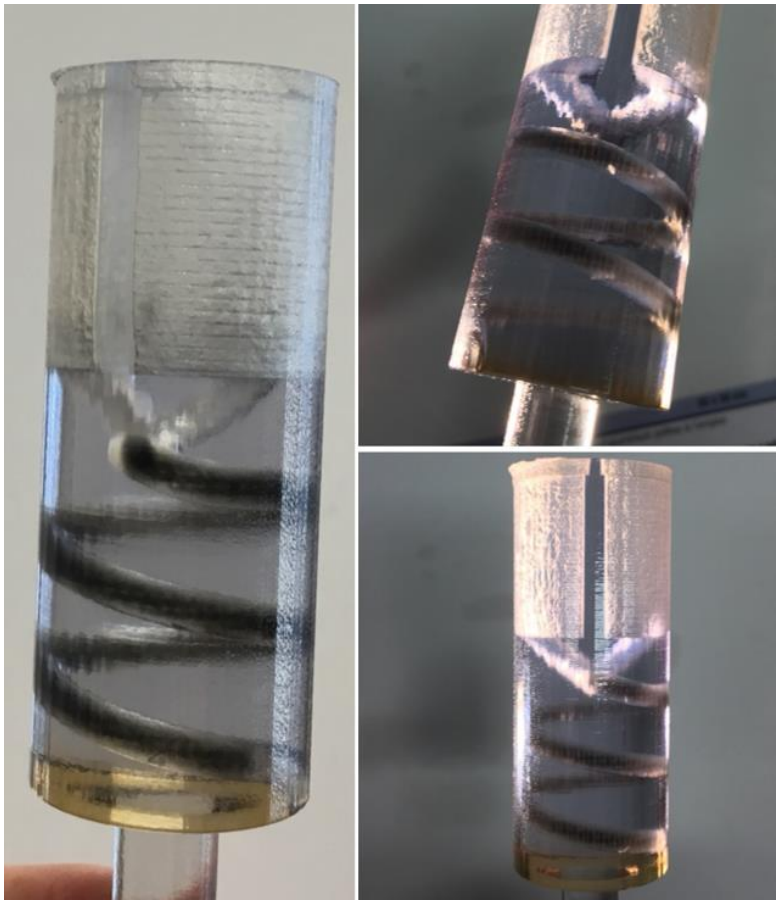

Figure 3.39 First VeroClear™ 3D printed RIAC prototype.

Nevertheless, a centrifuging test of the empty reactor was carried out for a mechanical evaluation. It was noted that the design of the tip of the bottom support was too narrow, causing high pressure

on a small contact surface during centrifuging (visible in Figure 3.38a). This, in combination with the weight of the VeroClear™ material, caused deformation of the bottom surface of the hosting centrifuge tube at 4500 rpm (revolution per minute), which are equivalent to 2268 rcf for a centrifuge with a 10 cm radius.

After these evaluations, it was decided to investigate the use of a lighter material, and the challenge of creating such a design from a cost-effective FDM 3D printer was embraced. As in the previous case, supporting material was needed when manufacturing certain architectures. However, for FDM 3D printing, the supporting material was made of filaments of the same printing material (PLA in the specific case), which were automatically created based on the design architecture and 3D printing orientation in a manner that they can be mechanically removed. Several design improvements were made for the second prototype and additional effort was needed to overcome FDM 3D printing limitations. Figure 3.40 shows the first intermediate design before the final one described in the material and methods' section (3.3.5), the concept of two separate pieces (main body and bottom support) was introduced.

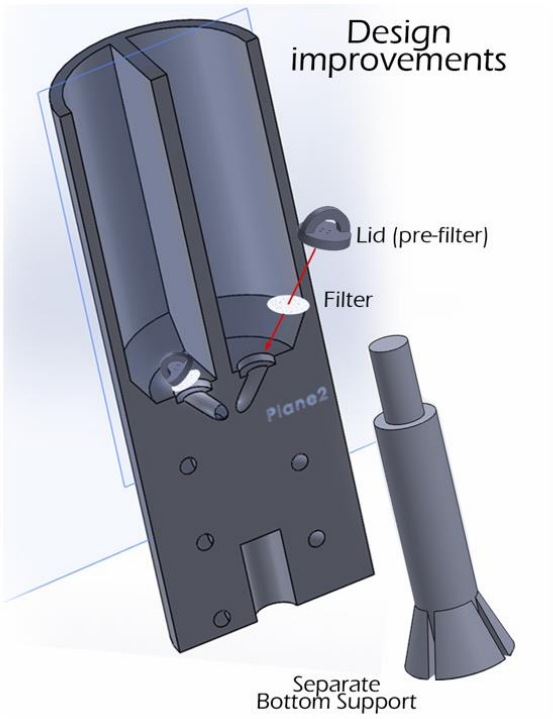

Figure 3.40 CAD design of the first concept that includes lid or filters at the bottom of the reservoirs and consist of two separate pieces.

The bottom support was separated from the main channel creating a modular structure, in which each piece was first printed individually and then connected to each other. In this manner, no supporting material was printed in the reservoirs when oriented upwards. Moreover, the tip of the bottom support was redesigned to increase the surface contact with the bottom of the centrifuge

tube, thus a better distribution of the pressure. Four vertical side apertures where created at the end of the bottom support to allow the collecting solution to flow through.

Most importantly, a first attempt to create some separation between the reservoirs and the mixing channel was tested by creating a seat (or recess) for each reservoir, with the idea to host a paper or sponge filter. This would prevent the reagents from flowing through the device before actuation (i.e. leakage). The device was successfully printed and flow through channels worked as expected when testing them only by gravity as a mixer channel. However, separating the reservoirs with paper or sponge filters was not ideal. In particular, paper filters, even though easily interchangeable, would degrade over time and contaminate the solution. Moreover, the lids (pre-filter) indicated in Figure 3.40 were not able to ensure a good fit, thus leading to non-reproducible flow. On the other hand, sponge filters could not be removed easily, and their performance is strongly dependent on their positioning in the seats at the bottom of the reservoirs. The final solution was eventually found using frit filters normally employed for high-performance liquid chromatography (HPLC). The design was then slightly changed to accommodate for the frit filters, and the final RIAC was manufactured.

During the printing process, reservoirs were kept upward to avoid the creation of supporting material inside them (Figure 3.41). This allowed accurate construction of the bottom of the reservoirs and the frit seats, and most importantly, it didn't require post-fabrication treatments. Adopting this device orientation, the supporting material was created only within the hole used for connecting the bottom support (Figure 3.41B). This material had no interference with the mixing channel architecture and could be easily removed. Notably, by prototyping an accurate rounded geometry within the angle limit of the 3D printer, no supporting material was generated at the outlet of the mixing channel (Figure 3.41B) and within the mixing channel itself.

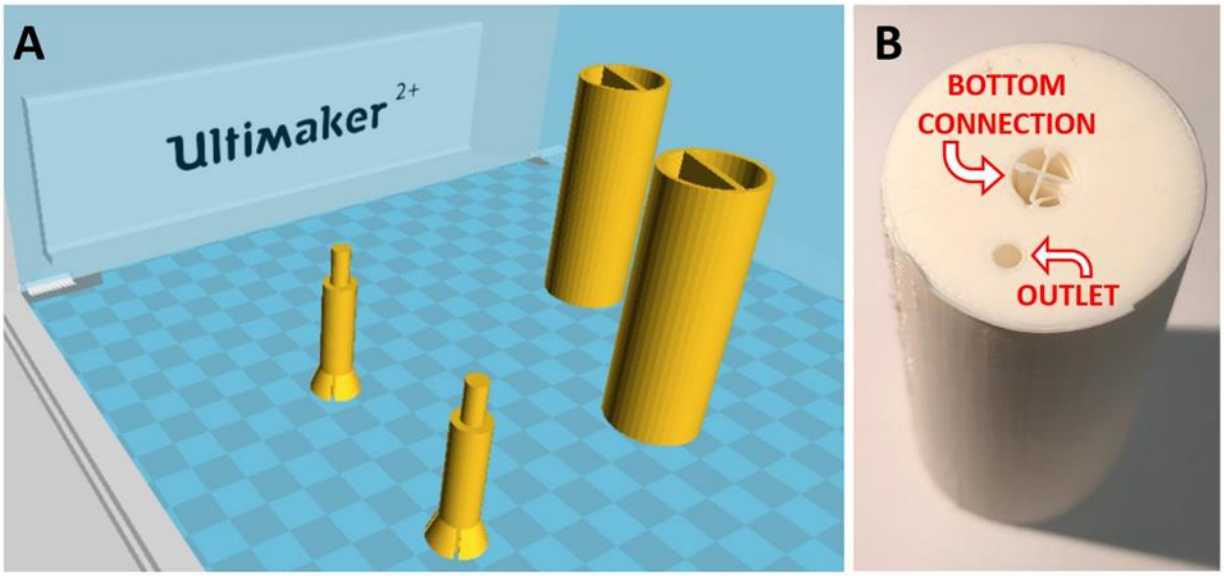

Figure 3.41 A) Orientation of the spiral-RIAC and its bottom support for the 3D printing manufacturing process. Image captured from the 3D printer software. B) Bottom of the spiral-RIAC showing the outlet and the hole for connection with the bottom support.

A centrifuging test was carried out to determine the structural integrity of the RIACs and the centrifuge tube. The RIAC was placed inside the centrifuge tube and reservoirs filled with 4.5 mL each with milli-Q water. The centrifuging test was repeated with 500 rpm increments until reaching the centrifuge limit of 11000 rpm (13552 rcf) with no damage to the RIAC, nor the centrifuge tube.

The straight-channel RIAC was printed as a single piece, by designing a bottom chamber that provided structural support to the device, and also facilitated the collection of the final product.

3.5 Conclusions

There has been increasing interest from industries in scaling-up nanoparticle's production while minimizing costs, particularly in the bio-medical sector. In this regard, flow-chemistry is playing an increasingly crucial role due to the high and repeatable stoichiometric control it offers over batch approaches. However, the batch- to flow-synthesis translation is challenging to accomplish, since custom-built and expensive reactors are often needed.

Over the last decades, the scalability of manufacturing processes for continuous-flow reactors has significantly improved with the advent of soft-lithography, in which multiple replica of a device can be fabricated from a single master mould. More recently, three-dimensional (3D) printing has emerged as a cost-effective and robust means to either fabricate flow reactors in a single step or generate master moulds for usage in soft-lithography. Nevertheless, if the channel architecture contains micrometre-sized features, expensive or customizable 3D printers are required. In the

soft-lithographic method, silicone elastomers (such as PDMS) are commonly used as the constitutive material of the channel replica. Furthermore, the PDMS replica require to be sealed onto a substrate (typically glass or PDMS), which is often achieved by treatment with oxygen plasma. The need for specialised instrumentation has thus limited the industrial translation and scalability of microfluidic-based flow reactor technologies.

This Chapter presents the analysis, manufacturing and characterisation of reactors conceived in this research, as well as the rationale behind their development. 3D printed moulds from a representative expensive high-resolution 3D printer (market value £150k) and a desk 3D printer (market value £1.5k) were compared, and several design alternatives were evaluated for the purpose of obtaining cost-effective 3D printed replica mould reactors. Morphological studies, both with profilometry and flow visualisation tests, helped in the evaluation of the advantages and disadvantages of materials and procedures based on the specific reaction. Alternatives for the bonding step were also characterised and adapted to specific purposes as demonstrated in the following Chapters.

Particularly, an easy-to-perform and cost-effective method for the fabrication of PDMS based continuous-flow reactors, through 3D printed mould casting (3DPM-C), was developed.[139] In this method, the positive mould was 3D printed using a desk FDM 3D printer, followed by PDMS casting to produce replica channels of millimetre or sub-millimetre width and height. Channels on the PDMS replica were then sealed using a commercially available pressure-sensitive adhesive tape. The entire fabrication process could be completed within 24 h from the CAD design of the channel architecture, at an average cost of £5 per reactor. Moreover, devices produced with this technique can be operated at relatively high total flow rates (> 20 mL/min), which is a desirable characteristic for application in continuous-flow chemical synthesis.

Furthermore, the possibility of creating reliable and reproducible hydrodynamic flow focusing reactors was demonstrated. As further described, this would lead to the demonstration of a cost-effective solution for temperature-controlled production of niosomes.[146]

In addition to the manufacturing process, the scalability of flow reactors is also affected by the type of fluid dispensing system used to deliver reagents. The large majority of microfluidic devices are operated using expensive and bulky syringe pumps, which profoundly limits the simultaneous operation of multiple reactors. Therefore, the 3D printed reactor-in-a-centrifuge (RIAC) concept was developed as a novel scalable, cost-effective, easy-to-use, and pump-free reaction technology. RIACs can be actuated by an ordinary centrifuge, and customised for specific functions. The manufacturing of the device is discussed and it will be tested for the synthesis of nanomaterials, with applications in both organic and inorganic chemistry.

The outcome of this research provided valuable information about the advantages and disadvantages of 3D printing technology for the manufacturing of flow reactors. Such constructed reactors have been employed successfully for the continuous synthesis of a range of nanoparticles in this project, as presented in Chapters 4 & 5.

Chapter 4 Flow-synthesis of Silver Nanoparticles

4.1 Introduction

There have been efforts in the production of AgNPs by adapting batch chemical protocols to flow–reactions with relatively simple architectures. An early example is the thermally controlled synthesis of silver nanomaterials by Lin *et al*. in 2004.[154] In this case silver pentafluoropropionate was used, as a single-phase reactant precursor, in the presence of trioctylamine. With only one inlet and one outlet, the device was not created to achieve a mixing regime, but it was used to allow thermal control throughout the reaction.

Over the years, reactors for the synthesis of metal nanoparticles have been developed using various architectures and employed as an alternative approach to batch synthesis, i.e. using the reducing agent method. The precursors were also changed over time; in particular, important advancements were made by Wagner *et al*., [155] who translated the synthesis of metal nanoparticles to microfluidics starting with gold, and then moving to silver, copper and more complex particles. Specifically, they introduced borohydride ions as reducing agents, which later became the most widely employed method. However, the quality of the produced particles was not only dependent on the employed chemicals, but was also affected by the design of the microfluidic architecture, the manufacturing protocols and employed materials. These important aspects play a crucial role in the efficiency of the reactors. An outstanding example was recently presented by Okafor *et al*.,[156] who employed 3D printing as a manufacturing method of producing continuous oscillatory baffled reactors (COBR). The oscillatory flow motion provided an effective heat and mass transfer while maintaining plug flow, this allows long residence time in a relatively contained channel length and an increased mixing.[157] However, this approach limited the total flow rate, thus was not suitable when aiming at the meso- to large-scale production, which was a main goal of the present research.

Droplet microfluidics was also used for the synthesis of AgNPs.[158] This technique was employed to create a micro environment in which nanoparticles can be formed, aiming at obtaining a more monodisperse product when compared to the batch reaction. Very recently Kašpar presented a detailed study on the governing factors behind the production of AgNPs *via* droplet microfluidics, followed by computational fluid dynamic simulations to explain the underlying mechanism.[159] However, it was not a straightforward process, nor a cost-effective solution, particularly for non-specialised users.[159] To facilitate the process, Baber et al. demonstrated a coaxial glass reactor for continuous-flow production of AgNSs.[122] This was an interesting approach, as the coaxial reactor creates a central stream which increased the diffusion with the adjacent streams, thus the overall control of the mixing.

The size and shape control of AgNPs, and the relative optical output due to the LSPR effect, has indeed attracted interested from the scientific community, with a particular focus on the prismatic shape. Many alternatives were proposed during the years for the AgNPrs synthesis, ranging from the photo-induced conversion[101] and the rapid thermal synthesis for thickness control [105], to the photochemical approach [102] and the microfluidic flow-formation.[67] Interestingly, the microfluidic approach was also implemented with an in-situ micro spectroscopic monitoring system used to detect the stage of the prism's formation.[147] One of the latest, and perhaps most practical synthesis solutions was presented in 2017 by Haber *et al*. [107] who significantly optimised multistep reactions of AgNPrs, based on Ag citrate-capped seeds aged overnight in a dark environment, and followed by adding the Ag precursor ($AgNO_3$) in the presence of L-ascorbic acid for increasing their stability. This was still a batch variation, and therefore not extremely suitable for continuous or large-scale production; however, the outcome can be fairly tuneable and reproducible. Notably, large-scale translation of these methods has not yet been implemented, which has limited their adoption from industries.

Therefore, the present Chapter addresses the above-stated research gap of the state-of-the-art by using the previously conceived and manufactured cost-effective flow-reactors (Chapter 3). Optimisation of the operating conditions, as well as advantages and disadvantages, of each reactor for the synthesis of AgNPs are described. AgNSs and AgNPrs were selected with the goal of achieving a large-scale production, which was considered in the order of mL per minute (mL/min) instead of mL per hour (mL/h), and diminishing production costs of such nanomaterials.

In particular, batch production protocols of nanospheres were readapted to the flow-synthesis approach in order to assess efficacy of the novel reactors (3D printed replica mould casted bonded on pressure-sensitive adhesive tape 3.4.2, and 3D printed reactor-in-a-centrifuge 3.4.4).

Moreover, AgNPrs were produced employing the hydrodynamic flow-focusing and the two inlets curved serpentine reactors. This demonstrated an improved size and shape control of the produced particles obtained using cost-effective flow-reactors and with fewer chemicals involved. It was demonstrated how the correct balance between chemicals' concentration, the architecture of the reactor and operating conditions can be studied to decrease products cost and increase production rates. Regarding the impact of the channel architectures, the effectiveness of the initial production of AgNPrs obtained by hydrodynamic flow-focusing was compared with the developed two-inlets curved serpentine flow-reactor. In the case of the AgNPrs the volume output increased up to 50 mL/min.

Finally, the first attempt to achieve photo-assisted flow-biosynthesis of AgNPs is herein discussed, showing preliminary results using the three reactors discussed in Chapter 3.

4.2 Materials and methods

4.2.1 Flow-synthesis of silver nanospheres

The flow synthesis of AgNSs was mainly carried out by modifying the chemical reduction method, previously adopted for their batch synthesis in Chapter 2, in order to suit the device's architecture. For this approach, the 3D printed replica mould casted reactor bonded on pressure-sensitive adhesive tape (3DP-RMC/Tape) and the reactor-in-a-centrifuge (RIAC) were used. The main adjustment was the introduction of the reducing agent. For all the flow-syntheses, $NaBH_4$ was prepared by dissolving the solid salt in water, before dilution with IPA, in order to obtain a reducing agent solution for loading into a syringe with the final ratio of 10% water to 90% IPA. Moreover, during the experiments with the RIAC, a green synthesis approach using tannic acid was evaluated. The preliminary data collected are presented in the appendix (C.1).

4.2.1.1 Flow synthesis of AgNSs: 3D printed replica mould casted reactor bonded on pressure-sensitive adhesive tape (3DP-RMC/Tape)

For the AgNSs produced *via* 3DP-RMC/Tape, silver nitrate 99.9999 % ($AgNO_3$), trisodium citrate dihydrate ≥ 99.0 % (TSCD), polyvinylpyrrolidone (PVP), and sodium borohydride 99 % ($NaBH_4$), were purchased from Sigma Aldrich UK (Gillingham, UK). As shown in Scheme 4.1, a 20 mL syringe was primed with a Milli-Q water solution containing $AgNO_3$ (1.02 mM), TSCD (15.02 mM), and PVP (0.45 M). The second syringe was filled with 15 mL of an IPA/Milli-Q solution (9:1 v/v) of $NaBH_4$ (5.28 mM). The Luer Lock syringes adopted (20 ml, BD Plastipak) were purchased from BD (Becton, Dickinson and Company, UK), and operated with syringe pumps (AL-1010), which were purchased from World Precision Instruments (UK). The total flow rate (TFR = FR_A + FR_B) was kept at the constant value of 1 mL/min, whereas four flow rate ratios (FRR = FR_A / FR_B) were tested, at the values of 5, 7, 9 and 11. FRRs were selected in line with the tested IPA/water ratio discussed in Chapter 2, in order to investigate around the FRR of 7. Each sample was collected in a 1.5 mL Eppendorf tube, and 1.5 mL were removed in a waste vial in between each experimental run. Furthermore, results were compared with the micromilled replica mould casted device bonded on glass *via* oxygen plasma treatment (µMi-REM*Glass). The manufacture of the µMi-REM*Glass device was performed following the protocol reported in the literature.[125] The PVA-TePla 300 plasma cleaner was employed to assist the bonding of the PDMS layer on a 50×70mm glass sheet (Corning® microscope slides, Sigma Aldrich, Gillingham, UK).

Finally, in order to evaluate the robustness and reliability of the reactors, syntheses were repeated in triplicate at the selected TFR and FRR values for both the 3DP-RMC/Tape and the µMi-REM*Glass devices.

Scheme 4.1 Scheme of the syringes connection to the device and the collecting vial and associated chemicals: a) AgNO3, TSCD, PVP in water; B) NaBh4 in water:IPA 1:9 v/v. The length of the outlet tube was 26.7 cm.

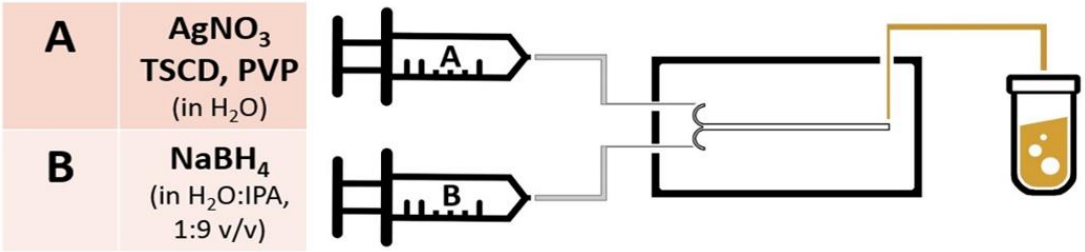

4.2.1.2 Centrifugal force driven synthesis AgNSs: *via* the reactor in a centrifuge (RIAC)

Silver nitrate 99.9999 % ($AgNO_3$), trisodium citrate dihydrate ≥ 99.0 % (TSCD), polyvinylpyrrolidone (PVP), and sodium borohydride 99 % ($NaBH_4$), were purchased from Sigma Aldrich UK (Gillingham, UK) and employed for the synthesis of AgNPrs *via* the RIAC. The following solutions were prepared:

(i) Silver source solution (SSS): A 20 mL milli-Q water solution, containing $AgNO_3$ (1.78 mM), TSCD (26.80 mM) and PVP (0.78 mM).

(ii) Reducing agent solution (RAS): 20 mL of milli-Q water containing $NaBH_4$ (1.33 mM) (a fresh solution is need).

(iii) Centrifuge tube solution (CTS): A 20 mL milli-Q water solution, containing TSCD (26.80 mM) and PVP (0.78 mM).

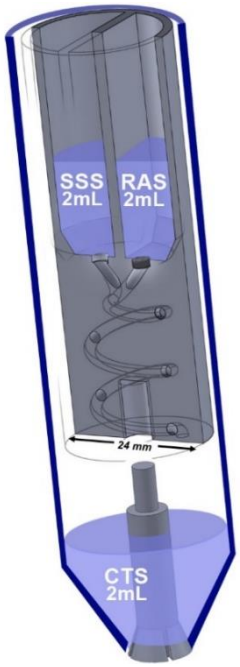

Figure 4.1 CAD design of the spiral RIAC reactor combined with a graphical representation of reagent positioning prior the synthesis.

As further discussed in the Results and Discussion (Section 4.3.1.2) various tests were carried out to identify the most suitable synthesis conditions. For the selected final protocol, one reservoir of the RIAC was filled with 2 mL of the SSS solution and the same volume (2 mL) of the RAS solution was poured into the second reservoir. To improve stabilisation, 2 mL of the CTS solution was added into the centrifuge tube (Figure 4.1). The centrifuge was activated for 2 min at 1789 rcf (frit filters mesh of 0.5 mm).

Regarding the centrifugation settings, relative centrifugal force (rcf) values were calculated from the revolution per minute (rpm) values, considering the centrifuge radius of 10 cm. For all experiments, RIACs were positioned always in the same orientation into an Eppendorf centrifuge 5804, where the centrifugal force drove fluids through the frit filters towards the mixing channel. Reservoirs were labelled in order to use the assigned solvent or chemicals only.

4.2.1.3 Photo-assisted Photo-assisted flow-synthesis of silver nanoparticles in a bacterial culture

The photo-assisted flow-biosynthesis of AgNSs was carried out in collaboration with T. Mabey, and with the support of Dr. P. He from the Physics Department. In this section, results and improvements related to the behaviour of the manufactured reactors (Chapter 3) are discussed, with a final UV-Visible characterisation of the produced particles. Unless otherwise stated, results presented are related to the products synthesised at the flow-condition of TFR of 1 mL/min and FRR = 1.

A 60 mW 405 nm laser was used, through an optical fibre (OF), as a light source for all reactors. The OF was then connected or positioned in a different manner based on the channel architecture and the setup. The bacterial culture medium (Morganella Psychrotolerans, Cell-Free Extract (CFE)) and a 20 mM water solution of $AgNO_3$ (Fisher Scientific, UK) were introduced from the two different inlets, *via* syringe pumps (World Precision Instruments; Aladdin 1010) connected by polytetrafluoroethylene (PTFE) inlets and outlet lines (1.6 and 0.6 mm, outer and inner diameter respectively). Specifically, a 300 mL Erlenmeyer flask was used for the growth of the M. psychrotolerans in 100 mL LB (no added NaCl) for 4 days in at 22 C and 120 RPM orbital shaking. CFE was prepared by 20 min centrifugation (3,000 x g) and filtration through a 0.22 mm filter.

Figure 4.2 shows the representative set-up in the case of Reactor 1, including the laser source connected to the optical fibre, and the two syringe pumps. In this case, the device was kept horizontal during the synthesis.

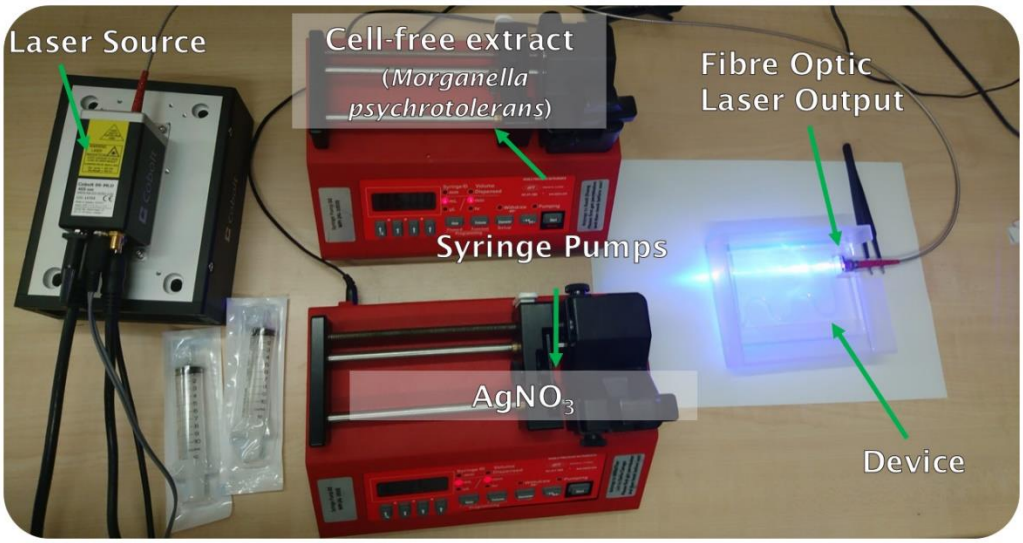

Figure 4.2 Set up of the photo-assisted synthesis of AgNPrs.

The OF was manually aligned until the laser beam was observed through (and parallel to) the channel. The same setting was adopted for Reactor 3 (heart shape, section 3.3.6.3). In this case, the alignment was fixed as the OF was embedded into the PDMS reactor's main body before curing.

Differently, Reactor 2 was operated at a 90° angle from the horizontal plane, in order to allow alignment between the OF, the diverging lens, and the PDMS channel. The lens was used to illuminate a longer area of the channel instead of a spotted beam, as shown in Figure 4.3.

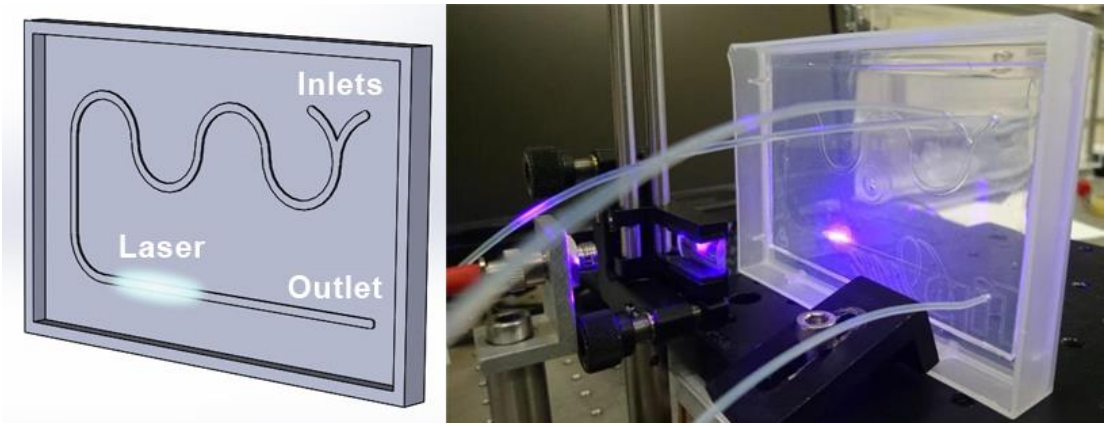

Figure 4.3 CAD design or Reactor 2 (left) compared with the experimental setup (right)

In the case of the photo-assisted flow-biosynthesis of AgNSs, the UV-Vis characterisation was performed using an Avantes Starline fibre optic spectrometer (AvaSpec-ULS2048L) and a PerkinElmer Lambda 35 UV-Vis spectrometer, equipped with a custom-designed and 3D printed sample older using the OC350 (Appendix A.2).

4.2.2 Flow-synthesis of silver nanoprisms

Different from AgNSs synthesis, the production of AgNPrs required precise control of the mixing due to the associated longer kinetics of particle's formation. Therefore, to translate the reaction to the flow-synthesis, longer and more complex architecture were adopted. Specifically, studies started by employing the three inlets hydrodynamic flow focusing serpentine channel (3DP-RMC/Glass using the OC350), which was then modified to the final two inlets curved serpentine (3DP-RMC/PDMS using the U2+).

4.2.2.1 AgNPrs synthesis: flow-focusing to serpentine approach

The hydrodynamic flow focusing serpentine device was employed for the initial synthesis of AgNPrs. In particular, the 3DP-RMC*Glass reactor was produced from the mould created with the high-resolution 3D printer (OC350) and the designed size of 0.25 mm (aspect ratio 1:1) (as described in section Three-inlet flow-focusing serpentine (3DP-RMC*Glass and 3DP-RMC*PDMS)3.3.2.1). Three 20 mL syringes were connected to the three inlets of the serpentine *via* PTFE tubes, as shown in Figure 4.4. Two reaction solutions were prepared. A Milli-Q water solution (20 mL) containing $AgNO_3$ (0.1 mM), TSCD (1.5 mM) and H_2O_2 (0.1 M), was connected to the central inlet. Differently, a 40 mL water/IPA 10%/90% (v/v) solution was prepared for the reducing agent ($NaBH_4$, 4 mM), and then divided in two 20 mL syringes, which were then connected to the lateral inlets. In order to maintain a stable flow-focusing condition, after preliminary tests, the selected FRR was maintained at the constant value of 0.5, whereas the TFR was changed, using values of 30, 15 and 7.5 ml/h for the investigation. However, a further sample was prepared at FRR = 0.4 and TFR = 70 mL/h for comparison.

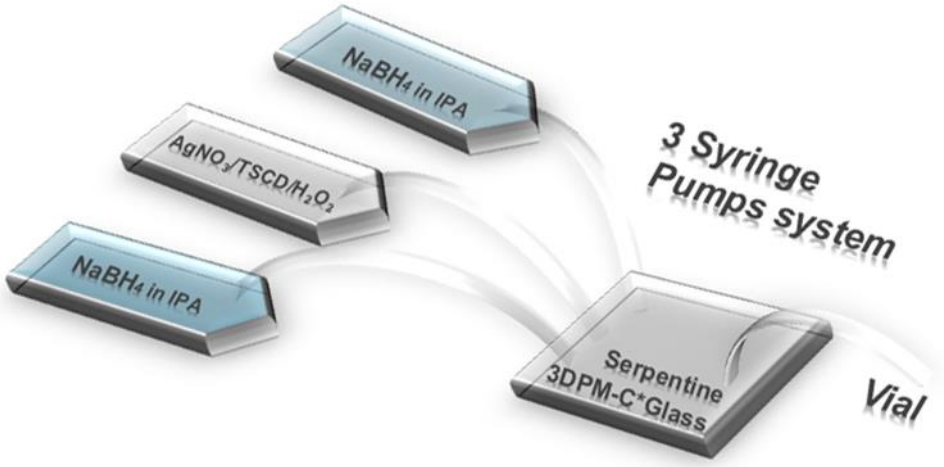

Figure 4.4 Representation of the experimental set-up and chemicals injected through syringes for the production of SNPs.

Regarding the connection with tubing, the same condition may also be realised through a **T** or **Y** junction connector which allows using a single syringe pump for the two lateral streams.

4.2.2.2 AgNPrs synthesis: two inlets curved serpentine reactor

In order to improve the efficiency of the flow-production, as well as the nanoparticle's size and shape control, the synthesis of AgNPrs was modified to be carried out with the two-inlet curved serpentine. In this case, the two syringes were prepared as follow:

- A 60 mL syringe containing: $AgNO_3$ (0.117 mM), TSCD (1.7 mM) and 450 uL of H_2O_2 (30%), in milli-Q water.
- A 12 mL syringe containing: $NaBH_4$ 8 (mM) in a 10%/90% water/IPA solution.

The FRR was kept at the fixed value of 7, and the TFR was tested at values of 1, 5 10, 20 and 50 mL/min. Additionally, in order to evaluate the efficiency of the reaction, the TFR of 10 mL/min was applied for 30 minutes after the preparation of the chemicals. Samples were collected in a 1.5 mL Eppendorf for further UV-Vis and TEM characterisation. Furthermore, in between each experiment, pumps were activated to remove the solution created by the previous synthesis, and the waste was collected separately. The waste procedure was activated for an amount of time at least equivalent to the residence time of the previous performed reaction.

4.2.3 UV-Vis and TEM characterisations

The UV-Vis characterization of AgNSs, produced through the 3DP-RMC/Tape and µMi-REM*Glass, was carried out using a Varian Cary300Bio UV-Vis spectrophotometer. All measurements were collected in the 200-900 nm range with a time per step value of 0.5 nm. For each sample, 1 mL was collected from the flow reactors and diluted to 3 mL in milli-Q water into a quartz cuvette. Similarly for the RIAC synthesis, the same instrumental settings were used for the UV-Vis characterisation, which was performed on a 1/3 (v/v) diluted samples, after gentle sonication. The baseline subtraction function was used for each experimental condition (i.e., considering the specific Milli-Q/IPA volume ratio).

For the photo-assisted flow-biosynthesis of Ag nanoparticles, the UV-Vis characterisation was performed as described in Section 4.2.1.3. Moreover, transmission electron microscopy (TEM) imaging was accomplished to consolidate the spectrophotometric results. Samples were prepared by drop-casting of the colloidal synthesis solution (5 µL), on carbon and Formvar coated Cu/Pd 200 mesh grids, and left to dry under atmospheric conditions at room temperature in low light. TEM images of AgNPrs were acquired using the Hitachi HT7700 on the same sample used for the UV-Via characterisation, after 1/3 further dilution.

4.2.4 CFD Simulations

Computational fluid dynamics (CFD) simulations were performed to analyse the fluid transport and the chemical species within the built reactors at the tested conditions. Specifically, the CFD analyses were carried out on the two inlets straight channel (3DP-RMC/Tape), for the synthesis of AgNSs. With respect to the AgNPrs production, CFD simulations were carried out for the three inlets hydrodynamic flow-focusing serpentine (3DP-RMC*Glass) and the two inlets curved serpentine (3DP-RMC*PDMS).

For the CFD simulations, the following steps were performed: (i) reactor design using Inventor Pro 2016 (Autodesk Inc., San Rafael, CA, USA) or Solidworks®; (ii) meshing of the fluidic domain in ICEM CFD 17.0 (Ansys Inc., Concord, MA, USA) using finite volumes of tetrahedral shape. The edge length of the mesh element was identified from a mesh dependence study as the optimal compromise between solution accuracy and computational cost at the value of 0.05 mm. (iii) solving for momentum and mass conservation equations (i.e., Navier-Stokes equations at laminar flow regime), and species transport (i.e., advection-diffusion) equations using Ansys® Fluent 17.0 (Ansys Inc., Concord, MA, USA).

To represent the experimental conditions, the following boundary conditions were imposed: (i) mass flow boundary condition at the inlets, (ii) atmospheric pressure at the outlet, and (iii) no-slip at the channel walls. The experimental values of TFR and FRR were replicated numerically.

Fluids were assumed incompressible and Newtonian, and the IPA-water diffusion coefficient was set to 1×10^{-9} m^2/s.[153,160] The effect of the solvent mixing on fluid density and viscosity was taken into consideration in the simulations. The mass fraction of IPA was calculated in a cross-sectional plane located in the vicinity of the outlet, and the mixing index in this specific location was determined for each TFR and FRR investigated.

4.3 Results and discussion

4.3.1 Flow-synthesis of silver nanospheres

4.3.1.1 Flow-synthesis and characterization of silver nanospheres with 3DP-C/Tape and comparison with the μMi-REM*Glass straight reactors

The first technical problem to overcome when planning the flow synthesis of AgNPs *via* reducing agent method was related to the formation of gas bubbles within the channels, specifically, H_2 produced from the degradation of $NaBH_4$ in water. To overcome this limitation, IPA was used in combination with water and tested over several FRRs. Although this effect may be less problematic in millimetre-scale flow-channels, this approach was adopted to minimise problems due to clogging events based on previous experience with similar devices in the research group. [67] An alternative approach may involve the generation of a strong basic condition (NaOH, 14 M) in water, as described by Baber *et al*. [122] However, aiming at meso- to large-scale production, and potentially industrial translation, this approach was not deemed ideal. Employing fewer reagents can strongly and positively affect production costs, as well as waste treatments, resulting in a more convenient solution.

The stoichiometry played a critical role in AgNSs synthesis, and although the numerical results showed a marginal increase in mixing efficiency at FRR = 11 (Figure 4.5), the most effective performance was obtained at FRR = 7. In fact, by adopting this condition a high-quality sample of AgNSs was produced, which was highlighted by the UV-Vis characterisation with the characteristic wavelength band [87] and an intense A_{max} of 2.9 ± 0.2, after 1:3 dilution with Milli-Q water. Final confirmation of the efficiency of the device was obtained by the comparison of the same protocol performed with an already validated manufacturing method (μMi-REM*Glass). Figure 4.6 shows the UV-Vis spectra of the production of AgNSs in triplicate for both reactors when operating at the selected suitable conditions of TFR = 1 mL/min and FRR of 7.

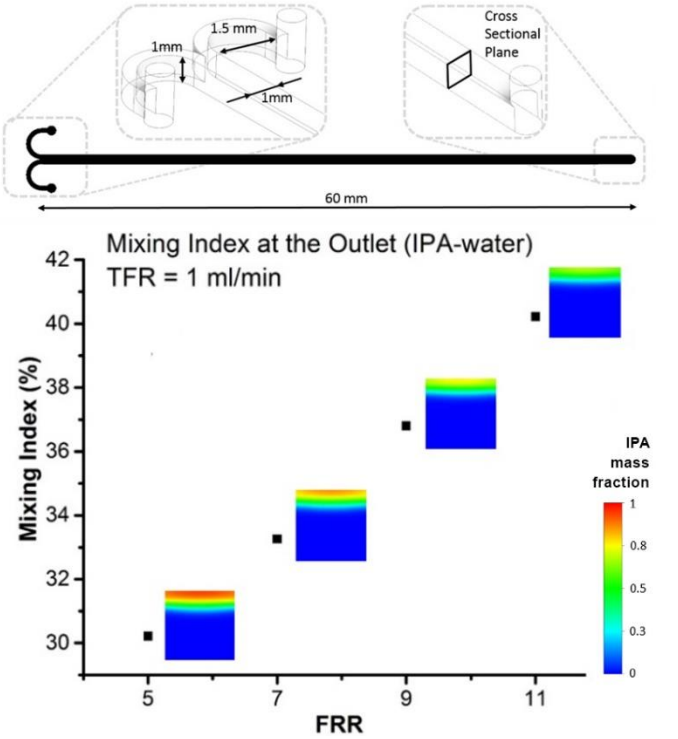

Figure 4.5 Mixing index calculated over a cross sectional plane in the proximity of the outlet surface, as shown in the illustration on the top of the graph. CFD of the IPA-water at TFR of 1 ml/min and FRRs of 5, 7, 9 and 11; Contours of IPA mass fraction are reported next to each data point.

Despite using different production methods, the spectra overlapped. In particular, the inset in Figure 4.6 reports the results obtained for the triplicate synthesis as TAPE A,B and C for the 3DPM-C/Tape reactor and Glass A,B and C for the µMi-REM*Glass reactor. For these samples, the A_{max} was equal to 3.252 ± 0.050 and 3.236 ± 0.068 for the 3DPM-C/Tape and the µMi-REM*Glass reactors, respectively.

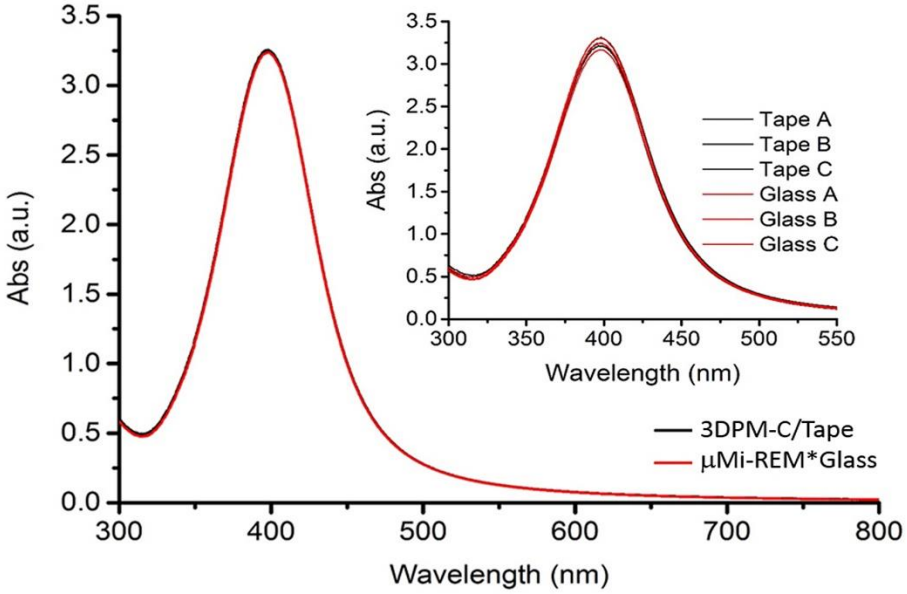

*Figure 4.6 a) UV-Vis characterization of AgNSs prepared using the 3DP-RMC/Tape (black) and the µMi-RMC*Glass (red) reactors. Spectra are shown as the mean of triplicate samples prepared using both types of reactor, at the same operating conditions (TFR = 1 ml/min; FRR = 7) (individual spectra are shown in the inset).*

More importantly, the maximum absorption wavelength value of 398.0 nm was obtained for both reactors, with no absorption shifts, further indicating a comparable performance. As previously mentioned, the wavelength shift was a crucial part for the characterisation of a colloidal sample and the value was also related to the particle size.[161] These samples were estimated to contain nanospheres ranging from 10 to 20 nm, which were then confirmed by TEM imaging shown in Figure 4.7.

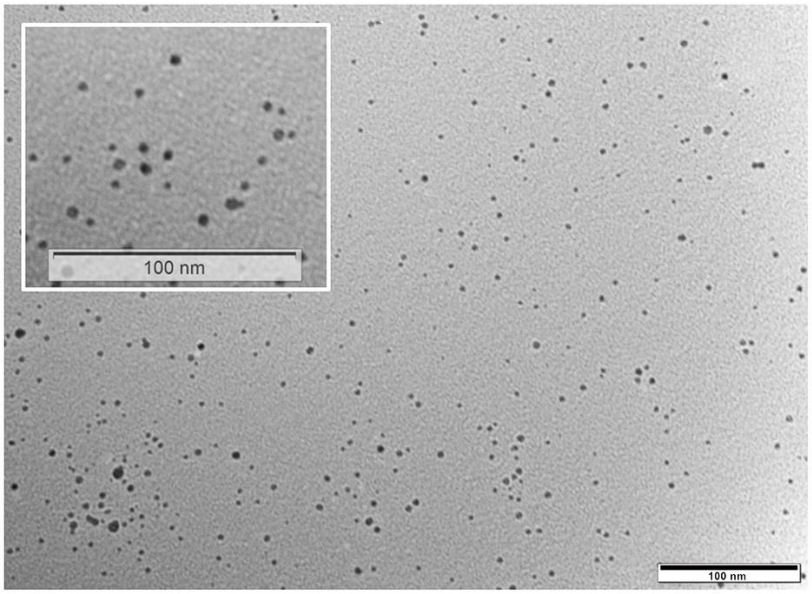

Figure 4.7 Representative TEM image of the AgNSs prepared with the 3DPM-C/Tape (TFR = 1 ml/min; FRR = 7); scale bar 100 nm and a magnified view shown in the inset.

These results were crucial to verify the reliability of the 3D printed replica mould reactor, particularly when compared with already validated manufacturing methods. Specifically, they allowed to demonstrate that the effect of the roughness and the grooves, created onto the 3D printed bottom surface as previously discussed in Chapter 3, are negligible for such synthesis. When manufacturing a 3D printed replica mould device from the FDM U2+, the squared PDMS channel reports the replica of the mould roughness for ¾ of the cross sectional perimeter (the channel roof and the 2 sides). Differently, the roughness of the bottom of the channel is due to the surface the PDMS replica is bonded on (glass, PDMS or, in this case, the pressure sensitive adhesive tape). The fact that the UV-vis spectra of the two identical reaction performed with the 3DPM-C/Tape and the μMi-RMC*Glass were overlapped is a solid indication of the maintenance of the flow performances. This can be stated considering two factors. Firstly, the shape of AgNPs, both with aggregation phenomena, can be strongly influenced by a not well-controlled flow behavior or stoichiometric ratio, leading to UV-vis band shape variations. Second, the UV-vis spectroscopy technique is a very sensitive method, and small variations would have been noted throughout the entire wavelength window of analysis.

4.3.1.2 RIAC: Synthesis of silver nanopheres using 3D printed reactor-in-a-centrifuge: The role of the solvent in the RIAC approach

The feasibility of using RIACs for inorganic purposes was subsequently evaluated. Being the first approach of this kind, many variations of the protocol and design were tested to define the manufacturing method, the desired architecture, the operating conditions and chemical concentrations. Here are presented the most relevant outcomes of this process. Specifically, the spiral-geometry RIAC was adopted, equipped with 0.5 μm frit filters. AgNSs were synthesized by re-adapting the previously described and published protocol adopted for the 3D printed replica mould device bonded on pressure-sensitive adhesive tape (Section 3.4.2). The experience previously gained with the 3DP-RMC/Tape helped in the understanding of the mechanism behind RIAC's actuation. However, a further factor had to be considered when operating a RIAC, which was the pressure generated by the centrifugal force, since - as already described - the synthesis of AgNPs is quite sensitive to the flow conditions.

A re-adaptation of the chemicals used was needed due to a limitation of the RIAC reactors related to the architecture. In particular, the volume ratio (VR), which can be considered an analogue to the FRR in a syringe-driven flow reactor, was fixed at the value of 1. In the case of reactions involving high FRRs, such as the previously discussed water/IPA synthesis (FRR = 7), this could be challenging to adapt.

4.3.1.2.1 Synthesis of silver nanospheres through the spiral RIAC in Water/IPA

When working with two reservoirs at the fixed VR of 1, one of which contained the reducing agent ($NaBH_4$) that needed to be introduced into a 10%/90% water/IPA solution, the final ratio of water/IPA was 55%/45%. This appeared to differ from that previously observed in batch (Chapter 2), as the IPA would negatively affect the production.

However, in order to also test other operative parameters such as rpm (revolution per minute), a first attempt was carried out introducing $AgNO_3$, TSCD and PVP in a water solution (into reservoir 1), and $NaBH_4$ in a 10%/90% water/IPA solution into the second reservoir. Results in Figure 4.8 show the UV-VisVis characterisation of the obtained products from such synthesis, as well as a picture of the bottom of the centrifuge tube (inset), after removing the supernatant (positioned into the vial). The adopted centrifuging settings were 4000 rpm for 2 minutes.

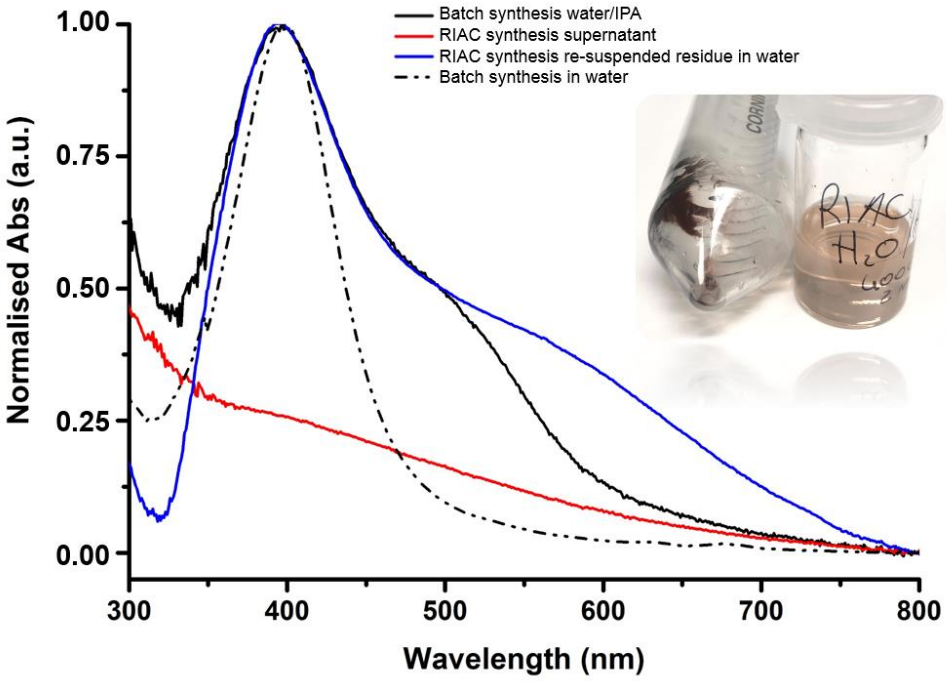

Figure 4.8 UV-Vis characterization of the water/IPA (55/45 v/v) synthesis of AgNSs: batch approach (black line); the RIAC approach (supernatant, red line); reaction residue re-dissolved in water (blue line). Batch reaction in water for comparison (black dotted line). Inset: picture of the residue at the bottom of the centrifuge tube after the reaction and the separated supernatant (vial). Synthesis conditions: 4000 rpm for 2 minutes.

The supernatant did not display the characteristic yellow/orange colour of the colloidal solution of AgNSs, and a dark residue of synthesis product remained on the bottom of the centrifuge tube. The synthesis was therefore not satisfactory. This is clearly notable from the spectrophotometric characterisation in Figure 4.8. The red line, which refers to the solution obtained directly from the RIAC (supernatant), shows a low and broad absorption band, with the absence of well-defined features. However, in order to characterise the dark residue at the bottom of the centrifuge tube (Figure 4.8, inset), the supernatant was removed and the residue was re-dissolved in water. The blue line was than compared with the batch results at the same conditions (black solid line), displaying a similarly shaped spectrum. Specifically, the bands around 400 nm, which indicates the presence of nanospheres, are almost overlapped for the two samples, and a prominent shoulder band is evident at around 560 nm and 500 nm for the RIAC and the batch synthesis products respectively.

Although this was not an unsurprising result overall, important information can be gathered particularly in relation to the absorbance shift of the shoulder band of more than 50 nm. This is a notable shift for plasmonic materials, and it lies in the wavelength region usually correlated with plated particles, which it might indicate a major effect of the applied pressure during the synthesis due to the centrifugal force. Nevertheless, the low quality of the product was attributed to the high-volume portion of IPA, similarly to that observed for the batch reaction.

4.3.1.2.2 Water-based synthesis of AgNSs through the spiral RIAC

Considering the above reported results, a water-based approach was then adopted. In particular, the synthesis was carried out by using an important advantage of RIAC devices, i.e. the possibility of performing a double step synthesis in a single operation. More specifically, chemicals can undergo a first mixing, when reagents reach the junction, followed by a further interaction with a third reagent positioned at the bottom of the centrifuge tube. The latter, other than being functional for collecting the product of the reaction that occurs into the flow-channel, opened a wide variety of possibilities important for the control of the reaction. These included a further dilution step, the regulation or the chemical order (molecular hierarchy), a further increase in concentrations, and a two-step VRs variation mechanism.

Therefore, for the production of AgNSs, a novel water-based configuration was explored. Reaction conditions such as the order of the reagents were varied, and in one case also the concentration of the capping agents. UV-Vis characterisation results of the most effective experiments are reported in Figure 4.9, corresponding to:

- **A)** Yellow line: The reducing agent in Reservoir 1, and capping agents (including the silver source) in Reservoir 2. This was the regular RIAC approach.
- **B)** Burgundy line: The reducing agent in Reservoir 1, the silver source only in Reservoir 2 and capping agents at the bottom of the centrifuge tube.
- **C)** Green line: The reducing agent in Reservoir 1, the silver source in Reservoir 2 with the capping agents, and a second portion of capping agents at the bottom of the centrifuge tube.
- Black line: equivalent to the water-based batch production.

The same quantities indicated in the material and methods section were used, and for each synthesis, RIACs were spun at 4000 rpm for 2 minutes.

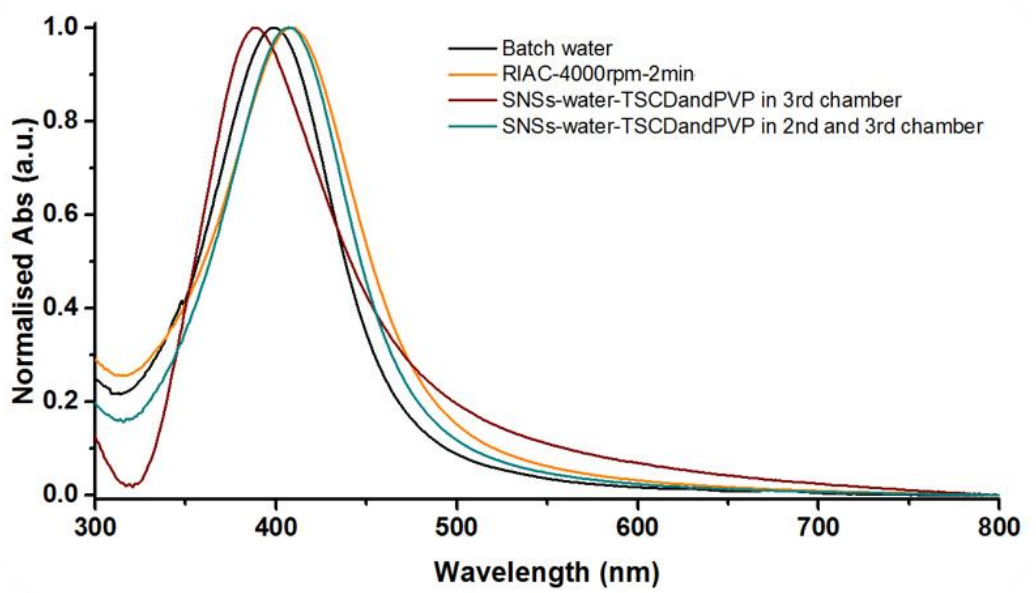

Figure 4.9 UV-Vis characterization of the RIAC water-based synthesis of AgNSs referring to protocols: A (Yellow line); B (Burgundy line); C (green line), described in the text in relation to reagent's order and position with respect to the reservoirs of the bottom of the centrifuge tube. The batch reaction in water for comparison (black line). Synthesis conditions: 4000 rpm for 2 minutes.

Differently from the water/IPA synthesis previously discussed, by comparing the normalised absorption spectra in Figure 4.9, it is possible to note that all the single bands are well-shaped around the characteristic wavelength region related to the LSPR of the AgNSs. However, differences highlight the effect of the diverse protocols involved. Firstly, as it can be seen by looking at the burgundy line, the absence of the capping agents in the second reservoir allowed the $AgNO_3$ to interact directly with the reducing agent at the junction, without the important mediating role of the TSCD and PVP. This was followed by sudden dilution and interaction with the stabilisers present into the bottom of the centrifuge tube. Based on the UV-Vis spectra, it was therefore possible to assume that the reaction occurred as expected. In particular, it can be hypothesised that instantaneous in-channel formation of small seeds occurred, which further dropped into the water phase below and into a TSCD and PVP capped dispersion. This justified the notable hypsochromic shift of the A_{max}, indicating that small AgNSs were predominantly produced. However, although the spectrum does not present a shoulder absorption, the band displays a notable asymmetry towards higher wavelengths. This likely indicates formation of slightly plated aggregates, probably due to the compression of clusters caused by the applied centrifugal pressure. The seeds/capping agent ratio might also play a role, as it technically changed overtime during the dropping of the formed seeds from the mixing channel to the capping agents' medium.

The rationale of the mechanism is further supported when considering the yellow and green spectra. In these cases, the stabilising agents were present in the second reservoir, allowing a

capped-AgNSs formation directly at the junction of the mixing channel, which was proven by the fact that there were no WA_{max} shifts between the two. However, the presence of TSCD and PVP also at the bottom (protocol C), appeared to be important in relation to the quality of the produced nanoparticles. This can be seen by the formation of a narrower absorption band, which highlights an improved size distribution. Moreover, the increased concentration of capping agents helped in counterbalancing the prior noted effect of the pressure and preserving particle' geometry.

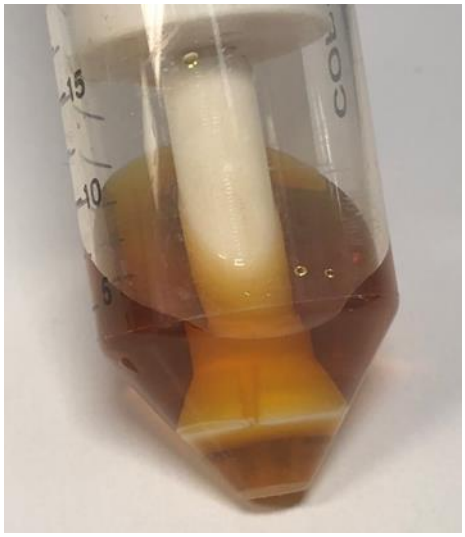

Figure 4.10 RIAC produced AgNSs.

The final product in Figure 4.10 shows the characteristic coloured solution of AgNSs directly after the RIAC synthesis, perfectly suspended within the solution. Differently from the water/IPA synthesis (inset Figure 4.8), no signs of separation between the supernatant and the particles are visible.

Protocol C, which included the capping agents in both the second and the third chamber, was therefore selected as the most suitable operating condition for AgNSs production with the RIAC method. The final imaging characterisation on sample C was performed *via* TEM analysis, which is shown in Figure 4.11 (B), both with the absorbance band with WA_{max} at 404 nm (A).

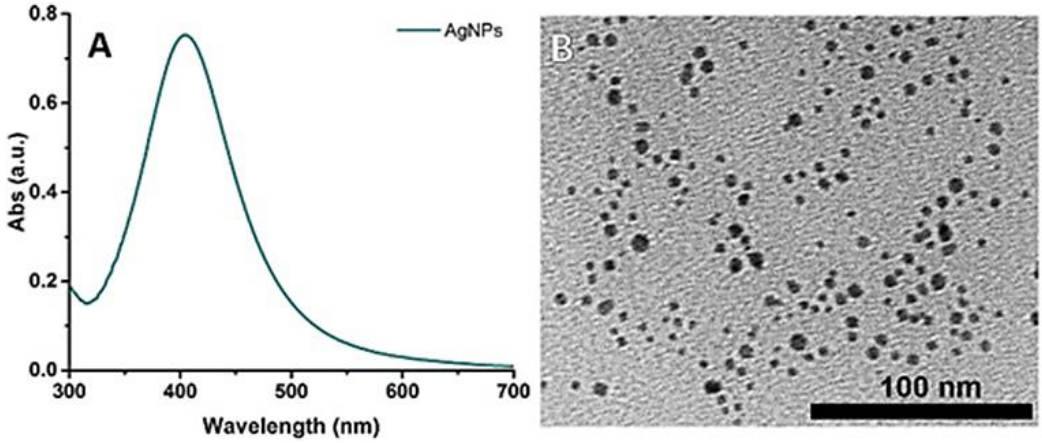

Figure 4.11 (A) UV-Vis spectrum of AgNPrs showing the maximum surface plasmon resonance (SPR) absorption at 404 nm. (B) TEM of the same sample after a 1.3 times dilution (scale bar = 100 nm).

4.3.1.3 Photo-assisted flow-synthesis of silver nanoparticles in a bacteria culture: a possible solution

The design of the photoreactors was created to allow an initial diffusive mixing between the two streams, slightly enhanced by the gentle curvature in the initial section of the architectures, to then reach the illuminated portion of the channel, where the light acted as catalyser for the formation of AgNSs. The light was shone in different ways, based on the design of the reactors, starting by the test for the first prototype produced (Reactor 1, section4.2.1.3). In this case, the flow solution moved from a smaller channel (squared cross-section of 1 mm) into a larger channel (squared cross-section of 3 mm), specifically created to be illuminated by the aligned laser from the OF.

Similarly to the other synthesis, also in this case, the colour transition of the solution was indicative of AgNSs formation. In particular, in the case of AgNss produced by bacteria, or in general into a culture medium, the solution appeared notably darker (almost brown when concentrated) than the yellow/orange one obtained from the chemical approach. This was likely due to the LSPR shift of AgNSs due to the interaction with the biological coating present in the medium. Therefore, from a simple visual analysis, it was possible to observe the efficacy of the reactor. Specifically for Reactor 1, in Figure 4.12A the formation of AgNSs is shown by the change in colour of the solution inside the straight reaction channel. Moreover, although the same chemicals were mixed, the fact that the initial serpentine portion of the reactor remained transparent, indicated that the reaction did not occur without light, supporting the photoreduction mechanism. This was a promising initial result, which was only limited by the formation of some bubbles in the area of channel size variation from 1 to 3 mm (aspect ratio 1), just before the light junction Figure 4.12B.

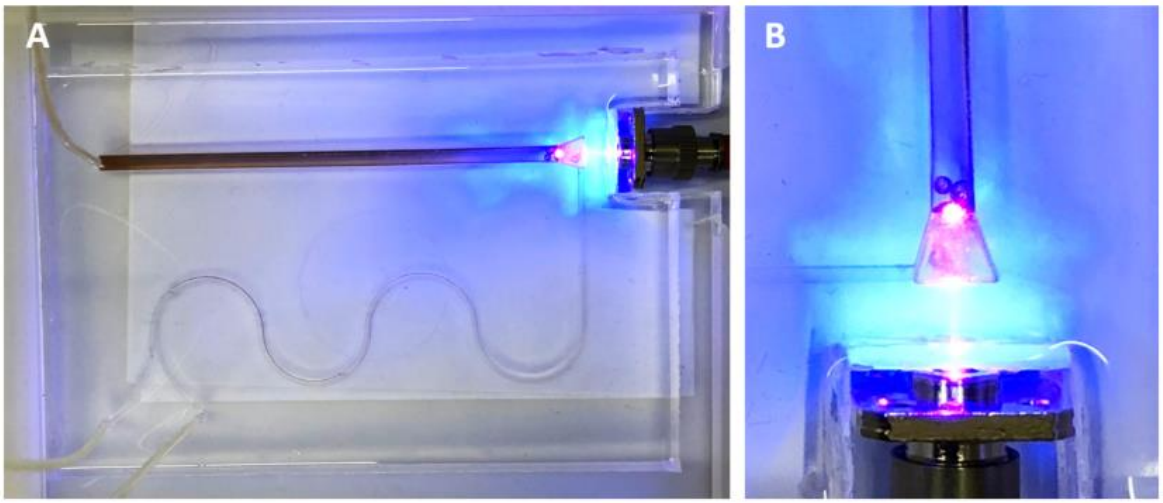

Figure 4.12 Reactor 1 after the photo-assisted flow-biosynthesis of AgNSs, clearly visible from the change in colour of the solution after laser exposure (A); magnification to highlight the formation of bubbles (B)

It was in fact noted that the production of AgNPrs was less effective over time. The partial loss of light intensity, due to scattering through the 0.5 cm of PDMS, or due to an inaccurate manual alignment of the laser beam with the straight channel, was considered. However, this error should be constant when maintaining the setup steady while operating the device. Therefore, the initial justification for product loss over time was related to scattering enhancement due to bubble formation in the proximity of the laser source. A second observation was related to the fact that, at the end of the test, it was difficult to remove part of the product that was adhered to the PDMS walls, particularly in proximity to the light source. Given the experience gathered through the batch synthesis, a washing procedure was carried out with H_2O_2 to re-oxidise the AgNSs and clean the reactor for further uses. This however revealed that a small portion of the produced particles somehow interacted with the PDMS surface creating a dark layer that acted as a further barrier for the light. Ideally, chemicals that have electrostatic interaction with the PDMS might remain closer to the surface leading to the formation of AgNSs in that region. The sample produced with Reactor 1 was collected and characterised *via* UV-Vis spectroscopy (results are further compared).

To overcome these limitations, a diverging lens was used and the light was positioned orthogonally to the rector top plane. The idea was to create an area where the light intensity was as constant as possible to avoid scattering, and a reactor design that minimises bubbles formation and dead volumes generated by 90° angled geometries. Reactor 2 was then conceived creating a consistent curved mixing channel of 0.5 x 3 mm (w x h). The rectangular cross-section was defined in order to allow a better transmission of the incident light and minimise scattering. However, although the light-beam diverged, the consequent loss in photon density, thus in light intensity, combined with the fact that only a small portion of the channel was exposed to the light, were significant limitations. The device was not effective and had poor yield. In order to obtain a reliable UV-Vis characterisation of the sample, experiments were run using a 10-times smaller TFR (0.1 mL/min instead of 1 mL/min).

Therefore, Reactor 3 was finally adopted as a combination of the previous two alternatives. Also in this case, the geometry did not present angled architectures, and the height of the channels was kept constant to minimise bubble formation. Moreover, a pre-aligned OF adjacent to the channel was embedded into the PDMS structure to maintain the same position throughout the experiments. Besides, the cross-section in the portion of the channel where the reaction occurred was smaller than the one designed for Reactor 1 (1 mm instead of 3 mm, aspect ratio 1 in both cases). The overall efficiency of Reactor 3, and the limitation of the technique, can be deduced from Figure 4.13. It was possible to notice that the light scattering at the connection of the OF, highlighted by the lateral light rays (Figure 4.13a), was greater than the one observed for Reactor 1 (Figure 4.12a). However, the light followed the inner path of the whole reaction channel until

reaching its outlet. This demonstrated a good alignment, even though the cross-section of the channel had a comparable size with the OF. The device appeared effective during experiments. This can be noted in Figure 4.13B by colour changing of the solution within the illuminated portion of the channel and at the outlet tube (white ellipse). However, product loss overtime occurred. Considering the absence of bubbles, it was more evident how the product remained adhered onto the inner PDMS walls and particularly in the proximity of the light junction, as clearly visible in Figure 4.13C.

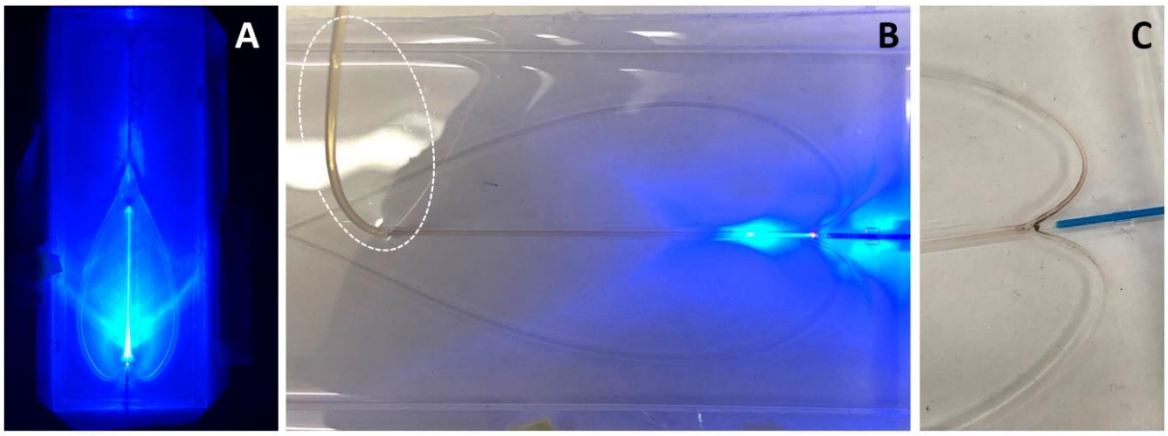

Figure 4.13 Reactor 3: evidence of the enhanced laser scattering (A); production of AgNSs highlighted from the change in colour of the solution toward the outlet (B); detail of the product deposition on the inner part of the PDMS walls, close to the light source.

Although with different efficiency, all the photoreactors were able to produce AgNSs. However, product adhesion became a major problem to be solved in order to obtain good reproducibility over time. Therefore, a second attempt on Reactor 1 was carried out, with some modifications. Specifically, a coating procedure with dodecyloxy-trimethylsilane was performed in order to minimise particle's adhesion. The treatment was firstly done on glass slides for a preliminary and successful test, followed by the same procedure on the polished glass OFs (Appendix Fig. 11). The synthesis was reproduced for both coated and non-coated OFs by inserting them into the main reaction channel, from the PDMS recess previously designed for the OF connector (Figure 4.14a,b). Adopting this solution the scattering was clearly minimised (Figure 4.14a) and the AgNSs production occurred as expected (Figure 4.14b). Moreover, the OF was pushed into the channel in a manner that any formed bubble was not interfering with the light source. Unfortunately, although the PDMS walls were clearer, and the coated OF performed better than the uncoated one, the adhesion of the product onto the OF polished cross-section occurred, limiting the light emission overtime (Figure 4.14c, black arrow, details in Appendix C.4).

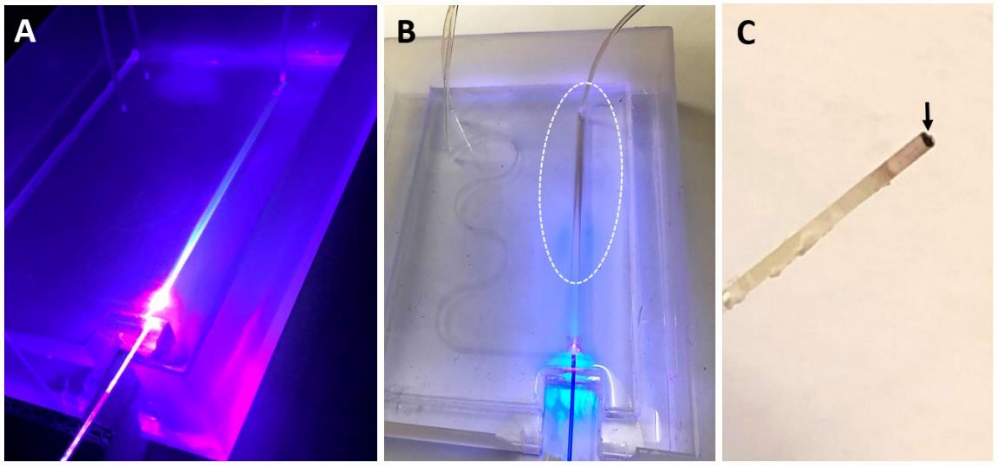

Figure 4.14 Reactor 1 with the introduced OF: clear laser efficiency and minimised scattering (A); production of AgNSs highlighted from the change in colour of the solution toward the outlet (B); product deposition at the surface of the OF (C).

At the end of each experiment, samples produced using each reactor were collected for the UV-Vis characterization, as shown in Figure 4.15 for comparison. Operating conditions were FRR=1 and TFR = 1 mL/min in all cases except for the Reactor 2 for which the TFR was ten times slower (0.1 mL/min). In line with the observation discussed above, results displayed greater efficacy, in terms of normalised absorbance, for Reactor 1 and its modification. This was visible for the band of the externally connected OF through 0.5 cm of PDMS (Reactor 1, magenta line), and with the coated OF into the channel (Reactor 1 + OF, black line). However, the absorption band of Reactor 1 appeared narrower, probably indicating a more uniform sample.

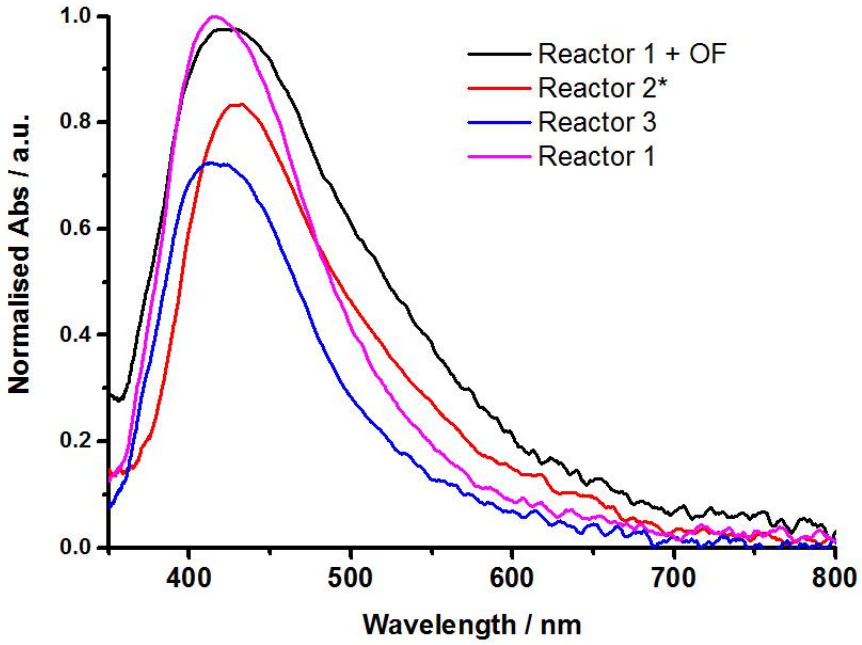

Figure 4.15 UV-Vis spectra of the produced AgNSs at FRR=1 and TFR=1 mL/min with Reactor 1 (magenta line), Reactor 2 (red line), Reactor 3 (blue line) and Reactor 1 with the inserted OF (Reactor 1 + OF, black line). The TFR adopted for Reactor 2 was ten times slower (0.1 mL/min).

Although some limitations, the photo-assisted flow-bio production of AgNSs was demonstrated, and several alternatives were discussed. Most importantly, progressive improvements of the technique led to the development of a novel and simple technological solution.

In fact, with the wavelength of the activating light also being an important factor, and in order to avoid using spotted beam in order to minimise product's adhesion, a common UV lamp was tested on Reactor 1. Preliminary results were extremely promising, as visible from the intense change in colour shown in Figure 4.16. Following studies were carried out in collaboration with T. Mabey in a UV-bath, which improved the production approach also by adopting the two inlets curved serpentine reactor, in order to increase reaction time due to the channel length (1 m).

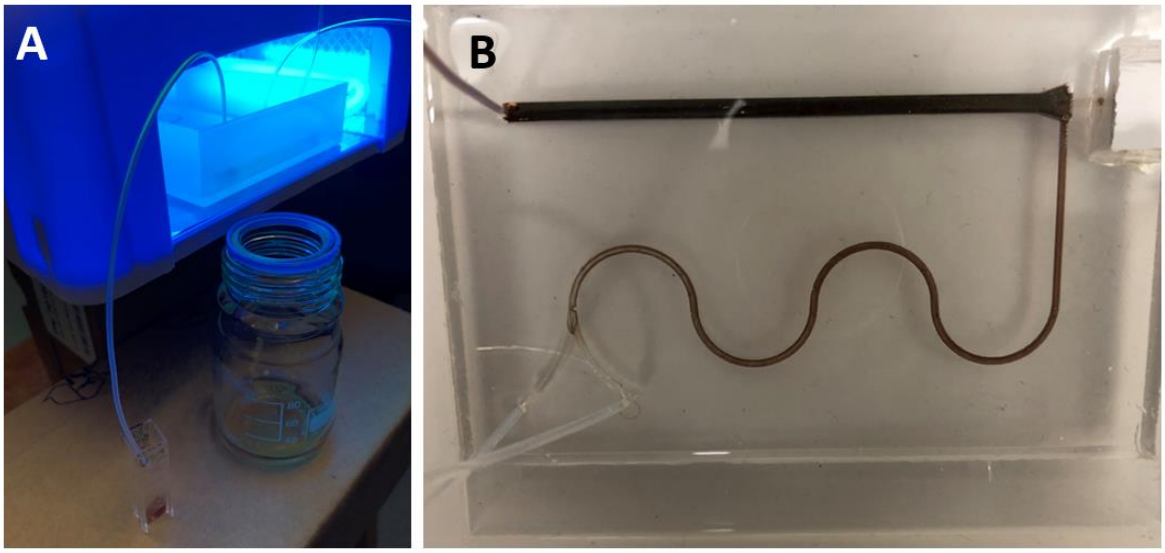

Figure 4.16 Preliminar pictures of the positioning of Reactor 1 into a UV-Vis lamp (A), and the clear production of AgNSs throughout the whole channel (serpentine included)(B).

4.3.2 Flow-synthesis of silver nanoprisms

4.3.2.1 Flow-synthesis of silver AgNPrs with a 3DP-C*glass three inlets flow focusing reactor (high-resolution 3D printer).

Studies on the synthesis of AgNPrs through flow-reactors were conducted as one of the major goals of the present research project. These were chosen in order to characterise the manufactured cost-effective reactors and improve AgNPrs flow-synthesis at the same time. However, the translation of the batch process to flow reactor systems was challenging due to several aspects here discussed.

The first approach used was the hydrodynamic flow synthesis, where the combination between suitable FRR values and precise concentrations of the chemicals needed optimisation. Without optimised fluidic control, the hydrodynamic flow-focusing could cease or the desired reaction would not occur.

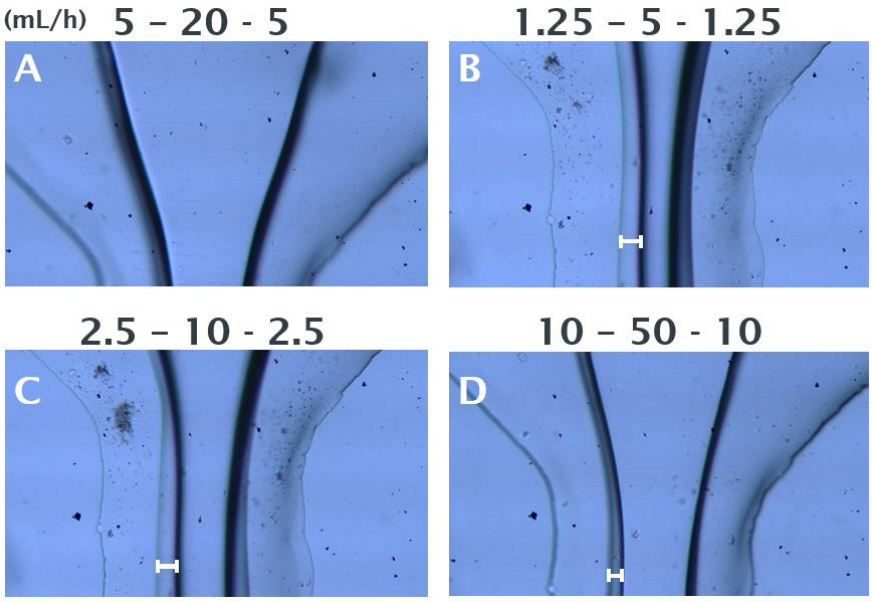

Figure 4.17 Images of the junction from above. Water solution in the central stream and IPA solutions in the lateral streams. The FRR was fixed at the value of 0.5 and the TFR was tested for 30, 7.5 and 15 ml/h for image A, B and C respectively. Image D refers to a higher TFR of 70 mL/min and a FRR of 0.4.

After several tests, a stable hydrodynamic flow-focusing was achieved. Figure 4.17 shows the images, taken just after the three inlets junction of the 0.25 mm 3DPM-C*Glass reactor, which represents the selected conditions. The suitable FRR was selected at the value of 0.5 and the TFR was tested for 30, 7.5 and 15 ml/h (Figure 4.17 A, B and C respectively). Moreover, a slight variation of the flow-synthesis is also shown in Figure 4.17C, in order to evaluate the effect that a small variation to the protocol can produce. These images highlight the stability of the flow-focusing, as well as the variation of the width of the central stream in relation to the FRR. Moreover, changing

the TFRs highlighted another effect that depended on the solvent's density, and it varied based on the fluid velocity. Particularly, looking at the images of the junction at different TFRs in Figure 4.17, it can be noted how the slower the TFR the wider is the separation of the two lines at the interface between water and IPA, which indicates a curved meniscus inside the channel (white bars). Noting this, CFD simulations were run for evaluating the mass fraction of water and IPA at the suitable condition for a stable hydrodynamic focusing (FRR = 0.5). Simulations were also useful to understand the behaviour of the solvents through the architecture, specifically at the junction and in the curved portions, obtained by modelling an average TFR of 20 mL/h. Figure 4.18 shows the obtained computational results in comparison with the corresponding experimental conditions (solvents only). Specific attention was focused on the areas of the junction (red outline) and the cross-section just after the first 90° curve of the channel architecture (blue outline). The hydrodynamic flow-focusing appeared as expected. The black and white "×" indicated in Figure 4.18 (CFD cross-section and experiment image), illustrate how the central stream bends due to the effect of the inertial force – which is dependent on the applied flow rate. This would increase the surface area of contact between the central and the two lateral streams, thus improving the diffusion process. It was also possible to notice that, although the behaviour of the streams was very similar between CFD and experiments, size and position of the curved features with respect to the channel edge presented some variations. This was probably due to the non-accurate reproduction of the channel design by the high-resolution 3D printing approach, in line with the previously discussed cross-sectional analysis in Chapter 3. Moreover, CFD simulations at a lower TFR further highlighted the effect of solvent's density on the mixing regimes (Appendix C.3).

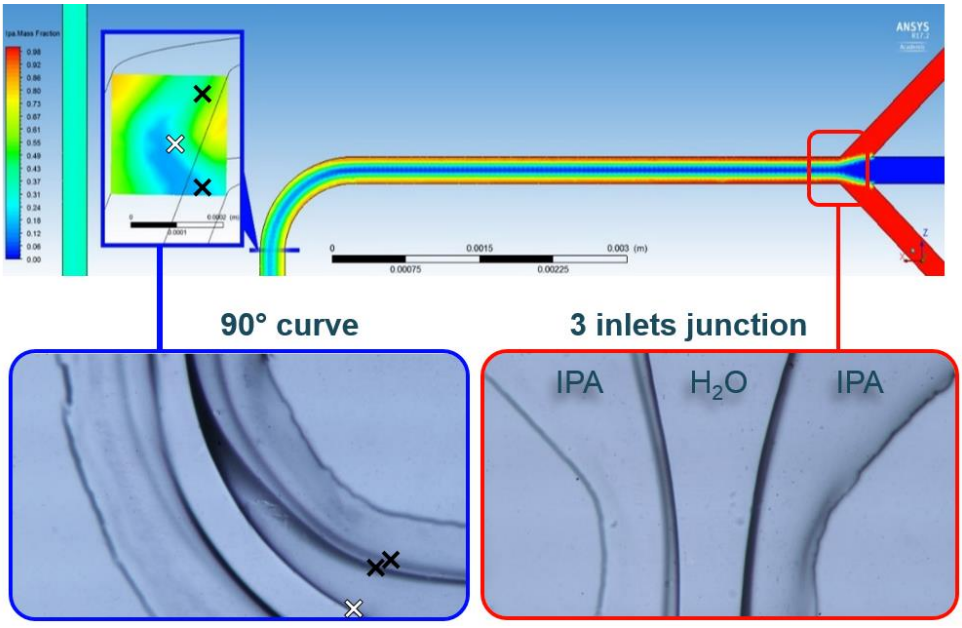

Figure 4.18 a) Images of the first curve of the serpentine channel from above. b) Preliminary CFD simulation of the FRR = 0.5 and TFR = 30 mL/h condition. Other than the flow focusing, the cross-section shows bending of the central stream similarly to the experimental observations.

The flow-synthesis of AgNPrs was then carried out, in order to evaluate the effectiveness of the device. Based on the understanding that colour is a great indicator for shape and size of AgNPs, [100] the first general information on the quality of the reaction was determined through a visual analysis. In particular, Figure 4.19 (left) shows the colloids produced under the indicated conditions (A, D, C and D). Moreover, knowing that the kinetics of the reactions has a major role on the particles production, samples were monitored over 2 hours after collection from the reactor (Figure 4.19, right).

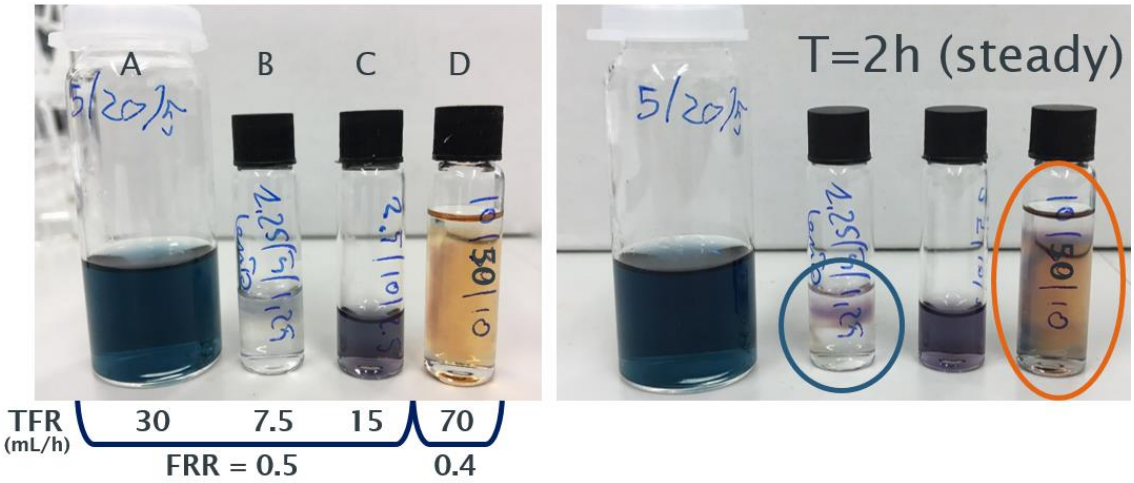

Figure 4.19 Colloids collected from the flow reactor. Fixed FRR = 0.5. TFR 30, 7.5 and 15 ml/h for conditions A, B and C, respectively. A) After the synthesis; B) after 2 hours steady.

The blue solution, characteristic of the prismatic shape, was evident for protocol A, which was related to the highest TFR among the FRR 0.5 conditions. Differently, an almost transparent solution, with slightly visible blue shades, and a purple solution, were produced from synthesis B and C, respectively. Although being not satisfactory, these two results showed an interesting trend, especially when observing them after 2 hours. In particular, the almost transparent solution (B), corresponds to the lowest TFR tested, and the purple/blue colour shades (blue circle), appeared to be formed without passing from the typical yellow/orange colour of the spheres. This was a key observation as it demonstrated that, when the stoichiometry ratios were addressed, the formation of a specific shape was mostly governed by the quality of the mixing. In this specific case, diffusion was effective but it led to a notably slower and uncomplete process of prism formation, thus it was not deemed convenient for the defined purposes. On the other hand, the intermediate protocol in terms of TFRs (C) produced a purple-coloured solution which, similarly to that obtained for the batch synthesis in Chapter 2, confirmed the prismatic shaped particles but with a smaller size.

The overall trend brought to the conclusion that the introduction of advection dominated mixing regimes, achievable by increasing the TFRs for curved geometries, might lead to a faster and more

consistent production if the stoichiometry was opportunely prepared. This was in fact proven by protocol D, which although being the one with the faster TFR, did not produce AgNPrs due to a slightly different FRR that affected chemical ratios. The variation from yellow/orange to blue stars occurred after 2 hours from the synthesis, and only for certain areas (Figure 4.19, right, orange circle).

Another important aspect to underline is related to the kinetics of the reaction as clearly observed (Figure 4.20). In fact, during the flow-production, the yellow/orange solution was visible at the outlet tube, whereas the blue solution was collected into the final reservoir (vial).

A video of one reaction test, that highlights the colour-changing, can be seen at the following link: https://www.youtube.com/watch?v=hpe8xEOdoGw

Therefore, it was possible to evaluate that part of the reaction might happen outside the flow reactor, e.g., along the output tube or even inside the collection vial.

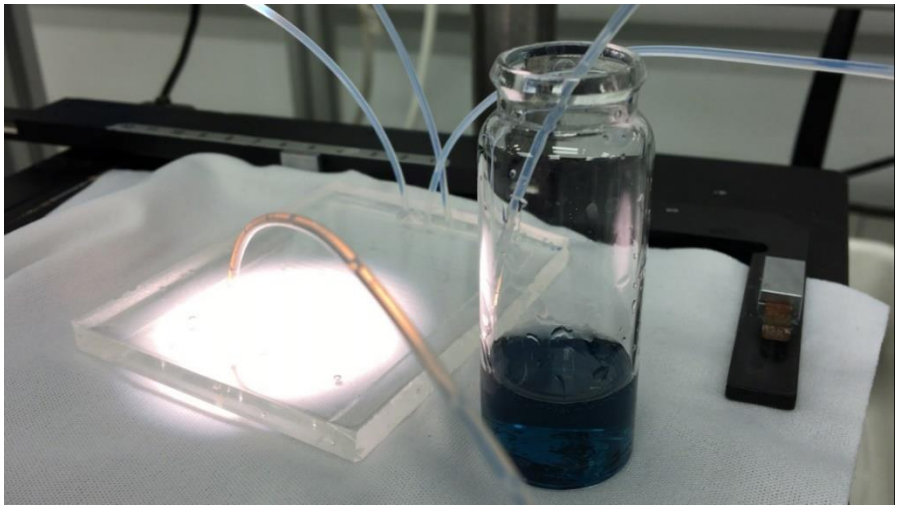

Figure 4.20 Transition from spheres to prisms during the flow-synthesis of AgNPrs using protocol A.

Reaction A was finally repeated, and the product collected (Figure 4.21b) for UV-Vis characterisation. The UV-Vis spectrum recorded after a 1:3 dilution (Figure 4.21a) presented all the relevant features related to the prismatic geometry of the particles, with a well-defined shape and a relatively red-shifted WA_{max} > 860nm. However, the small band at 399 nm revealed that a minor portion of AgNSs was present as well. This can also be seen by a slightly green shade at the bottom of the solution (Figure 4.21, b).

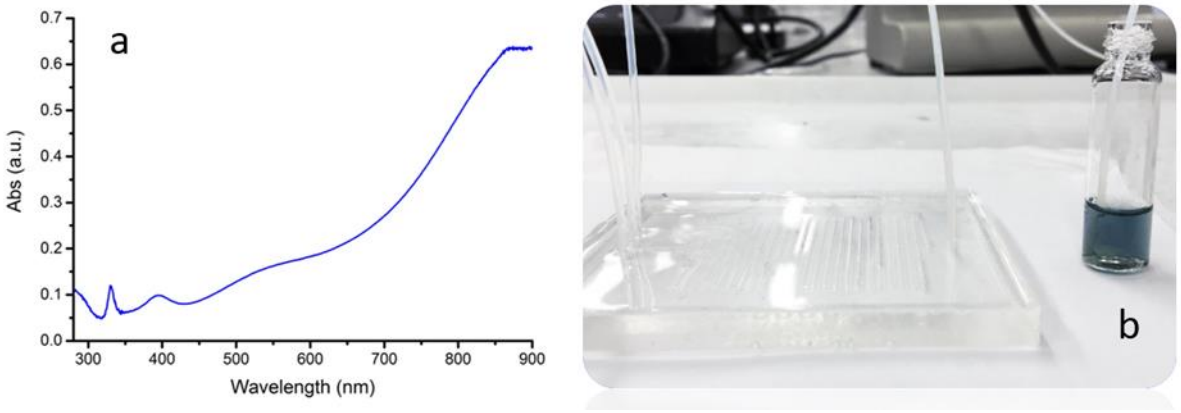

Figure 4.21) UV-Vis spectrum of 1:3 diluted sample from the flow synthesis (FRR = 0.5; TFR = 30 mL/h). b) Picture of the reactor and the vial for the collection.

These results have shown that AgNPrs can be obtained *via* cost effective flow-reactors, and they brought to the realisation that several modifications can be applied to improve the size and shape control of the produced colloids, as well as increasing the TFR towards meso- to large-scale production.

Firstly, the higher TFR performed better than lower TFR. This is likely due to the enhanced effect of the inertial forces at the curvature of the channel, and it can be seen in Figure 4.19, when comparing the transparent solution obtained at TFR 7.5 ml/min with the typical blue colloid obtained at TFR 30 ml/min. Enhancing this effect will be part of the next design modification, which can be achieved by creating a continuously curved architecture to augment secondary flows, leading to a more effective mixing. Moreover, this can be done without the hydrodynamic flow focusing approach that, despite being highly effective for diffusion-driven reactions, it introduces limitations in terms of usable TFR and FRR. It was also important to minimise the volume of IPA for the flow-synthesis.

Secondly, although similar observations were made between CFD simulations and experiments, the cross-section of the real channels needs to be further characterised to understand the effect of the channel architecture on the mixing process.

Finally, in relation to the control over the kinetics of the reaction, it is possible to evaluate and eventually demonstrate that complete mixing within the channels is the key factor that leads to the formation of a prismatic shape.

4.3.2.2 Validation of CFD simulations on mixing along the curved serpentine channel made with the Objet Connex 350: measured vs designed cross sections

The two-inlet curved serpentine reactor was created to overcome the previously mentioned limitations for improving the synthesis of AgNPrs. However, it is important to gather a better understanding of the effect of the real geometry on the mixing regimes, especially when designing curved channels. As demonstrated in the literature, the Dean flow is exhibited with the right combination of TFRs and curved architectures, creating controlled vortexes and enhanced mixing.[148] In this case, the inertial force starts to play a crucial role, by pushing the stream on the curved walls of the channels and generating flow rotations. This phenomenon is therefore drastically dependent of the angle of the inner walls.

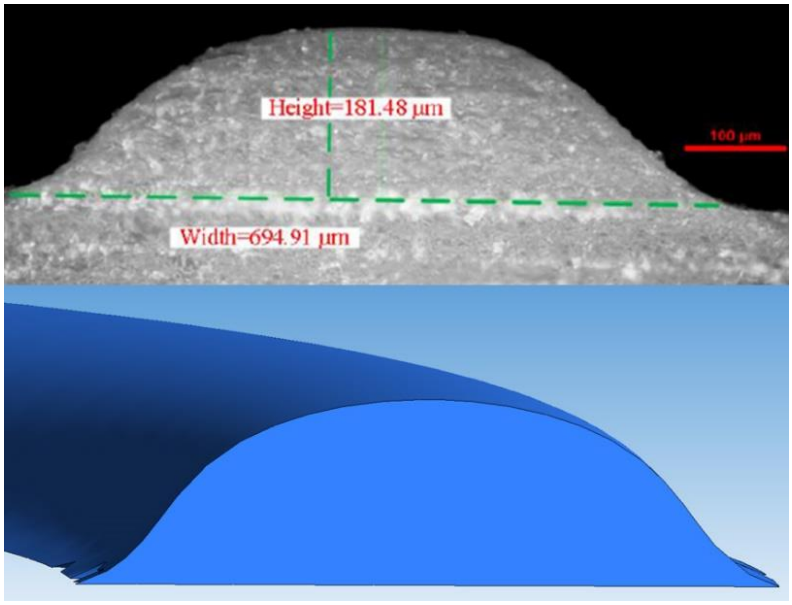

Figure 4.22 Measured cross-section of a Veroclear master mould channel (above); the respective designed channel on ICEM for CFD analysis on Fluent (bottom).

Based on the previous characterisation of the high-resolution mould profiles, and on a microscope image previously obtained by Dr. Ali Mosayyabi (Bioengineering, University of Southampton), which represents the measured cross-section of the positive mould channel obtained from a square design (Figure 4.22), a CAD design representing the actual features was created. The same architecture of the two inlets curved serpentine was maintained in terms of channel length and curvature radius, but instead of the squared cross-section, the measured profile was used (Figure 4.22, below).

Subsequently, the novel representative design was meshed for CFD simulations, which were carried out for gathering information on the solvents mass fraction, thus the mixing efficiency (Figure 4.23). Specifically, the value of FRR = 7 between water (red stream, right inlets) and IPA (blue stream, left inlet) was used. This was the same value used for the batch synthesis of AgNPrs and the flow-

synthesis of AgNSs. The visual mass fraction colour scale in Figure 4.23 represents the horizontal plane at half-height into the channel.

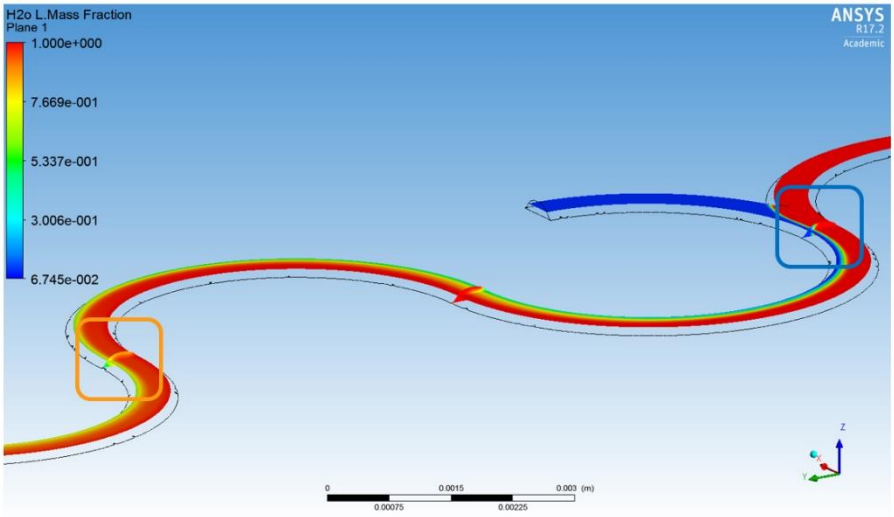

Figure 4.23 CFD simulations of the water mass fraction: reaction condition FRR=7, TFR 30 mL/h. Simulations were run in collaboration with Dr. Aly Mosayyebi.

For a better understanding of the mixing, the blue and orange squares in Figure 4.23, which correspond to the cross-section after the junction and after the second curve respectively, are reported in Figure 4.24 for both the real geometry and the equivalent squared design. Running the CFD for both architectures provided a more precise insight on the limitation created by the channel obtained from the high-resolution mould.

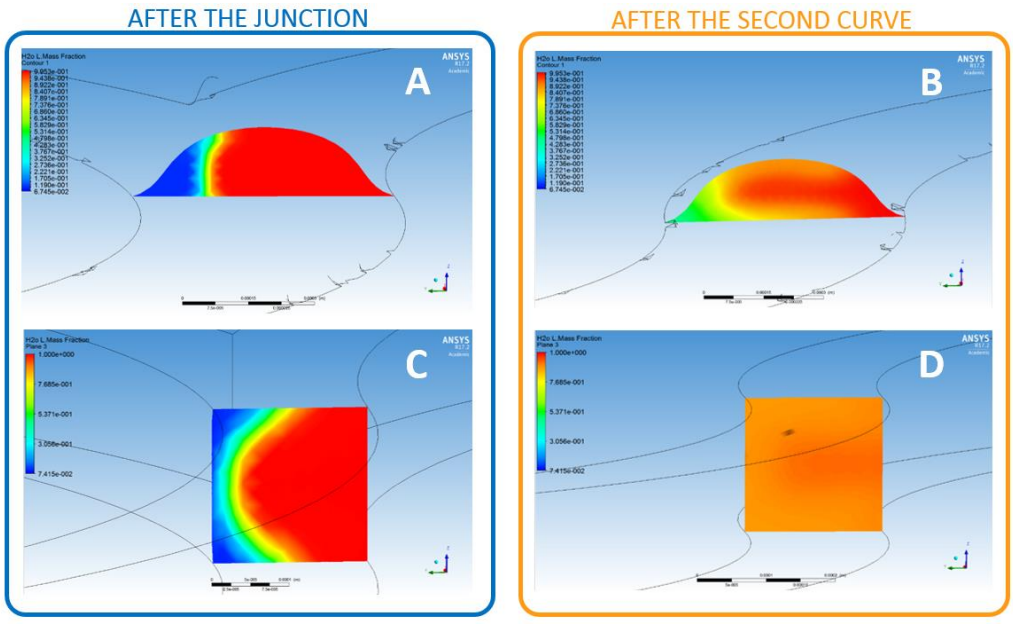

Figure 4.24 CFD simulation of the water/IPA mass frraction (FRR 7) for the realistic (A and B) and squared (C and D) geometries. A and C refer to the cross section just after the juction, whereas B and D after the second curve.

In fact, when observing the cross section after the inlet (A for the realistic and C for the squared channels), it is possible to visualise a similar behaviour of the two solvents, even though a hint of

curvature is already visible between the two streams for the squared one. However, after the first two curves, differences are evident. In the case of the realistic geometry, the curvature of the channel walls and the lower angle, tend to retain the solvent without allowing a full vortex to be generated. This is indicated from the green colour of the mass fraction colour scale on the lower left angle for the real geometry (B), when compared with the better mixing achieved by the designed channel (almost entirely orange).

Combining the obtained mixing information with the previous profilometric characterisation, the final manufacturing method was carried out using the desk 3D printer (U2+). The two-inlet curved serpentine replica mould casted device was created and bonded on PDMS by oxygen plasma treatment (3DP-RMC*PDMS), as shown in Figure 4.25. It was then used as final reactor for the further described production of AgNPrs. This design was also conceived to prove whether a complete mixing within the channel led to the formation of the AgNPrs, even without being continuously stirred after the collection of the produced product into the vial, thus affecting the kinetics.

*Figure 4.25 two inlet curved serpentine replica mould casted device, bonded on PDMS by oxygen plasma treatment (3DP-RMC*PDMS)*

4.3.2.3 Flow-synthesis of silver nanoprisms with 3DP-C*PDMS two inlets curved serpentine reactor (desk 3D printer)

Given the information obtained from the previous experiments and CFD simulations, the flow synthesis was re-designed and adapted for the two-inlet curved serpentine reactor. This approach presented improvements in many aspects. The manufacturing of the reactor was less expensive as the desk 3D printer U2+ was employed for the production of the PLA moulds, instead of the HR OC350. Concerning the bonding, the pressure-sensitive adhesive tape method could not be adopted for two reasons: the potential leakage when using TFR higher than 20 mL/min; and the interaction between H_2O_2 and the coated layer on the tape, which was noted to affect the synthesis and affect the bonding. Therefore, in order to sustain higher TFRs, the synthesis was performed using a reactor bonded on PDMS *via* plasma exposure (in a plasma chamber). However, the same architecture was reliable up to 10 mL/min also when the bonding procedure was performed *via* plasma treatment *via* the corona gun protocol (in air). This gave the possibility of adopting this soft-lithographic approach in almost any environmental condition, without the need for specialised facilities, and the mould can be reused over time. The use of FDM 3D printer, although producing more rough moulds, ensured a more accurate reproduction of the designed cross-sectional shape of the channel, which was crucial for enhancing the effect of the Dean flow due to vertical side walls. The adopted settings of the re-designed flow synthesis conditions are presented in Table 4.1.

Table 4.1 FRR, TFR settings and related Dean number for the tested flow production of AgNPrs adopting the cost-effective two inlets curved serpentine reactor.

TFR (mL/min)	1	5	10	20	50
FR H_20	0.875	4.375	8.75	17.5	43.75
FR IPA	0.125	0.625	1.25	2.5	6.25
FRR	7	7	7	7	7
Dean number	838.50	4192.50	8384.99	16769.98	41924.94

In particular, in order to evaluate the effect of the architecture on the synthesis, the FRR was maintained at 7, and the TFR was gradually increased. The selected TFR values were: 1, 5, 10, 20 and 50 mL/min (Table 4.1). Most importantly, for improving the mixing efficiency and attempting to demonstrate the control over the kinetics, the Dean number was increased by operating at higher TFR, and the product of the flow synthesis was collected without further mixing. The elimination of the further mixing during collection of the sample had a strong impact on the demonstration of control over the reaction kinetics.

The synthesis was then carried out and all the observations on the colour variations of the solution, order of execution, and reaction time are grouped in Table 4.2.

Moreover, considering that the TFR of 10 mL/min was deemed to be the ideal flow-condition towards the meso- to large-scale production, this specific TFR setting was employed in the first synthesis (TFR 10a), and then repeated after 30 minutes from the initial chemicals' preparation (TFR 10). This was planned in order to evaluate reagents stability over time.

Table 4.2 TFRs, time of the colour transition to blue (from the collection into the vial), notes on the colour variations, and order of execution of the experiments.

Order	3rd	2nd	4th	1st	5th	6th
Colour variation note	Starting yellow. Spots of blue start forming after 2' creating blue and yellow areas until the complete blue solution is observed. The shade of final blue colour is not as the other samples. Which indicates the not properly competed transition to apparently not properly complete.	Yellow in 20 sec. After 1' 50'' Blue starts forming from the bottom of the vial, and intense yellow at the top, turning completely blue after other 50 seconds	Pale yellow in 20 sec. 2' 10'' Yellow and blue shades start forming from the bottom of the vial towards the top. Complete transition in 40''.	Pale yellow in 20 sec. 2' 00'' Yellow and blue shades start forming from the bottom of the vial towards the top. Complete transition in 40''	Starting transparent and staying so with only slightly visible yellow. After 1' 50'' Blue spots start forming almost without yellow seeds. From 2' 00'' to 2' 30'' Blue and yellow motions are observed and the solution rapidly turns blue.	Starting pale yellow. Turing dark yellow after 1' 00'' Almost homogenously turned blue in 1' 30''. The blue solution also remains into the channel Leakages are observed from the diagonal groves.
REACTION TIME From collection to blue (Min ' sec '')	4' 50''	2' 40''	2' 50''	2' 40''	2' 30''	1' 30''
TFR (mL/min)	**1**	**5**	**10**	**10a**	**20**	**50**

From the colours of the products as shown in Figure 4.26a, it was possible to notice that the production rate of 1 mL/min did not perform as well as the other TFR conditions. In fact, the typical blue-coloured colloidal solutions of AgNPrs was obtained for the TFR of 5, 10a, 10, 20 and 50 mL/min, whereas a different blue tone, which presents greenish shades was obtained for the slower TFR setting. This is actually in line with what expected for this condition due to the lower Dean number indicating the less predominant effect of inertial forces and less effective mixing. It should

not be underestimated that the waste solution remained orange/yellow. The waste was collected by manually activating the pumps between each reaction in order to remove any product residue within the channel, related to the previous synthesis. Because the pumps were manually activated, the FRR was not controlled accurately, therefore the chemical concentrations could be different from those needed for prism formation. This further highlighted the importance of chemical ratios for this reaction, which would have led to the variation of the solution into blue as it contained the same chemicals.

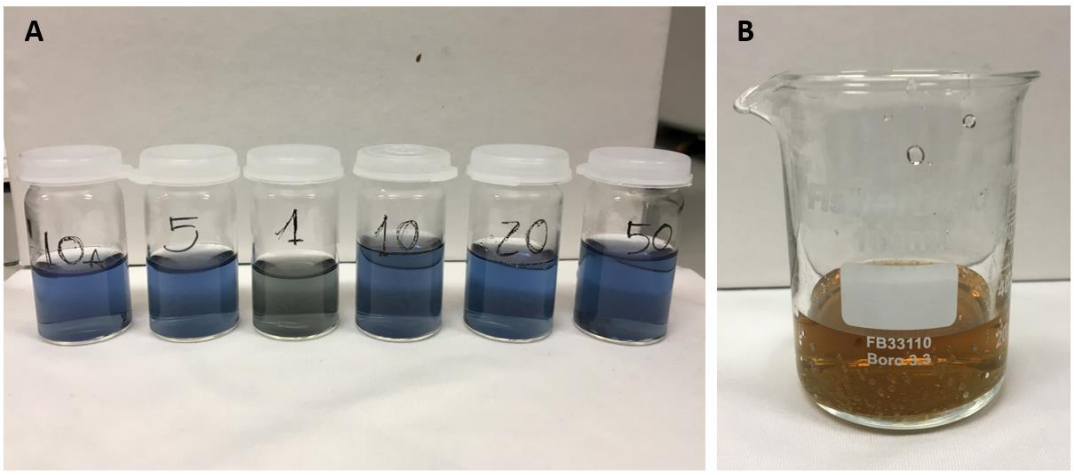

Figure 4.26 Flow-synthesis of AgNPrs: A) Collected products based on the TFR and order of reaction from left to right. B) Waste solution collected between each flow-production

The UV-Vis characterisation displayed in Figure 4.27 confirmed the visual results. Starting with the spectra of the waste solution, which shows the absence of any characteristic feature related to the prismatic shape, and confirms the production of sphere-like nanoparticles due to the incorrect chemical ratios.

Differently, by examining the spectra of the blue samples, the uncomplete formation of prisms is evident for the 1 mL/min (black line). This shows a broad absorption band that can be assigned to the sum of several shaped particles. The small peak at 330 nm, combined with the rising of the absorption towards higher wavelengths, indicates the presence of plated triangles. Nevertheless, the absorption band between 400 and 450 nm, reveals the presence of sphere-like particles, thus giving to the solution the greenish colour tone (as a combination of blue and yellow/orange). Proceeding with increasing TFRs, the 5, 10a and 10 mL/min samples (red, blue and magenta respectively), are almost overlapped, and the WA_{max} reaches a value of 870 nm. This proved consistency over time, and a good balance between flow-rates and quality of the sample. The spectral shape shows all the features related to the prismatic geometry, with the absence of absorption bands around the 400 nm range. Similarly, the 20 mL/min condition reveals the features of the prismatic nanoparticles. However, it presents a blue-shift of the WA_{max} when compared to

the 5, and 10s mL/min samples. As further discussed, based on the experimental results and on the TEM imaging (Figure 4.29), this might occur due to the increased pressure within the channel which often tends to break bigger prisms causing the WA_{max} shift. Finally, the 50 mL/min band appears notably broader and slightly less intense (dark blue band). Also in this case, the high pressure can break the prisms. If breaking did not occurred, the mixing efficiency would be high enough to form the biggest particles, which are suitable for NIR purposes.

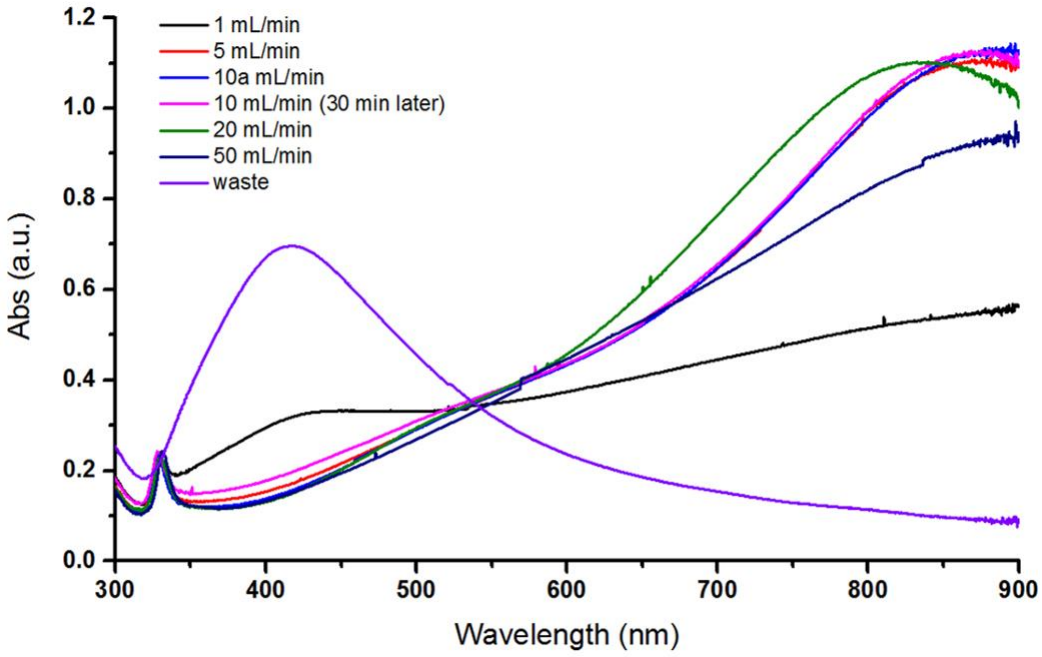

Figure 4.27 UV-Vis characterisation of the produced AgNPrs and waste (purple line), based on the TFR conditions of 1, 5, 10a, 10, 20 and 50 mL/min (black, red, light blue, magenta, green and dark blue respectively). Fixed FRR at 7.

Although further TEM imaging characterisations were needed, results obtained after changing reactor seemed in line with the hypostasized improvements. In fact, a further confirmation of the mixing efficiency, in relation to the kinetics of the reaction, is represented in Figure 4.28, which reports the transition time (from the collection into the vial to the complete colour variation into blue) vs the TFRs. It can be seen that, at the 1 mL/min condition, the reaction time was notably slower and, based on the obtained UV-Vis results, the overall quality of the prisms was poor. Due to the alternate serpentine design, it was not possible to determine the precise mixing improvement that the inertial forces (*De* number) had on the mixing regimes. However, a *Re* number of 175.4 for the 1 mL/min condition (calculated assuming a straight channel), strongly suggests that the reaction was diffusion-dominated, which appeared to not be the ideal operating condition for the specific reaction. Differently, higher TFRs shortened the reaction time. Particularly, a plateau is was reached for the 5, 10a and 10 mL/min samples, which appeared to be the suitable range in terms of reaction time (Re of 1753.8 for the 10 mL/min). The general trend

indicated by the blue curve suggests that the higher the TFR, the slower the transition time would be, as expected by the increasing of inertial forces. In case of the 50mL/min flow-synthesis, the blue colour variation was also detectable into the channel after just 30 seconds from the activation of the pumps. However, the broad absorption band indicates a lower control over the size of the produced particles.

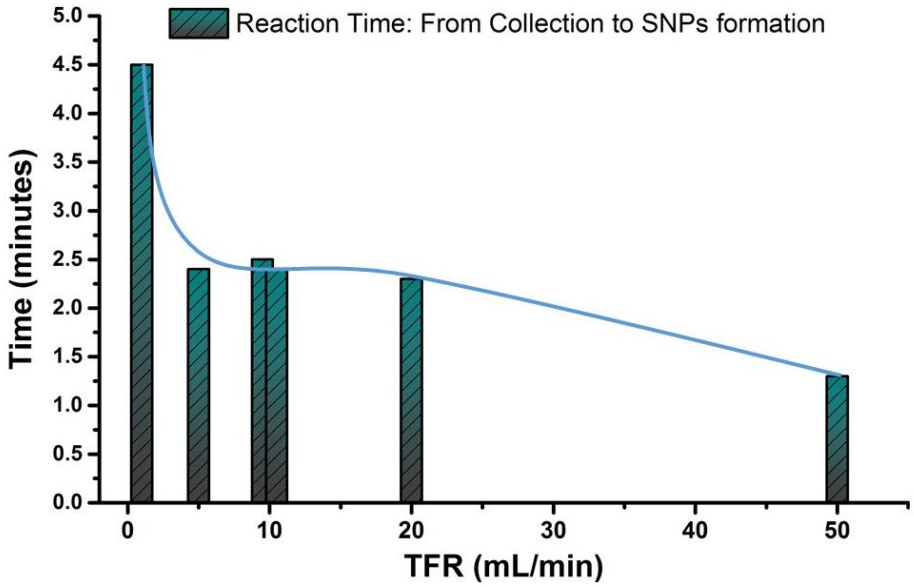

Figure 4.28 Reaction time vs TFR for the flow-reactions. The reaction time is considered as the time between starting collecting the sample into the vial and the complete colour variation into blue.

A video of the experiments that highlights the colour variation over time, thus the AgNPrs formation, can be watched at the following link: https://www.youtube.com/watch?v=hpe8xEOdoGw).

A size distribution analysis was carried out from the TEM images. Particles were counted using software Image-J, and their edge lengths were measured to demonstrate the trend of the flow-reactions. Similarly to the procedure adopted for the batch synthesis, the magnification of the TEM images was selected in order to detect a region as wide as possible, while obtaining a reliable pixel counting for the scalebar used as a dimensional reference. This is important for a realistic representation of the samples. Specifically, results related to the 5, 10 and 20 mL/min synthesis are compared in Figure 4.29 (a, b and c), and the normalised average edge length, with respective SD, is shown over 994, 352 and 650 counts for conditions a, b and c, respectively. In relation to the size distribution analysis, counts are reported against the edge length range of 0-200 nm. Although the highest counts for each sample lies around the 35-45 nm range (yellow dotted line through the graphs), the normalised average distribution is displayed as it better represents the size distribution by involving the counts of the bigger particles. Different from the AgNSs, in the case of AgNPrs it

was not possible to assign a proper extinction coefficient to each size range, consequently it was not possible to estimate the impact of the bigger particles on the WA_{max} shifts.

From the distribution analysis, it was possible to notice that the 5 and 10 mL/min conditions revealed similar results, with slightly bigger particles on average for the 5 mL/min synthesis (47.14 nm), against the 43.84 nm obtained with the 10 mL/min setting. However, the standard deviation was better for the latter (15.20 nm), with respect to the 17.40 nm obtained for the 5 mL/min. This was an important finding as it indicated the increased size control achieved with the TFR that was more suitable for the meso- to large-scale production.

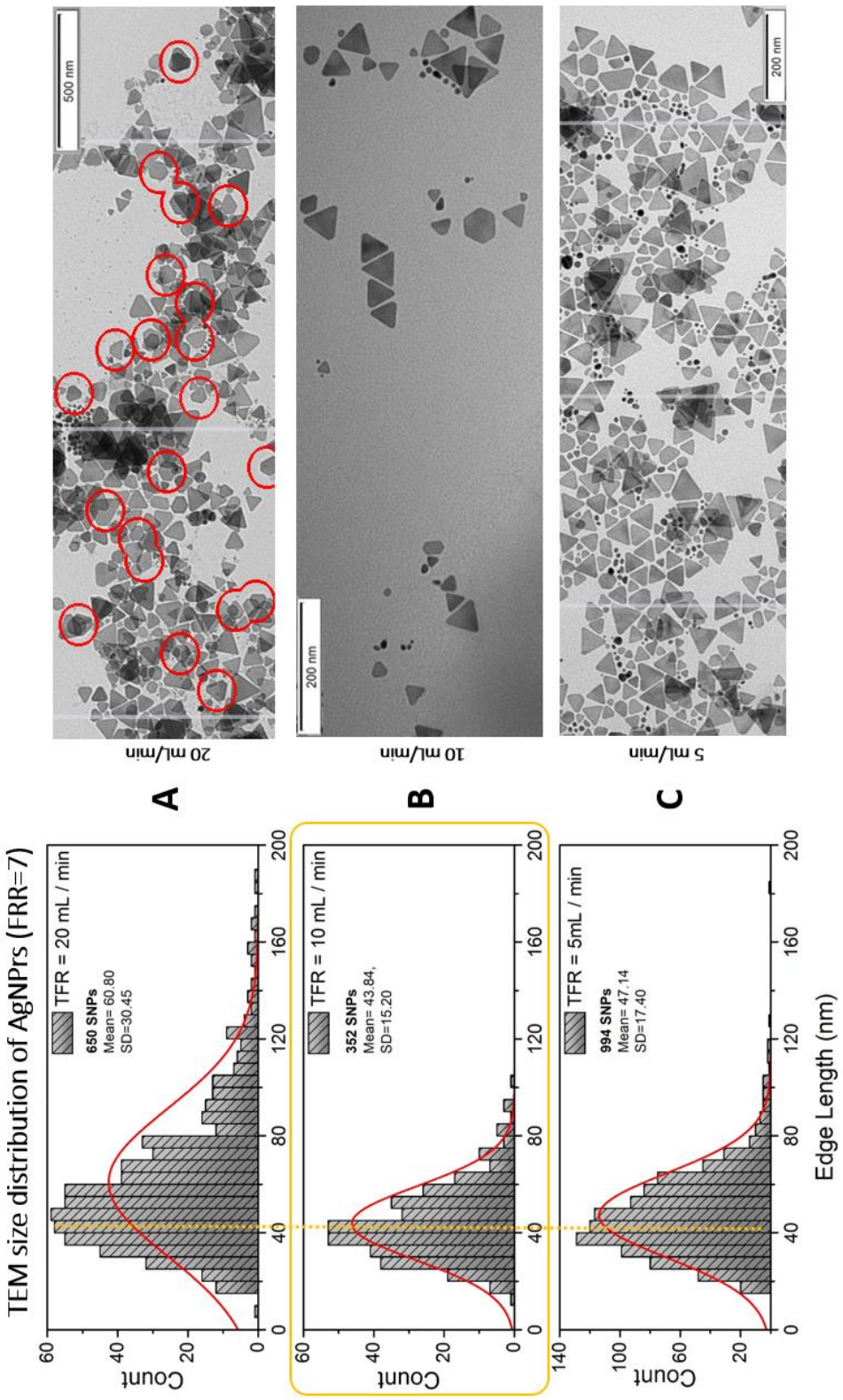

Figure 4.29 Size distribution obtained by measuring the edge length of the AgNPrs from TEM imaging for the 5, 10 and 20 mL/min (a, b, and c). Sizes were measured via software Image-J.

Differently, the 20 mL/min sample showed a broader size distribution. The presence of bigger particles is clearly visible from the histogram and the average size was 60.80 nm, with SD of 30.45 nm, which is notably different from the one obtained from the previous two experiments. This demonstrated a large dispersion in particle size. If counterbalanced with the presence of prisms over 100 nm in edge length, it can lead to a similar optical output of a more monodisperse sample

that averages a smaller size. Moreover, based on the TEM and UV-vis results combined, it was noted that the larger particles tend to break their tips more easily when increasing TFRs. This was observed throughout the experiments, and the red circles shown in Figure 4.29A highlight some examples for the 20 mL/min condition. Broken tips cause shorter edge length of the particles, and consequently, UV-vis shifts. This is mainly suggested by the presence of prisms with asymmetrically broken tips (only one or two, as the three broken tips could also be an unformed prism). Specifically, the proposed cause is related to the effect of the increased pressure within the channel when increasing the flow velocity (i.e. higher TFRs). This is probably due to the fact that AgNPrs have a high aspect ratio (edge length vs thickness), which makes them fragile. Moreover, the broken tip makes a smaller prism itself, contributing to the UV-vis blue shift (shorter edge length). This could be an interesting topic for further investigations, particularly related to find the suitable operative pressure values through CFD calculations to confirm, and eventually minimise, this phenomena.

Finally, the trend in size dispersion increased by augmenting the TFR and, at the same time, larger particles were produced. Particularly, the 50 mL/min protocol, presented in Figure 4.30a, showed the production of particles over 200 nm in edge length with an outstanding example of 337 nm (Figure 4.30b). Clearly, the size dispersion was extremely poor, as indicated by the UV-Vis. However, the efficiency of the reaction for the production of bigger sized particles was proven. Larger prisms are difficult to obtain due to their thickness to length ratio, which makes them fragile. In fact, they tend to break before reaching such dimensions and often breaking the prisms tips, which creates smaller prisms that generate a shift of the absorption spectrum.

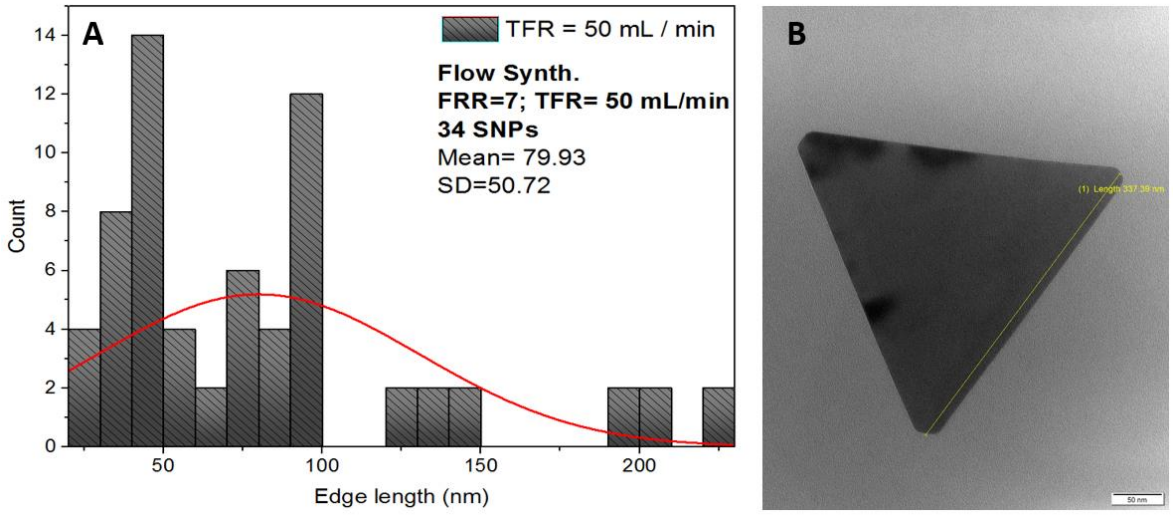

Figure 4.30 (A) Size distribution obtained by measuring the edge length of the AgNPrs from TEM imaging for the 50 mL/min sample. The biggest prisms observed (>337 nm) in edge length (B). The image in B was recreated in its artistic coloured version for participating in the RSC Photography Award 2019 (Appendix C.2).

However, with the improved size distribution being a goal of this research, the selected (Figure 4.29b, yellow selection) TFR condition was considered to be the most suitable for the controlled flow-synthesis of AgNPrs. Therefore, the experiment was then repeated for the last reproduction test before the final comparison with the previously reported batch synthesis (Chapter 2). The third experiment at 10 mL/min showed a highly consistent efficiency, producing AgNPRs having a normalized mean edge length of 45.13 nm and an SD of 15.71 nm (Figure 4.31).

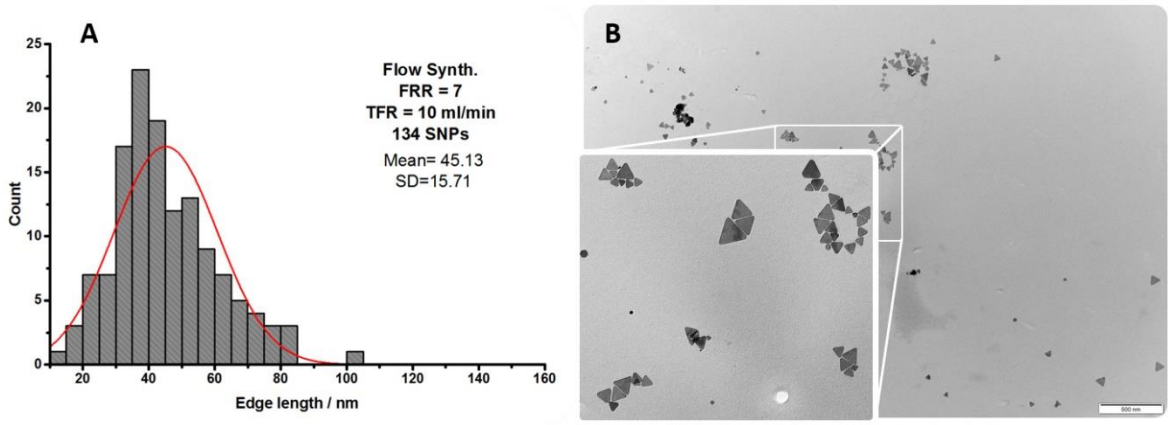

Figure 4.31 Size distribution obtained by measuring the edge length of the AgNPrs from TEM imaging for the third repetition of the 10 mL/min production (A). The corresponding TEM imaging characterisation (B).

Having a comparable triplicate was already a significant improvement with respect to the batch synthesis, which showed different UV-Vis results even though produced following the identical protocol (RT-A2 and RT-A3, described in Chapter 2). On the other hand, the flow-reaction demonstrated a great reproducibility. Most importantly, an interesting outcome of the research related to the size control over the reaction, which can be deduced from the UV-Vis comparison in Figure 4.32.

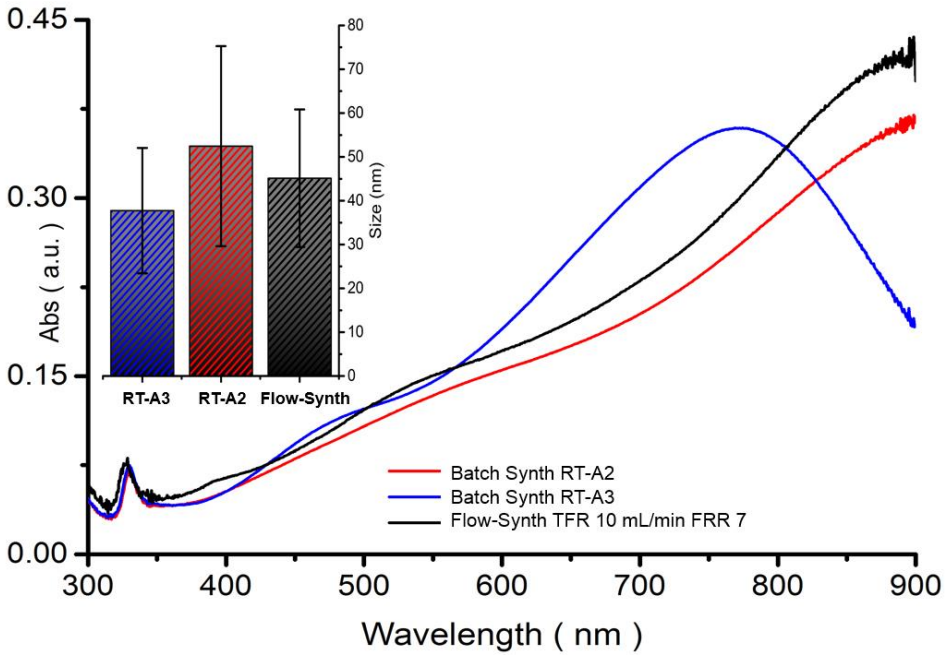

Figure 4.32 UV-Vis spectra of the batch synthesis (RT-A2 and RT-A3, blue and red lines respectively), with respect to the flow-synthesis at TFR 10 and FRR 7 (black line). The insert reports the histograms of the mean and SD for the three samples.

Specifically, when comparing the UV-Vis spectra of the RT-A2 batch synthesis (red line) to that from the flow-synthesis (black line), it was possible to notice that the WA_{max} for both samples laid close to 900 nm. This is ideal for NIR applications as planned. In order for the batch synthesis sample to absorb at said wavelength the average size of the particles was the highest (52.45 nm, section 2.5.6) of the three batch test samples. Differently, in the flow-synthesis method at 10 mL/min, the improved control over the size distribution allowed the smaller average sized particles (45.13 nm) to achieve the same optical result due to the improved SD. In particular, it was possible to obtain over 200 nm in edge length by simply varying the TFR.

4.4 Conclusions

Through this Chapter, the effectiveness and reliability of cost-effective flow-reactors were discussed *via* their application for the synthesis of AgNPs. Reactors were not just tested or used for repeating defined flow-reactions for AgNSs and AgNSs, but they were specifically conceived for the modified and simplified synthetic approach.

The novel 3DP-RMC/Tape was compared with the already developed μMi-REM*Glass, showing comparable performance in the case of the AgNSs production. Differently, the hydrodynamic flow-focusing serpentine (3DP-RMC*Glass) device was employed for the synthesis of AgNPrs. Although the device worked to some extent, deeper studies were carried out and discussed, including CFD simulations, to make further improvements and gain further understanding of the effect of the geometry on the device performance and potentially achieve greater flow-production rates. This step informed the selection of the best materials, flow-channel architecture, chemicals and their concentrations, and operating conditions (TRF and FRR) to allow the most accurate synthesis of AgNPrs by using an economic and easy-to-make reactor. The two-inlet curved serpentine flow-reactor (3DP-RMC*PDMS) was made from an extremely cheap and reusable mould made with a desk 3D printer (U2+). Finally, results were compared with that obtained from the previously performed batch synthesis, demonstrating superior reproducibility and improved size and shape control.

Moreover, it was verified that the novel RIAC approach is a valid solution for nanoparticle synthesis, and with high potential for novel multi-step production approaches.

Finally, the photo-assisted flow-biosynthesis of AgNSs was presented and the advantages and disadvantages of the employed reactors discussed. Also in this case, this approach can potentially open the doors for many photo-assisted reactions towards a facile large-scale production at low costs.

Chapter 5 Flow-synthesis of organic vesicles

5.1 Introduction

Nanovesicles are uni- or multi-lamellar closed layer structures within the nanometre scale, formed by self-assembled amphiphilic molecules enclosing an aqueous core. Many molecules can generate this type of supra-molecular aggregates, conferring them a diverse range of properties.[162] [163] These characteristics make them some of the most suitable products for the transport and release of pharmaceutical agents.[164] Specifically, the main advantage of using nanovesicles for drug delivery is related to their capability to load both hydrophobic of hydrophilic molecules.[162] Moreover, the vast range of compounds that can be used for their formation, unlocks an enormous potential regarding their functionalization,[165,166,167] including the production of genetically engineered vesicles,[168] making them highly tuneable with respect to specific purposes.

Among all possible formulations and families of nanovesicles, liposomes – that derives from the combination of the two Greek words 'Lipos' meaning fat and 'Soma' meaning body[169] - are probably the most employed. Specifically, liposomes are formed by one or more phospholipid bilayers, which can include many other molecules ranging from cholesterol as stabiliser to even proteins as sensors.

The graphical representation in Figure 5.1, adopted from the work of Safinya and Ewert,[165] clearly shows the structure and potential of nanovesicles, in particular of liposomes. Panel A refers to simple liposomes, which can carry hydrophobic molecules within the hydrophobic bilayer portion (red spheres), while hydrophilic molecules into the aqueous core (green star). Differently, Panel B refers to stealth liposomes; in this case, the external layer is covered with bio-polymers, which can be further functionalised for instance with peptides (blue rectangle) aiming at specific targets. Panel C refers to multi-layered cationic liposomes that include DNA complexes (purple rods), and Panel D highlights deep cavitand vesicles that can be used as multicompartmental hosts for sub-nanometer sized guests.[170]

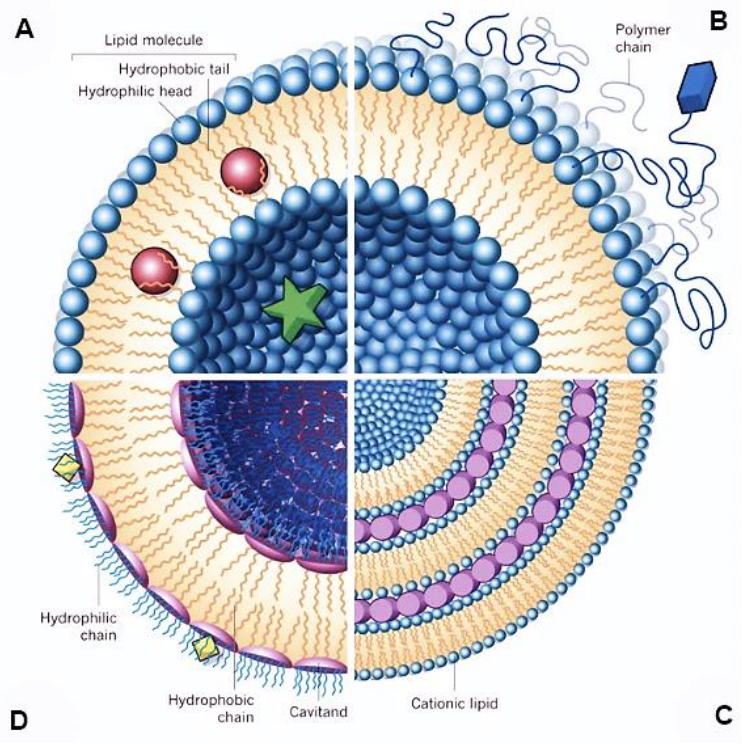

Figure 5.1 Graphical representation of functionalisation alternatives for liposomes (image from Safinya and Ewert 2012)[165]

As presented by Bozzuto and Molinari et al., [171], since their discovery during the 1960s[162] many applications and production methods were developed. In particular, an interesting overview was presented by Anwekar *et al*. [169] to address both advantages and disadvantages of liposomes for drug delivery purposes based on their composition. Briefly, liposomes are suitable drug carriers as they are non-toxic, flexible, biocompatible, completely biodegradable, and non-immunogenic for systemic and non-systemic administrations materials. On the other hand, their solubility can be limited based on the formulation used, and phospholipid might lead to oxidation and hydrolysis-like side reactions. Therefore, many studies were carried out with the aim of finding the right balance between composition and application. Clearly, research has drastically evolved during the

years, and the potential of liposomes became so significant to be used in real-time clinical applications such as cancer therapy, viral vaccines, photodynamic therapy, analgesics and fungal diseases, as discussed in a review by Bulbake *et al*.[172]

Other than lipid-based vesicles, also niosomes and polymersomes are frequently reported in the literature.[173,174] Specifically, the versatility of polymersomes (nanoparticles made of organic polymers), allows them to be largely employed as carriers, due to their colloidal stability and the capacity of integrating a broad range of drugs. Moreover, their circulation time into the bloodstream can be prolonged, for example by creating copolymers with poly(ethylene glycol), thus tuning drug's release.[174]

Differently, niosomes are non-ionic surfactant synthetic vesicles that can be considered as a more economic and stable alternative compared to liposomes, due to their chemical and sometimes physical characteristics. Moreover, they show high potential for technological applications.[173]

Specifically, due to their nature, also niosomes present important advantages such as: a greater physico-chemical stability due to the absence of oxidation-related degradation phenomena; a simpler functionalisation for stability enhancement or bioconjugation; the possibility of using a broad range of surfactant's structures (i.e. single or double acyl chain, different length or saturation); high immunological tolerance. Most importantly, with respect to liposomes, they can be notably more cost-effective to produce.

For these reasons, other than drug delivery, niosomes are nowadays applied in many fields ranging from food industry,[175] to therapeutics, including metal nanoparticles' encapsulations,[176] or even gene delivery.[177]

Similarly to what discussed for inorganic nanomaterials, also in the case of vesicles' formation the size control and distribution are crucial to achieve. For instance, particularly, a clinically acceptable diameter would allow nanovesicles to pass in between cells for reaching the aimed target. Although various methods have been used for their production,[178,179] better size-controlled and monodisperse vesicles can be obtained through flow reactions.[180,181]

Therefore, with the aim to validate the flow reactors developed in this study, and also considering their scientific relevance, liposomes and niosomes were selected as representative organic nanomaterials to be produced using flow reactors.

Categories, mechanisms of formation and application of vesicles were recently summarised in a detailed work by Isalomboto *et al.*[182] This includes emulsomes, enzymosomes, sphyngosomes, transfersomes, ethosomes, pharmacosomes and virosomes, which are lipid-based liposomes

analogous, whereas the non-lipid-based liposomes analogous are aquasomes, bilosomes and niosomes.

5.1.1 Microfluidic approach

Microfluidics provides remarkable advantages for the synthesis of nanovesicles, particularly the ability of obtaining nanoparticels with homogeneous properties, when compared to their analogous bulk counterparts.[113,183] In fact, the fluidic approach represents an efficient and high reproducible solution that enables a precise control of the lipid hydration process, a narrower size distribution, and improvements in the control over particles' composition and size.[180] Furthermore, nowadays microfluidics allows synthesizing hybrid and complex products, such as lipid biomimetic nanoparticles with specific biological properties in a standardized and continuous manner.[181] It has to be considered that thermodynamically stable vesicles only form in the presence of proper surfactants, and membrane-stabilizing agents like cholesterol, at a temperature above the gel/liquid transition (Tt) of the main lipid forming vesicles.[184] The Tt corresponds to the temperature above which phospholipids exist in liquid crystalline phase. In this fluid state, hydrophobic tails of phospholipids are randomly oriented but ready to form closely continuous bilayered vesicles (liposomes). Below the Tt, phospholipids exist in gel state, thus not able to form liposomes.[182] Also the hydrophilic-lipophilic balance value (HLB), is important, particularly to evaluate drugs encapsulation efficiency. Intuitively, this value affects the physico-chemical characteristics of the particles at room temperature (RT), as well as at any stage of their formation. Most importantly, it affects their temperature for the gel-to-liquid transition. It is important to estimate these values because, generally, formulations with great loading capacity show low release rate and stability in solution, and can be solid at RT. This is a further reason for preferring the microfluidic approach, as it allows maintaining an accurate temperature control during the mixing process.[185]

As described in detail by Carugo *et al*., many microfluidic approaches were conceived for the production of liposomes.[183] They include electroformation and hydration, extrusion, pulsed jetting, double emulsion templating, ice droplet hydration, transient membrane ejection, droplet emulsion transfer and hydrodynamic flow focusing (HFF). Clearly, chemical formulations and synthetic procedures define the outcome of the product for all of the cited techniques. However, most of them are not suitable for the production of nanoscale vesicles with the exception of HFF.[186] A further advantage of the latter method relates to the high level of control over the mixing process, which can be ideal for governing synthesis that require reagents with lower solubility. Considering that the HFF route was less explored for the production of niosomes, this approach was further investigated in this study. Moreover, it was designed to provide thermal control with a low-cost setup for continuous-flow production, using one of the most common reagents (Span60).

The HR 3DP-RMC*Glass HFF straight channel was therefore fabricated, and experiments were carried out in collaboration with P. Garcia-Manrique from the University of Oviedo (Spain), leading to a recent publication.[146]

Among the many diverse flow-preparation routes,[112] the production of liposomes was performed *via* solvent exchange mechanism in two inlets continuous-flow reactors, in order to validate the U2+ 3DP-RMC/Tape (section 3.3.3) for organic purposes. In this case, the collaboration was carried out with the colleague F. Yanar. and results were published.[139]

5.2 Materials and methods

5.2.1 Flow synthesis of liposomes *via* the two inlets straight channel 3DP-RMC/Tape

The same experimental set-up adopted for the production of AgNSs (Chapter 4, section 4.3.1.1) was used for the synthesis of liposomes (Scheme 5.1). In this case, Phospholipon® 90G (lipids) and purified phosphatidylcholine from soybean lecithin were provided by Lipoid GmbH (Germany). Pure ethanol (99.9%) was purchased from Sigma-Aldrich Company Ltd. (UK).

For the flow-synthesis, a 100 mM ethanol solution of lipid was prepared. Luer Lock syringes 20 mL (BD Plastipak) were purchased from BD (Becton, Dickinson and Company, UK). Syringe A was filled up with Milli-Q water and connected to the first inlet, whereas the ethanol solution containing lipids was introduced through the second inlet (Syringe B) (Scheme 5.1). The lipid concentration and FRRs were selected based on the experiments performed by F. Yanar, who worked for adapting several batch conditions (specifically the ethanol injection method),[183] to perform the continuous flow-production. Moreover, such high concentration appeared to be more suitable for a better characterisation. All the syntheses were performed in triplicate.

Scheme 5.1 Schematic representation of the setup. Two syringes connected to the two curved inlets; outlet connected to the vial for sample collection.

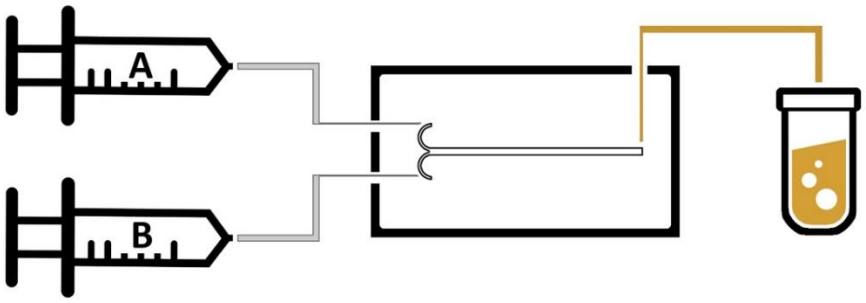

With respect to the operating conditions, the TFR was varied at the values of 1, 3 and 6 mL/min, in order to demonstrate the durability of the device at higher production rates, while the FRR was kept constant at 25.

Computational fluid dynamic analysis was performed using the same criteria and conditions described in Chapter 4 (section 4.2.4).

5.2.2 Flow synthesis of liposomes using reactor-in-a-centrifuge (RIAC): optimising the formulation

RIACs were also employed and tested for the production of liposomes, prior to the synthesis of AgNSs, following the development timeline presented in section 4.3.1.2. This helped in identifying reactor performances.

In order to identify a suitable protocol for producing liposomes, different parameters were initially evaluated, including the lipid formulation and concentration, the volume of fluids in the reservoirs, the volume of water at the bottom of the centrifuge tube, the centrifugation time and relative centrifugal force (rcf). Ultimately, the hereby described final formulation was carefully evaluated over 15 types of tests (as further discussed in the following results section).

Finally, Liposomes were prepared by using phosphatydilcoline (PC) (Lipoid GmbH, Germany), dimethyldioctadecylammonium bromide 98% (DDAB) (Sigma-Aldrich Co., USA) and ethanol absolute (Fisher Scientific Ltd., UK). Milli-Q water was collected using the QGard purification filter, connected to the Milli-Q Gradient A10 system (Merck Millipore, USA). The final adopted ratio of 9:1 PC:DDAB was used for the 20 , 40, 60 and 80 mM solution (referring to the PC concentration).

Moreover, a two-step production procedure was conceived for the selected PC:DDAB ratio. Liposomal samples were prepared by adding Milli-Q water (2 mL) into one reservoir, and the ethanol solution containing the selected PC:DDAB concentration (2 mL) into the second reservoir, followed by an additional 6 mL of water at the bottom of the centrifuge tube where the RIAC was hosted. To prepare the desired concentration, the stock solutions were obtained by weighing the required amount of each compound and dissolving it in ethanol. The obtained solution was then filtered using a 0.20 µm pore size Millex®-GN syringe filter (Merck Millipore Ltd., UK).

5.2.3 Flow-synthesis and characterization of niosomes using the flow-focusing 3DP-RMC*Glass reactor under controlled temperature

The hydrodynamic flow-focusing reactor, manufactured with the HR OC350 by 3DP-RMC*Glass method (section 3.3.4), was adopted for the synthesis of noisomes under thermal control. Polytetrafluoroethylene (PFTE, 0.5 mm I.D.) pipes (Cole-Parmer, UK) were used for the peripheral flow connections of inlets and outlet to the syringes and the collecting vial (2.5 mL for each experiment). Specifically, Luer lock syringes (Becton, Dickinson and Company, UK) of 1, 10 or 20 mL, were connected to NE-300 syringe pumps (NEW ERA Pump Systems Inc., USA), and a T junction was used in order to employ only one syringe for the two lateral streams.

Once the reactor was made and effectively sealed, the following steps were performed for the realisation of the thermal chamber. A box-shaped geometry and a separate lid were entirely 3D printed in PLA with the U2+ printer to create a thermal-bath. Two tubes were connected to opposite sides of the box, in order to create an inlet and outlet for the warmed water to flow through. In order to allow the visual control and image capturing with the inverted microscope (IN200TAB series, AmScope, USA), a microscope glass slide of 50 x 70 mm (Corning®) was glued at the designed aperture at the bottom of the box. A transparent plastic cap, with apertures for the connecting pipes, was adapted to close the lid. The recirculation system for temperature controlling (F12-MC, Julabo GmbH, Germany) was connected to the custom thermal-bath, and a peristaltic pump (MasterFlex®, Cole-Parmer Instruments Company, USA), was used to permit the recirculation of the warm water. A sensor probe (Testo 110, Testo SE & Co., Germany) was introduced into the thermal chamber for digital temperature monitoring. The reactor was then connected to the syringes and entirely embedded into the custom-made thermal bath for the reaction. An overview of the setup, including a legend indicating each component, is shown in Figure 5.2.

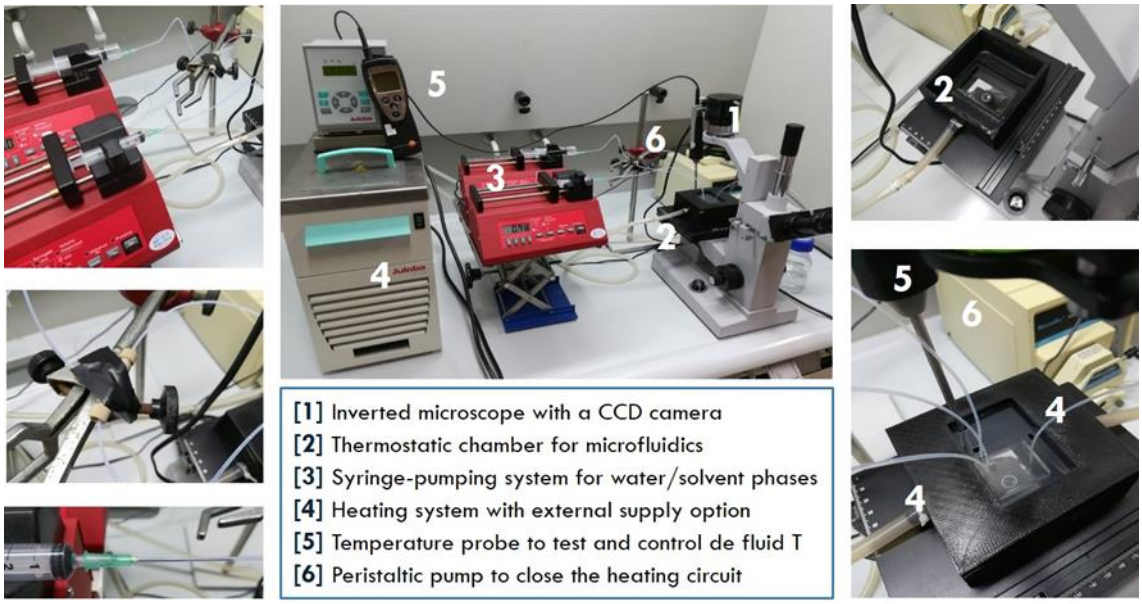

Figure 5.2 Setup consisting of: 1 inverted microscope with CCD camera, 2 thermostatic chamber, 3 syringe-pumps of the flow-synthesis, 4 heating system, 5 temperature prob, 6 peristaltic pump for the thermal bath. Image from Garcia-Manrique et al [146]

For achieving the most uniform temperature, four thermic resistant plastic spacers (3 mm in length), were glued at the bottom corners of the glass-base of the reactor, allowing the warm water to flow underneath the reactor, thus minimising thermal dispersion.

Regarding the reagents' preparation, stock solutions (50 mM) were used to prepare 5 and 20 mM solutions of Span® 60:cholesterol and Span® 20:cholesterol (1:0.5 molar ratio) in organic solvent.

Specifically, due to its good miscibility in aqueous buffer (PBS, 10mM pH 7.4), ethanol absolute was used. Representative results for the 5 mM solution are herein reported.

The device was introduced into the thermal-bath and the temperature increased until the final operative value was reached. Differently from what performed for the hydrodynamic flow-focusing synthesis of AgNPrs, for the production of niosomes the aqueous buffer was introduced from the two lateral inlets whereas the ethanolic solution containing the niosomes building blocks was injected through the central inlet.

Particularly, three different TFRs were studied (50, 100 and 200 µL/min), at five FRRs of 5, 15, 25, 35 and 50 (aqueous:organic). Based on the properties of the material, with respect to the temperature conditions, the Span® 20:cholesterol formulation was operated at 30, 40, 50 and 60 °C, whereas the Span® 60: cholesterol was only injected at 50 °C. Each condition was tested twice, and each batch was measured by triplicate.

As presented below, the representative operative conditions are discussed in order to validate the efficiency of the setup and the reliability of the developed reactor and customised operative conditions. Further details can be found in the published outcome of the research.[146]

5.2.4 Characterisation of the produced vesicular systems

A dynamic light scattering (DLS) technique was used to measure the mean diameter (z-average), the polydispersity index (PDI), and zeta potential of all liposomal and niosomal formulations using the Zetasizer Nano ZS (Malvern, UK).

The produced samples (1 mL) were transferred into a disposable Fisherbrand™ polystyrene cuvette (Fisher Scientific Ltd., UK), and prior to the measurement, they were equilibrated for 120 seconds (in order to reach a temperature of 21 °C). Each sample was measured over three runs, and up to twelve scans were performed for each run. The average liposome size (expressed in terms of Z-average) and size distribution (expressed in terms of polydispersity index, PDI) was obtained from the Zetasizer Software (Malvern Instrument Ltd, U.K., version 7.12), considering the refractive index of 1.33, and absorption coefficient = 0.

For liposomes produced with both U2+ 3DP-RMC/Tape and μMi-REM*Glass reactors (Phospholipon® 90G lipids and purified phosphatidylcholine from soybean lecithin), a stability test was also performed over time for samples stored at two different conditions: 4 °C and 25 °C. Measurements were performed every 5 days for a total 30 days.

In the case of niosomes produced *via* HFF with the HR 3DP-RMC*Glass reactor (Span® 20:cholesterol), a 173° backscatter detector and disposable low volume cuvettes (Malvern Instruments Ltd, Malvern, UK) were employed.

Moreover, other than DLS measurements, in the case of liposomes produced through the U2+ RIAC (phosphatydilcoline and dimethyldioctadecylammonium bromide), also a negative-stained transmission electron microscopy characterisation was accomplished, in collaboration with Dr. J. Owen from Oxford University. Specifically, an aliquot of the nanovesicle solution (10 μL) was placed on a 200-mesh Formvar-coated copper grid (Agar Scientific, Stansted, Essex), and allowed to air-dry. The sample was then negatively stained with 2% w/v uranyl acetate, and allowed to air dry. A Tecnai (T12, FEI, Hillsboro, OR) was used for image acquisition.

5.3 Results and discussion

5.3.1 Flow-synthesis and characterization of liposomes: 3DP-RMC/Tape vs µMi-REM*Glass straight reactors

In Chapter 4, the design, fabrication and application of flow-reactors with 3DP-REC/Tape for the synthesis of AgNSs were presented. Moreover, the comparable effectiveness of this novel approach with already known techniques (µMi-REM*Glass) was demonstrated.

Building on these developments, the application of the 3DP-REC/Tape reactor was extended by validating its usability for organic nanoparticles' synthesis, in particular, the continuous-flow synthesis of liposomes. Specifically, the lipid concentration was selected and adapted to the design architecture, with the aim to demonstrate the ability of cost-effective and easy-to-make flow-reactors to produce liposomes of clinically-relevant size and mass, based on the findings previously shown in the literature. [113186183]

The synthesis was also calibrated, in terms of TFRs, to demonstrate its potential for scaled-up production, which was significantly higher than those typically used in microfluidic reactors.[151] Also in this case, the same architecture was recreated with two different manufacturing techniques for comparison.

Figure 5.3 shows the size (z-average) and polydispersity index (PDI) of liposomes produced at TFR values of 1, 3, 6 mL/min and at a fixed FRR of 25.

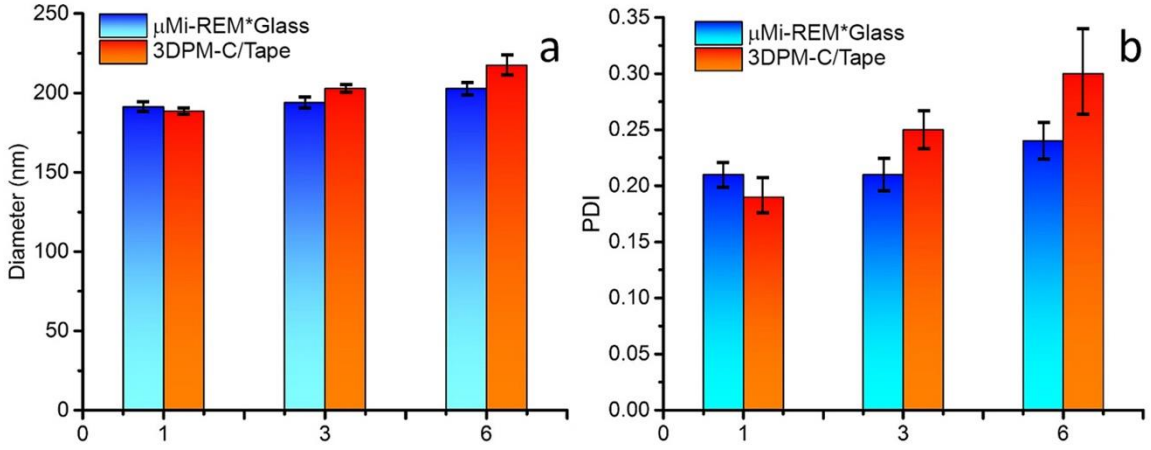

*Figure 5.3 Comparison of liposome size and dispersity. Size (z-average) (a) and dispersity (PDI) (b) of liposomal formulations produced by µMi-REM*Glass and 3DP-RMC/Tape reactors. Each experiment was performed at TFR of 1 ml/min, 3 ml/min and 6 ml/min, at a fixed FRR of 25. Data are reported as the mean of three independent samples, with the corresponding standard deviation.*

Notably, results showed that liposome size and dispersity were very similar for both reactors at all hydrodynamic conditions investigated. For instance, liposomes produced with the 3DP-RMC/Tape and μMi-REM*Glass reactors at TFR = 1 ml/min and FRR = 25, had a diameter of 188.61 ± 1.62 nm and 191.37 ± 3.19 nm, respectively. Moreover, liposome size was in all cases smaller than 250 nm, which demonstrated the possibility to obtain the desired clinically acceptable sizes.

Results were also consistent in terms of size distribution as shown by the representative DLS data in Figure 5.4, obtained for a sample produced using the μMi-REM*Glass reactor, operated at TFR = 1 mL/min (FRR = 25). The distribution appeared uniform and symmetric, clearly demonstrating the presence of a single population.

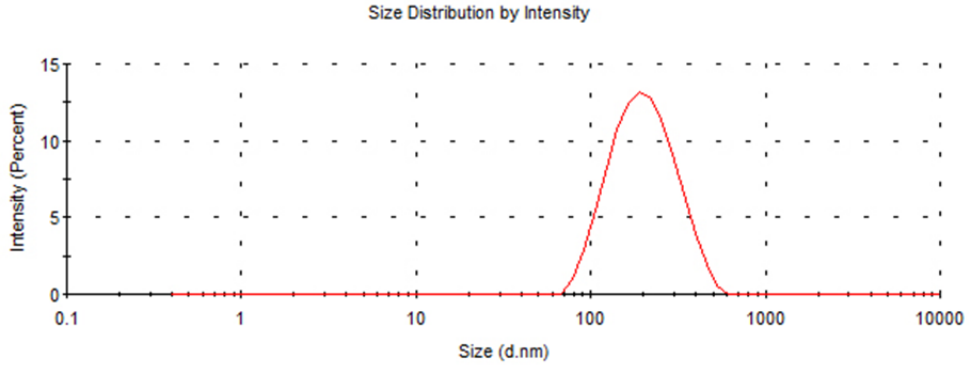

Figure 5.4 Representative liposome size distribution obtained by DLS, at TFR of 1 ml/min and FRR of 25. All liposomes have mean hydrodynamic radius between 63 and 615 nm. The mean diameter is of 190 nm, with a PDI of 0.180

Nonetheless, referring once more to Figure 5.3, by increasing the TFR from 1 to 6 mL/min, a slight increase in liposome diameter can be observed for both devices. This appeared coherent with the numerical results obtained by the CFD simulations, which highlighted differences in the mixing index at the different flow regimes investigated (Section 5.3.1.1).

Furthermore, Figure 5.3b highlights the relatively small size dispersity of the produced liposomes. The PDI slightly increased when increasing the TFR from 1 to 6 mL/min. This is a trend that can be observed for both manufacturing methods. However, liposomes produced by the 3DP-RMC/Tape reactor had a larger mean dispersity at the higher flow rates investigated. Values changed from 0.2 to 0.25 for the µMi-REM*Glass, and from 0.20 to almost 0.35 for the 3DPM-C/Tape. This could be potentially attributed to a combination of factors that include the surface roughness of the PDMS channels, originating from the PLA mould, and the effect of the junction geometry as further explained in the CFD section 5.3.1.1. Nevertheless, in all cases liposomes of clinically relevant controlled size, specifically <230 nm, were successfully produced *via* the cost-effective method.

In addition, the diameter of the produced liposomes was investigated every 5 days over a month after their production.

The selected samples were produced through the 3DP-RMC/Tape reactor at FRR = 25 and TFR = 1 mL/min. This experiment was carried out in order to investigate liposomes' stability over time when stored at two different temperature conditions of 4 and at 25°C. Figure 5.5 displays the diameter variation (expressed in %) vs time (days). It can be noted that liposomes stored at 4 °C increased in size over time, until reaching a maximum % increase of approximately 15% after 30 days. Although referring to different Phospholipon90G-based liposomal formulations, these results are comparable with the ones previously reported by Briuglia *et al*.[187] The increase in vesicle diameter could be attributed to sterical hindrance of bilayer stability [188] or aggregation, which may result in liposomes' coalescence. [189] In contrast, the size of liposomes stored at 25°C showed only a very slight increase over time.

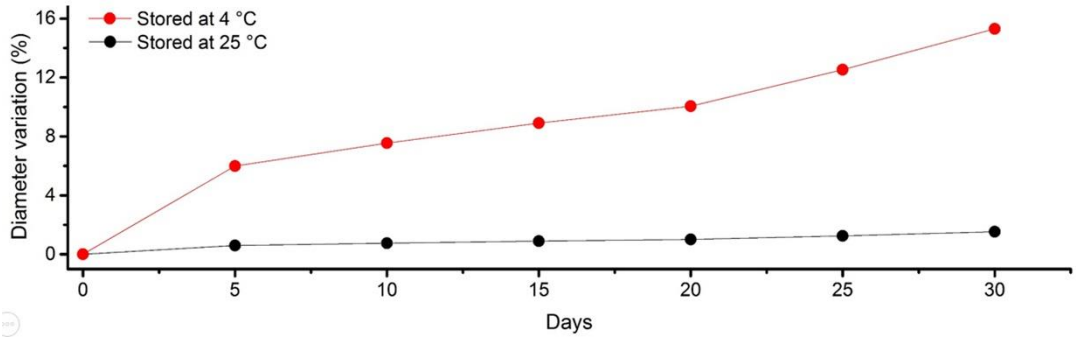

Figure 5.5 Size stability of liposomal formulations produced by 3DP-RMC/Tapereactor, at FRR of 25 and TFR of 1 ml/min. Liposome size was measured every 5 days and up to 30 days, at storage temperatures of both 4°C and 25°C

Moreover, the obtained zeta potential value of -15.06 mV, obtained from liposomes produced using the 3DP-RMC/Tape rector at FRR of 25 and TFR of 1 mL/min, was also coherent with the published literature results.[190]

5.3.1.1 CFD simulations

CFD simulations, carried out in collaboration with Dr. Ali Mosayyebi, were performed in order to gain insights into the flow behaviour and the transport of chemical species within the reactor, and to gain information for the interpretation of the experimental findings.

The mixing index, used for defining the efficiency of mixing between water and ethanol,[191] was calculated under different fluidic conditions employed for the production of liposomes (Figure 5.6).

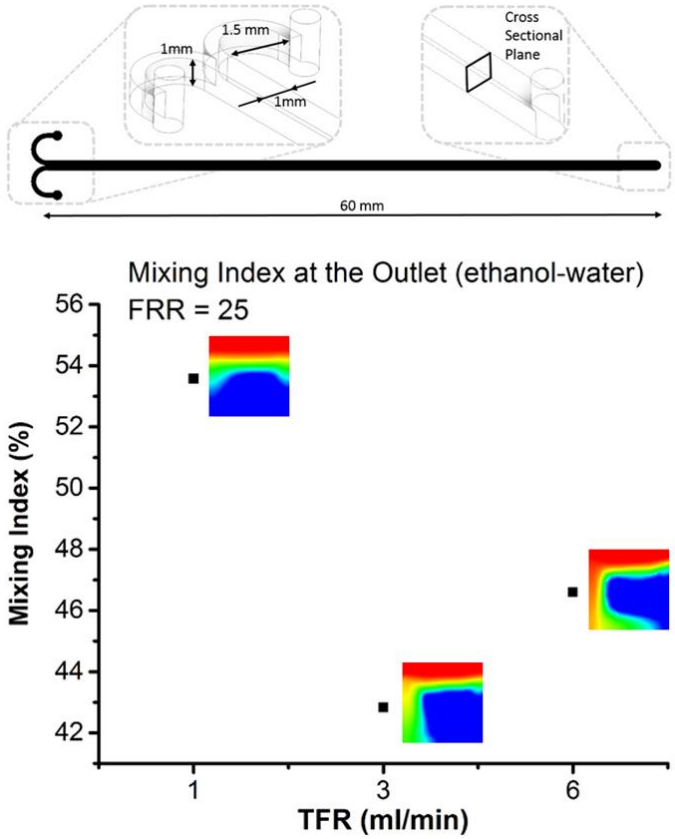

Figure 5.6 Mixing index calculated over a cross sectional plane in the vicinity of the outlet surface (cross section plane above). Results refer to ethanol-water at TFRs of 1, 3 and 6 mL/min and FRR of 25. Contours of ethanol mass fraction are reported next to each data point.

It shows that the increase in TFR from 1 to 6 mL/min, at a fixed FRR of 25, resulted in a reduction of the mixing efficiency between ethanol and water due to the shortened residence time

Initially, this was attributed to the roughness of the channel. However, considering that the increasing PDI trend can be observed for both manufacturing methods (as earlier described in Figure 5.3), this is may not be the only contributing factor. It is possible that, since the cross-section of the inlet channels is the same but the volumetric flow rate is different, the average fluid velocity between the two inlet channels will be different, and this might have caused mixing variations. Although further investigations can be performed, these results demonstrated the comparable performance of the novel 3DPM-C/Tape manufacturing method with the established µMi-REM*Glass.

5.3.2 Flow-synthesis and characterization of liposomes: reactor-in-a-centrifuge (RIAC)

Various formulations were initially tested in order to identify a suitable protocol for the preparation of liposomes using RIACs. Figure 5.7 shows the average liposome diameter and dispersity (PDI) values of liposomes produced at varying lipid concentration, type of stabilizing agent, centrifugation time, volume of liquid in the reservoirs, and relative centrifugal force (rcf).

Initially, lipid solutions in ethanol at different concentrations and ratios of phosphatydilcoline (PC) and dimethyldioctadecylammonium (DDAB) or cholesterol (Chol), were pipetted into one reservoir of the spiral-RIAC. Water was added into the second reservoir, and different operational conditions were verified (Figure 5.7a, formulations 1-6). Among those, the device was also evaluated under static conditions, in which fluid flows were driven by gravity-only (in the absence of frit filters). Two different stabilising agents were evaluated in these static tests (Figure 5.7a, formulations 3 and 5). Initial results produced vesicles with a relatively large diameter (>500 nm, formulations 1 and2). On the other hand, increasing the rcf and the PC concentration resulted in lower liposome diameter (Figure 5.7A, formulations 1-2, 4, 6). However, the liposome dispersity did not show a clear trend.

Overall, from the results reported in Figure 5.7A, the 9:1 PC:DDAB formulation was identified as the preferred one.

Subsequently, the effect of sample dilution was investigated, by adding an amount of water at the bottom of the centrifuge tube as well (formulation with bottom dilution, Figure 5.7B, formulations 7-15). This approach not only diminished the ethanol concentration in the final liposomal suspension, but it was found that also significantly reduced both liposome size and dispersity. Using a dilution volume of 6 mL led to liposomes smaller than 300 nm (PDI < 0.4), as shown for formulations 11-14 (Figure 5.7B). A higher dilution volume (9 mL) was also tried, which produced vesicles having a slightly smaller diameter and lower dispersity (Figure 5.7B, formulation 15 vs 11). However, the minor differences in liposome size and dispersity did not justify the reduction in lipid concentration due to the greater volume of water, thus it was not ideal for clinical uses.

Based on these findings, it was hypothesised that liposomes formed within the RIAC's mixing channel due to rapid mixing between ethanol and water (first step), and were subsequently conveyed into the additional volume of water located at the bottom of the centrifuge tube (second step).

The resulting liposome dilution may minimise the detrimental effects of high centrifugal forces, which could cause liposome aggregation or rupture, thus compromising the method's reproducibility and tunability.

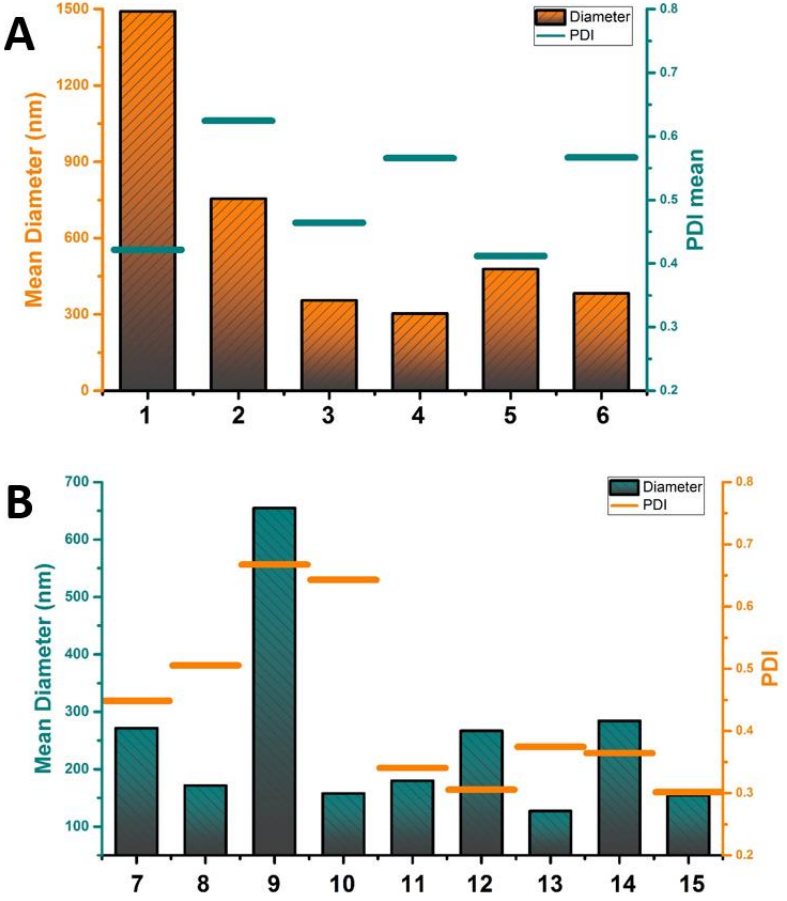

Figure 5.7 Preliminary formulation tests, without (A) and with (B) bottom dilution.

FORMULATIONS WITHOUT BOTTOM DILUTION

1= PC 4 mM (28 rcf/4 min/3 mL per res)
2= PC 4 mM (28 rcf/4 min/2 mL per res)
3= PC 18 mM + DDAB 2 mM (gravity/1 mL per res)
4= PC 18 mM + DDAB 2 mM (112 rcf/4 min /2mL per res)
5= PC 18 mM + Chol 2 mM (gravity/ 1mL per res)
6= PC 90 mM + DDAB 10 mM (447 rcf/2 min/4 mL per res)

FORMULATIONS WITH BOTTOM DILUTION

7= PC 90 mM + DDAB 10 mM (447 rcf/2 min/4 mL per res/3 mL bottom)
8= PC 40 mM + DDAB 4.4 mM (447 rcf/2 min/4 mL per res/3 mL bottom)
9= PC 90 mM + DDAB 10 mM (28 rcf/4 min/4 mL per res/3 mL bottom)
10= PC 40 mM + DDAB 4.4 mM (447 rcf/2 min/4 mL H_2O/2 mL EtOH/4 mL bottom)
11= PC 40 mM + DDAB 4.4 mM (1789 rcf/2 min/2 mL per res/6 mL bottom)
12= PC 60 mM + DDAB 6.7 mM (1789 rcf/2 min/2 mL per res/6 mL bottom)
13= PC 20 mM + DDAB 2.2 mM (1789 rcf/2 min/2 mL per res/6 mL bottom)
14= PC 80 mM + DDAB 8.9 mM (1789 rcf/2 min/2 mL per res/6 mL bottom)
15= PC 40 mM + DDAB 4.4 mM (447 rcf/2 min/2 mL per res/9 mL bottom)

Based on the preliminary tests shown in Figure 5.7B, the 6 mL bottom dilution formulation, with a 2 mL volume per reservoir and a 9:1 PC:DDAB ratio, was identified as the most suitable operating condition for further investigations, and it was tested over different reagents' concentrations.

5.3.2.1 Liposome production: effect of lipids concentration, channel geometry, and centrifugation parameters.

Under the identified conditions, in terms of formulation, volume ratios and protocol, different physical parameters were varied to investigate size-controlled production of liposomes using the RIACs developed (as detailed in section 3.3.5). The key operating parameters included the initial concentration of lipid and stabilizer, mixing channel geometry (straight vs. spiral), relative centrifugal force (range: 447-1789 rcf), and frit mesh size (0.5–2.0 μm). Results reported in Figure 5.8 showed a significant effect of the mixing channel geometry on the average size of liposomes obtained at varying initial lipid concentrations (PC range 20-80 mM, at a fixed PC:DDAB molar ratio of 9:1). Although the straight-RIAC generated liposomes having a lower mean diameter overall, liposome dispersity was consistently greater (PDI >0.5), demonstrating a lower control on the formation of the nanovesicles, thus not suitable for the aimed reproducibility for clinical purposes compared to the spiral design (Figure 5.8B). The PDI is an indication of particle quality, with respect to the size distribution, for which a smaller number represents a narrower size distribution.[192]

In contrast, liposomes obtained using the spiral geometry had significantly lower dispersity. This was likely due to the rapid advective mixing between ethanol and water within its channels, caused by the curved architecture. The longer residence time and improved mixing in this case, the more efficient formation of liposomes was obtained before dropping into the water solution at the bottom of the reservoir. Furthermore, the spiral-RIAC provided adequate control over liposome diameter (from 100-200 nm to 250-325 nm) with increasing the initial lipid concentration (from 20-40 mM to 60-80 mM) (Figure 5.8A).

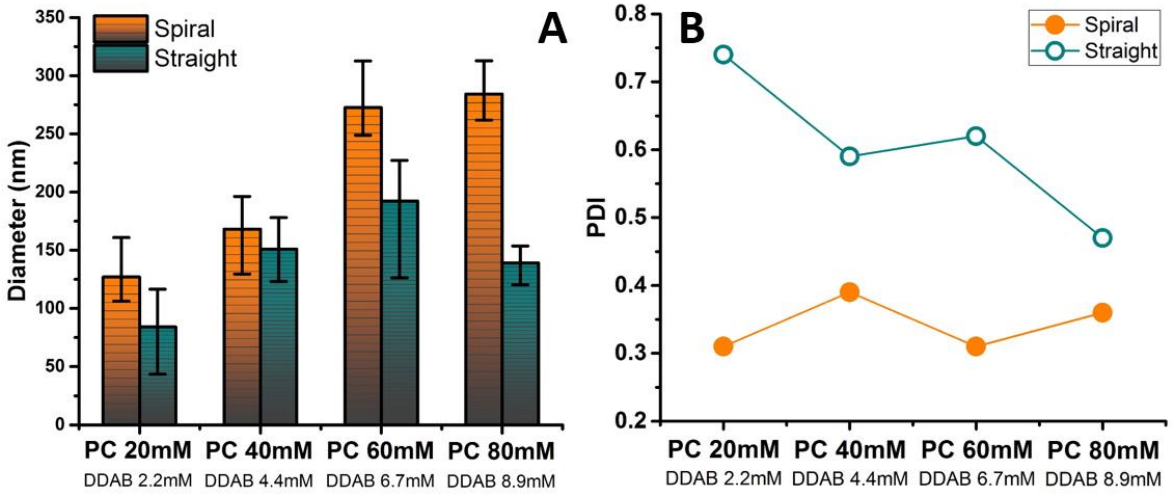

Figure 5.8 Average liposome diameter (including max-min values over four repeats), and average PDI for the spiral vs. straight RIACs (frit size: 2.0 μm). (A) Comparison of four different initial PC:DDAB concentrations (PC range 20-80 mM, 9:1 molar ratio with DDAB) operated at 1798 rcf for 2 minutes, (B) and the respective PDI.

Although liposomes produced from PC:DDAB at 20:2.2 mM had the lowest diameter and dispersity, a more in-depth analysis of their size distribution, from the DLS graphs, revealed the presence of multiple peaks. Figure 5.9 demonstrates the effect of liposome size distribution on the measured average liposome size. Liposomes produced using the PC:DDAB 20:2.2 mM formulation resulted in an overall smaller average diameter of 127 nm (Figure 5.8A). However, when observing the size distribution graph in Figure 5.9A, the presence of at least two vesicle populations is evident.

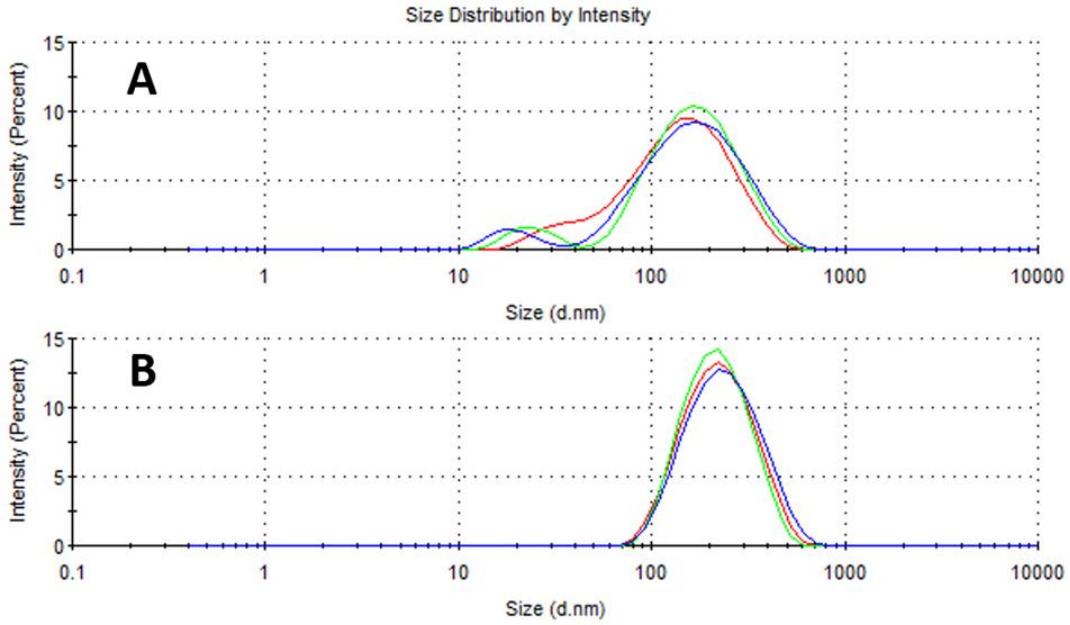

Figure 5.9 Size distribution measured from DLS, for comparison between: A) PC:DDAB 20:2.2 mM and B) PC:DDAB 40:4.4 mM. In both cases, centrifuge settings were 1789 rcf for 2 minutes.

In contrast, although presenting a slightly larger average diameter of 168 nm, the size distribution of liposomes produced using the PC:DDAB 40:4.4 mM formulation showed a single and narrower population (Figure 5.9B). The latter was also representative of the distribution for the PC:DDAB 60:6.7 and PC:DDAB 80:8. mM formulations. Therefore, a PC:DDAB concentration ratio of 40:4.4 mM was selected as the preferred formulation, and subject to further investigations. Notably, the final lipid concentration under these operating conditions was significantly greater than the one typically used in microfluidic reactors, and was within the clinically accepted range.[183]

Moreover, additional experiments were carried out to investigate the effect of g-force on liposome dimensions. In these experiments, the chosen formulation was tested for both reactors at 447, 1006 and 1789 rcf (frit mesh size = 2.0 μm). The results are reported in Figure 5.10. Consistently with the previously obtained trend, the straight-RIAC formed liposomes with lower mean diameter (between 100 and 150 nm, Figure 5.10A); nevertheless, liposome size dispersity was significantly greater compared to the spiral-RIAC (Figure 5.10A).

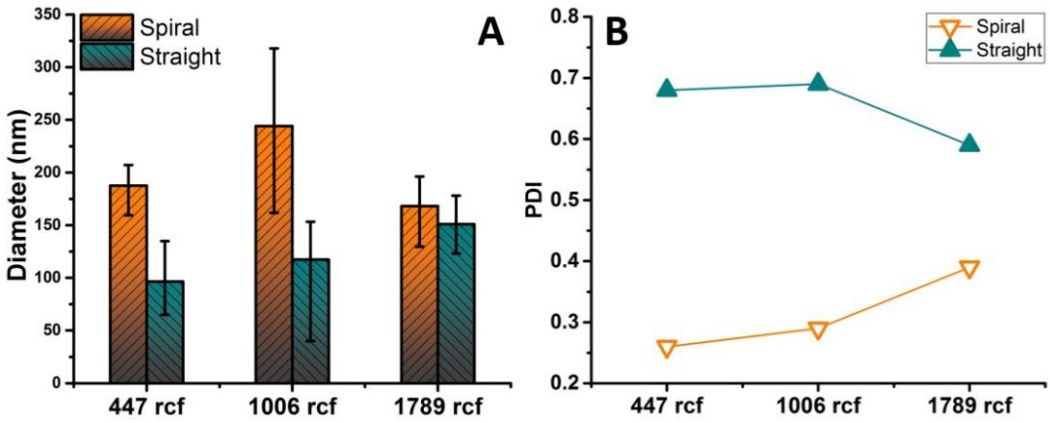

Figure 5.10 Average liposome diameter (including max-min values over four repeats), and average PDI for the spiral vs. straight RIACs (frit size: 2.0 μm). (A) Effect of the g-force (range: 447-1789 rcf) on liposome diameter, for the selected PC:DDAB (40:4.4 mM) formulation, and (B) the respective PDI values.

From the obtained values it was possible to deduce that, operating the device at 447 rcf for 2 minutes resulted in the highest reproducibility and the lowest liposome dispersity (PDI = 0.26), for the selected formulation of PC40:DDAB at 40:4.4 mM (Figure 5.10).

Furthermore, investigation was carried out on the effect of frit pore size (0.5 μm vs. 2.0 μm) using the spiral RIAC and the selected lipid formulation. From Figure 5.11 it is possible to observe that RIACs having frits with different mesh size produced liposomes with comparable mean diameter and dispersity. Moreover, comparing results shown in Figure 5.10A and Figure 5.11A - obtained under the identical operating conditions (orange histograms) - demonstrated high experimental reproducibility. The frit pore size however, appeared to influence the reproducibility of the

production method, with the 0.5 μm frit offering superior performance with respect to the obtained max-min values (Figure 5.11A).

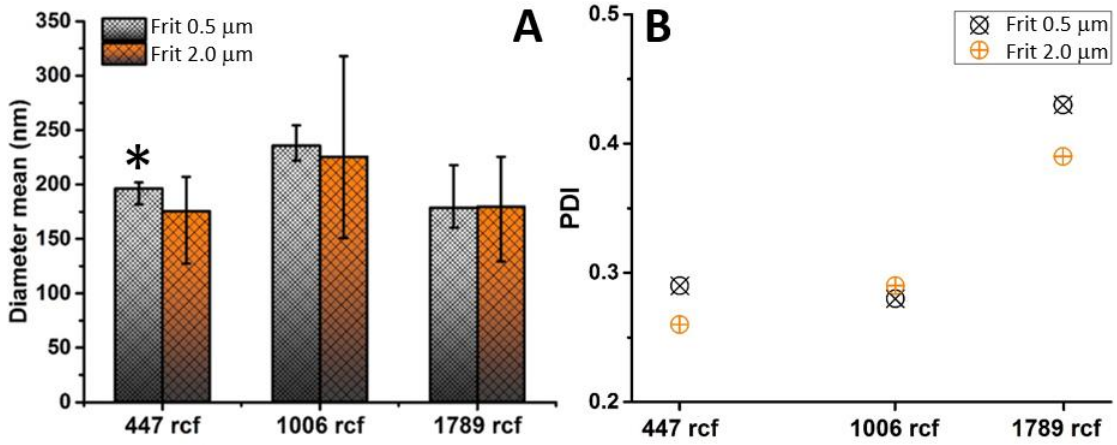

Figure 5.11 Effect of frit mesh size on the average diameter (A) and dispersity (B) of liposomes produced using the spiral-RIAC at different rcf values.

Finally, in order to confirm the clinically acceptable diameter, samples produced at 447 rcf (indicated with the * in Figure 5.11A), were selected for TEM characterization. The negative-stained technique allows to imaging the organic vesicles in Figure 5.12 with respect to a scale bar of 500 nm. The imaging characterisation confirmed the DLS results by highlighting the absence of liposomes > 230 nm in diameter.

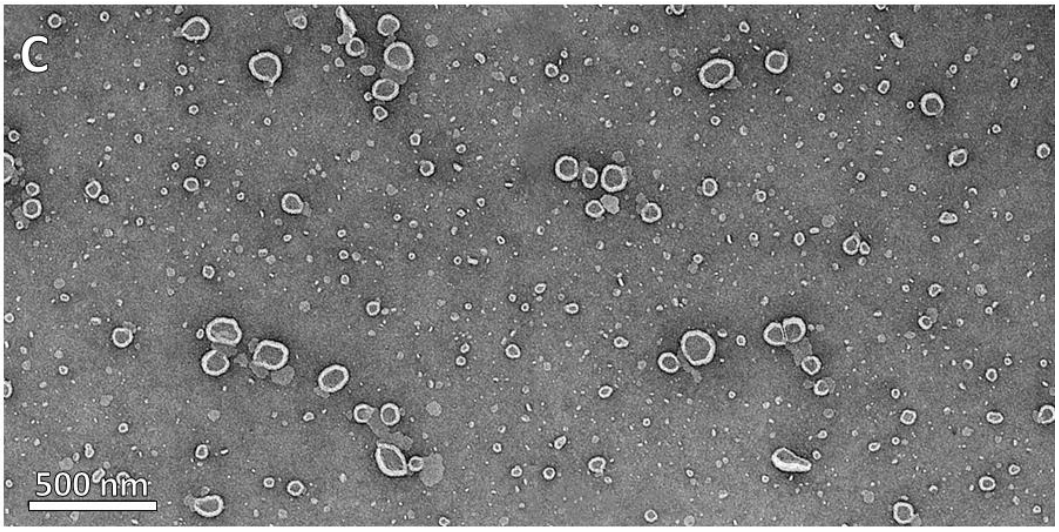

*Figure 5.12 TEM images of two different areas merged together of the representative sample (indicated with * in Figure 5.11) produced under the following conditions: 2 mL of PC:DDAB 40:4.4 mM in EtOH (reservoir 1); 2 ml of water (reservoir 2); 6 mL of water at the bottom of the centrifuge tube; centrifuge parameters: 447 rcf for 2 minutes. Scale bar = 500 nm.*

Although many further experiments and improvements are needed, the cost effective production of liposomes through a novel approach was demonstrated. This developments was also presented at the microTAS conference in Taiwan,[145] receiving great interest from the scientific community.

5.3.3 Flow-synthesis and characterization of niosomes with 3DP-RMC*Glass reactors under controlled temperature

The production of niosomes was performed so as to achieve two goals: (i) the validation of a cost-effective flow reactor that can be reliable to use when submerged into a thermal bath, and (ii) improving the HFF production of such nanovesicles. To achieve these, a reagent commonly-used for the production of non-ionic surfactants (Span® 60),[193] was selected in order to overcome the limit of its low solubility at RT. However, once formed, Span® 60 have the advantage that at room temperature, behave as gelators by themselves. Moreover, previous studies in the literature only covered the flow-production of niosomes with Span® 20 and Span® 80 within the -30 to 25 °C range.[194]

Therefore, a specific watertight flow-reactor was conceived and tested. As previously described in (section 3.4.1.3), this was fabricated through the HR 3DP-RMC*Glass manufacturing process with a three-inlet flow-focusing straight geometry.

The principle was based on the advantage of the HFF approach, where the organic phase stream was contained between the two aqueous side streams. This allowed a diffusion process between the aqueous and organic solvents, which can lead to the formation of niosomes at the interfaces between streams, once the critical concentration was reached (gel-to-liquid transition).

Moreover, experiments were designed in a manner to verify the outcome of the produced niosomes based on the variation of concentration, FRRs and TFRs, in order to achieve a continuous-flow production with high size–control.

As a first attempt, the reaction was performed at room temperature (RT) in order to assess the surfactant's solubility. As expected, the precipitation of the unstructured product was clearly visible at the interface between the organic and aqueous solutions (Figure 5.13A). The reactor was then introduced into the thermal-bath, and the flow-protocol was executed at different temperatures. The representative sample produced at 50 °C is shown in Figure 5.13B. In line with the rationale of the synthesis approach, niosomes were formed at the focusing region, and in particular within the PBS lateral streams, with no signs of precipitation.

Moreover, the device demonstrated a complete sealing with no leakages from the inside of the channel at the different TFRs tested, nor infiltration of water from the thermal-bath, even at the highest tested temperature of 60 °C.

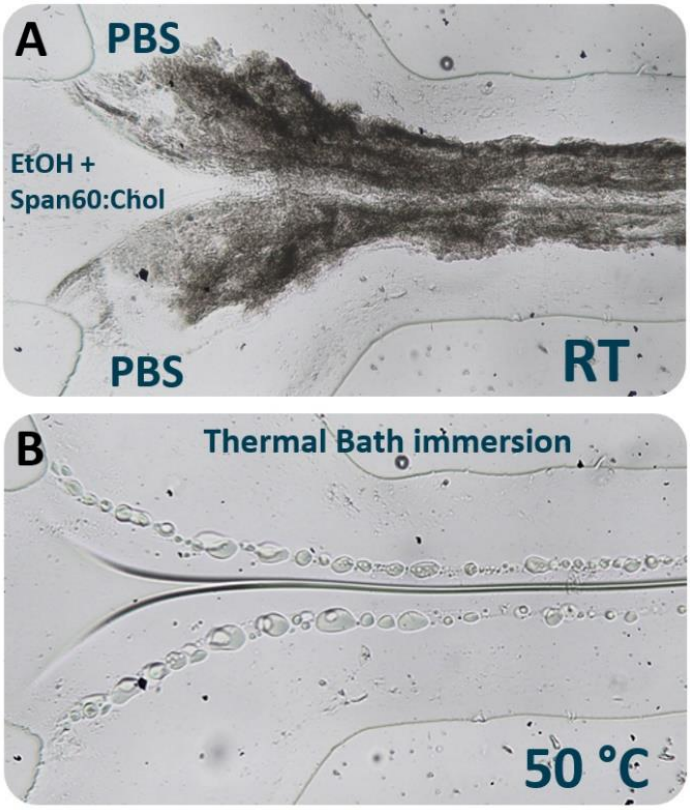

Figure 5.13 A 400 mm reactor was used for the preparation of organic particles (niosomes), formulated with non-ionic surfactants in a microfluidic hydrodynamic focusing device. Due to the low solubility of Span60 at room temperature, the reactor was maintained in a thermal bath at 50 °C. The integrity of the device was preserved.

Niosomes were then produced under the selected conditions in order to evaluate the effect of the variation of TFRs and FRRs on the produced nanovesicles. Figure 5.14 shows the effect of such variation in relation to the size (nm) and size distribution (PDI, a.u.). Results are presented for the undiluted samples formulated with Span® 60:Cholesterol (1:0.5 molar ratio) at 5 mM (Figure 5.14A,C) at controlled temperature (50 °C).

A common trend can be clearly noticed for both conditions with respect to particle size when increasing FRRs, and for all TFRs tested (Figure 5.14A,B). Specifically, at the 5 mM concentration (Figure 5.14a), the particle size decreased on average from 278, 298 and 358 nm (FRR=5) to 155, 129 and 143 nm (FRR=50), for TFR of 50, 100 and 200 µL/min, respectively. Similarly, at a concentration of 20 mM (Figure 5.14b), the particle size reduced from 342, 361 and 386 nm (FRR=5) to 164, 147and 151 nm (FRR=50) for TFR of 50, 100 and200 µL/min, respectively.

Moreover, a rapid drop was notable between FRR 5 and 15, followed by a less pronounced decrease between FRR 15 and 50. When varying the FRRs, the ratio between chemicals - thus the overall chemical composition - was affected, where the reduced concentration of bilayer building blocks led to the formation of smaller particles. Another consequence of the increased FRR was the narrowing of the width of the central stream, which in turn affected the mixing process allowing

the critical concentration to be reached more quickly. This was a unique advantage as nanovesicles were formed within the flow-channel.

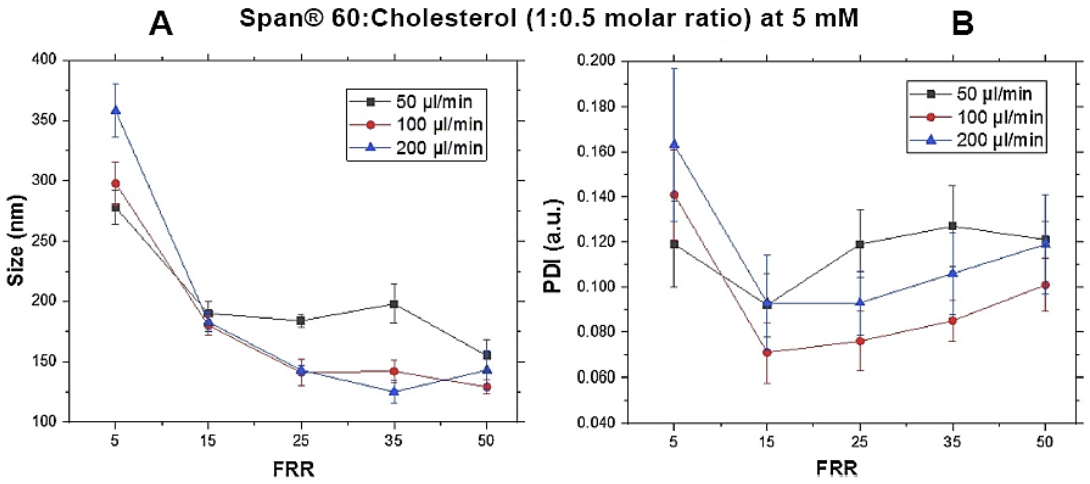

Figure 5.14 Size (nm) (A) and size distribution (PDI, a.u.)(B) measured by DLS in undiluted samples from niosomes formulated with Span® 60:Cholesterol (1:0.5 molar ratio) at 5 mM in a continuous flow microreactor based on hydrodynamic flow focusing at controlled temperature (50 °C). Each condition was tested twice, and each batch was measured by triplicate. [146]

In summary, the discussed results demonstrated the effectiveness of the manufactured reactor for producing niosomes with controlled size. Further details and additional comparisons between different concentrations can be found in the published [146]

5.4 Conclusions

This Chapter covers diverse fluidic approaches for the synthesis of organic nanoparticles. The main goal was to demonstrate the effectiveness of the manufactured cost-effective reactors for the production of nanovesclicles. This is crucial for allowing researchers to synthetize size-controlled materials that can be then adopted for their studied. Moreover, some of the discussed alternatives confirmed the meso- to large-scale outcome, reaching the magnitude of mL/min (TFR).

Specifically, the 3DP-RMC/Tape reactors showed comparable performance to reactors fabricated using more laborious and expensive fabrication methods. The use of a replica mould casted reactor created from a FDM 3D printer, in combination with the bonding on a simple pressure-sensitive adhesive tape, showed the enormous advantage to avoid sophisticated instrumentation and time-consuming multistep procedures.

The FDM 3D printer was also used to conceive the novel RIACs (reactor-in-a-centrifuge), which were fully tested. It was demonstrated that the scalable, cost-effective, easy-to-use, and pump-free method, can be adopted for the synthesis of nanovesicles. The novel approach was investigated, in term for reagents concentrations, formulations and ratio, as well as on architecture, and settings. The complete optimization of the production protocol was discussed. Notably, RIACs can produce size-controlled nanoliposomes, with a clinically relevant diameter <230 nm. Notably, RIACs they can be utilized and fabricated by users without specific expertise in flow reactor manufacturing. At the same time, expert designers have the flexibility to prototype architectures that best fit different applications. The developed technology could lead to the realization of a one-step synthesis/separation protocol for nanomaterials, where RIACs are employed simultaneously for synthesis and differential centrifugation of the end-product. Moreover, it was proven that the availability of a bottom reservoir for reaction quenching and pre-purification further adds to the flexibility of the RIAC. As several RIACs can be employed in parallel, this approach will allow for a rapid screening and optimization of different reaction conditions

Finally, the HR 3DP-RMC*Glass reactor introduced into a customised thermal bath, was presented as a novel approach for the synthetic production of niosomes when employing surfactants with Tm over RT. The HFF technique was suitable for increasing the size control of niosomes, and several FRRs and TFRs were discussed as alternatives to obtain the desired samples. Results showed that temperature was an essential parameter to take into consideration when employing such surfactants. Initially, and more importantly from the manufacturing point of view, such manufactured reactors demonstrated a complete sealing and strong adhesion of the bonding, without leakages at all the tested temperatures and flow conditions. Although the low reproducibility of the channel cross-section was observed with respect to the CAD design, the 3D

printed mould casted reactor was sensible to each variation of the operative condition, thus allowing a good focusing control. This was crucial for the overall efficiency of the device for such reaction. It was also observed that the size distribution was highly influenced by the mixing regimes. In general terms, with relation to the produced niosomes, it was noted that a narrower focused stream led to the formation of smaller particles, which caused by the injection of a smaller amount of the chemical building blocks with respect to the solvent ratios.

Chapter 6 Conclusions, future work and research outcomes

6.1 Conclusions

The present research project, aimed at the development of meso- to large-scale production of size-controlled inorganic and organic nanoparticles, through the realization of cost-effective and reliable flow-reactors. Representative inorganic nanomaterials included Ag nanoparticles in both spherical and prismatic shape, whereas vesicles were selected as demonstrative material for organic nanoparticles, specifically liposomes and niosomes. The selection was indeed based on the importance that such materials have in their respective fields, in terms of number and variety of applications involved. Another important reason lies in the high stoichiometric control needed for the production of these particles, which translates into a technological challenge when developing scalable manufacturing processes. Both types of particles were thus particularly suitable for evaluating the performance of the manufactured reactors; moreover, the production of AgNPrs generated particular interest from the defence science and technology laboratory (Dstl) because of NIR-applications. As a result, technological developments from this research could benefit applications across different fields and disciplines.

Batch synthesis of nanoparticles. Initially, batch studies on the effects of the chemical formulation (i.e. concentration and ratio between chemicals) over the repeatability of the process were carried out for metal nanoparticles, in order to find the best reaction conditions that could be translated to a flow-synthesis process. The adopted approach was significantly different from the one previously developed by this research group.[67] Specifically, a batch synthesis method [97] was tested and re-adapted, involving the minimum number of chemicals to decrease reaction costs in future steps of the research, and with the intent of obtaining a red-shifted LSPR absorption band of the AgNPrs. Although successful formation of the prismatic shape was achieved, the batch synthesis demonstrated low reproducibility, with the produced particles having a more than 100 nm shift in WA_{max} even when synthesized using the same chemicals and operating conditions. This was mainly due to the poor mixing capacity, with respect to maintaining the stoichiometric ratios that control the AgNPrs growth, thus representing one of the most important challenges to be overcome by flow-synthesis. The role of the solvent on reagents' reactivity was also investigated, as well as the optimisation of volume ratio conditions between water and IPA. The water/IPA volume ratio of 7 was found to be the most suitable to favour a faster kinetic and an enhanced bathochromic shift of the WA_{max} of the produced AgNPrs. This initial work allowed a better understanding of the nanoparticle's formation mechanism, which was crucial for defining reactors' designs in the following steps of the research.

3D printing for manufacturing of flow reactors. Subsequently, attention focused on the manufacturing methods of flow reactors, with the goal to bridge the gap between lab-based research and industrial translation and scalability of flow-reactor technologies, which is still limited by the need for specialised instrumentation. Particularly, 3D printing was adopted for either creating the positive master moulds used to produce transparent flow-reactors made of PDMS (here called 3D printed replica mould casted devices), or for direct construction of the entire reactors. Two highly different 3D printers - an expensive high-resolution Objet Connex 350 (market value £150k) and a desk 3D printer Ultimaker 2+ (market value £1.5k) – were employed and compared to investigate advantages and disadvantages for the production and resulting performance of flow-reactors. Further studies were carried out, including CFD simulations, and experimental investigations on both 3D printing aspects and the effect over the manufacturing/performances. Parameters such as minimum printable feature size, surface morphology, roughness, channel profile, accuracy in reproducing the CAD design, supporting materials were characterised and discussed. Subsequently, the effects of the resulted geometry on the flow-condition, post-treatments needed for the moulds, bonding alternatives for the PDMS replicas, effects of design on fluid mixing based on the channel geometry and control of

hydrodynamic flow focusing conditions were investigated on order to optimise the prototype reactors for the specific application.

The overall results suggested the that HR OC350 can create smoot moulds (maximum peak-to-valley of 15 μm measured from the PDMS profile), with respect to the U2+ (groves with peak-to-valley of~ 85 μm). These moulds favoured a more durable bonding of the replica PDMS on glass or PDMS surfaces by oxygen plasma treatment, and were more suitable for sealing using a cost-effective pressure-sensitive adhesive tape technique developed.

However, low accuracy in reproducing the nominal CAD geometry was observed when designing a squared- or rectangular channel cross-section. This is due to the 3D printing method and it is especially notable for smaller features. Specifically, while a 1.00 x 1.00 mm (w x h) designed cross-section was printed having the half-height and bottom widths of 1.14 and 1.38 mm respectively (with curved upper edges). Differently, when attempting printing a 100 x 100 μm design, the final channel had a bottom width between 400 and 550 μm and a completely curved shape.

For all the 3D printer replica mould casted reactors, the large-scale flow condition (here considered in the order of tens of mL/min) was achieved, demonstrating significant improvements over flow rates generally adopted in the literature (for example with respect to the AgNPrs which were produced at flow rates of few mL/h). Moreover, the increasing production rate can be further enhanced due to the high potential of such devices for parallelisation, potentially allowing outputs of hundreds of mL/min (i.e. 10 parallelised reactors operating at 10 mL/min each). Moreover, the relatively large channel sizes (cross-sectional area within 1 mm^2), minimises the risk of clogging during the synthesis of nanomaterials, and reduces the risk of pressure variations when operating multiple reactors with only one set of pumps.

On the other hand, the common desk U2+ can be successfully adopted for creating channels down to 500 μm (width), showing a good accuracy in reproducing a rectangular or squared cross-section channel design. This was crucial in the case of advection-dominated mixing, as it allowed a more effective formation of secondary flows, as demonstrated during the synthesis of AgNPrs with the two-inlets curved serpentine reactor. Moreover, despite the greater roughness with respect to the OC350, 3DP-RMC reactors produced using the U2+ can be operated up to 20 mL/min when bonded on pressure-sensitive adhesive tape (for straight channel geometries). This means that, although the notable groves created by the 3D printing nozzle, for water flowing into the designed straight channel geometry of 1 x 1 x 60 mm (w x h x l) at 20 mL/min, the bonding of the flow-reactor on the pressure sensitive adhesive tape was able to handle a pressure of 6.24 mbar.

Channel reproducibility in this case were more precise. The width of the channel varied from 1.035 to 1.007 mm (at 2 and 10 mm from the junction respectively), and the radius of the FDM 3D printed curved inlets was maintained within 0.025 mm for each mould reproduction. Differently, the 1 meter long curved reactors bonded on PDMS via oxygen plasma treatment, started to leak when tested at 50 mL/min. In this case, it is no possible to have a precise information of the pressure due to the alternate serpentine design, but just considering a straight channel of the same cross section the pressure would be ~ 1.1 bar. Finally, the lifetime of the devices was also evaluated; the 3D printed moulds could be reused multiple times, further reducing the production costs when testing prototypes.

As a key outcome of the study, a novel, easy-to-perform and cost-effective method for the fabrication of PDMS based continuous-flow reactors was developed, demonstrating a simple and fast manufacturing method (within 24 h form the CAD design) and low-cost production (average cost of £5 per reactor).[139] Notably, a commercial pressure-sensitive adhesive tape was used for the first time on desk (U2+) 3D printerd replica mould casted channels made of PDMS, in order to entirely bypass the most common oxygen plasma bonding method. 3DP-RMC/Tape devices were also validated through the synthesis od AgNSs and liposomes with controlled size, and the results compared with the known soft lithographic methods (μMi-REM). Furthermore, with respect to the AgNSs, these studies confirmed that the best performance was achieved when operating at FRR of 7 (which coresponded to the volume ratio in batch synthesis for AgNPrs) and TFR of 10 mL/min. Differently, liposomes were obtained at the water/ethanol FRR of 25 and TFR 1 mL/min. In both cases, the development of customised protocols and reagents' concentrations was demonstrated.[139]

Continuous-flow synthesis of AgNPrs and niosomes. 3D printing was also employed to create master moulds with geometries suitable to generate hydrodynamic flow focusing (HFF) conditions. HFF devices were produced, characterised and tested, confirming stable maintenance of such flow characteristics. Ultimately, they were employed for the production of AgNPrs and thermally controlled synthesis of niosomes, and to investigate the effects of chemical formulations and concentrations as well as operative conditions, such as FRR and TFR. Whilst the production of AgNPrs through the HFF reactor was demonstrated, results suggested the possibility of further improvements based on the reactor's design, to achieve kinetic control over the reaction. Thus, a different approach was subsequently adopted, involving a two inlet curved serpentine channel, with the advantage of enhancing mixing because of inertial forces created when increasing the TFR. In-depth studies on the flow conditions were carried out, assisted by UV-Visible, TEM imaging, and size distribution characterization of the produced particles. In this particular case, limitations of the

HR 3D printer were highlighted, and the less expensive desk 3D printed resulted in a more effective method for generating the desirable mixing regimes.

AgNPRrs were then successfully produced at different TFRs (5, 10, 20 and 50 mL/min), and at the selected FRR of 7. Size analyses were carried out, as well as reproducibility tests, confirming a better-controlled production and size distribution with respect to the batch approach. In fact, comparable WA_{max} were obtained even though AgNPrs produced through the curved serpentine (U2+ 3DP-RMC*PDMS reactor, TFR 10 mL/min, FRR water/IPA 7) averaged an edge length of 45.13 nm, and those produced with the batch averaged 52.45 nm. Specifically, when having comparable WA_{max}, a good sample from the batch synthesis showed a SD of 22.82 nm, against the 15.20 nm obtained from the flow-production at the selected conditions. Moreover, the UV-Vis characterisation showed almost overlapping spectra for the flow-produced particles at the same conditions, instead of the various outcome of the batch synthesis due to uncontrollable mixing. This proved the improved size control on the LSPR of the AgNPrs produced by the flow-synthesis, as well as the effectiveness of the designed architecture. Moreover, by evaluating the kinetics of the reaction it was noted that a complete mixing within the reactor will lead to the formation of the prismatic shape, even after collection of the samples into vials with no further stirring.

Regarding the production of organic vesicles, the HFF approach was used to successfully produce size-controlled niosomes. This method not only involved a consistent study of diffusion-driven reaction conditions, but more importantly, proved the reliability of the performance of such cost-effective 3DP-RMC reactors when placed in a water thermal bath operated up to 50 °C. Moreover, different formulations were tested and the results demonstrated the continuous flow production of size-controlled niosomes by using precursors with low solubility at room temperature. These conditions were employed for the first time as a novel approach for the production of clinically acceptable sized niosomes. Specifically, the smaller (129 nm) niosomes were produced at FRR = 50 and TFR 100 µL/min when using Span® 60:Cholesterol (1:0.5 molar ratio) at 5 mM, operating at 50 °C.[146]

Directly 3D printed reactors. With respect to entirely 3D printed reactors, a novel technology was developed, hereby referred to as reactor-in-a-centrifuge (RIAC). The RIAC concept represents a scalable, cost-effective, easy-to-use, and pump-free flow method that can be customisable, employed by non-expert users, and adopted for a large spectrum of applications. RIACs were described throughout the thesis, as well as the procedure that led to their first functioning prototype made with the U2+ printer. Moreover, detailed studies were carried out on the synthesis methods and protocols, demonstrating the production of both AgNSs (WA_{max} 404 nm) and size-controlled (<230 nm) liposomes.

Finally, light-assisted flow-biosynthesis of AgNSs achieved by an optical fibre connected 3DP-RMC devices was described. Several customised reactors were designed and fabricated, and their advantages and disadvantages were demonstrated for producing AgNPs involving bacteria. Particularly, optical fibres where embedded or connected into PDMS reactors. The light alignment is a key factor for a good production rate, together with effective mixing induced by a curved channel geometry. However, the reduction in particle's formation over time was observed, due to the deposition of the produced material on the PDMS walls.

6.2 Avenues for future research

In this study, it has been demonstrated that 3D printing can be successfully employed in the manufacturing of reliable and cost-effective flow reactors. At the same time, it has been demonstrated that, if properly conceived, modifications of the batch synthesis of nanomaterials can effectively assist translation to continuous flow production in a more controllable manner. This approach can be applied to encompass a wide range of nanomaterials and nanocomposites. When considering that the global market projections for investments on such fields are of $2.0 billion in 2017 to $7.3 billion by 2022, [195] interest from the scientific and industrial communities has become progressively greater, as well as the perception of and the high potential for future work. Whilst microfluidics has already been adopted for nanomaterials synthesis, demonstrating outputs of similar or greater quality and lower operational costs, there are still challenges associated with its scalability for large-scale production.

In this projects, steps towards the development of scalable continuous-flow reactors for nanomaterial's production have been made. However, due to the cross-disciplinary application of these systems, there is potential for future research that embraces many research fields. These paths for future investigations are described below.

(1) SILICA COATED SILVER NANOPRISMS

One future avenue of research relates to the production of silica-coated AgNPrs (SiO_2@AgNPrs). This is potentially an important step of a large-scale production process for AgNPrs, since it provides particle's protection against mechanical or chemical etching. Furthermore, silica coating also facilitates nanoparticle's chemical functionalization which, although may cause shifts of the LSPR WA_{max}, maintains their characteristic NIR absorption. These advantages make SiO_2@AgNPrs suitable for NIR-related applications such as energy-saving glazing. [99]

Therefore, the ultimate goal of achieving a single- or multi-step flow synthesis of SiO_2@AgNPrs was considered throughout the project. Scheme 6.1 gives a graphical representation of the working flow of the major steps that need to be accomplished to achieve this ambitious goal. The thesis covered the steps related to the translation of batch synthesis into flow production, the characterization of 3D printed materials and moulds, as well as the realization or reliable 3DP-RMC reactors. However, the development of methods to achieve silica coating was carried out in parallel. Following the same approach adopted for AgNPrs synthesis, a first step of the study focused on defining the most reproducible batch protocol that minimizes formation of aggregates and creates a uniform coating for each AgNPr. This was not a straightforward task and involved several iterations, as reactions often did not occur as expected, often creating agglomerates of silica with embedded AgNPrs.

Scheme 6.1 Scheme of the major steps required for achieving cost-effective and large-scale flow-production of size- and shape-controlled AgNPrs, and their silica coating (blue), towards the ideal realisation of a single or multistep flow-production of SiO_2@AgNPrs(orange).

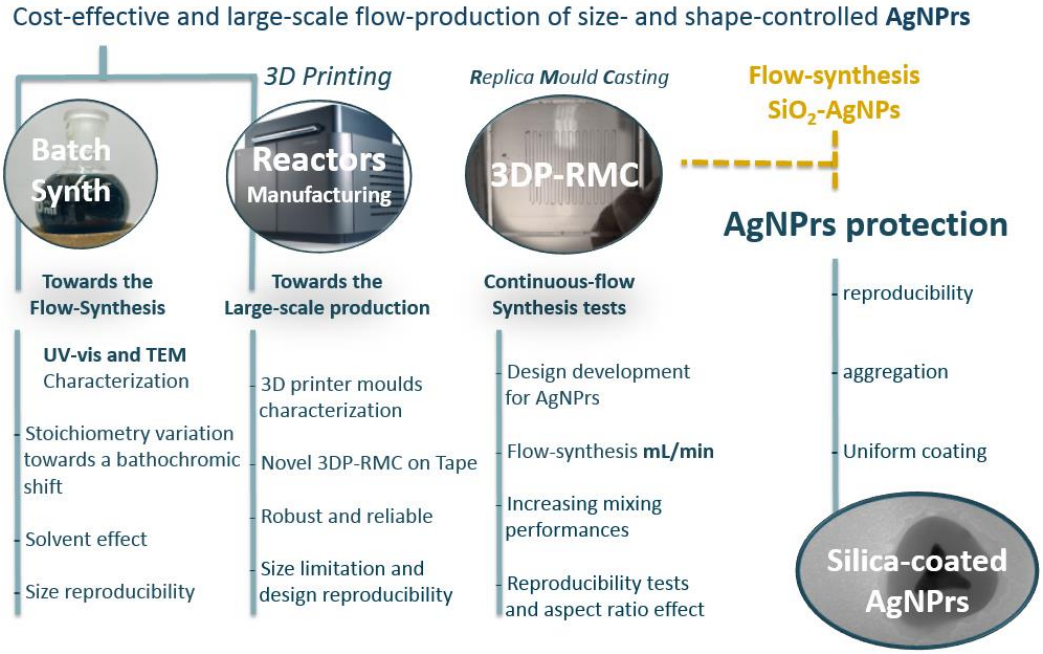

Several experiments were carried out, starting by evaluating the difference between using purified or unpurified AgNPrs as the starting sample of the coating reaction, and the effect on the LSPR of the samples (D.1). The influence of the pH was also evaluated (D.2). Furthermore, multiple protocols (20) were performed including modifying reaction time, dissolving ratios, sonication parameters, reagents' order of addition and solvents (D.3). Finally, a high-quality product was obtained as shown in the TEM images in Figure 6.1 (final adopted protocol described in D.4)

The goal of achieving a single or multi-step flow production of SiO_2@AgNPrs still remains far from being fully accomplished, mainly due to the purification and centrifugation steps. However, the outcome of these preliminary studies was important for several reasons. Firstly, it has demonstrated the potential of such materials for NIR purposes. Secondly, their employability has been shown as water-based nanofluid for improving the efficiency of direct absorption solar collectors (DASCs), under natural sunlight exposure (NSL)(See D.5).[29]

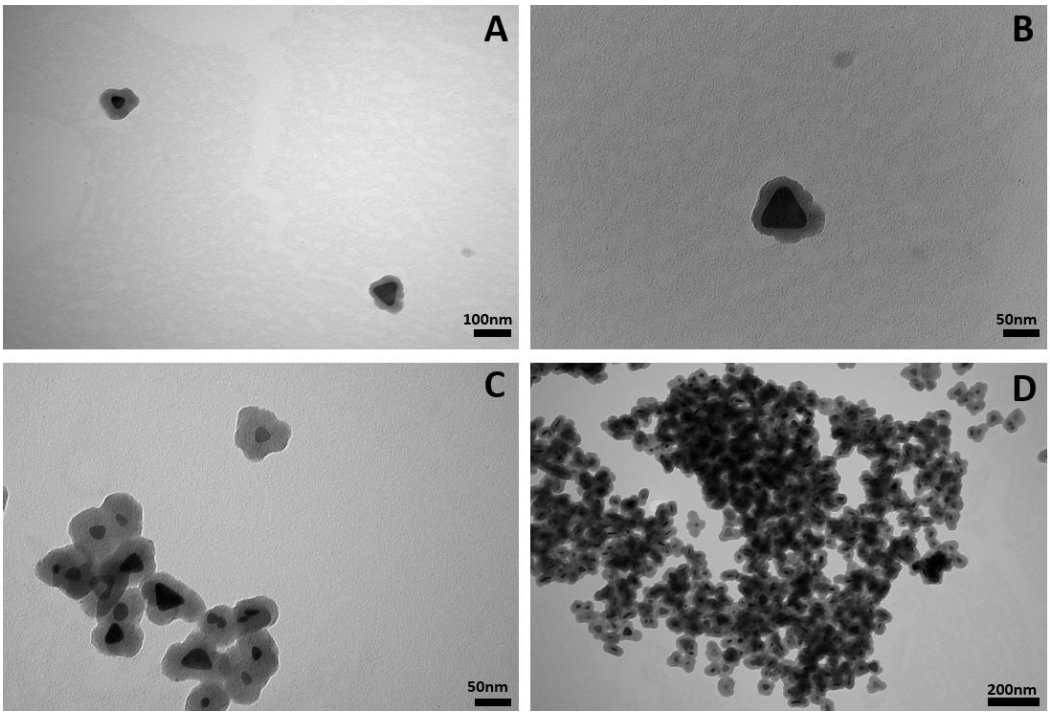

Figure 6.1 Representative TEM images of samples of produced silica coated AgNPrs.

Furthermore, this investigation helped in conceiving the reactor-in-a-centrifuge (RIAC) approach developed during the research.

(2) RIAC

The RIAC concept was initially developed when evaluating a solution for the batch to flow translation of the synthesis of SiO_2@AgNPrs. Ideally, RIACs could partially overcome the multiple centrifugation steps needed for sample purification during the coating procedures on AgNPrs.

Scheme 6.2 shows an ideal evolution of the RIAC concept involving, for instance, different 3D printing technologies, modifications to the design, or creation of lego-like reactors for application in the production of a large variety of inorganic and organic nanomaterials. Most importantly, they can be adapted for drug encapsulation and/or differential centrifugation purposes. The advantage of the use of the centrifugal force in this technique opens up many possibilities for future applications, ranging from simple drug-encapsulation to single-step synthesis and separation. Moreover, the manufacturing strategy adopted, displayed an extremely cost-effective approach, and its simplicity of use would allow any operator to perform fundamental science regardless of its prior expertise.

Scheme 6.2 Further steps for the RIAC technology involving new manufacturing materials and designs, synthesis of novel materials, drug encapsulation, single-step synthesis and separation.

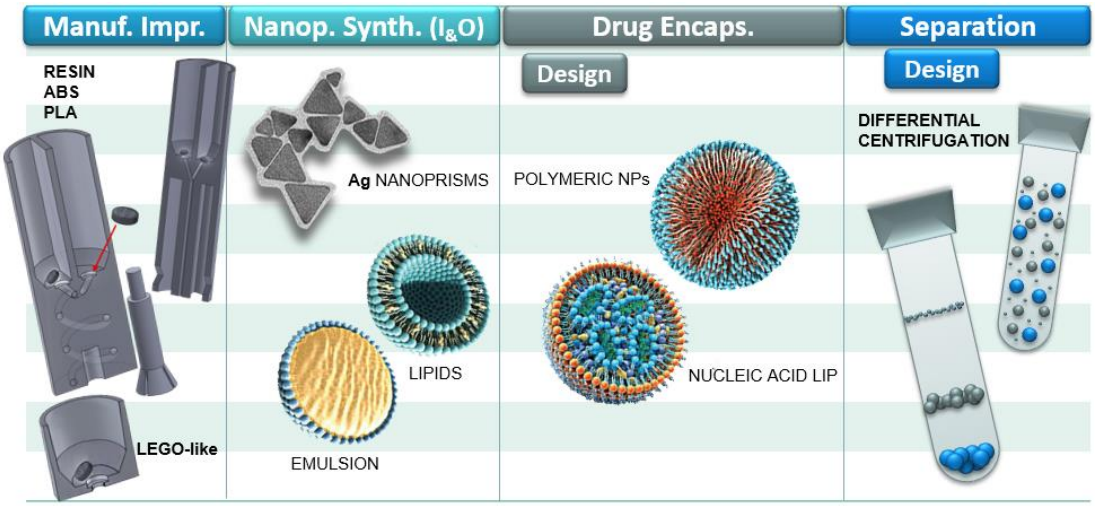

Due to its low-cost and the possibility to embrace a large number of multidisciplinary applications, future applications can be healthcare oriented, ranging from in situ drug preparation protocols (suitable for application in low-income settings), to fast scaling-up synthesis approaches (RIACs parallelization).

(3) **HYBRID NANOMATERIALS AND SUPRAMOLECULAR CONTROL**

In general, the use of smaller quantities of reagents is one of the most important advantages of the flow-approach (particularly microfluidics), along with the fine stoichiometric control. This makes flow-synthesis extremely suitable for a large amount of applications in the biosensing field, where reagents' cost is extremely high. For instance, during the PhD project, different parallel investigations were carried out on the synthesis of cobalt-porphyrin functionalised single-strand DNA probes coated on gold and silver nanoparticles (D.6). In this case, gold nanoparticles were produced by a modified batch approach. Although several centrifugations steps were needed during the production, the flow-method can be prototyped for performing intermediate steps of the process. For instance, the ratio of the number of DNA single strands molecules per particle can be more accurately tuned, in order to obtain more uniform samples.

For such reactions, the limit of 3D printed mould casted flow-reactor is related to the printable channel size, which might be too large for the volumes involved. Therefore, further studies focusing on 3D printing of smaller features for similar reactions are necessary.

Other improvements can relate to the flow-controlled aggregation of chiral supramolecular structures. This is a very interesting topic (anticipated in Appendix B.2, with the spiral reactor) with

potential in the field of sensors. The idea of a two specular spiral geometries was created to attempt the enantiomeric separation of chiral supramolecular aggregates based on Dean's flow. However, due to the inability of the HR 3D to reproduce the square cross section of the channels, the device did not perform as expected. A future plan would be to create a 3DP-RMC reactor able to induce clockwise and counterclockwise controlled vortexes for the self-assembly of supramolecular aggregates. A particular application might focus on porphyrins. For example, Figure 6.2 shows an interesting design architecture that combines spiral flow formation with HFF, demonstrated by Frankowski et al.[196]

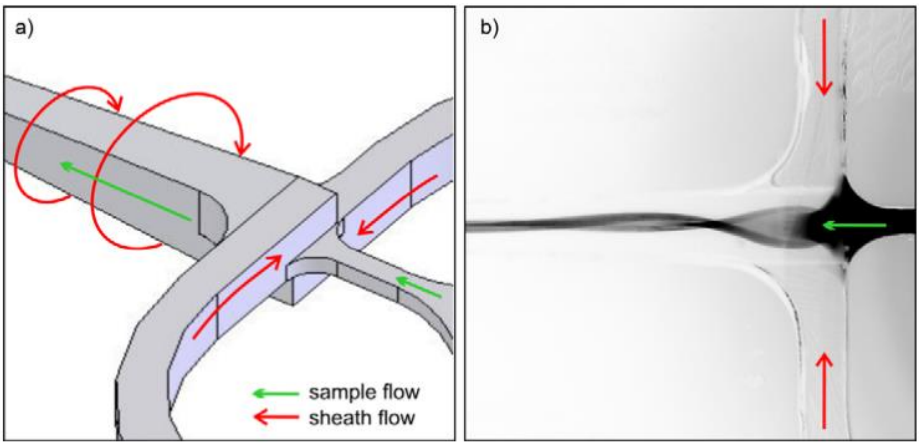

Figure 6.2 HFF for spiral flow: design (A) and manufactured microreactor (B) by Frankowski et al.[196]

Moreover, AgNSs and AgNPrs can interact with carrier aggregates such as the produced liposomes. Preliminary flow-synthesis studies (performed in collaboration with F. Yanar) have demonstrated an interaction between the metal nanoparticles and the organic vesicles (TEM in Figure 6.3B). However, it is not yet clear whether AgNPrs can be encapsulated, included within the hydrophobic bilayer or just attached onto liposomes.

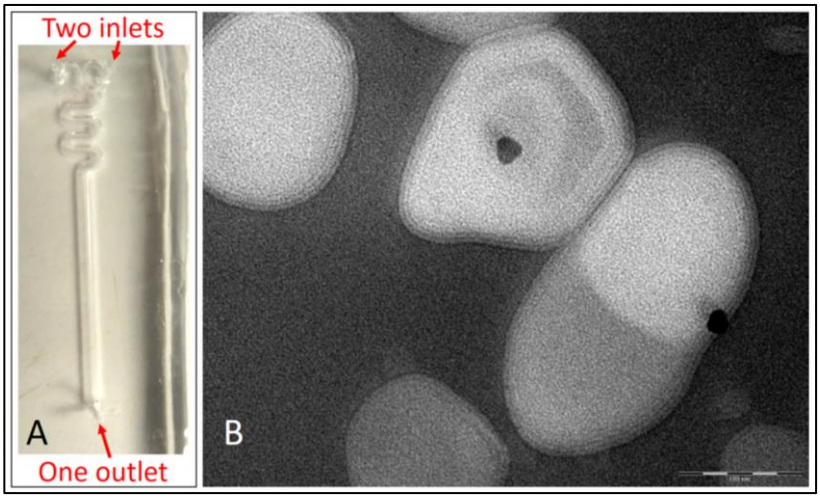

Figure 6.3 A) Flow reactor for the first attempt of AgNPrs-loaded liposomes. B) TEM imaging of the interaction between the AgNPrs and liposomes.

A custom 3DP-RMC device could be potentially prototyped to favor supramolecular aggregation of liposomes around an aqueous core containing the metal colloids. This remains an interesting research as AgNs-loaded liposomes could have a strong impact as drug delivery systems. For instance, the diverse LSPR of AgNSs and AgNPrs can be used to selectively activate the release of a certain drug encapsulated into liposomes.

(4) LIGHT-ASSISTED FLOW DEVICES

Finally, future work can focus on developing light-activated flow-reactors. This approach has great potential as it can embrace flow-production of any photocatalised reaction, combining the advantages of flow-synthesis with the cost-effectiveness of the device. Further studies can be carried out with respect to channel's functionalization to avoid particles' adhesion. However, if no interactions are present between the PDMS or glass and the synthesis products, the technique can be employed to allow free customization of the design architecture based on the research purpose. This applies for both the OF-embedded devices and the reactors positioned into the UV-vis chamber.

6.3 Outcome of the research

This interdisciplinary PhD research was carried out across the bioengineering, chemistry and MiNaTher (micro and nano therapies) research groups at the University of Southampton. A productive collaboration was also established with the University of Oviedo (Spain). Additionally, there was a parallel collaboration with the defence science and technology laboratory for the entire project.

The outcome of the present research project has led to a number of high impact publications, and further papers are in preparation. Below listed are the produced review, journal articles, conferences, seminars and presentations, as well as the co-supervised Bachelor's and Master's theses, related to the work performed during the PhD research.

Peer-reviewed review articles published:

- Bacteria and nanosilver: the quest for optimal production.
  Thomas Mabey, Domenico Andrea Cristaldi, Petra Oyston, Karl P. Lymer, Eugen Stulz, Sandra Wilks, Charles William Keevil and Xunli Zhang
  Critical Review in Biotechnology, 39, **2019**.

Peer-reviewed research articles published:

- Thermal performance and physicochemical stability of silver nanoprismbased nanofluids for direct solar absorption
  Harriet Kimptona, Domenico Andrea Cristaldi, Eugen Stulz, and Xunli Zhang
  Solar Energy, 199, **2020.**

- Continuous flow production of size-controllable niosomes using a thermostatic microreactor.
  Pablo García-Manriquea, Gemma Gutiérrez, María Matos, Domenico Andrea Cristaldi, Ali Mosayyebi, Dario Carugo, Xunli Zhang, and María Carmen Blanco-López
  Colloids and Surfaces B: Biointerfaces, Volume 182, **2019**.

- Approaching single DNA molecule detection with an ultrasensitive electrochemical genosensor based on gold nanoparticles and Cobalt-porphyrin DNA conjugates
  Balwinder Kaur, Kamila Malecka, Domenico Andrea Cristaldi,
  Clarissa S. Chay, Iwona Mames, Hanna Radecka, Jerzy Radecki and Eugen Stulz

Chem Commun, 54*,* **2018.**

- Easy-to-perform and cost-effective fabrication of continuous-flow reactors and their applications for nanomaterials synthesis
  Domenico Andrea Cristaldi, Fatih Yanar, Ali Mosayyebi, Pablo García-Manrique, Eugen Stulz, Dario Carugo, and Xunli Zhang
  New Biotechnology, 47, **2017.**

Peer-reviewed research articles submitted:

- 3D printed reactor-in-a-centrifuge (RIAC): making flow-synthesis of nanoparticles pump-free and cost-effective.
  Domenico Andrea Cristaldi, Alessio Labanca, Tomas Donal Pottinger, Joshua Owen, Eugen Stulz, Xunli Zhang, and Dario Carugo
  Submitted to: *Chemical Engineering Journal*

Peer-reviewed research articles under preparation:

- Light-activated flow-biosynthesis of silver nanoparticles *via* 3D printed replica mould casted reactors.
- Size-controlled silver nanoprisms: the translation from batch- to cost-effective and large-scale flow-production.

Conferences, seminars, presentations and prizes:

- Developing Silver Nanoparticle Production for Optically Active Materials
  Materials Research Exchange – Dstl event, 2019

- 3D printed reactor-in-a-centrifuge (RIAC): a novel approach to the production of organic nanomaterials
  INTERNATIONAL CONFERENCE ON MINIATURIZED SYSTEMS FOR CHEMISTRY AND LIFE SCIENCE (μTAS 2018) - Kaohsiung, Taiwan from 11th - 15th November 2018 (Conference paper)

- Producing Silver Nanoprisms: Biological and Microfluidic Approaches
  DSTL SHOWCASE – (Defence Science and Technology Laboratory)

Edinburgh 14th – 15th May 2018 (winner of “flash presentation and poster prize”)

- Large-scale production on nanomaterials using a continuous-flow reactor for energy saving glazing BIOENINEERING FACULTY SEMINAR - Southampton, 21ST March 2018

- Silver nanoprisms and chemotherapeutics dual loaded liposome for drug delivery.

- 3D printers for continuous flow reactors: an easy manufacturing method for silver nanoparticles and niosomes production.
  VI FEE PG CONFERENCE - Southampton, 6th January 2018 (posters)

- Preparation of Organic Colloids in a Hydrodynamic Flow Focusing Microreactor at Controlled Temperature
  X WORLD CONGRESS OF CHEMICAL ENGINEERING
  Barcelona, 1st - 5th October 2017

- The development of easy-to-make continuous flow reactors for biological and inorganic purposes
  IV INTERNATIONAL IMTB
  Bled, Slovenia, 23rd – 26th April 2017 (Oral presentation and Poster)

- Large-scale production on nanomaterials using a continuous-flow reactor for energy saving glazing
  V FEE PG CONFERENCE Southampton, 2nd November 2016
  (Winner of “best oral presentation prize”)

Assistant supervisor for bachelors and master thesis:

- Green synthesis of silver nanospheres *via* 3D printed reactor-in-a-centrifuge (RIAC) (Student: *Thomas pottinger*, University of Southampton - UK).

- Understanding Batch Synthesis and Silica Coating of Silver Nanoprisms for Translation into Continuous Flow Synthesis (Student: *Angharad Jenkins*, University of Southampton - UK)

- Gold and silver nanoparticles as electrochemical genosensors with cobalt-porphyrin labelled single-stranded DNA (Student: *Clarissa Chay*, University of Southampton - UK)

Appendix A Green batch approach, optical fibre and thermal camera

A.1 Green batch synthesis of silver nanospheres *via* tannic acid

Tannic acid (TA) has been evaluated as suitable reducing agent for silver nitrate in presence of TSCD. The reducing complex has the capability to also act as capping agent for the formed nanospheres.[93] Therefore, many preliminary studies have been performed for attempting a flow-translation.

A.1.1 Synthesis at reflux

Following the synthesis presented by Neus G. Bastús *et al.*,[94] was reproduced dissolving TSCD (4.4 mM) and TA (25 mM) in 100 mL MilliQ water followed by heating to reflux. $AgNO_3$ (25.3 mM), was dissolved in 1 mL MilliQ water and then added to the refluxing solution until the typical colour was obtained. The product was then centrifuged at 13200 rpm for 30 mins, with the residue being resuspended and analysed using UV-Vis at a 1 mL in 3 dilution. The supernatant was also analysed by UV-Vis at a 1 mL in 3 dilution. A separate smaller centrifuge the Eppendorf Centrifuge 5415 D was used for the purification of 1 mL samples can be purified. The supernatant would then be removed and the residue resuspended in the same volume of MilliQ water.

A.1.2 Synthesis at room temperature

Initially, two experiments were performed in order to verify the effect of the presence of TSCD on three different concentrations of TA (1.25, 0.5 and 0.25 mM) while maintaining the fixed the $AgNO_3$ concentration at 2.5 mM. TSCD was not used in protocol 1, whereas a 0.5 mM concentration was used for protocol 2 (Appendix Table 1).

Appendix Table 1 Chemicals concentration for protocol 1 and 2 a room conditions.

	Protocol 1	Protocol 2
AgNO3	2.5 mM	2.5 mM
TSCD	none	0.5 mM
TA	1.25 mM 0.5 mM 0.25 mM	1.25 mM 0.5 mM 0.25 mM

Both sets were dissolved in 5 mL of MilliQ water and shaken. For each TA concentration in set 1, UV-vis was taken at a 1 mL in 3 dilution at 30 and 60 mins, and then centrifuged at 13200 rpm for

15 mins and UV-vis performed again at the same dilution as above. For set 2, the solutions were purified at 13200 rpm (13660 rcf) for 15 mins after half an hour of agitation and UV-vis performed at 1 mL in 6 dilution. The supernatant was also analysed at 1 mL in 3 dilution.

A direct comparison to the heated batch synthesis was also performed, with 4.25mg of AgNO3 (25 mM), 0.135 g of TSCD (4.6 mM) and 4.3 mg of TA (0.0253 mM) were weighed into vials. The TA & TSCD were dissolved in 100 mL MilliQ water and stirred. The AgNO3 was dissolved in 1 mL MilliQ water and then added to the stirring solution. UV-Vis was then taken at 10, 20, 30, 40, 60, 135, 200, and 270 minutes after addition at 1 mL in 3 dilution for all. Samples from 10, 150 and 270 minutes were also purified at 13200 rpm (13600 rcf) for 15 mins and analysed at 1 mL in 3 dilution

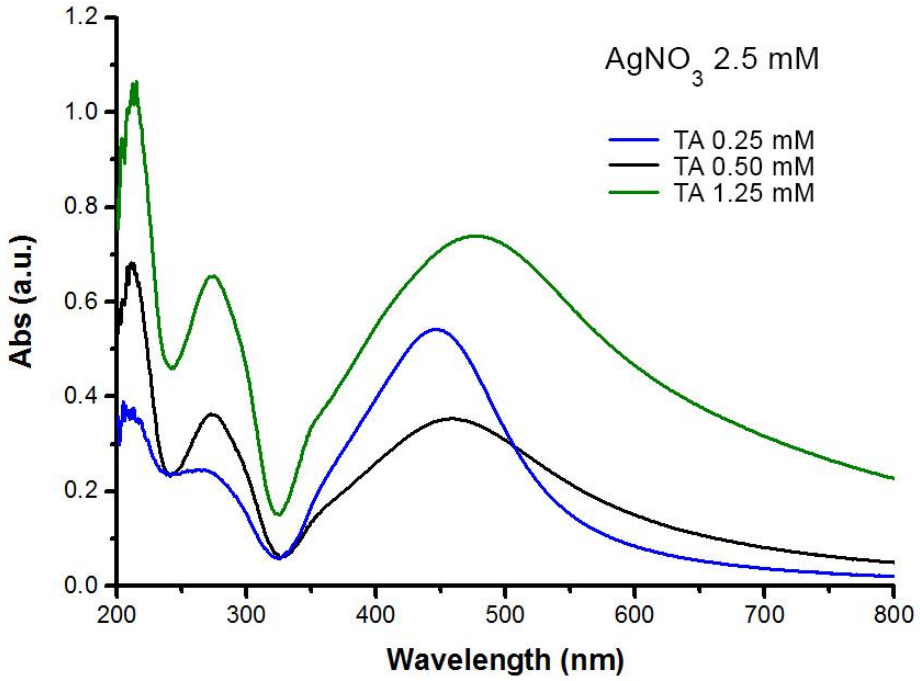

Appendix Fig. 1 AgNO3 2.5 mM and TA 0.25/0.50/1.25 mM, re-suspended after centrifugation and (1:6 dilution)

A.2 Optical fibre for UV-Vis characterisation and custom cuvette older

A custom cuvette older for the 3 mL quartz cuvette adopted for the UV-vis characterisation was designed and 3D printed. The high resolution 3D printer Objet Connex 350 was employed and black rubber-like material was used for enhancing absorption and minimising backscattering. This was created to be able to collect a spectrum windows up to 1400 nm in wavelength, covering a portion of the infrared region. The setup was used for some experiments.

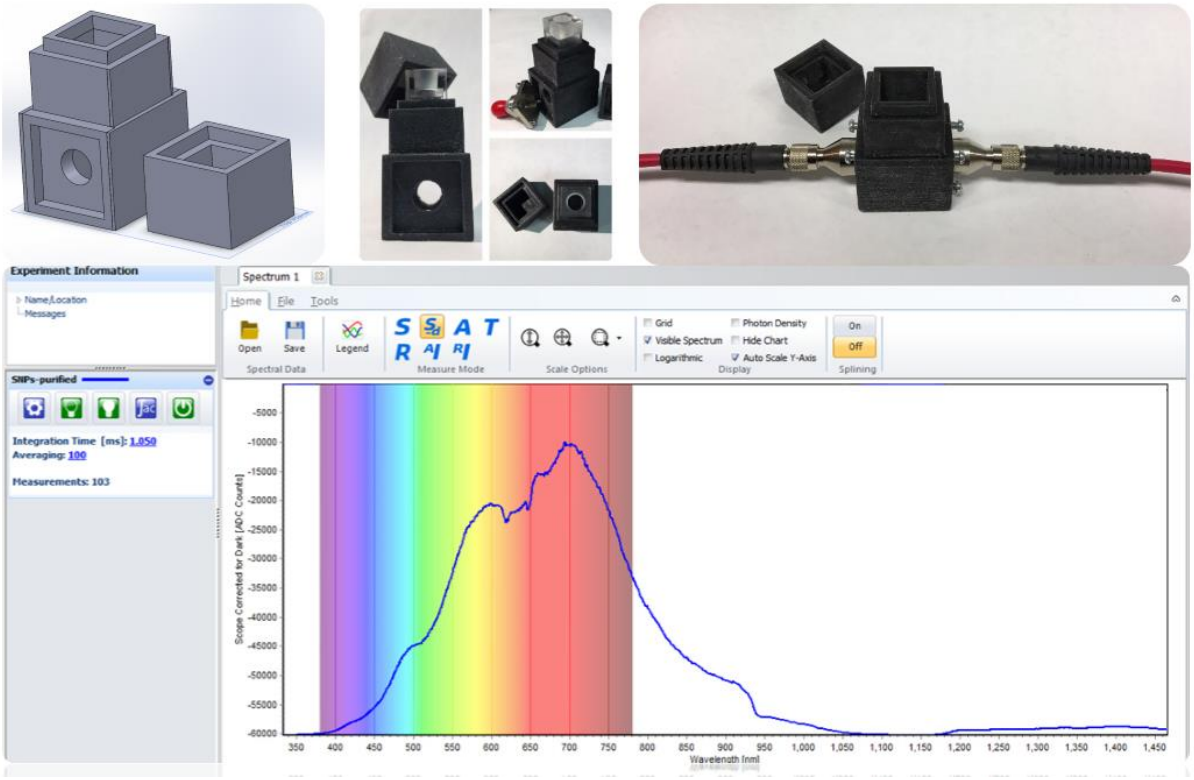

Appendix Fig. 2 Designed and 3D printed cuvette older connected with the optical fibre portable UV-vis spectrometer. The region of the collecting signal is reported and the UV-vis region highlighted by the rainbow colours.

A.3 Thermal camera test

During the collaboration with T. Mabay for the Dstl project, and for a better understanding of the NIR absorption capabilities of AgNPrs, a light box setup was arranged and 3 cuvettes positioned in front of it to be recorded with a thermal camera. The cuvettes contained a centrifuged and 10 times concentrated sample of AgNPrs (spin vac centrifuge), water and a freshly prepared solution of AgNPrs directly from the batch production with the adopted formulation (left to right in Appendix Fig. 3a). The thermal camera was regulated between 24 and 35 C°, in a manner that allows temperatures in between to be detected in its scale. Appendix Fig. 3b shows the thermal camera screen while capturing the cuvettes in front of the box. The green colour for the fresh sample of AgNPrs indicates a hottest temperature when compared to the other two. This is due to the good NIR absorption of the sample. However, by increasing the concentration of the sample *via* centrifugation, it has been noted the formation of almost eye visible clusters and the NIR abortion effect decreases so much that is comparable with the pure water.

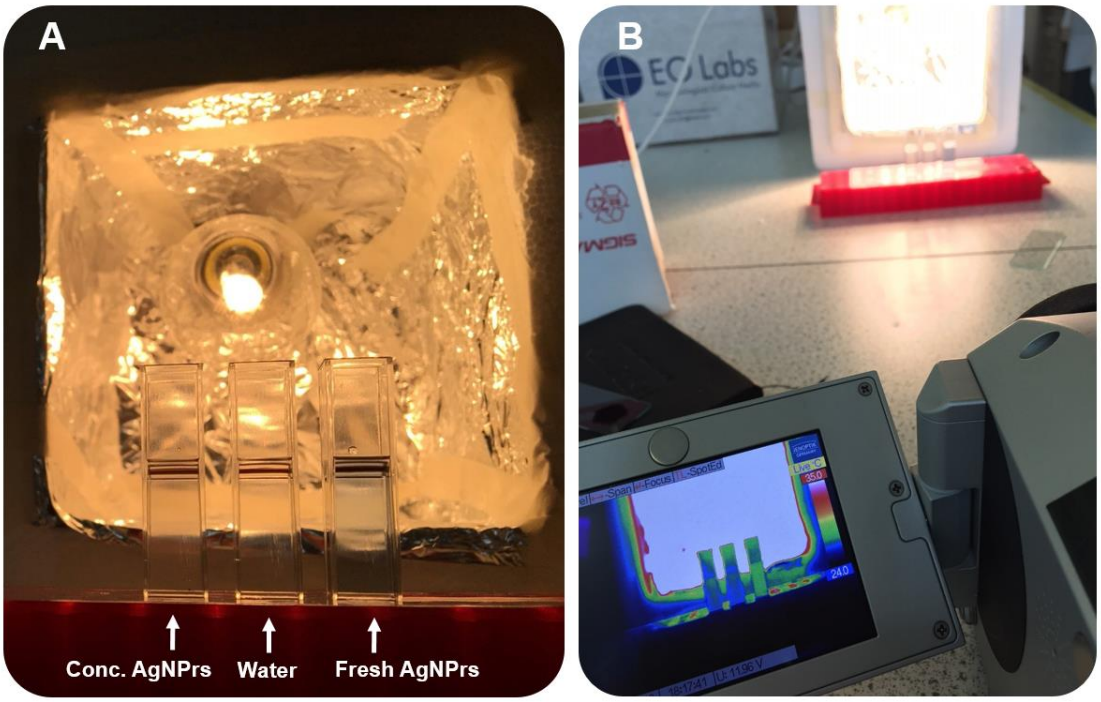

Appendix Fig. 3 A) The tree cuvettes in front of the light box: 10 times concentrated sample of AgNPrs (spin vac centrifuge), water and a freshly prepared solution of AgNPrs (from left to right). B) Thermal camera positioned in front of the light box shows the different temperature of the samples.

Appendix B Design and manufacturing alternatives

As stated in the main text, many manufacturing protocols were tested and different reactors were created. Here some alternatives:

B.1 ABS channel and 3D pen approach

Flow channels architectures were also 3D printed in acrylonitrile butadiene styrene (ABS) and embedded into a PDMS layer as suggested by Saggiomo *et al.*[197] For the creation of the channels both The U2+ and a 3D pen were used. The approach is based on the proposed mechanism of dissolution of the ABS material by acetone, and it would have the advantage of avoiding the bonding step. However, the method was found to be not effective and with low reproducibility. It was not possible to remove the ABS from the channel as expected even though several attempts were carried out.

Appendix Fig. 4 Hydrodynamic flow focusing channel CAD design to be 3D printed in Acrylonitrile dutadiene styrene (ABS) with the U2+ and further embedded into a PDMS layer. The dissolution of the ABS architecture with acetone, to leave the empty channel, was not achieved.

B.2 Spiral reactor

A side project was carried out with the idea to create a reactor for enantiomeric separation of supramolecular aggregates (Porphyrins). Two spiral reactors were produced with opposite rotation in order to generate secondary flow (controlled vortexes). After several tests, the reactors did not performed as expected. However, this experience lead to a better understanding on the limit of the HR 3D printing with the OC350, and it was the key of the further geometrical characterisations

shown in Chapter 4. There is a notable margin for improvements in this field which has high potential.

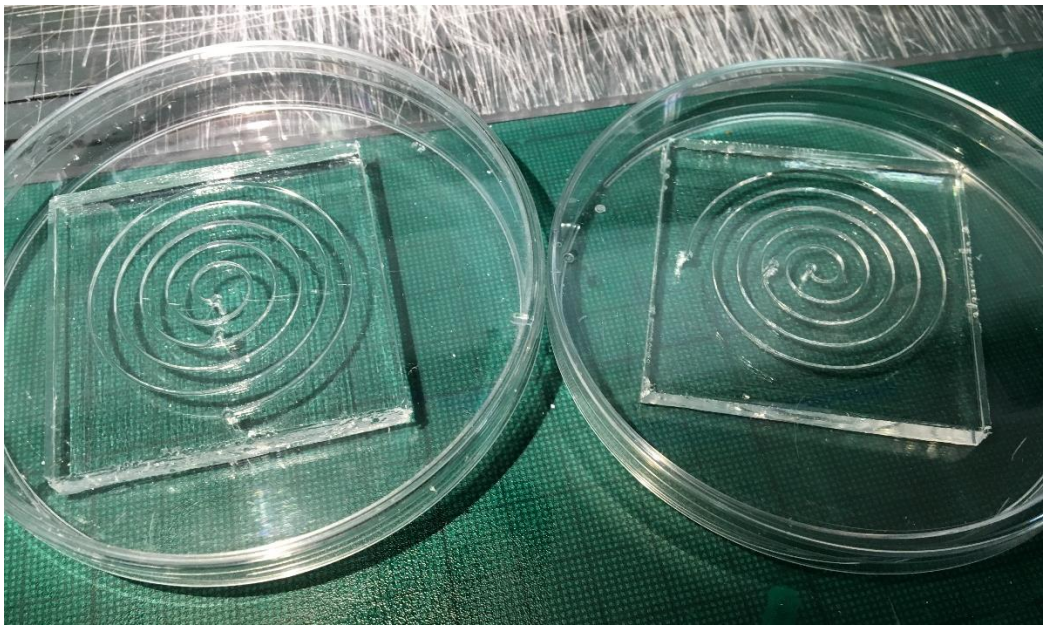

Appendix Fig. 5 Opposite two-inlet spiral reactors for the enantiomeric separation of supramolecular aggregates.

B.3 Roof channel

In this case, after the morphological characterisation of the moulds created with the U2+, a variation of the protocol was attempted. The channel was 3D printed on a lid designed to cover a box reservoir (roof channel). The box was filled with PDMS and the lid-channel was partially embedded from above. The PDMS did not touch the lid surface, and cured at room temperature in air creating a smooth surface suitable for the following bonding step. However, due to the surface tension of the PDMS on the PLA surface, after removing the lid that includes the geometry, the remaining channel was not consistent and the bonding was hard to achieve *via* oxygen plasma because of the meniscus formation at the contact edge between the PDMS and the PLA mould.

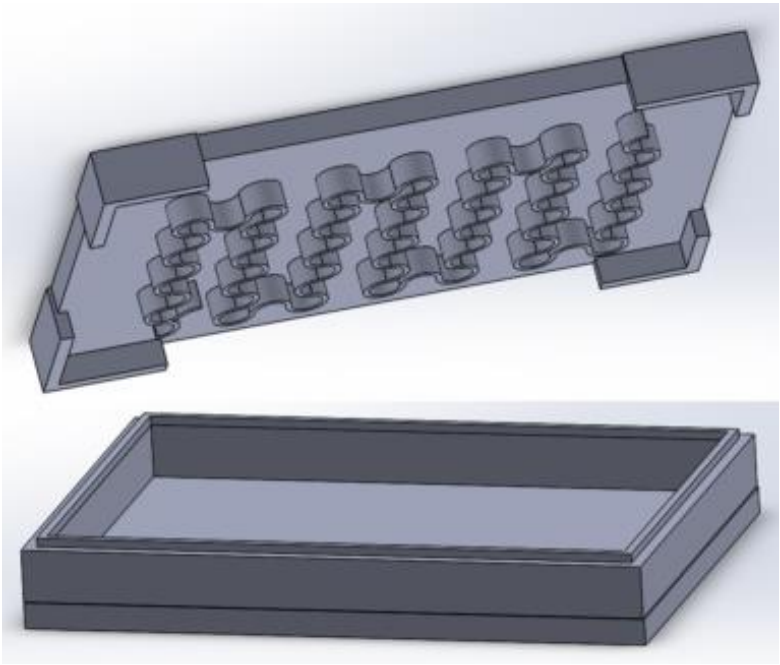

Appendix Fig. 6 CAD design of the Roof channel attempting the two-inlets curved serpentine design.

B.4 HFF junction 3D printed using the U2+

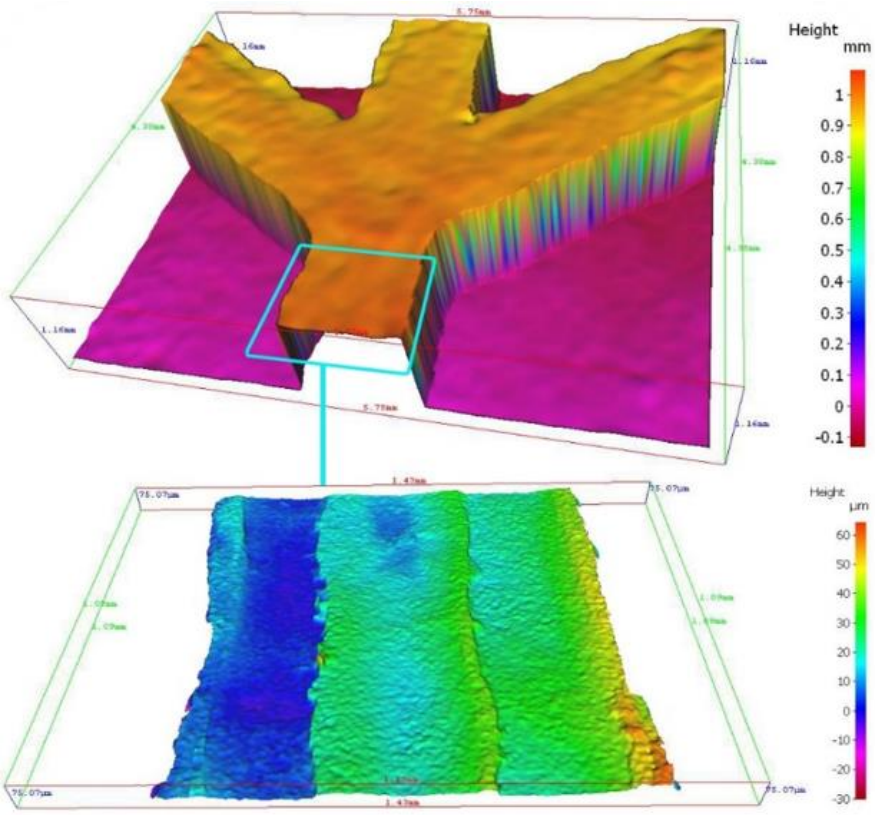

Appendix Fig. 7 Optical morphology of the HFF junction made with the U2+ (above), showing the clear details of the three runs that the nozzle (400 µm in diameter) of the FDM 3D printer made to realise the channel (1 mm in width).

Appendix C Maximum AgNPrs size, supporting CFD and optical fibre coating

C.1 RIAC: green synthesis of AgNSs

Reagents:

- $AgNO_3$ 1mM
- TA 0.025 mM + TCSD 5 mM

The TA/TSCD solution was placed in one reservoir of the RIAC (3 mL), and AgNO3 in the other (3 mL). Centrifuged at 4000 rpm for 2 mins for the synthesis to occur, followed by a further centrifugation at 13.2 (x1000) rpm for 15 mins for purification. Samples were then re-suspended in water and characterised by UV-Vis before and after sonication (gentle for 30 min).

The UV-Vis spectra resulted already in line with the LSPR for AgNSs, even though slightly red-shifted. After sonication, cluster were desegregated demonstrating the characteristic absorption band.

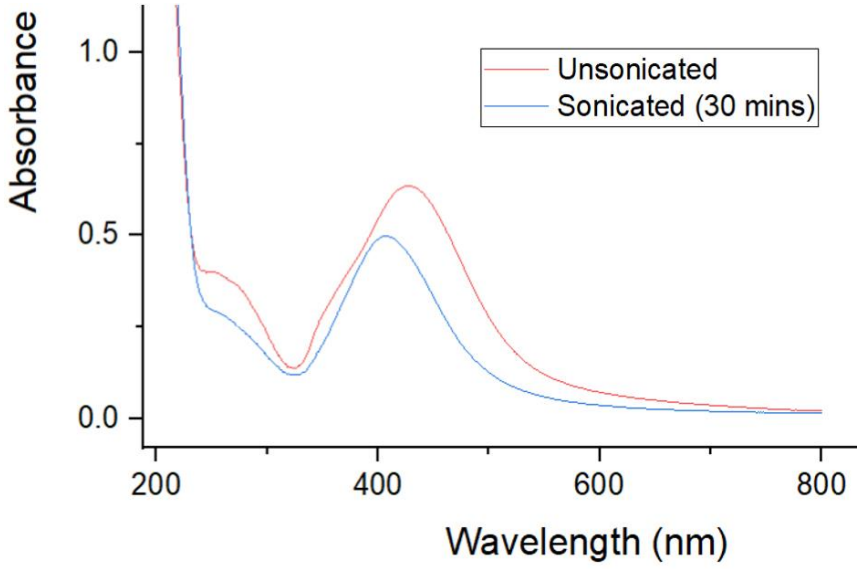

Appendix Fig. 8 UV-Vis bands of the AgNSs produced via the RIAC method, prior and after sonication.

C.2 TEM of the biggest AgNPr produced

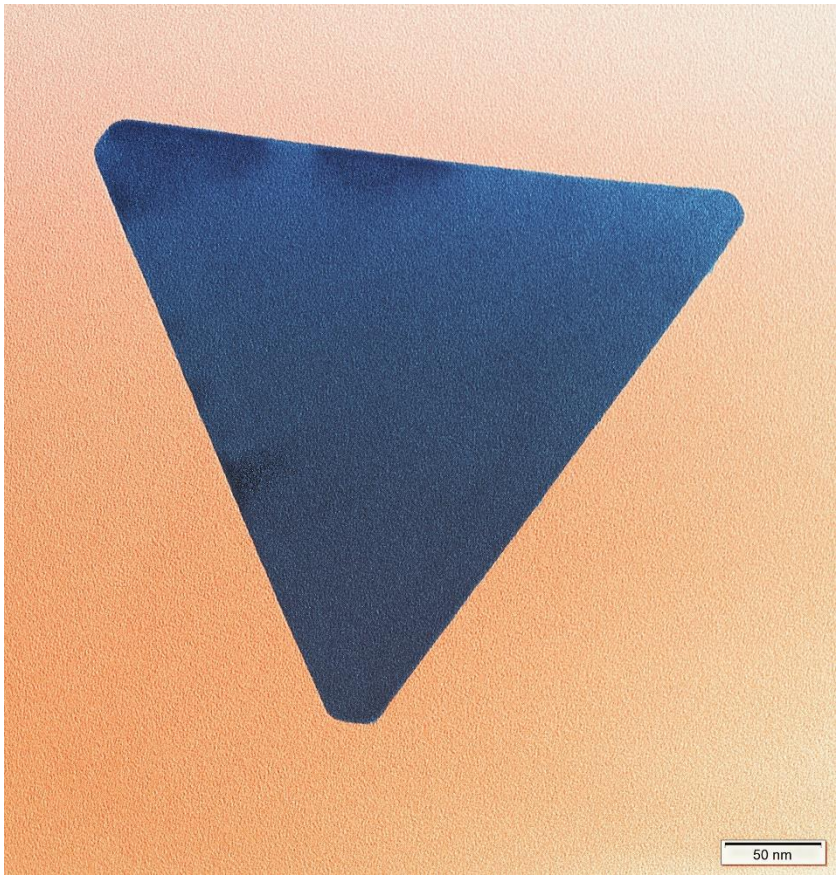

Appendix Fig. 9 The biggest AgNPrs produced (>300 nm) through the flow synthesis via the two inlets serpentine (TFR=50mL/min; FRR=7). Due to the relation with the edge length and the absorption shift towards the NIR, the aim was to try to obtain larger particles without breaking them. The TEM image, in this coloured version, was selected to participate to the RSC photography award 2019

C.3 CFD simulation

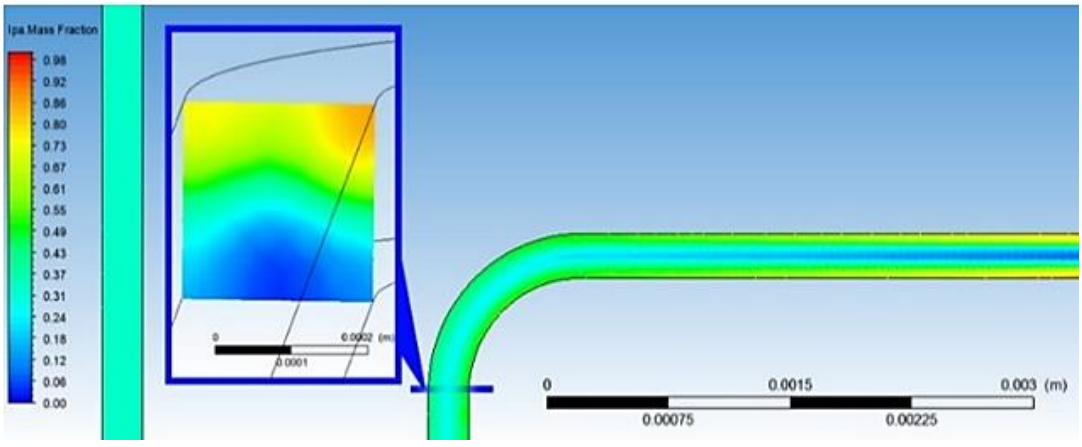

Appendix Fig. 10 Water (blue) IPA (red) mass fraction on CFD at TFR = 4mL/h and FRR 0.5. Cross section visualisation after the curved geometry show the effect of density in mass fraction distribution thus mixing and diffusion processes.

C.4 Coated optical fibre

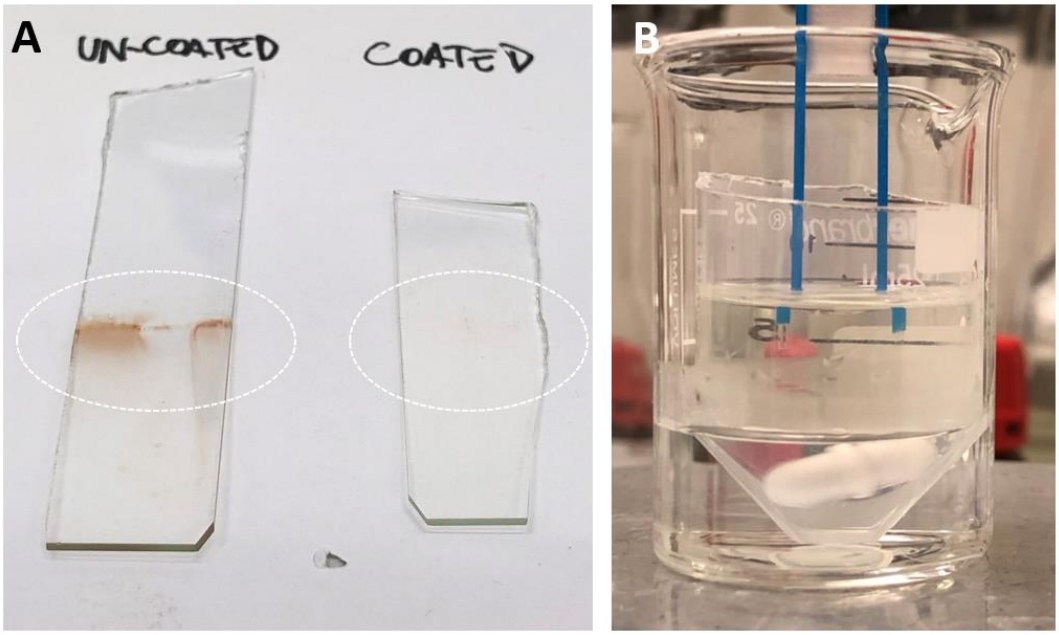

Appendix Fig. 11 A) Coated vs uncoated glass after immersion into a AgNSs solution (15 minutes). B) Photo taken during the coating procedure of two OFs.

Appendix D Silica coating and side projects

D.1 Purification test

The purification steps consisted in 30 minutes of centrifugation to evaluate the effect of the substitution of the TSCD with the mercaptohexanoic acid (MHA) on the LSPR (A_{max} and WA_{max} shifts).

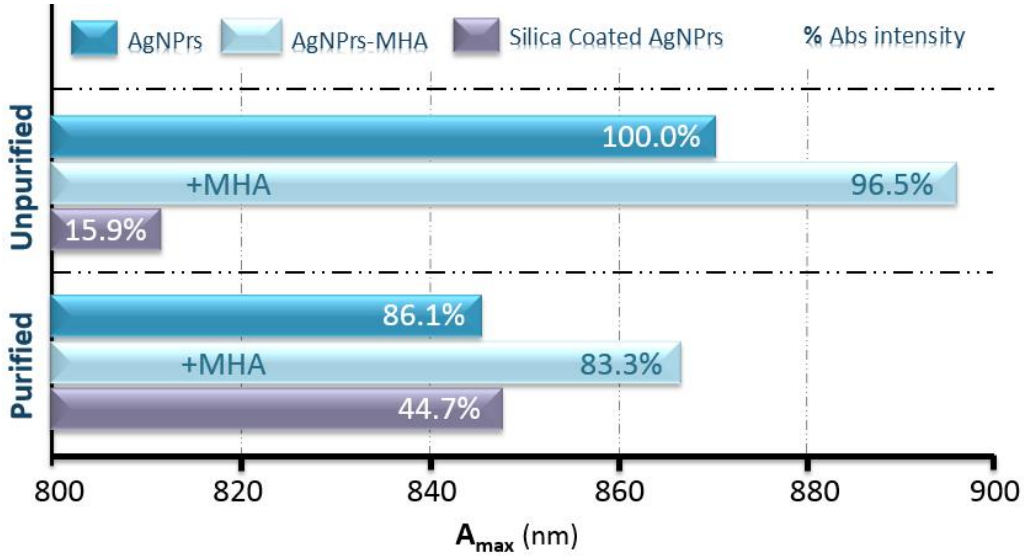

Appendix Fig. 12 Considering the WA_{max} of the starting samples at 870 nm with A_{max} 100%, this graph shows the absorption shifts and intensity drops after each step, referring to the purified and unpurified samples, after their interaction with MHA and the first coating protocol.

D.2 pH test

A pH test was performed in order to evaluate the effect of the MHA on the particles' surface and therefore on the LSPR. The AgNPrs (4mL) solution was centrifuged twice for 15 mins 13000 rpm to purify the sample and then re-dispersed in 4 mL milli-Q water. MHA (20 µL, 4 mM) was added, followed by 30 second shaking then left to stand for 3 minutes. Further centrifuged for 15 min at 13000 rpm, re-dispersion in milli-Q water and gentle sonication. Aliquots of HCl (0.01M) were added to gradually lower the pH and UV spectra were taken.

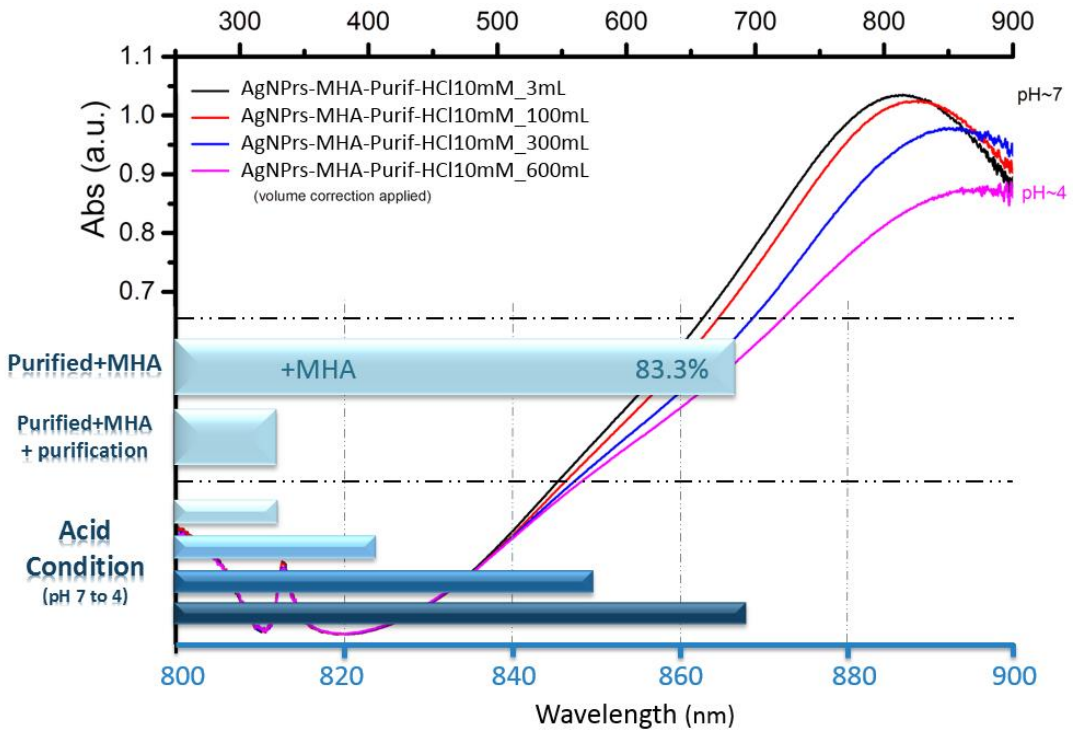

Appendix Fig.13 UV visible characterisation of the AgNPrs-MHA after each addition of HCl (X-axis at the top referring to the UV-vis spectra). Horizontal histograms describe the WA_{max} after a second purification and after adding the HCl (X-axis referring at the bottom from 800 to 900 nm).

D.3 Coating protocols adopted

The adopted coating protocols were tested with the help of the MSc student Angharad Jenkins. A modified Stober approach was adopted [198], which implies using tetraorthosilicate (TEOS) in basic ethanoic solution [199,200] and mercaptohexanoic acid (MHA) transfer to the basic ethanoic solution,[67]

Here 4 representative TEM over the 20 protocol variations tested named 1, 2(A,B); 3()A,B); 4(A,B,C); 5(A,B,C); 6(A,B,C); 7(A,B,C); 8(A,B,C). The number indicates variation in chemical order, centrifugation settings or reaction time; the letters indicate variation in reagents concentration and/or solvents.

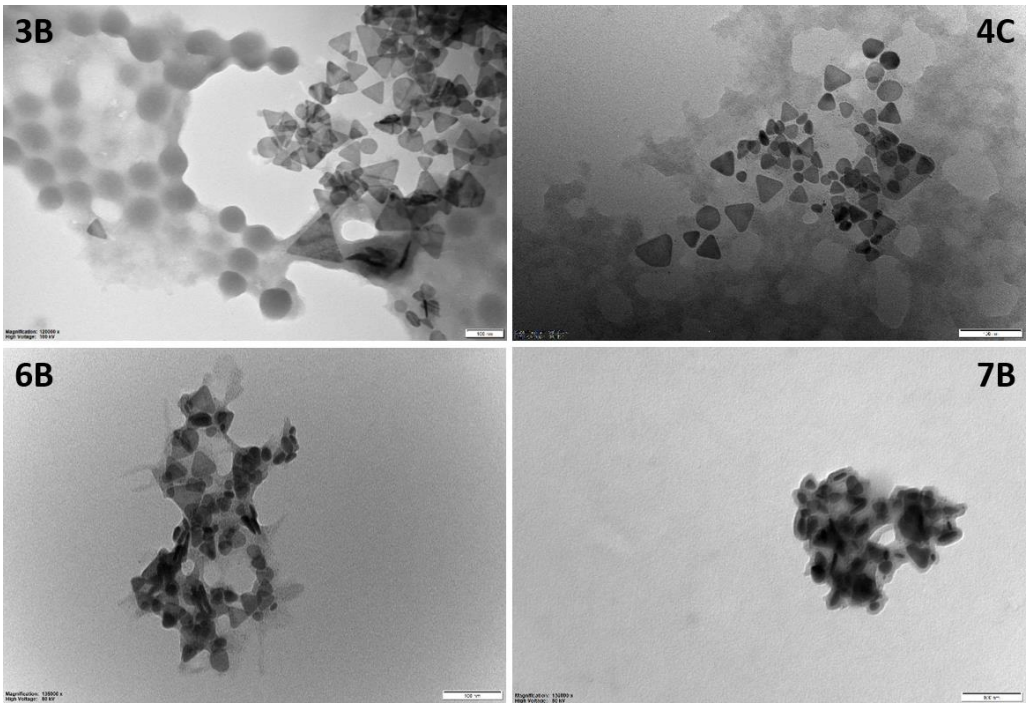

Appendix Fig. 14 Representative TEM imaging of the samples obtained during the research of the optimal formulation. It can be seen the formation of non-uniform coatings and silica clusters.

D.4 Final coating procedure

The adopted protocol corresponding to Figure 6.1 is described below:

- 4 x 1 mL samples centrifuged at 10000rpm for 30 mins
- Supernatant 950 µL removed. redispersed in 950 µL EtOH
- 80µL MHA (1mM) added – shaken for 30 seconds and left to stand for 5 minutes
- Gentle sonication
- Centrifuged for 30 minutes at 10000rpm
- Supernatant 950 µL removed. Over 4 samples, 3 redispersed in 950 µL EtOH, 1 redispersed in 950 µL water, mixed and gentle sonication.
- 100µL TEOS (40mM) added (1 mM overall)
- 310 µL DMA (50%) added and left to stir for 1 hour
- Quenched with 15 mL Ethanol
- Centrifuged at 11000rpm 30 minutes, supernatant removed and SNPs put in EtOH

D.5 Reaction scheme for nanofluids

In depth studies were carried out in collaboration with H. Kimpton on the SiO_2@AgNPrs employed for the thermal nanofluids, and the performance was also compared with silica- and AgNPRs-based nanofluids. [29]

Appendix scheme 1 Final reaction scheme adopted for the production of SiO_2@AgNPrs employed for thermal nanofluid characterisation

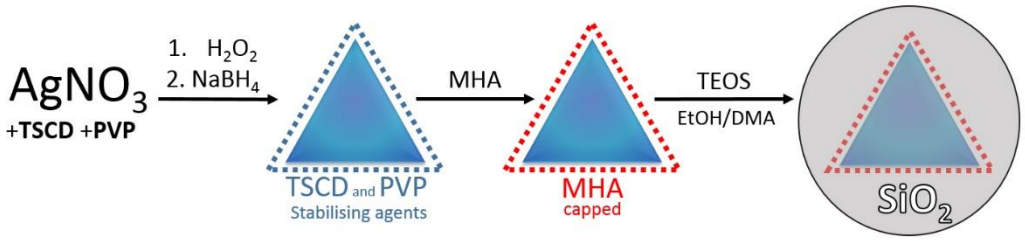

D.6 DNA-gold nanoparticles

Cobalt-porphyrin functionalised single strand DNA probes were connected onto gold nanoparticles in order to produce an ultrasensitive electrochemical genosensor. AuNs were initially produced, followed by the batch synthesis of the genosensor, which was carried out creating different DNA-AuNPs ratios. The published research described the electrode demonstrating the capability of approaches single molecules detection.[34]

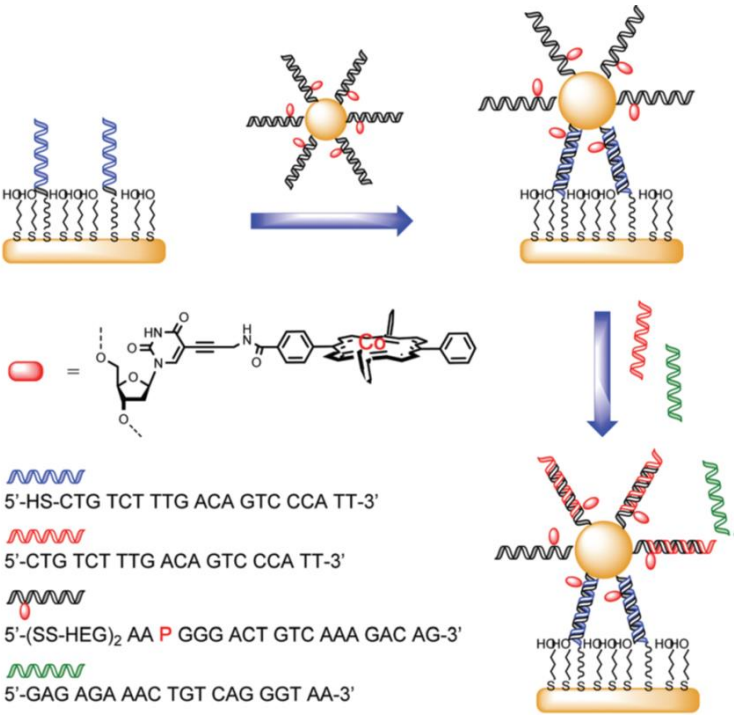

Appendix Fig.15 Schematic representation of the genosensor fabrication for the detection of the complementary DNA single strands.

Bibliography

1. Bhagyaraj, S. M. & Oluwafemi, O. S. Learn more about Lycurgus Cup Nanotechnology : The Science of the invisible. *Micro Nano Technol.* **Chapter 1**, 1–18 (2018).

2. Polette-Niewold, L. A., Manciu, F. S., Torres, B., Alvarado, M. & Chianelli, R. R. Organic/inorganic complex pigments: Ancient colors Maya Blue. *J. Inorg. Biochem.* **101**, 1958–1973 (2007).

3. Nordmann, A. Invisible origins of Nanotechnology: Herbert Gleiter, materials science, and questions of prestige. *Perspect. Sci.* **17**, 123–143 (2009).

4. Bera, D., Qian, L., Tseng, T. K. & Holloway, P. H. Quantum dots and their multimodal applications: A review. *Materials (Basel).* **3**, 2260–2345 (2010).

5. Iravani, S., Korbekandi, H., Mirmohammadi, S. V & Zolfaghari, B. Synthesis of silver nanoparticles: chemical, physical and biological methods. *Res. Pharm. Sci.* **9**, 385–406

6. Heinz, H. *et al.* Nanoparticle decoration with surfactants: Molecular interactions, assembly, and applications. *Surf. Sci. Rep.* **72**, 1–58 (2017).

7. Sumio I. Helical microtubules of graphitic carbon. *Nature* **354**, 56–58 (1991).

8. Kroto, W. H., Heath, J. R., O'Brien, S. C., Curl, R. F. & Smalley, R. C60 - The Thrid Man. *Nature* **318**, 162–163 (1985).

9. Gao, C., Guo, Z., Liu, J. H. & Huang, X. J. The new age of carbon nanotubes: An updated review of functionalized carbon nanotubes in electrochemical sensors. *Nanoscale* **4**, 1948–1963 (2012).

10. Yan, Q. L., Gozin, M., Zhao, F. Q., Cohen, A. & Pang, S. P. Highly energetic compositions based on functionalized carbon nanomaterials. *Nanoscale* **8**, 4799–4851 (2016).

11. Lin, J., Chen, X. & Huang, P. Graphene-based nanomaterials for bioimaging. *Advanced Drug Delivery Reviews* **105**, 242–254 (2016).

12. Owens, D. E. & Peppas, N. A. Opsonization, biodistribution, and pharmacokinetics of polymeric nanoparticles. *International Journal of Pharmaceutics* **307**, 93–102 (2006).

13. Hu, Q.-D., Tang, G.-P. & Chu, P. K. Cyclodextrin-Based Host–Guest Supramolecular Nanoparticles for Delivery: From Design to Applications. *Acc. Chem. Res.* **47**, 2017–2025 (2014).

14. Miceli, E., Kar, M. & Calderón, M. Interactions of organic nanoparticles with proteins in physiological conditions. *J. Mater. Chem. B* **5**, 4393–4405 (2017).

15. Venkatesh, N. Metallic Nanoparticle: A Review. *Biomed. J. Sci. Tech. Res.* **4**, 3765–3775 (2018).

16. Daniel, M.-C. & Astruc, D. Gold Nanoparticles: Assembly, Supramolecular Chemistry, Quantum-Size-Related Properties, and Applications toward Biology, Catalysis, and Nanotechnology. *Chem. Rev.* **104**, 293–346 (2004).

17. Panáček, A. *et al.* Silver colloid nanoparticles: Synthesis, characterization, and their antibacterial activity. *J. Phys. Chem. B* **110**, 16248–16253 (2006).

18. Zeng, S. *et al.* A Review on Functionalized Gold Nanoparticles for Biosensing Applications. *Plasmonics* **6**, 491–506 (2011).

19. Crooks, R. M., Zhao, M., Sun, L., Chechik, V. & Yeung, L. K. Dendrimer-Encapsulated Metal Nanoparticles: Synthesis, Characterization, and Applications to Catalysis. *Acc. Chem. Res.* **34**, 181–190 (2001).

20. Jiang, Y. & Pu, K. Advanced Photoacoustic Imaging Applications of Near-Infrared Absorbing Organic Nanoparticles. *Small* **13**, (2017).

21. Wu, F. *et al.* Small-Molecule Porphyrin-Based Organic Nanoparticles with Remarkable Photothermal Conversion Efficiency for in Vivo Photoacoustic Imaging and Photothermal Therapy. *ACS Appl. Mater. Interfaces* (2019). doi:10.1021/acsami.9b06866

22. Madamsetty, V. S., Mukherjee, A. & Mukherjee, S. Recent trends of the bio-inspired nanoparticles in cancer theranostics. *Front. Pharmacol.* **10**, 1264 (2019).

23. Guan, Y., Sun, T., Ding, J. & Xie, Z. Robust organic nanoparticles for noninvasive long-Term fluorescence imaging. *Journal of Materials Chemistry B* **7**, 6879–6889 (2019).

24. Chang, C., Han, L., Zhao, Y. & Li, F. pH-sensitive fluorescent organic nanoparticles: Off-on fluorescent detection of furfural in transformer oil. *Talanta* **197**, 383–389 (2019).

25. Boucard, J. *et al.* Phosphonic Acid Fluorescent Organic Nanoparticles for High-Contrast and Selective Staining of Gram-Positive Bacteria. *ACS Omega* **3**, 17392–17402 (2018).

26. Ahmed, M., Faisal, M., Ihsan, A. & Naseer, M. M. Fluorescent organic nanoparticles (FONs) as convenient probes for metal ion detection in aqueous medium. *Analyst* **144**, 2480–2497 (2019).

27. Ng, S. M., Koneswaran, M. & Narayanaswamy, R. A review on fluorescent inorganic nanoparticles for optical sensing applications. *RSC Adv.* **6**, 21624–21661 (2016).

28. Peiris, S., McMurtrie, J. & Zhu, H. Y. Metal nanoparticle photocatalysts: Emerging processes for green organic synthesis. *Catal. Sci. Technol.* **6**, 320–338 (2016).

29. Kimpton, H., Cristaldi, D. A., Stulz, E. & Zhang, X. Thermal performance and physicochemical stability of silver nanoprism-based nanofluids for direct solar absorption. *Sol. Energy* **199**, 366–376 (2020).

30. Zhou, H. *et al.* Biodegradable Inorganic Nanoparticles for Cancer Theranostics: Insights into the Degradation Behavior. *Bioconjug. Chem.* **31**, 315–331 (2020).

31. Mohammed, L., Gomaa, H. G., Ragab, D. & Zhu, J. Magnetic nanoparticles for environmental and biomedical applications: A review. *Particuology* **30**, 1–14 (2017).

32. Miller, K. P., Wang, L., Benicewicz, B. C. & Decho, A. W. Inorganic nanoparticles engineered to attack bacteria. *Chemical Society Reviews* **44**, 7787–7807 (2015).

33. Park, H. Y. *et al.* Green synthesis of carbon-supported nanoparticle catalysts by physical vapor deposition on soluble powder substrates. *Sci. Rep.* **5**, 1–8 (2015).

34. Kaur, B. *et al.* Approaching single DNA molecule detection with an ultrasensitive electrochemical genosensor based on gold nanoparticles and cobalt-porphyrin DNA conjugates. *Chem. Commun.* **54**, 11108–11111 (2018).

35. Shi, Z. *et al.* Self-assembled metal-organic nanoparticles for multimodal imaging-guided photothermal therapy of hepatocellular carcinoma. *J. Biomed. Nanotechnol.* **14**, 1934–1943 (2018).

36. Purcell, M. & Morin, D. J. *Electricity and Magnetism*. (Cambridge University Press, 2013).

37. Millikan, R. A. A direct photoelectric determination of planck's 'h'. *Phys. Rev.* **7**, 355–388 (1916).

38. Cristaldi, D. A., Impellizzeri, G., Priolo, F., Gupta, T. & Gulino, A. Structural, Electronic, and Electrical Properties of Y-Doped Cd 2 SnO 4. *J. Phys. Chem. C* **116**, 3363–3368 (2012).

39. Granqvist, C. G., Lansåker, P. C., Mlyuka, N. R., Niklasson, G. A. & Avendaño, E. Progress in chromogenics: New results for electrochromic and thermochromic materials and devices. *Sol. Energy Mater. Sol. Cells* **93**, 2032–2039 (2009).

40. Fracçkowiak, D., Planner, A., Wiktorowicz, K., Planner, A. & Wiktorowicz, K. *Near-Infrared Applications in Medicine*. (CRC Press, 2019).

41. Robitaille, P.-M. *Kirchhoff's Law of Thermal Emission: 150 Years*. *Progress in Physics* **4**, (2009).

42. Willets, K. A. & Van Duyne, R. P. Localized Surface Plasmon Resonance Spectroscopy and Sensing. *Annu. Rev. Phys. Chem.* **58**, 267–297 (2007).

43. Noguez, C. Surface Plasmons on Metal Nanoparticles: The Influence of Shape and Physical Environment. *J. Phys. Chem. C* **111**, 3806–3819 (2007).

44. D'Urso, A. *et al.* Sequence, stoichiometry, and dimensionality control in porphyrin/ biscalix[4]arene self-assemblies in aqueous solution. *Chem. - A Eur. J.* **16**, 10439–10446 (2010).

45. Cristaldi, D. A., Impellizzeri, G., Priolo, F., Gupta, T. & Gulino, A. Structural, Electronic, and Electrical Properties of Y-Doped Cd2SnO4. *J. Phys. Chem. C* **116**, 3363–3368 (2012).

46. Wang, Z. L. Transmission Electron Microscopy of Shape-Controlled Nanocrystals and Their Assemblies. *J. Phys. Chem. B* **104**, 1153–1175 (2002).

47. Carlo, S. De & Harris, J. R. *NIH Public Access*. **42**, (2012).

48. Lyumkis, D. Challenges and opportunities in cryo-EM single-particle analysis. *J. Biol. Chem.* **294**, 5181–5197 (2019).

49. Stetefeld, J., McKenna, S. A. & Patel, T. R. Dynamic light scattering: a practical guide and applications in biomedical sciences. *Biophysical Reviews* **8**, 409–427 (2016).

50. Kraemer, E. O. & Dexter, S. T. The Light-Scattering Capacity (Tyndall Effect) and Colloidal Behavior of Gelatine Sols and Gels. *J. Phys. Chem.* **31**, 764–782 (1927).

51. Whitesides, G. M. The origins and the future of microfluidics. *Nature* **442**, (2006).

52. *Microfluidics: Technologies and Applications*. (Springer, 2011).

53. Links, D. A. Microfluidic electronics. *Lab Chip* 2782–2791 (2012).

54. Belliveau, N. M. *et al.* Microfluidic Synthesis of Highly Potent Limit-size Lipid Nanoparticles for In Vivo Delivery of siRNA. *Mol. Ther. Acids* 1–9 (2012).

55. Volpatti, L. R. & Yetisen, A. K. Commercialization of microfluidic devices. *Trends Biotechnol.*

32, 347–350 (2014).

56. Shestopalov, I., Tice, J. D. & Ismagilov, R. F. Multi-step synthesis of nanoparticles performed on millisecond time scale in a microfluidic droplet-based system. *Lab Chip* **4**, 316–21 (2004).

57. Hood, R. R., Shao, C., Omiatek, D. M., Vreeland, W. N. & DeVoe, D. L. Microfluidic synthesis of PEG- and folate-conjugated liposomes for one-step formation of targeted stealth nanocarriers. *Pharm. Res.* **30**, 1597–607 (2013).

58. Gobby, D., Angeli, P. & Gavriilidis, A. Mixing characteristics of T-type microfluidic mixers. *J. Micromechanics Microengineering* **11**, 126–132 (2001).

59. Zhang, J. X. J. & Hoshino, K. Microfluidics and Micro Total Analytical Systems. in *Molecular Sensors and Nanodevices* 103–168 (Elsevier, 2014).

60. Gou, Y., Jia, Y., Wang, P. & Sun, C. Progress of inertial microfluidics in principle and application. *Sensors (Switzerland)* **18**, 1762 (2018).

61. Di Carlo, D. Inertial microfluidics. *Lab Chip* **9**, 3038 (2009).

62. Capretto, L., Carugo, D., Cheng, W., Hill, M. & Zhang, X. Continuous-flow production of polymeric micelles in microreactors: Experimental and computational analysis. *J. Colloid Interface Sci.* **357**, 243–251 (2011).

63. Illg, T., Löb, P. & Hessel, V. Flow chemistry using milli- and microstructured reactors-From conventional to novel process windows. *Bioorganic Med. Chem.* **18**, 3707–3719 (2010).

64. Kitson, P. J., Rosnes, M. H., Sans, V., Dragone, V. & Cronin, L. Configurable 3D-Printed millifluidic and microfluidic 'lab on a chip' reactionware devices. *Lab Chip* **12**, 3267 (2012).

65. Eggersdorfer, M. *et al.* Parallelization of microfluidic flow-focusing devices. *Phys. Rev. E* **95**, 1–6 (2017).

66. Hood, R. R. & Devoe, D. L. High-Throughput Continuous Flow Production of Nanoscale Liposomes by Microfluidic Vertical Flow Focusing. *Small* **11**, 5790–5799 (2015).

67. Carboni, M., Capretto, L., Carugo, D., Stulz, E. & Zhang, X. Microfluidics-based continuous flow formation of triangular silver nanoprisms with tuneable surface plasmon resonance. *J. Mater. Chem. C* **1**, 7540 (2013).

68. Kim, J. S. *et al.* Antimicrobial effects of silver nanoparticles. *Nanomedicine*

Nanotechnology, Biol. Med. **3**, 95–101 (2007).

69. Le Ouay, B. & Stellacci, F. Antibacterial activity of silver nanoparticles: A surface science insight. *Nano Today* **10**, 339–354 (2015).

70. Sosa, I. O., Noguez, C. & Barrera, R. G. Optical properties of metal nanoparticles with arbitrary shapes. *J. Phys. Chem. B* **107**, 6269–6275 (2003).

71. Alshehri, A. H. *et al.* Enhanced Electrical Conductivity of Silver Nanoparticles for High Frequency Electronic Applications. *ACS Appl. Mater. Interfaces* **4**, 7007–7010 (2012).

72. Si, G., Ma, Z., Li, K. & Shi, W. Triangular Au–Ag Nanoframes with Tunable Surface Plasmon Resonance Signal from Visible to Near-Infrared Region. *Plasmonics* **6**, 241–244 (2011).

73. Keblinski, P., Phillpot, S. R., Choi, S. U. S. & Eastman, J. A. Mechanisms of heat flow in suspensions of nano-sized particles (nanofluids). *Int. J. Heat Mass Transf.* **45**, 855–863 (2001).

74. Navjot, Tovstolytkin, A. & Lotey, G. S. Plasmonic Enhanced Photocatalytic Activity of Ag Nanospheres Decorated BiFeO3 Nanoparticles. *Catal. Letters* **147**, 1640–1645 (2017).

75. Zhang, X. *et al.* Plasmonic silver nanosphere enhanced ZnSe nanoribbon / Si heterojunction optoelectronic devices. *Nanotechnology* **27**, (2016).

76. Zhang, X. F., Liu, Z. G., Shen, W. & Gurunathan, S. Silver nanoparticles: Synthesis, characterization, properties, applications, and therapeutic approaches. *Int. J. Mol. Sci.* **17**, (2016).

77. Polte, J. *et al.* Formation mechanism of colloidal silver nanoparticles: Analogies and differences to the growth of gold nanoparticles. *ACS Nano* **6**, 5791–5802 (2012).

78. Sun, Y. & Xia, Y. Shape-controlled synthesis of gold and silver nanoparticles. *Science (80-.).* **298**, 2176–2179 (2002).

79. Nikoobakht, B. & El-Sayed, M. A. Preparation and growth mechanism of gold nanorods (NRs) using seed-mediated growth method. *Chem. Mater.* **15**, 1957–1962 (2003).

80. Sun, Y., Yin, Y., Mayers, B. T., Herricks, T. & Xia, Y. Uniform silver nanowires synthesis by reducing AgNO3 with ethylene glycol in the presence of seeds and poly(vinyl pyrrolidone). *Chem. Mater.* **14**, 4736–4745 (2002).

81. Millstone, J. E., Hurst, S. J., Métraux, G. S., Cutler, J. I. & Mirkin, C. A. Colloidal gold and

silver triangular nanoprisms. *Small* **5**, 646–664 (2009).

82. Lo, V. K. Y., Chan, A. O. Y. & Che, C. M. Gold and silver catalysis: From organic transformation to bioconjugation. *Org. Biomol. Chem.* **13**, 6667–6680 (2015).

83. Wang, Y. & Xia, Y. Bottom-up and top-down approaches to the synthesis of monodispersed spherical colloids of low melting-point metals. *Nano Lett.* **4**, 2047–2050 (2004).

84. Zhang, X. F., Liu, Z. G., Shen, W. & Gurunathan, S. Silver nanoparticles: Synthesis, characterization, properties, applications, and therapeutic approaches. *International Journal of Molecular Sciences* **17**, (2016).

85. Dakal, T. C., Kumar, A., Majumdar, R. S. & Yadav, V. Mechanistic basis of antimicrobial actions of silver nanoparticles. *Front. Microbiol.* **7**, (2016).

86. Lee, S. H. & Jun, B. H. Silver nanoparticles: Synthesis and application for nanomedicine. *International Journal of Molecular Sciences* **20**, (2019).

87. Amendola, V. & Meneghetti, M. Laser ablation synthesis in solution and size manipulation of noble metal nanoparticles. *Phys. Chem. Chem. Phys.* **11**, 3805–3821 (2009).

88. Hamouda, R. A., Hussein, M. H., Abo-elmagd, R. A. & Bawazir, S. S. Synthesis and biological characterization of silver nanoparticles derived from the cyanobacterium Oscillatoria limnetica. *Sci. Rep.* **9**, (2019).

89. Siddiqi, K. S., Husen, A. & Rao, R. A. K. A review on biosynthesis of silver nanoparticles and their biocidal properties. *Journal of Nanobiotechnology* **16**, (2018).

90. Mabey, T. *et al.* Bacteria and nanosilver: the quest for optimal production. *Crit. Rev. Biotechnol.* **39**, 272–287 (2019).

91. Ganaie, S. U., Abbasi, T. & Abbasi, S. A. Green synthesis of silver nanoparticles using an otherwise worthless weed mimosa (Mimosa pudica): Feasibility and process development toward shape/size control. *Part. Sci. Technol.* **33**, 638–644 (2015).

92. Roy, A., Bulut, O., Some, S., Mandal, A. K. & Yilmaz, M. D. Green synthesis of silver nanoparticles: Biomolecule-nanoparticle organizations targeting antimicrobial activity. *RSC Advances* **9**, 2673–2702 (2019).

93. Ranoszek-Soliwoda, K. *et al.* The role of tannic acid and sodium citrate in the synthesis of silver nanoparticles. *J. Nanoparticle Res.* **19**, (2017).

94. Bastús, N. G., Merkoçi, F., Piella, J. & Puntes, V. Synthesis of highly monodisperse citrate-stabilized silver nanoparticles of up to 200 nm: Kinetic control and catalytic properties. *Chem. Mater.* **26**, 2836–2846 (2014).

95. Carboni, M. Silver Nanoprisms Embedded in a Polymeric Matrix for Energy Saving Glazing. *PhD Thesis* (University of Southampton, 2014).

96. Khan, Z., Al-Thabaiti, S. A., Obaid, A. Y. & Al-Youbi, A. O. Preparation and characterization of silver nanoparticles by chemical reduction method. *Colloids Surfaces B Biointerfaces* **82**, 513–517 (2011).

97. Panzarasa, G. Just What Is It That Makes Silver Nanoprisms so Different, so Appealing? *J. Chem. Educ.* **92**, 1918–1923 (2015).

98. Paramelle, D. *et al.* A rapid method to estimate the concentration of citrate capped silver nanoparticles from UV-visible light spectra. *Analyst* **139**, 4855–61 (2014).

99. Carboni, M., Carravetta, M., Zhang, X. L. & Stulz, E. Efficient NIR light blockage with matrix embedded silver nanoprism thin films for energy saving window coating. *J. Mater. Chem. C* **4**, 1584–1588 (2016).

100. Pastoriza-Santos, I. & Liz-Marzan, L. M. Colloidal silver nanoplates. State of the art and future challenges. *J. Mater. Chem.* **18**, 1724–1737 (2008).

101. Jin, R. *et al.* Photoinduced conversion of silver nanospheres to nanoprisms. *Science (80-.).* **294**, 1901–1903 (2001).

102. Saade, J. & De Araújo, C. B. Synthesis of silver nanoprisms: A photochemical approach using light emission diodes. *Mater. Chem. Phys.* **148**, 1184–1193 (2014).

103. Aherne, D., Ledwith, D. M., Gara, M. & Kelly, J. M. Optical Properties and Growth Aspects of Silver Nanoprisms Produced by a Highly Reproducible and Rapid Synthesis at Room Temperature. *Adv. Funct. Mater.* **18**, 2005–2016 (2008).

104. Zhang, Z. *et al.* pH-controlled growth of triangular silver nanoprisms on a large scale. *Nanoscale Adv.* **1**, 4904–4908 (2019).

105. Metraux, G. S. & Mirkin, C. A. Rapid thermal synthesis of silver nanoprisms with chemically tailorable thickness. *Adv. Mater.* **17**, 412–415 (2005).

106. Zhang, Q., Li, N., Goebl, J., Lu, Z. & Yin, Y. A Systematic Study of the Synthesis of Silver Nanoplates : Is Citrate a “ Magic ” Reagent ? 18931–18939 (2011).

107. Haber, J. & Sokolov, K. Synthesis of stable citrate-capped silver nanoprisms. *Langmuir* **33**, 10525–10530 (2017).

108. Pastoriza-Santos, I. & Liz-Marzán, L. M. Colloidal silver nanoplates. State of the art and future challenges. *J. Mater. Chem.* **18**, 1724–1737 (2008).

109. Tsuji, M. *et al.* Rapid Transformation from Spherical Nanoparticles, Nanorods, Cubes, or Bipyramids to Triangular Prisms of Silver with PVP, Citrate, and H2O2. *Langmuir* **28**, 8845−8861 (2012).

110. Akwi, F. M. & Watts, P. Recent applications , challenges and limitations. *Chem. Commun.* **54**, 13894–13928 (2018).

111. Elvira, K. S., Casadevall, X., Wootton, R. C. R. & Andrew, J. reactor technology in chemical synthesis. *Nat. Chem.* **5**, 905–915 (2013).

112. Capretto, L., Carugo, D., Mazzitelli, S., Nastruzzi, C. & Zhang, X. Microfluidic and lab-on-a-chip preparation routes for organic nanoparticles and vesicular systems for nanomedicine applications. *Advanced Drug Delivery Reviews* **65**, 1496–1532 (2013).

113. Swaay, D. van & deMello, A. Microfluidic methods for forming liposomes. *Lab Chip* **13**, 752–767 (2013).

114. Hao, N., Nie, Y. & Zhang, J. X. J. Microfluidic synthesis of functional inorganic micro-/nanoparticles and applications in biomedical engineering. *Int. Mater. Rev.* **63**, 461–487 (2018).

115. Leester-Schadel, M., Lorenx, T., Jurgens, F. & Richter, C. *Fabrication of Microfluidic Devices*. (Springer International Publishing Switzerland, 2016).

116. Ma, Y., Thiele, J., Abdelmohsen, L., Xu, J. & Huck, W. T. S. Biocompatible macro-initiators controlling radical retention in microfluidic on-chip photo-polymerization of water-in-oil emulsions. *Chem. Commun. (Camb).* **50**, 112–4 (2014).

117. Dong, J., Liu, J., Kang, G., Xie, J. & Wang, Y. Pushing the resolution of photolithography down to 15nm by surface plasmon interference. *Sci. Rep.* **4**, 5618 (2014).

118. Jafek, A. *et al.* A Review of Current Methods in Microfluidic Device Fabrication and Future Commercialization Prospects. *Inventions* **3**, 60 (2018).

119. Hood, R. R., Wyderko, T. & DeVoe, D. L. Programmable digital droplet microfluidics using a multibarrel capillary bundle. *Sensors Actuators B Chem.* **220**, 992–999 (2015).

120. Carrilho, E., Martinez, A. W. & Whitesides, G. M. Understanding Wax Printing: A Simple Micropatterning Process for Paper-Based Microfluidics. *Anal. Chem.* **81**, 7091–7095 (2009).

121. Yuen, P. K. & Goral, V. N. Low-cost rapid prototyping of flexible microfluidic devices using a desktop digital craft cutter. *Lab Chip* **10**, 384–387 (2010).

122. Baber, R., Mazzei, L., Thanh, N. T. K. & Gavriilidis, A. Synthesis of silver nanoparticles in a microfluidic coaxial flow reactor. *RSC Adv.* **5**, 95585–95591 (2015).

123. Xia, Y. & Whitesides, G. M. Soft lithography. *Annu. Rev. Mater. Sci.* **28**, 153–184 (1998).

124. Whitesides, G. M., Ostuni, E., Jiang, X. & Ingber, D. E. Soft lithography in biology and biochemistry. *Annu. Rev. Biomed. Eng* 335–73 (2001).

125. Carugo, D. *et al.* Facile and cost-effective production of microscale PDMS architectures using a combined micromilling-replica moulding (μ Mi-REM) technique. *Biomed Microdevices* **18**, 1–10 (2016).

126. European Centre for Ecotoxicology and Toxicology of Chemicals. *Linear Polydimethylsiloxanes*. **9**, (2011).

127. Lucas, N., Demming, S., Jordan, A., Sichler, P. & Büttgenbach, S. An improved method for double-sided moulding of PDMS. *J. Micromechanics Microengineering* **18**, 075037 (2008).

128. Bhattacharya, S., Datta, A., Berg, J. M. & Gangopadhyay, S. Studies on surface wettability of poly(dimethyl) siloxane (PDMS) and glass under oxygen-plasma treatment and correlation with bond strength. *J. Microelectromechanical Syst.* **14**, 590–597 (2005).

129. Lamberti, A., Marasso, S. L. & Cocuzza, M. PDMS membranes with tunable gas permeability for microfluidic applications. *RSC Adv.* **4**, 61415–61419 (2014).

130. Chan, H. N. *et al.* Direct, one-step molding of 3D-printed structures for convenient fabrication of truly 3D PDMS microfluidic chips. *Microfluid. Nanofluidics* **19**, 9–18 (2015).

131. Chen, Z., Han, J. Y., Shumate, L., Fedak, R. & Devoe, D. L. High Throughput Nanoliposome Formation Using 3D Printed Microfluidic Flow Focusing Chips. **1800511**, 1–9 (2019).

132. Hassan, S.-U., Nightingale, A. M. & Niu, X. Continuous measurement of enzymatic kinetics in droplet flow for point-of-care monitoring. *Analyst* **141**, 3266–73 (2016).

133. Comina, G., Suska, A. & Filippini, D. PDMS lab-on-a-chip fabrication using 3D printed templates. *Lab Chip* **14**, 424–30 (2014).

134. Gaal, G. *et al.* Simplified fabrication of integrated microfluidic devices using fused deposition modeling 3D printing. *Sensors Actuators B Chem.* **242**, 35–40 (2017).

135. Chen, C. *et al.* 3D-printed Microfluidic Devices: Fabrication, Advantages and Limitations-a Mini Review. *Anal. Methods* **8**, 6005–6012 (2016).

136. Gong, H., Beauchamp, M., Perry, S., Woolley, A. T. & Nordin, G. P. Optical approach to resin formulation for 3D printed microfluidics. *RSC Adv.* **5**, 3627–3637 (2015).

137. Gong, H., Bickham, B., Woolley, A. T. & Nordin, G. P. Custom 3D printer and resin for 18 µm × 20 µm microfluidic flow channels. *Lab Chip* (2017).

138. Serra, M. *et al.* A simple and low-cost chip bonding solution for high pressure, high temperature and biological applications. *Lab Chip* **17**, 629–634 (2017).

139. Cristaldi, D. A. *et al.* Easy-to-perform and cost-effective fabrication of continuous-flow reactors and their application for nanomaterials synthesis. *N. Biotechnol.* **47**, 1–7 (2018).

140. Kong, L. X., Perebikovsky, A., Madou, M., Moebius, J. & Kulinsky, L. Lab-on-a-CD. *Annu. Rev. Biomed. Eng.* 8:601-28 (2006).

141. Kong, L. X., Perebikovsky, A., Moebius, J., Kulinsky, L. & Madou, M. Lab-on-a-CD: A Fully Integrated Molecular Diagnostic System. *J. Lab. Autom.* **21**, 323–355 (2016).

142. Peytavi, R. *et al.* From cellular lysis to microarray detection, an integrated thermoplastic elastomer (TPE) point of care Lab on a Disc. *Lab Chip* **15**, 406–416 (2014).

143. Kloke, A. *et al.* The LabTube-a novel microfluidic platform for assay automation in laboratory centrifuges. *Lab Chip* **14**, 1527–1537 (2014).

144. Hoehl, M. M. *et al.* A versatile-deployable bacterial detection system for food and environmental safety based on LabTube-automated DNA purification, LabReader-integrated amplification, readout and analysis. *Analyst* **139**, 2788–2798 (2014).

145. Cristaldi, D. A., Labanca, A., Owen, J., Stulz, E. & Carugo, D. 3D Printed Reactor-in-a-Centrifuge (Riac): a Novel Approach To the Production of Organic Nanomaterials. in *XXII International Conference on Miniaturized Systems for Chemistry and Life Sciences (µTAS)* 2142–2144 (2018).

146. García-Manrique, P. *et al.* Continuous flow production of size-controllable niosomes using a thermostatic microreactor. *Colloids Surfaces B Biointerfaces* **182**, 110378 (2019).

147. Zmijan, R., Carboni, M., Capretto, L., Stulz, E. & Zhang, X. In situ microspectroscopic monitoring within a microfluidic reactor. *RSC Adv.* **4**, 14569–14572 (2014).

148. Nivedita, N., Ligrani, P. & Papautsky, I. Dean Flow Dynamics in Low-Aspect Ratio Spiral Microchannels. *Sci. Rep.* **7**, (2017).

149. Nivedita, N. & Papautsky, I. Continuous separation of blood cells in spiral microfluidic devices. *Biomicrofluidics* **7**, 54101 (2013).

150. Zhang, J. *et al.* Fundamentals and applications of inertial microfluidics: A review. *Lab on a Chip* **16**, 10–34 (2016).

151. Carugo, D., Bottaro, E., Owen, J., Stride, E. & Nastruzzi, C. Liposome production by microfluidics: potential and limiting factors. *Sci. Rep.* **6**, 25876 (2016).

152. Kim, Y. M., Kim, W. S., Lee, S. H. & Baek, J. Y. Effects of surface roughness on the flow characteristics in PDMS microchannels. in *3rd IEEE/EMBS Special Topic Conference on Microtechnology in Medicine and Biology* **2005**, 292–295 (2005).

153. Bottaro, E., Mosayyebi, A., Carugo, D. & Nastruzzi, C. Analysis of the diffusion process by pH indicator in microfluidic chips for liposome production. *Micromachines* **8**, 1–16 (2017).

154. Lin, X. Z., Terepka, A. D. & Yang, H. Synthesis of silver nanoparticles in a continuous flow tubular microreactor. *Nano Lett.* **4**, 2227–2232 (2004).

155. Wagner, J., Tshikhudo, T. R. & Köhler, J. M. Microfluidic generation of metal nanoparticles by borohydride reduction. *Chem. Eng. J.* **135**, 104–109 (2007).

156. Okafor, O. *et al.* Advanced reactor engineering with 3D printing for the continuous-flow synthesis of silver nanoparticles. *React. Chem. Eng.* **2**, 129–136 (2017).

157. Harvey, A. P., Mackley, M. R. & Stonestreet, P. Operation and optimization of an oscillatory flow continuous reactor. *Ind. Eng. Chem. Res.* **40**, 5371–5377 (2001).

158. Xu, L., Peng, J., Yan, M., Zhang, D. & Shen, A. Q. Droplet synthesis of silver nanoparticles by a microfluidic device. *Chem. Eng. Process. Process Intensif.* **102**, 186–193 (2016).

159. Kašpar, O., Koyuncu, A. H., Pittermannová, A., Ulbrich, P. & Tokárová, V. Governing factors for preparation of silver nanoparticles using droplet-based microfluidic device. *Biomed. Microdevices* **21**, (2019).

160. Hills, E. E., Abraham, M. H., Hersey, A. & Bevan, C. D. Diffusion coefficients in ethanol and

in water at 298K: Linear free energy relationships. *Fluid Phase Equilib.* **303**, 45–55 (2011).

161. Paramelle, D. *et al.* A rapid method to estimate the concentration of citrate capped silver nanoparticles from UV-visible light spectra. *Analyst* **139**, 4855–4861 (2014).

162. Bangham, A. D., Standish, M. M. & Watkins, J. C. Diffusion of univalent ions across the lamellae of swollen phospholipids. *J. Mol. Biol.* **13**, 238–252 (1965).

163. Akbarzadeh, A., Rezaei-sadabady, R., Davaran, S., Joo, S. W. & Zarghami, N. Liposome : classification , preparation , and applications. *Nanoscale Res. Lett.* **8**, 1–9 (2013).

164. Wadhwa, S. *et al.* Nanovesicles for nanomedicine: Theory and practices. in *Methods in Molecular Biology* **2000**, 1–17 (Humana Press Inc., 2019).

165. Safinya, C. R. & Ewert, K. K. Materials chemistry: Liposomes derived from molecular vases. *Nature* **489**, 372–374 (2012).

166. Zhu, X., Peng, Y. & Qiu, L. Amino-functionalized nano-vesicles for enhanced anticancer efficacy and reduced myelotoxicity of carboplatin. *Colloids Surfaces B Biointerfaces* **157**, 56–64 (2017).

167. Goh, W. J. *et al.* Doxorubicin-loaded cell-derived nanovesicles: An alternative targeted approach for anti-tumor therapy. *Int. J. Nanomedicine* **12**, 2759–2767 (2017).

168. Zhang, P. *et al.* Genetically Engineered Liposome-like Nanovesicles as Active Targeted Transport Platform. *Adv. Mater.* **30**, 1705350 (2018).

169. Anwekar, H., Patel, S. & Singhai, A. K. Liposome-as drug carriers. *Int. J. Pharm. Life Sci.* **2**, 945–951 (2011).

170. Kubitschke, J., Javor, S. & Rebek, J. Deep cavitand vesicles - Multicompartmental hosts. *Chem. Commun.* **48**, 9251–9253 (2012).

171. Bozzuto, G. & Molinari, A. Liposomes as nanomedical devices. *Int. J. Nanomedicine* **10**, 975–99 (2015).

172. Bulbake, U., Doppalapudi, S., Kommineni, N. & Khan, W. Liposomal formulations in clinical use: An updated review. *Pharmaceutics* **9**, 1–33 (2017).

173. Abdelkader, H., Alani, A. W. G. & Alany, R. G. Recent advances in non-ionic surfactant vesicles (niosomes): Self-assembly, fabrication, characterization, drug delivery applications and limitations. *Drug Delivery* **21**, 87–100 (2014).

174. Lee, J. S. & Feijen, J. Polymersomes for drug delivery: Design, formation and characterization. *Journal of Controlled Release* **161**, 473–483 (2012).

175. Gutiérrez, G. *et al.* Iron-entrapped niosomes and their potential application for yogurt fortification. *LWT - Food Sci. Technol.* **74**, 550–556 (2016).

176. De, S., Kundu, R. & Biswas, A. Synthesis of gold nanoparticles in niosomes. *J. Colloid Interface Sci.* **386**, 9–15 (2012).

177. Puras, G. *et al.* Protamine/DNA/niosome ternary nonviral vectors for gene delivery to the retina: The role of protamine. *Mol. Pharm.* **12**, 3658–3671 (2015).

178. Justo, O. R. & Moraes, Â. M. Analysis of process parameters on the characteristics of liposomes prepared by ethanol injection with a view to process scale-up: Effect of temperature and batch volume. *Chem. Eng. Res. Des.* **89**, 785–792 (2011).

179. Grimaldi, N. *et al.* Lipid-based nanovesicles for nanomedicine. *Chemical Society Reviews* **45**, 6520–6545 (2016).

180. Yu, B., Lee, R. J. & Lee, L. J. Microfluidic Methods for Production of Liposomes. *Methods in Enzymology* **465**, 129–141 (2009).

181. Liu, C., Feng, Q. & Sun, J. Lipid Nanovesicles by Microfluidics: Manipulation, Synthesis, and Drug Delivery. *Adv. Mater.* **31**, 1804788 (2019).

182. Isalomboto Nkanga, C., Murhimalika Bapolisi, A., Ikemefuna Okafor, N. & Werner Maçedo Krause, R. General Perception of Liposomes: Formation, Manufacturing and Applications. in *Liposomes - Advances and Perspectives* (IntechOpen, 2019). doi:10.5772/intechopen.84255

183. Carugo, D., Bottaro, E., Owen, J., Stride, E. & Nastruzzi, C. Liposome production by microfluidics: Potential and limiting factors. *Sci. Rep.* **6**, 1–15 (2016).

184. Sahin, N. O. Niosomes as nanocarrier systems. in *Nanomaterials and Nanosystems for Biomedical Applications* 67–81 (Springer Netherlands, 2007).

185. Van Swaay, D. & Demello, A. Microfluidic methods for forming liposomes. *Lab Chip* **13**, 752–767 (2013).

186. Jahn, A., Vreeland, W. N., Gaitan, M. & Locascio, L. E. Controlled Vesicle Self-Assembly in Microfluidic Channels with Hydrodynamic Focusing. *J. Am. Chem. Soc.* **126**, 2674–2675 (2004).

187. Briuglia, M.-L., Rotella, C., McFarlane, A. & Lamprou, D. A. Influence of cholesterol on liposome stability and on in vitro drug release. *Drug Deliv. Transl. Res.* **5**, 231–242 (2015).

188. Thoma, K. & Jocham, U. E. Liposome Dermatics: Assessment of Long-Term Stability. in *Liposome Dermatics* 150–166 (Springer Berlin Heidelberg, 1992).

189. Takeuchi, H. *et al.* Physical stability of size controlled small unilameller liposomes coated with a modified polyvinyl alcohol. *Int. J. Pharm.* **164**, 103–111 (1998).

190. Mahmud, M., Piwoni, A., Filiczak, N., Janicka, M. & Gubernator, J. Long-Circulating Curcumin-Loaded Liposome Formulations with High Incorporation Efficiency, Stability and Anticancer Activity towards Pancreatic Adenocarcinoma Cell Lines In Vitro. *PLoS One* **11**, e0167787 (2016).

191. Hashmi, A. & Xu, J. On the quantification of mixing in microfluidics. *J. Lab. Autom.* **19**, 488–91 (2014).

192. Danaei, M. *et al.* Impact of particle size and polydispersity index on the clinical applications of lipidic nanocarrier systems. *Pharmaceutics* **10**, 1–17 (2018).

193. Ge, X., Wei, M., He, S. & Yuan, W. E. Advances of non-ionic surfactant vesicles (niosomes) and their application in drug delivery. *Pharmaceutics* **11**, (2019).

194. Lo, C. T., Jahn, A., Locascio, L. E. & Vreeland, W. N. Controlled self-assembly of monodisperse niosomes by microfluidic hydrodynamic focusing. *Langmuir* **26**, 8559–8566 (2010).

195. Nanocomposites, Nanoparticles, Nanoclays and Nanotubes: Global Markets to 2022. Available at: https://www.bccresearch.com/market-research/nanotechnology/nanocomposites-nanoparticles-nanoclays-and-nanotubes-global-markets.html.

196. Frankowski, M. *et al.* Microflow Cytometers with Integrated Hydrodynamic Focusing. *Sensors* **13**, 4674–4693 (2013).

197. Saggiomo, V. & Velders, A. H. Simple 3D Printed Scaffold-Removal Method for the Fabrication of Intricate Microfl uidic Devices. *Adv. Sci.* 1–5 (2015).

198. Stober, W., Fink, A. & Ernst Bohn, D. *Controlled Growth of Monodisperse Silica Spheres in the Micron Size Range 1*. *Journal of Colloid and Interface Science* **26**, (1968).

199. Graf, C., Vossen, D. L. J., Imhof, A. & Van Blaaderen, A. A general method to coat colloidal

particles with silica. *Langmuir* **19**, 6693–6700 (2003).

200. Lismont, M., Páez, C. A. & Dreesen, L. A one-step short-time synthesis of Ag@SiO2 core–shell nanoparticles. *J. Colloid Interface Sci.* **447**, 40–49 (2015).